UNIVERSITY COLLEGE LONDON

Faculty of Mathematics and Physical Sciences

Department of Physics & Astronomy

A Theoretical Framework to Understand the Diversity of Exoplanet Atmospheres with Current and Future Observatories

Thesis submitted for the Degree of Doctor of
Philosophy at University College London

by

Marcell Tessenyi

Supervisors:
Professor Giovanna Tinetti
Professor Alan Aylward

Examiners:
Professor Ian Howarth
Dr. Pierre Drossart

April 27, 2014

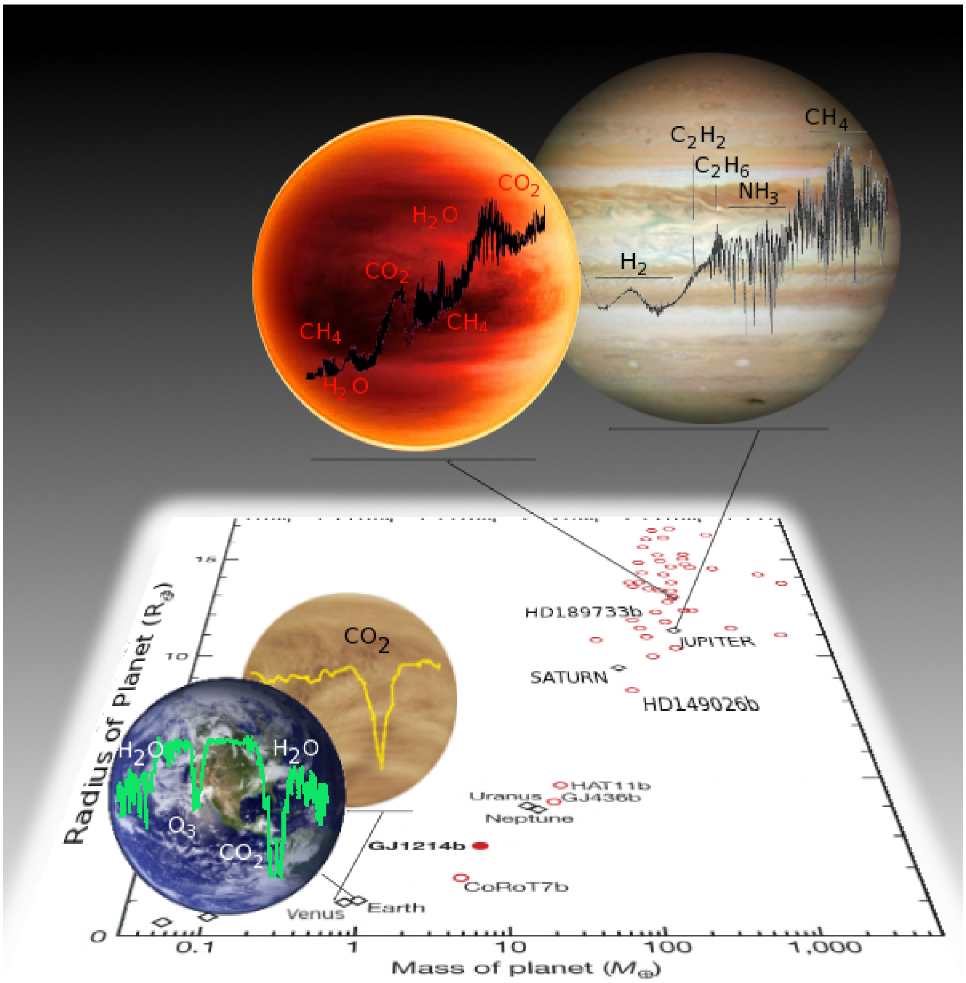

Figure 0.1: Planets of similar mass and radius can have very different atmospheres, as demonstrated in our solar system by Venus and Earth, and also with one of the most observed exoplanets to date (HD189733b) compared to Jupiter. To fully understand these worlds and place our solar system planets into context, it is essential to study the atmospheres of exoplanets. This is the underlying motive of the work presented in this thesis.

I, Marcell Tessenyi, confirm that the work presented in this thesis is my own. Where information has been derived from other sources, I confirm that this has been indicated in the thesis.

Abstract

The exoplanet field has been evolving at an astonishing rate: nearly two thousand planets have been detected and many more are awaiting confirmation. Astronomers have begun classifying these planets by mass, radius and orbital parameters, but these numbers tell us only part of the story as we know very little about their chemical composition. Spectroscopic observations of exoplanet atmospheres can provide this missing information, critical for understanding the origin and evolution of these distant worlds. Currently, transit spectroscopy and direct imaging spectroscopy are the most promising methods to achieve this goal. Ground and space-based observations (Very Large Telescope (VLT), W. M. Keck Observatory, Infrared Telescope Facility (IRTF), Spitzer Space Telescope, Hubble Space Telescope (HST)) of exoplanets have shown the potentials of the transit method. However, the instruments used in the past ten years were not optimised for this task: the available data are mostly photometric or low resolution spectra with low signal to noise. The interpretation of these — often sparse — data is generally a challenge.

With the arrival of new facilities (Gemini Planet Imager (GMI) on the Gemini Telescope, Spectro-Polarimetric High-contrast Exoplanet Research (SPHERE) on the VLT, the European Extremely Large Telescope (E-ELT), the James Webb Space Telescope (JWST)), and possibly dedicated space instruments such as the Exoplanet Characterisation Observatory (EChO), many questions needed to be tackled in a more systematic way. The focus of this thesis is to provide a theoretical framework to address the question of molecular detectability in exoplanet atmospheres with current and future facilities.

The atmospheric components and their spectroscopic signals depend strongly on the planetary temperature and size, therefore I have simulated a significant sample of planets out of a range of sizes and temperatures, to describe comprehensively the chemical compositions

that can be expected in those exotic worlds. Such simulations were convolved through instrument simulators to assess performance and limitations of current and future facilities. While my study has been inspired by transit spectroscopy with a hypothetical EChO-like space-based instrument, the methodology and results of this thesis are applicable to observations with other instruments and techniques.

To my family and loved ones.

Contents

List of Figures

List of Tables

Chapter 1

Introduction

The exoplanet field has been evolving at an astonishing rate: over 1700 planets have been detected (Schneider 2014) and many more are awaiting confirmation (Borucki *et al.* 2011; Batalha *et al.* 2013; Fressin *et al.* 2013). Astronomers have begun classifying these planets by mass, radius, age and orbital parameters, but these numbers tell us only part of the story as we know very little about their chemical composition. Spectroscopic observations of exoplanet atmospheres can provide this missing information, critical for understanding the origin and evolution of these far away worlds. At present, transit spectroscopy and direct imaging spectroscopy are the most promising methods to achieve this goal. Ground and space-based observations (VLT, Keck, IRTF, Spitzer, and the Hubble Space Telescope) of exoplanets have shown the potentials of the transit method: current observations of hot gaseous planets have revealed the presence of alkali metals, water vapour, carbon monoxide and dioxide and methane in these exotic environments (e.g. Charbonneau *et al.* 2002; Knutson *et al.* 2007b; Tinetti *et al.* 2007; Beaulieu *et al.* 2008; Redfield *et al.* 2008; Grillmair *et al.* 2008; Snellen *et al.* 2008; Swain *et al.* 2008b, 2009b,a; Bean *et al.* 2010; Beaulieu *et al.* 2010; Crossfield *et al.* 2010; Stevenson *et al.* 2010; Snellen *et al.* 2010; Tinetti *et al.* 2010b; Berta *et al.* 2012; Crouzet *et al.* 2012; de Kok *et al.* 2013; Deming *et al.* 2013; Swain *et al.* 2013; Waldmann *et al.* 2013b). However, the instruments used in the past ten years were not optimised for this task, so the available data are mostly photometric or low resolution spectra with low signal to noise. Additionally, multiple observations are often required, during which many effects can alter the signal: from the weather on the planet to other sources of noise including instrument systematics and stellar variability. The interpretation of these — often sparse — data is generally a challenge (Swain *et al.* 2009b,a; Madhusudhan and Seager 2009; Lee *et al.* 2012; Line *et al.* 2012).

The arrival of new facilities such as Gemini/GPI, VLT/SPHERE, E-ELT and *JWST*, and possibly dedicated space instruments such as *EChO* (Tinetti *et al.* 2012a), is opening up a new era for the spectral observation of exoplanets.

The work presented in this thesis is based on these developments, and provides a theoretical framework which looks at all the parameters needed to be able to understand the chemical compositions of newly found exoplanets with current and upcoming facilities.

In this chapter, we present the state of the field in terms of exoplanets known today and the expected results in the near future. In chapter 2, we discuss the concepts of radiative transfer and their application to simulations of planetary spectra. In chapter 3, we discuss the limits of detectability of molecules in exoplanet atmospheres. Finally in chapter 4, we present the limits on the target types that are expected to be observed with a dedicated space telescope through calculation of integration times.

1.1 The exoplanets we know today

The work presented in this thesis would not be possible were it not for the groundbreaking discoveries of the first exoplanets (PSR-1257+12B by Wolszczan and Frail (1992), and 51 Pegasus B by Mayor and Queloz (1995)), which were followed by a cascade of planet discoveries that have helped set up this field and turn it into one of the most exciting topics in modern astrophysics. What follows is a brief summary of the various techniques devised and used to find these new worlds, and what information is gained as a byproduct of the discovery process.

1.1.1 Methods of Detection

1.1.1.1 Radial velocity and Astrometry

Radial velocity and astrometric measurements both rely on the same phenomenon: the movement of a star due to the gravitational pull of its surrounding planet(s). The difference between the methods lies in how this movement is measured: astrometry records the change in position of a star in the sky plane, as it is orbiting the centre of mass of the system, while the radial velocity technique records the change in Doppler shift of the star as it moves away or towards the point of observation. If, due to the inclination of the planetary orbit, a star moves predominantly in a radial direction to our line of sight, the radial velocity method is best suited, but if the movement is tangential, astrometry is the appropriate measurement method.

1.1.1.2 Radial Velocity

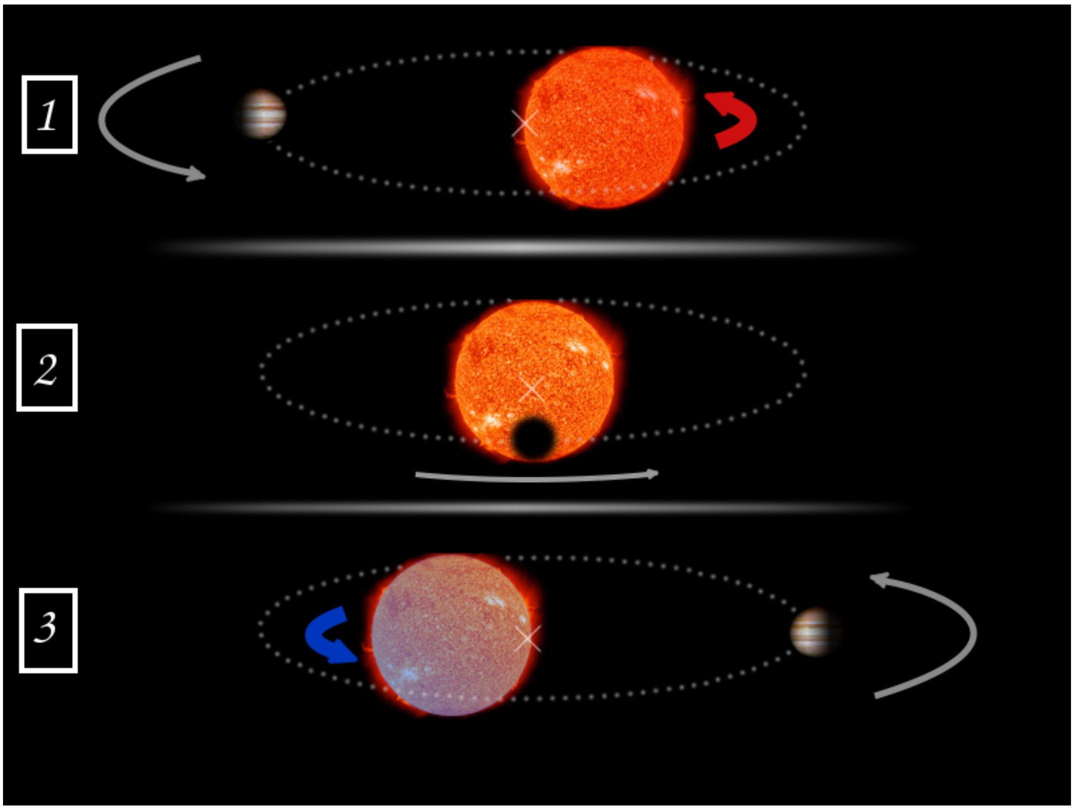

Figure 1.1: The radial velocity method relies on measuring the movement of the star to and from the observer, as it orbits around the planet+star center of mass (indicated as a white cross). 1: the planet is on a slightly inclined orbit, traveling counter-clockwise. As it is traveling towards the observer, the host star travels away, in effect appearing redder due to the doppler effect. 2: as the planet and star are aligned with our line of sight, the observed radial velocity of the star due to the planet is nul. 3: the planet travels away from the observer, and the star is blueshifted as it travels towards the observer.

Information retrieved: Period, semi-major axis, minimum planet mass. Most sensitive to large-mass planets in close orbits.

The radial velocity technique relies on measuring the Doppler shift of spectral lines from the star, as it moves towards or away from the observer (see Figure 1.1). The observed system gives the period and velocity amplitude. If the mass of the star is known, the period (Kepler's third law: $P = 2\pi\sqrt{a^3/GM_*}$) provides the semi-major axis a:

$$a^3 = \frac{GM_*}{4\pi^2} P^2 \tag{1.1}$$

From which the orbital velocity of the planet is calculated:

$$v_{pl} = \sqrt{GM_*/a} \tag{1.2}$$

And with conservation of momentum the mass of the planet is found via the mass and velocity of the star:

$$M_{pl} = \frac{M_*\, v_*}{v_{pl}} \tag{1.3}$$

The velocity amplitude of the star will depend on the inclination of the planetary orbit with respect to our line of sight. If this value is unknown, only a minimum velocity $v_* = v_* sin(i)$ and hence minimum mass of planet can be determined. Figure 1.2 illustrates the change in orbital velocity of the star as a function of orbit phase. This technique has

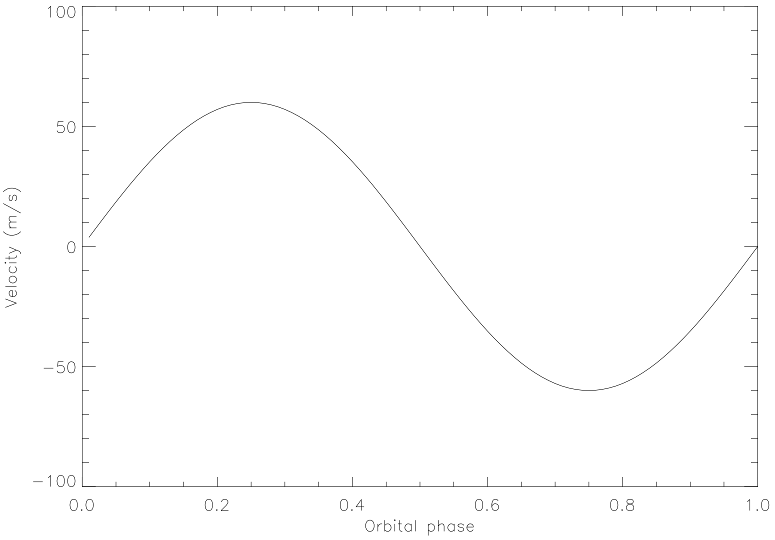

Figure 1.2: Velocity of the star as a function of orbital phase. As the star travels back and forth along our line of sight, the doppler effect on the observed spectrum reveals the stellar velocity. This is a minimum value however, if the inclination of the orbit is not known.

been the most successful in finding planets until recently, with over 550 planets discovered[1]. The transit technique has however recently surpassed this method in the number of planet discoveries. The first successful discovery of an exoplanet with this method, Pegasi 51 b, was published by Mayor and Queloz (1995).

1.1.1.3 Astrometry

Information retrieved: Period, semi-major axis, orbit inclination, planet mass. Sensitive to massive planets on large orbits.
The astrometric method requires high accuracy measurements (e.g.: a Jupiter-mass planet in a 5-year orbit around a Sun-type star at 200pc will have an apparent semi-major axis of the motion of the star of $\alpha \sim 15\mu as$ (Casertano and Sozzetti 1999), see equation 1.4), which are difficult to achieve with ground based instruments. While this method has been used to monitor binary star systems, no exoplanet has been found with this method to date. The upcoming GAIA space mission, using this method is expected to detect up to a thousand planets (Sozzetti 2010b) during its operating lifetime. The difficulty of this method is highlighted by the following equation, the apparent semi-major axis of the stellar orbit (Sozzetti 2010a):

$$\alpha = \left(\frac{M_p}{M_\odot}\right)\left(\frac{M_\odot}{M_*}\right)\left(\frac{a_p}{1\ \mathrm{AU}}\right)\left(\frac{\mathrm{pc}}{d}\right) \tag{1.4}$$

where M_p is the mass of the exoplanet, a_p the semi-major axis of the exoplanet and d the distance from the observer in pc. From this equation it can be seen that large planetary mass, small stellar mass and large semi-major axis systems are the most suited for these measurements.

---

[1] The Extrasolar Planet Encyclopedia, retrieved April 4 2014, http://www.exoplanet.eu

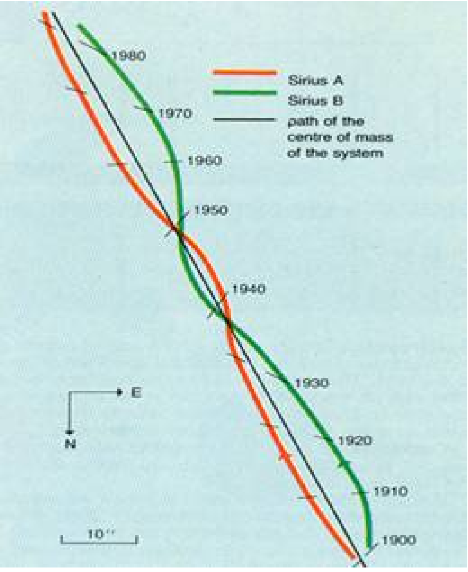

Figure 1.3: The astrometry detection method was first used on binary stars, observing the changes in position of the star along its travel path. The same principle can be applied to monitoring planets orbiting their star, however on smaller orbits and shorter periods.

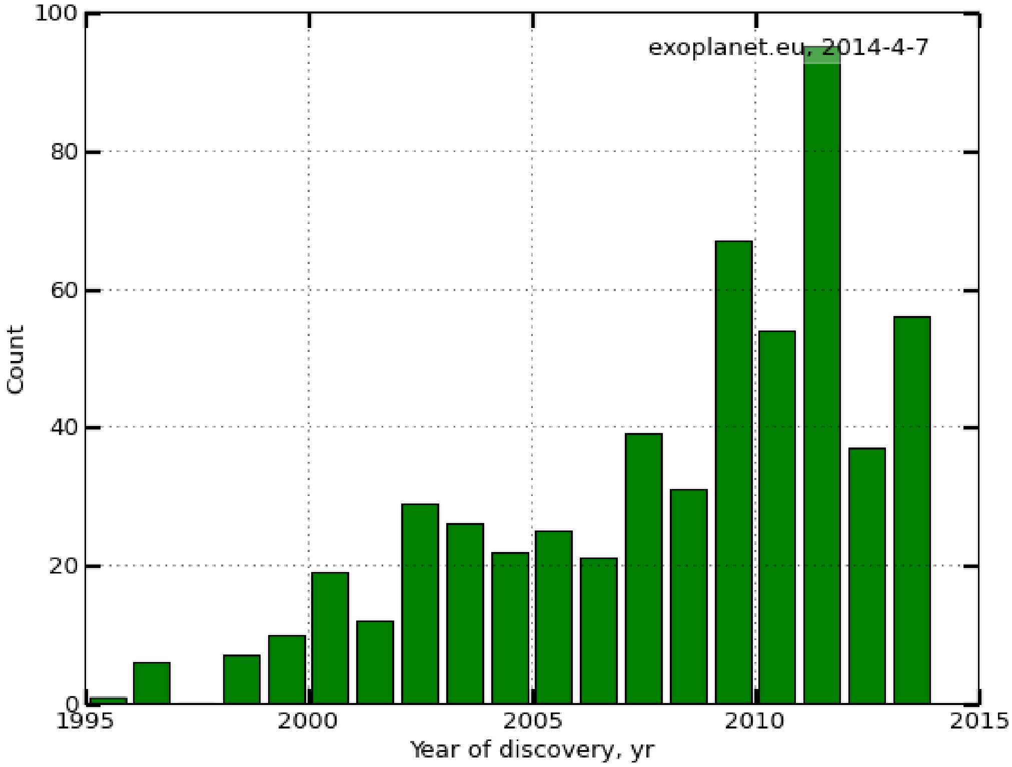

Figure 1.4: Number of planets discovered with the radial velocity and astrometry methods per year. The radial velocity method has been the most successful at detecting exoplanets, with over 550 planets found.

1.1.1.4 Transit method

Information retrieved: Period, planet radius (relative to star), orbit inclination. Sensitive to planet/star cross-section ratio (R_p/R_s), in particular to large planets in close orbits. The transit method is suited only to detect planets that have an orbital inclination very close to our line of sight, and thus "transit" in front of their host star. When a planet transits in front of its star, an event referred to as *primary transit*, the observed brightness of the star is diminished by a small amount for the duration of the transit. The depth of the reduction in brightness is in fact related to the cross-section ($\sigma = \pi \cdot R^2$) ratio between the planet and the star (κ):

$$\kappa = \sigma_p/\sigma_* \tag{1.5}$$

κ changes significantly for different planet/star types: in Table 1.1, we give σ_* for a few key stellar types, along with the cross-section ratio value κ for three planetary types considered. It is worth noting that a Jupiter-sized planet orbiting a Sun-like star and a super-Earth orbiting a M4.5 dwarf will both have a similar cross-section ratio $\kappa \sim \kappa_{Jup.}$.
During a transit, the light passing through the atmosphere of the planet will cross a small annulus:

$$\frac{2R_p\pi\Delta z}{\pi{R_\star}^2} = \frac{2R_p\Delta z}{{R_\star}^2} \tag{1.6}$$

where R_p is the radius of the planet, $R_\star$ the radius of the star and Δz the height of the atmosphere. From observations $\Delta z = nH$, with typically $n \sim 5$, depending on the spectral resolution and wavelength. H is the scale height defined by:

$$H = \frac{k\,T}{\mu\,g} \tag{1.7}$$

where k is the Boltzmann constant, g is the gravity acceleration and μ the mean molecular mass of the atmosphere.
Half an orbit later, when the planet is close to being occulted by its star, the (dayside) surface of the planet is in full view. During this part of the orbit, the planet shows maximum reflection and thermal emission to our telescopes, which increases slightly the brightness of the observed system. As the planet travels behind its star, the brightness

drops to the natural brightness of the star; this event is referred to as *secondary eclipse*. The difference in flux during a secondary eclipse is thus the emission from the star only and the star+planet contribution, and so this difference is smaller than during the primary transit event. This difference is expressed as the flux emitted and/or reflected by the planet in units of the stellar flux:

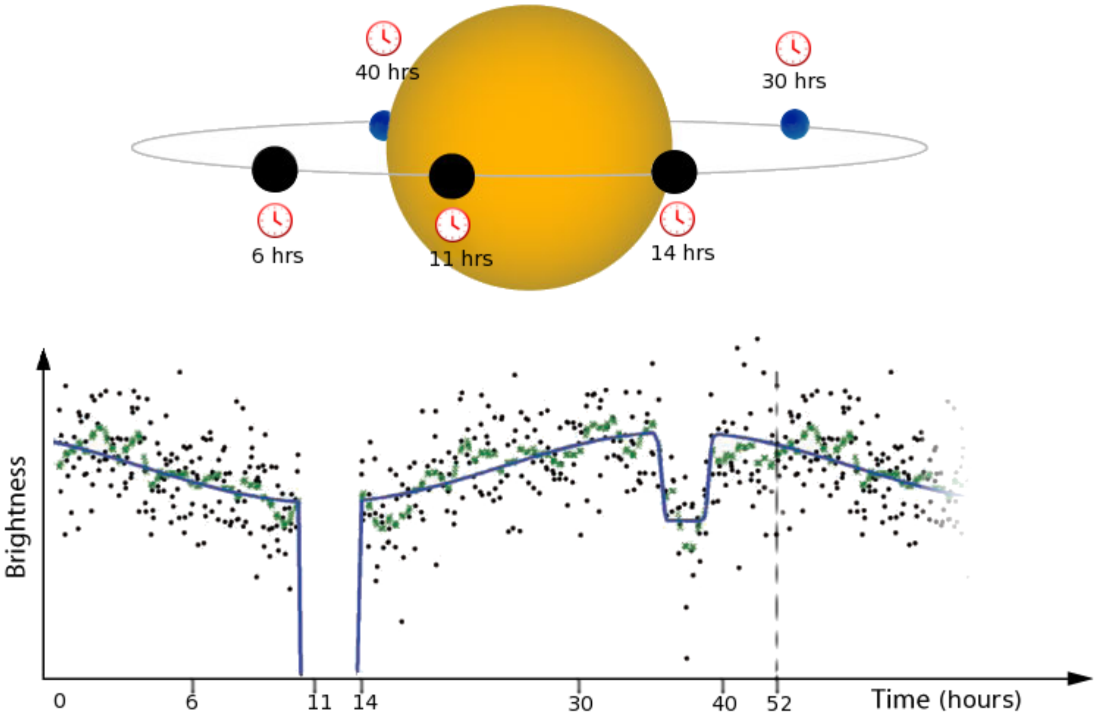

Figure 1.5: Transiting planets: the brightness of the star+planet system observed by Kepler during a full orbit of a transiting planet, HAT-P 7b (Borucki *et al.* 2009). During the primary transit ($t = 10 - 14hrs$) the brightness of the star drops clearly, then recovers and increases as the planet starts reflecting light as it is close to travel behind its host star ($t = 30hrs$). During the secondary eclipse, the brightness drops again, and recovers when the planet re-appears and is reflecting light again ($t = 40hrs$).

$$F_{II}(\lambda) = \kappa \frac{F_p(\lambda)}{F_*(\lambda)} \tag{1.8}$$

where κ is again the cross-section ratio (eq. 1.5) and $F_{p,*}(\lambda)$ are the wavelength dependent fluxes of the planet and star, respectively. Figure 1.5 illustrates the effect of both the primary transit and secondary eclipses on a full orbit observed brightness.

This method has recently become the most successful at finding exoplanets, with over 1100 planets found, and many more awaiting confirmation (Borucki *et al.* 2011; Batalha *et al.* 2013; Fressin *et al.* 2013).

Star type	Temp. (K)	Radius ($R_\odot$)	σ_* ($\sigma_\odot$)	$\kappa_{Jup.}$ (κ_J)	$\kappa_{Nept.}$ (κ_J)	κ_{SE} (κ_J)
F3V	6740K	1.56	$\sigma_{F3} \sim 2.4$	~ 0.5	~ 0.05	$\sim$0.01
G2V	5800K	1	$\sigma_G = \sigma_\odot$	1	~ 0.1	~ 0.02
K1V	4980K	0.8	$\sigma_{K1} \sim 0.6$	~ 2	~ 0.2	~ 0.03
M1.5V	3582K	0.42	$\sigma_{M1.5} \sim 0.18$	~ 6	~ 0.7	~ 0.1
M3.5V	3376K	0.26	$\sigma_{M3.5} \sim 0.07$	~ 15	~ 2	~ 0.3
M4.5V	3151K	0.17	$\sigma_{M4.5} \sim 0.03$	~ 35	~ 4	~ 0.7
M6V	2812K	0.12	$\sigma_{M6} \sim 0.01$	~ 70	~ 9	~ 2

Table 1.1: Cross section $\sigma_* = \pi R_*^2$ for different stellar types and corresponding κ values for the three planet sizes considered: Jupiter-like, Neptune-like and super-Earth. It is worth noting that super-Earths in the orbit of late M stars have a similar ratio κ to a Jupiter in the orbit of a Sun-like star.

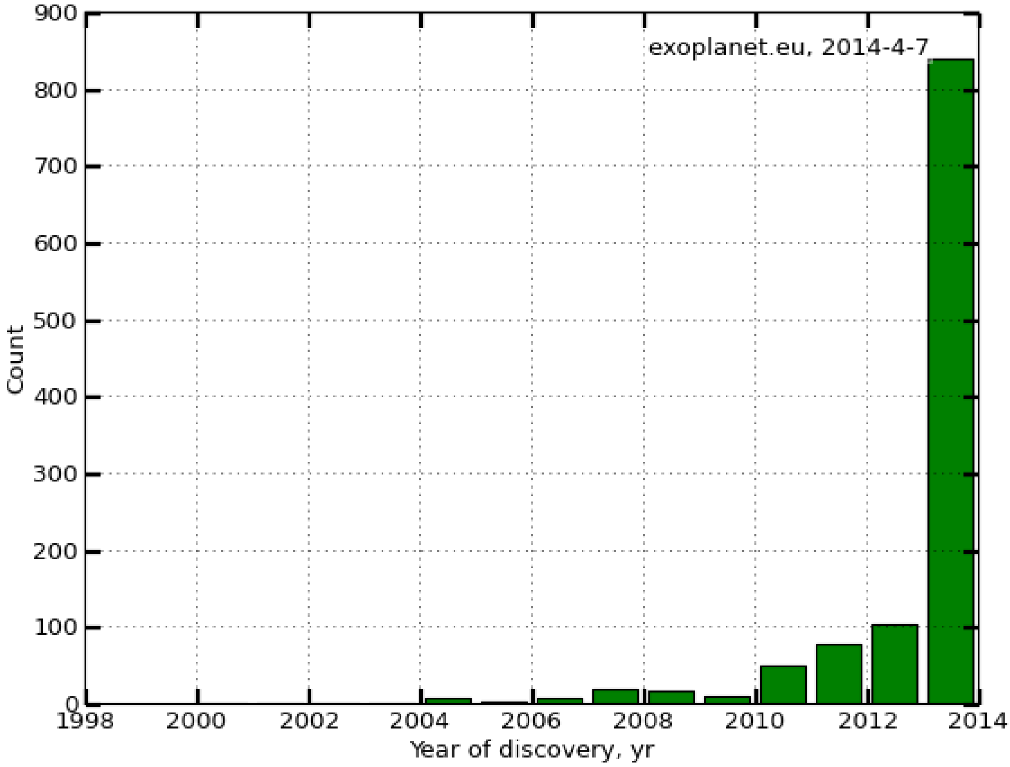

Figure 1.6: Number of planets discovered with the transit technique per year.

The transit technique is of particular interest for this thesis, as it allows us to probe the atmospheres of exoplanets by the use of spectroscopic measurements. These planets are thus the main focus of this thesis as they play a key role in our understanding of the diversity of exoplanets. The remote sensing methods used to probe their atmospheres are detailed in the following chapters.

1.1.1.5 Microlensing

Information retrieved: Mass of planet, semi-major axis.

Most sensitive to planets with semi-major axis between 1 and 5 AU, can find planets with masses down to $\sim 1M_{\oplus}$.

First discussed by Einstein (1936), this method relies on a stochastic event that takes place across large distances. Gravitational microlensing occurs when a massive object, usually a star, happens to travel momentarily across the line of sight between a distant luminous source and the observer. The gravitational field of the lensing object bends the light rays coming from the distant observed source, and acts as a focusing lens. An increase in brightness may then be observed for a finite time. The geometry of a lensing event is depicted on Figure 1.7. The apparent position of the source (indiciated by I on the diagram) relative to the real position S is defined by the angles β and θ:

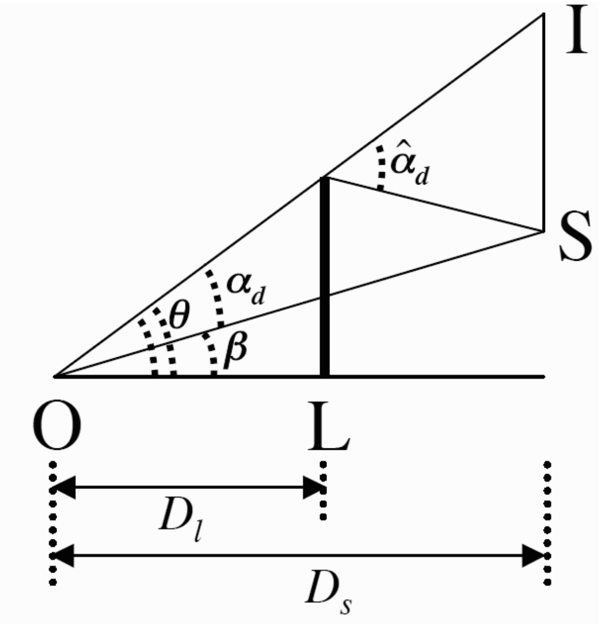

Figure 1.7: Geometry of microlensing events. The observer O is located at a distance D_s from the source (S) plane, with the lensing object (L) located at a distance D_l. The apparent location of the source is indicated by I, at an angle θ. If the source S travels into a position along the line OL, the lensing object L acts as a focusing lens, and a momentary increase in brightness is observed at O. If the lensing object hosts a planet, the planet's gravitational field can be an extra source of magnification. From Gaudi (2011).

$$\beta = \theta - \frac{4GM}{c^2\theta}\frac{D_s - D_l}{D_s D_l} \tag{1.9}$$

where M is the mass of the lensing object, and $D_{s,l}$ the distances from the observer to source planet and lensing plane. When the source and lensing objects are aligned with the observer, the angle $\theta = 0$, and equation 1.9 becomes:

$$\theta_E = \sqrt{\frac{4GM}{c^2}\frac{D_s - D_l}{D_s D_l}} \tag{1.10}$$

where θ_E is referred to as angular radius of the *Einstein ring.*

For observations, such a ring will magnify the brightness of a distant source, and if the lensing object is accompanied by a planet, an additional magnification component will appear. Figure 1.8 shows an example of a lensing magnification event as a function of time, that is perturbed by a small planet. For exoplanet detection surveys, monitoring a high number of distant sources is required, as the lensing events are rare and cannot be predicted. Lensing events happen only once, and usually cannot be followed up due to the large distances at which the lensing object are from us (typically many kiloparsecs). This method has thus been helpful at obtaining a statistical understanding of planet occurrence rates (Cassan *et al.* 2012), and so far over 20 planets have been directly found with this technique. This method has the benefit of not being biased towards large planets in close orbits; in fact it is most efficient at detecting planets on Earth to Jupiter orbits (1 to 5 AU). Additionally, this technique has the potential of revealing free floating planets (Gould and Yee 2013).

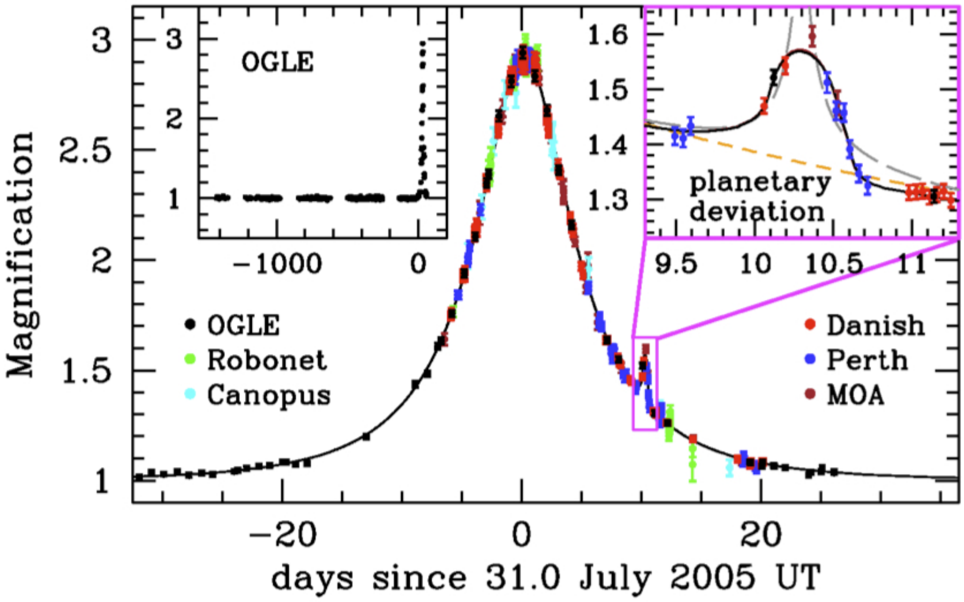

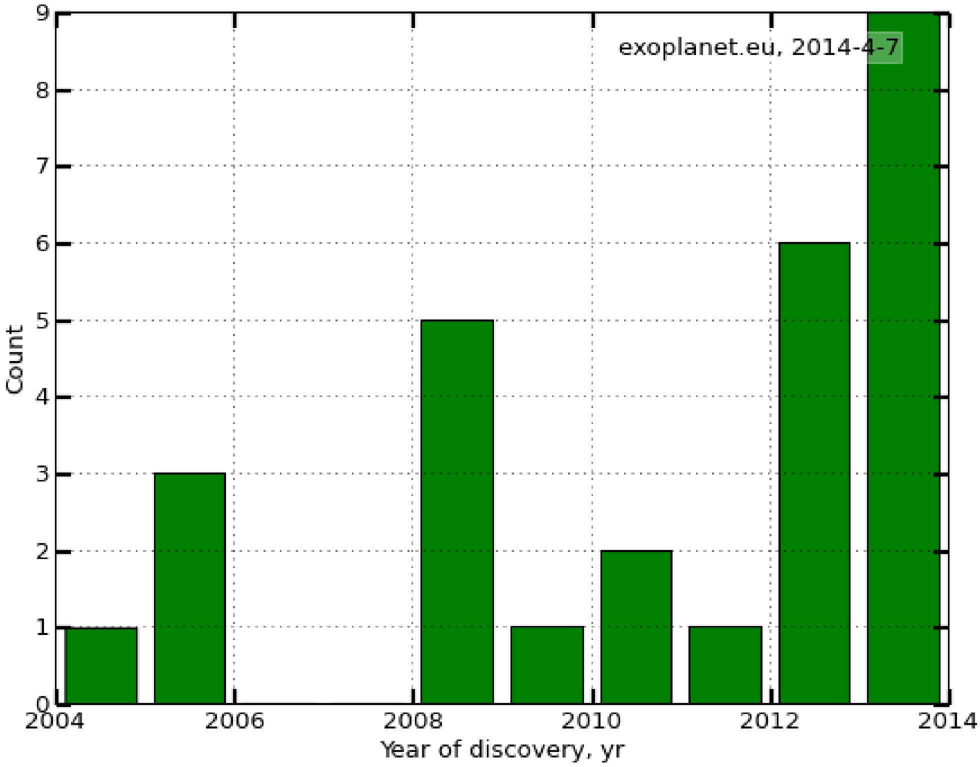

Figure 1.8: *Top:* Observed light curve of a microlensing event (OGLE-2005-BLG-390). A small peak can be seen, revealing the presence of a small planet (5.5 Earth masses) orbiting the lensing object (Beaulieu *et al.* 2006). *Below:* Number of planets discovered with the microlensing technique per year.

1.1.1.6 Pulsar Timing

Information retrieved: Period, mass, semi-major axis, eccentricity.

Pulsar timing works by measuring the frequency of the radio signal emitted by the fast-spinning neutron star. Small variations in the timing can be detected if a planet orbits a pulsar. At the time of writing, 14 planets have been detected with this method.

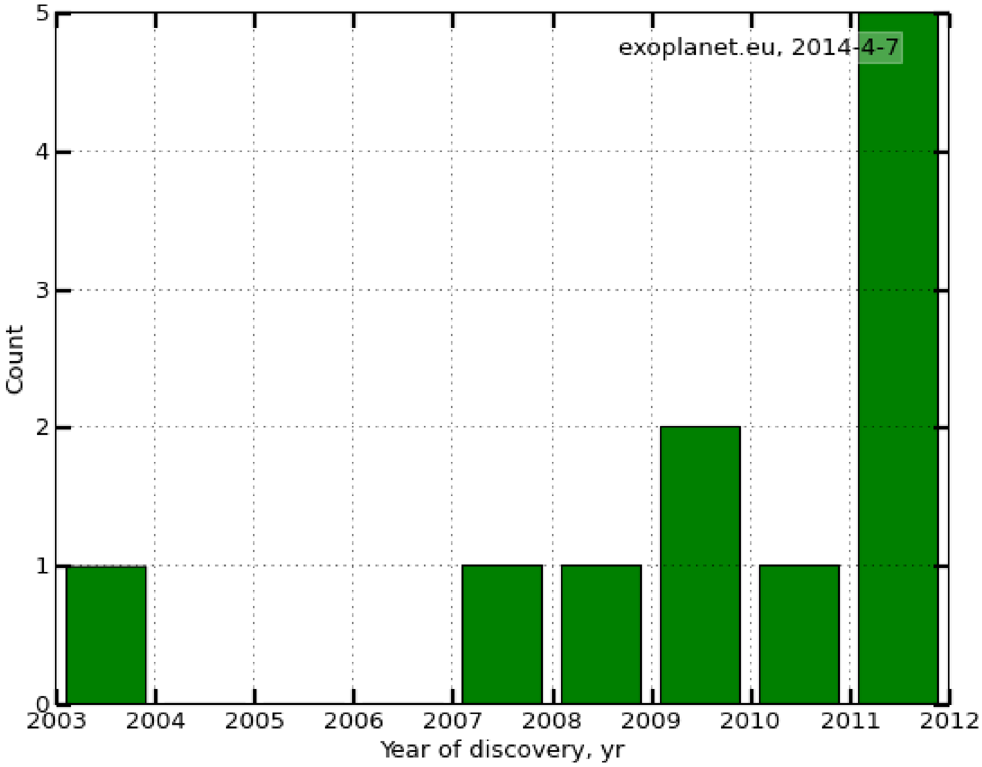

Figure 1.9: Number of planets discovered with the pulsar timing technique per year.

1.1.1.7 Direct Imaging

Information retrieved: The detections of planets with this technique involve objects on long periods, for which multiple measurements are needed to model the orbit. If the star has a disk it can be used to constrain knowledge of the inclination.

The direct imaging technique involves blocking the light from a star, and observing the orbiting objects in its orbit. A coronagraph is usually used to block the central star, but other methods such as nulling interferometry have been proposed (Bracewell 1978). Multiple-band photometry and spectroscopy in the near-infrared (1-5 μm) have been obtained for a few young gaseous planets, such as β Pic-b (Bonnefoy *et al.* 2013; Currie *et al.* 2013), GJ 504 b (Janson *et al.* 2013) and the planets orbiting HR 8799 (Konopacky *et al.* 2013), shown on Figure 1.10. With this method, over 30 planets have been detected so far. This technique is growing in importance, with the ESO-VLT SPHERE (Beuzit *et al.* 2008), Gemini Planet Imager (Hartung *et al.* 2013) and SUBARU SCExAO (Jovanovic *et al.* 2013) instruments built to detect young, massive planets at large separation from the stars, a regime not yet well explored till now.

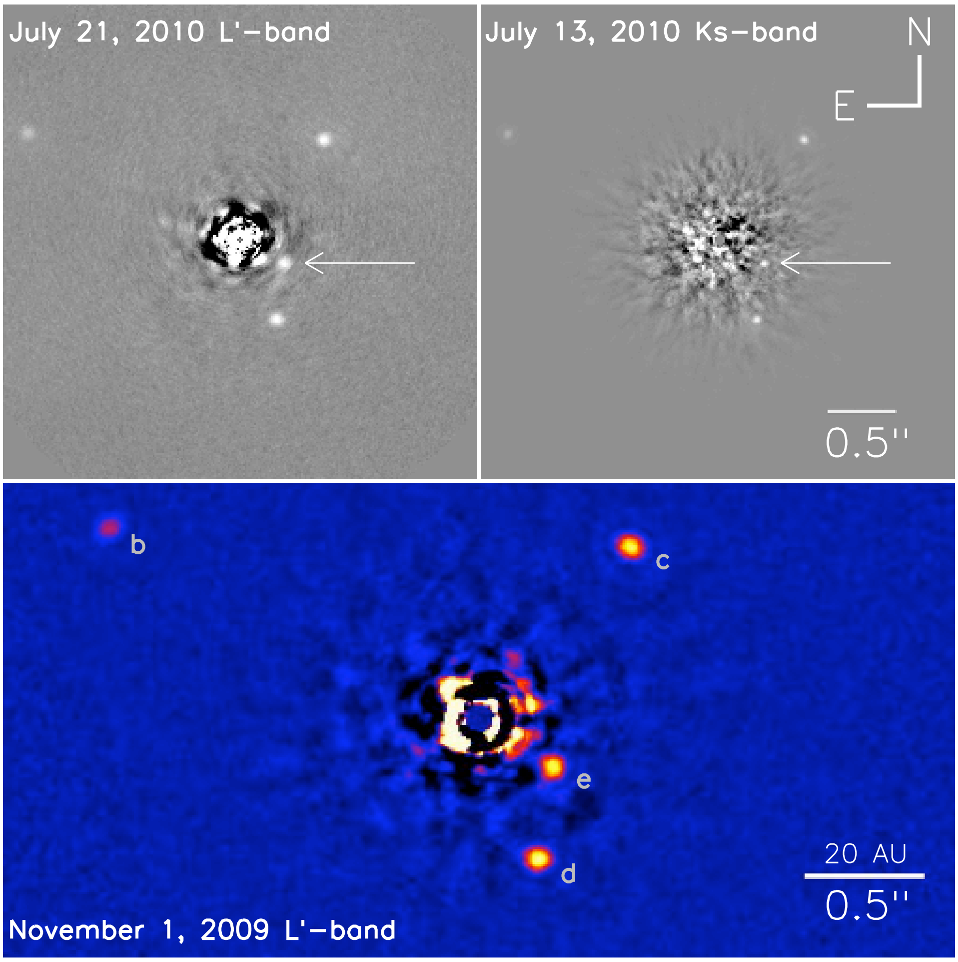

Figure 1.10: Four planets observed orbiting HR 8799, observed by direct imaging. From Marois *et al.* (2010)

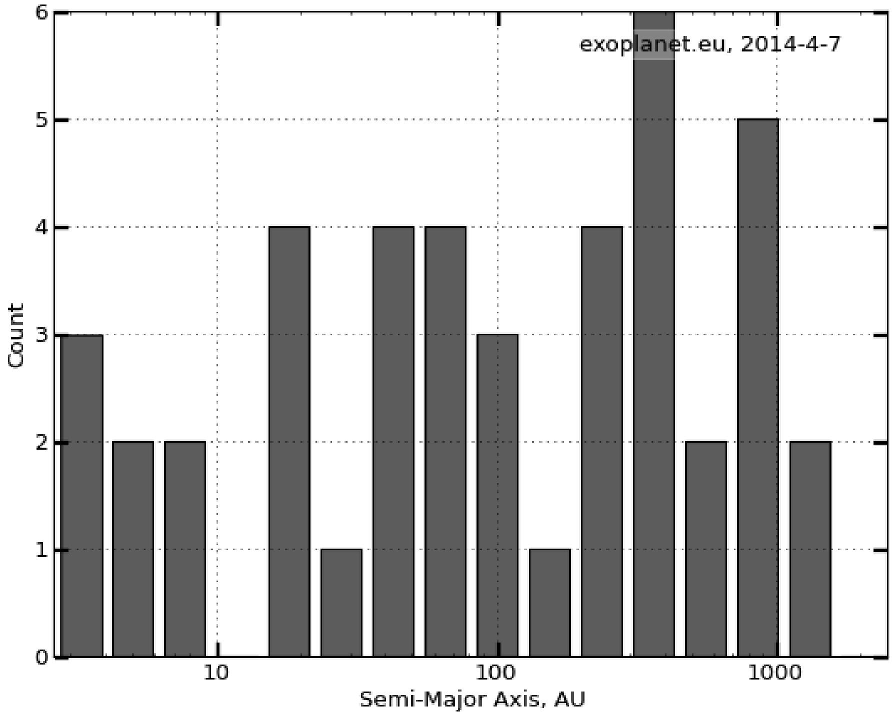

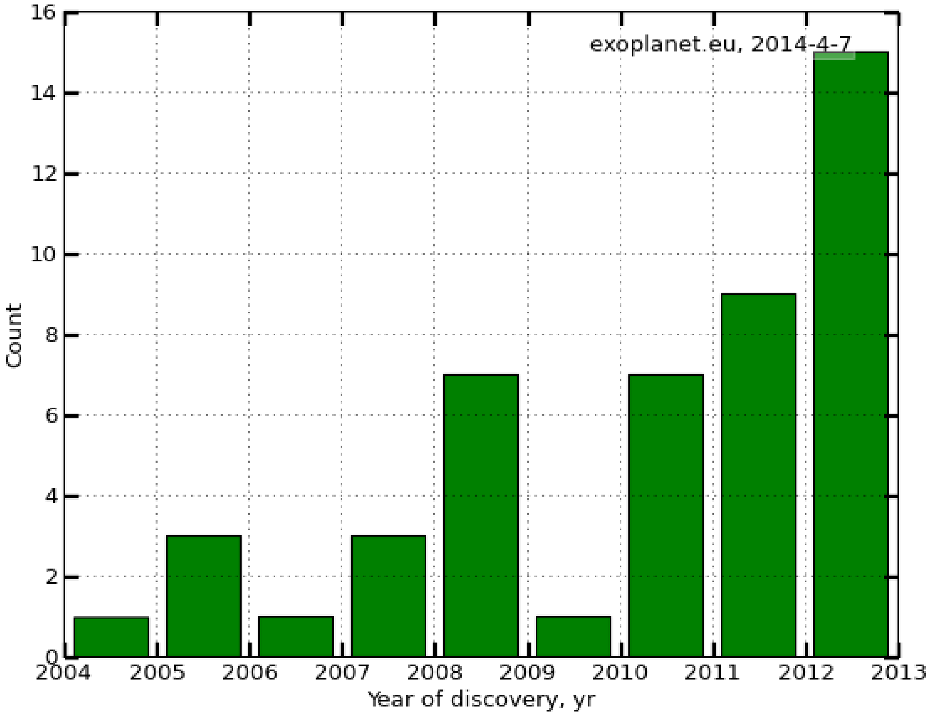

Figure 1.11: *Top:* Semi-major axis values of direct imaging detections: most of the planets found are far away from their central star, where the glare is less strong. *Bottom:* Number of planets discovered with the direct imaging technique per year.

1.1.2 Current parameter space probed

The methods and discoveries described above, when combined, give us a glimpse of the extent of diversity found with exoplanets. The total number of planets detected up to April 2014 is approaching 2000, out of which most have been detected by the radial velocity and transit techniques. As the histograms detailing the number of planet detections per year in Figures 1.4 and 1.6 show, the detection rate progress varies between linear and nearly exponential. These two methods are the most effective at finding Jupiter mass/radius range planets. Unsurprisingly, most detections to date have mass and size parameters similar to Jupiter, as shown in Figure 1.12. Recent detections by the Kepler mission are however beginning to populate the lower mass/radius range of this graph. Multiple new surveys are now looking for planets spanning a wider parameter range; these are discussed in the following section.

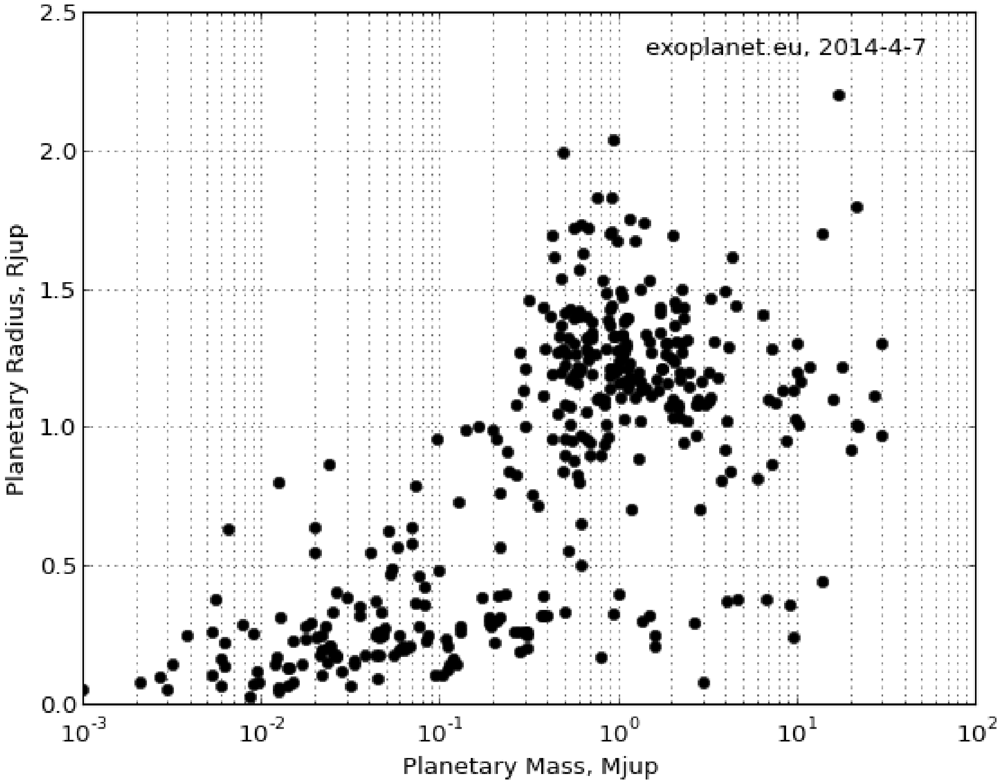

Figure 1.12: Exoplanet mass versus radius, in Jupiter units. Most of the planets detected to date have a mass and radius close to Jupiter's, but detections by the Kepler mission are populating the lower left-hand side of this graph with smaller and less massive planets.

Despite the detection biases on the sample of objects currently available, we are already seeing a vast diversity of orbit eccentricities and semi-major axis values (Figure 1.13). As most detection methods involve observing multiple planetary orbits, exoplanets with large semi-major axis and consequently long periods are difficult to detect, explaining the cutoff near ∼6 AU. Planets with a large semi-major axis will be best observed by the direct imaging technique. Current planets detected by direct imaging have semi-major axes typically over 10 AU (Fig. 1.11).

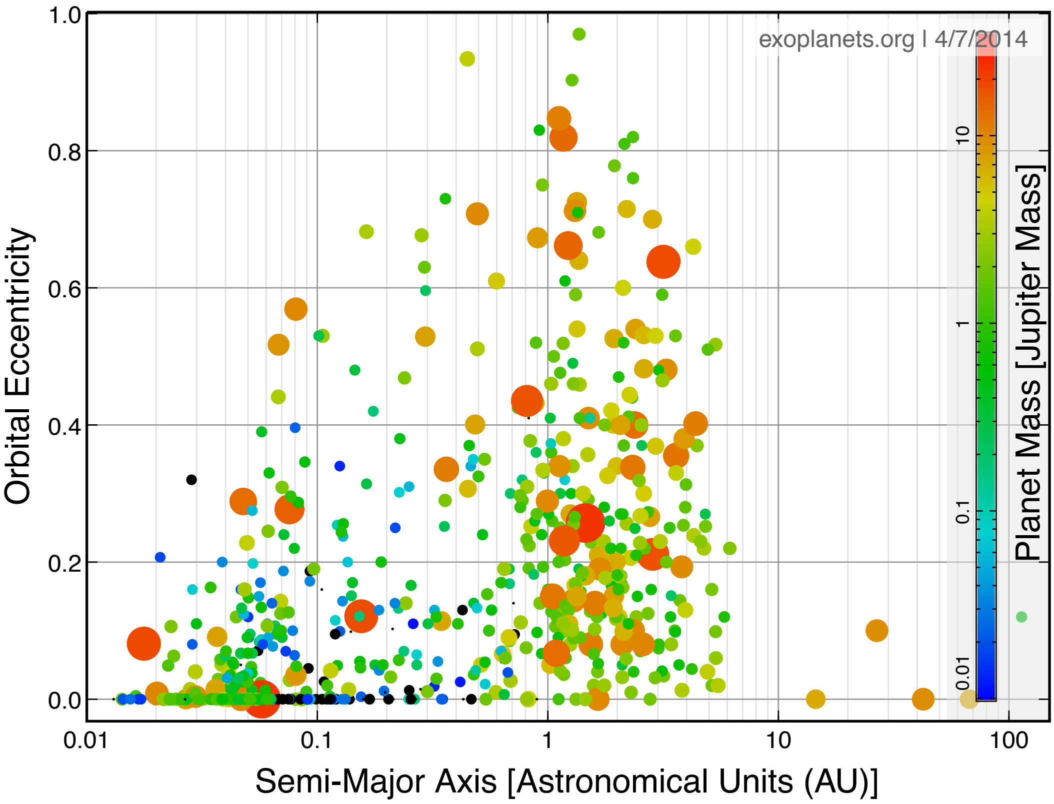

Figure 1.13: Semi-major axis and orbital eccentricity of currently known exoplanets. The size and colour indicate the measured mass of the planets. The cutoff near ∼6 AU reflects the detection methods used, which favour short period planets. Direct imaging is best suited for these large semi-major axis planets, with currently known planets typically having > 10 AU orbits.

With the exception of some of the nearest systems, most exoplanets have been found orbiting stars that have temperatures ranging between $4000 < T_{eff} < 7000$ K (Figure 1.14), at distances up to a few hundred parsecs. While this is only a fraction of the existing nearby stars, this reflects the youth of the field: early detections focused on the bright nearby targets that offered the best signal-to-noise values. We know however from microlensing surveys that planets also exist much further, at distances frequently over 5000 parsecs. Observing distant stars and planets is a challenge however, as the number of

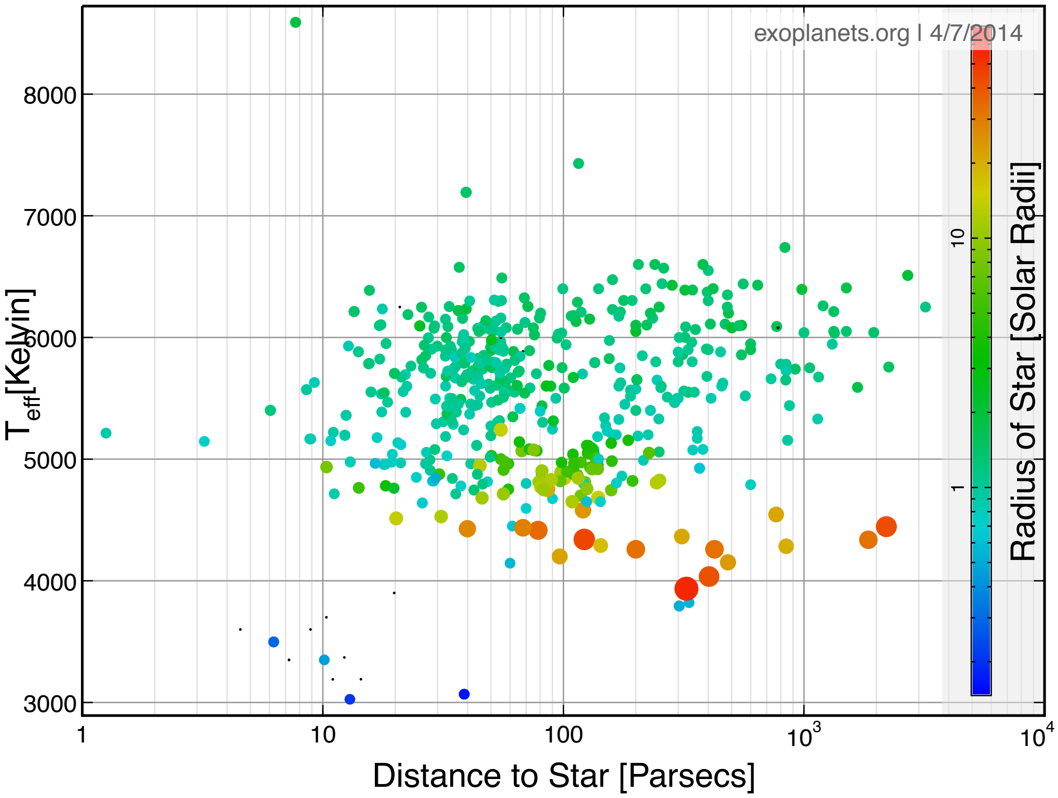

Figure 1.14: Distance to and temperature of the exoplanet host stars currently known. The size and colour indicate the radius of the stars. Most stars have a temperature between 4000 − 7000 K, with a small number of nearby M dwarfs at ∼10 pc. A handful of exoplanets have been found orbiting giant stars with temperatures ∼4000 K. The 8500 K star located at 8 pc is Fomalhaut, hosting the famous planet *Fomalhaut b* detected by direct imaging.

photons that reach us falls by the square of the distance.

From the Hipparcos survey, 90% of stars in our solar neighbourhood are of M-type (Perryman and ESA 1997), yet only a handful of these stars are present on this graph. This is mostly due to the faintness of M dwarf stars, but new surveys are aiming to better characterise these stars, and possibly find exoplanets around them. A discussion on completeness of observations is presented in the following section.

1.2 Completeness of catalogues

There are $\sim 10^{11}$ stars in our galaxy, out of which only a fraction are known, and microlensing studies indicate that on average every star is expected to host at least one planet (Cassan *et al.* 2012). How can we get closer to finding every exoplanet in our solar neighbourhood?

1.2.1 Stellar catalogues

As shown on Figure 1.14, most exoplanets have been found orbiting F, G and K stars. A small sample has been found orbiting the nearest M dwarfs, but few stars populate the lower part of this graph.

Many surveys are now aiming to find planets around these stars, and the most complete catalogue of late-type nearby stars available today is the Lépine and Gaidos (2011) catalogue, which includes nearly 9000 M dwarfs with magnitude J $<$ 10. According to the authors, the catalogue represents $\sim$ 75 % of the of the estimated $\sim 11,900$ M dwarfs with J$<$ 10 expected to populate the entire sky. A complementary catalogue by Frith *et al.* (2013) of nearby M dwarfs based on a different proper motion catalogue (the Position and Proper Motion Extended-L, Roeser *et al.* (2010)), uses a cutoff of K magnitude $<$ 9. The authors report that combining their results with the Lépine and Gaidos results under the same cutoff magnitude and in the same galactic region, a total of 8479 M dwarfs with magnitude K$<$ 9 are found. Figure 1.15 shows the proper motions of stars that are unique in both catalogues. The Frith *et al.* catalogue is more sensitive to the low proper motion targets, while the Lépine and Gaidos catalogue has more targets at large proper motions. These results are consistent with an evaluation of the number of M stars in a magnitude-limited sample derived from the analysis of the 100 RECONS nearest star systems (RECONS 2011). The distribution in distance of these objects shows that while the M1-4V star sample is evenly distributed within 6.6 pc, the M5-8V sample is significantly incomplete beyond 4-5 pc (see Fig. 1.16). This analysis supports the hypothesis that a significant number of stars are still missing in catalogues also in the very close solar neighborhood.

Launched at the end of 2013, the GAIA mission (Lindegren 2010), in its all-sky astrometric survey, will deliver direct parallax estimates and spectrophotometry for nearby main-sequence stars down to R$\sim$20. At the magnitude limit of the survey, distances to relatively bright M stars out to 20-30 pc will be known with 0.1%-1% precision (depending

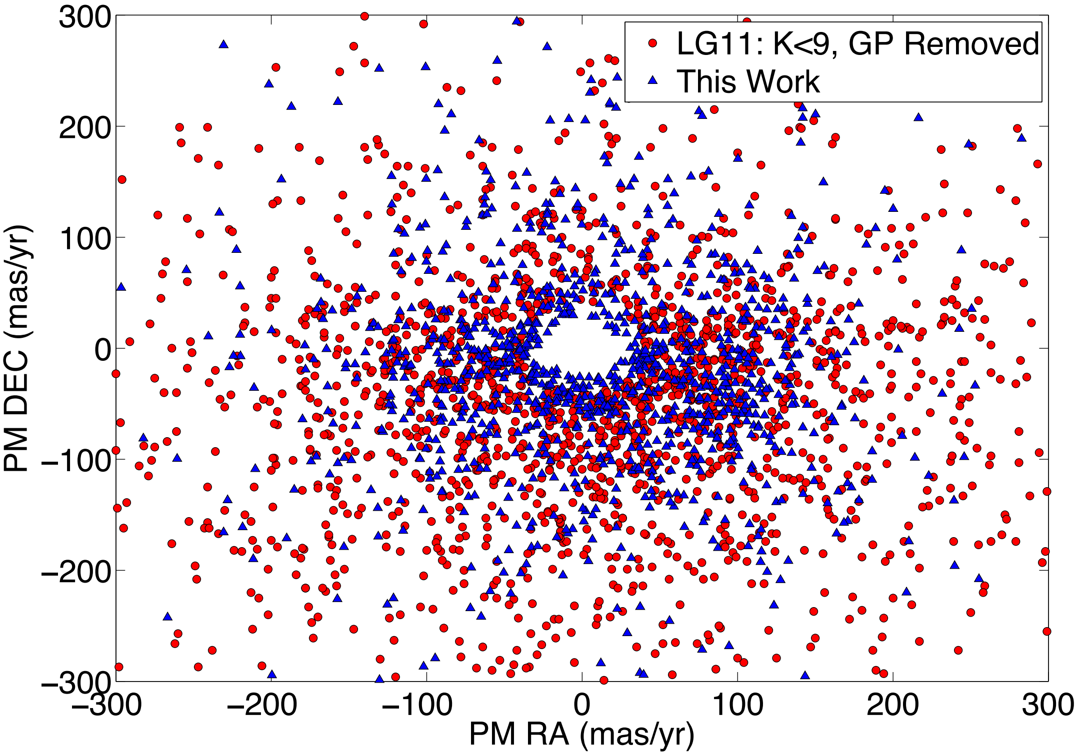

Figure 1.15: Proper motions of the mag. K< 9 M dwarfs that are unique to both Lépine and Gaidos and Frith *et al.* catalogues. A total of 8479 M dwarfs are shown. From Frith *et al.* (2013).

on spectral sub-type). This will constitute an improvement of up to over a factor 100 with respect to the typical 25%-30% uncertainties in the distance reported for low-mass stars identified as nearby based on proper-motion and colour selections (e.g. Lépine and Gaidos 2011). Starting with early data releases around mid-mission, the Gaia extremely precise distance estimates, and thus absolute luminosities, to nearby late-type stars will allow us to improve significantly standard stellar evolution models at the bottom of the main sequence.

For transiting planet systems, updated values of masses and radii of the host stars will be of critical importance. Model predictions for the radii of M dwarfs show today typical discrepancies of $\sim$ 15% with respect to observations, and, as shown by the GJ 1214b example (Charbonneau et al. 2009), limits in the knowledge of the stellar properties significantly hamper the understanding of the relevant physical characteristics (density, thus internal structure and composition) of the detected planets. For comparison, based on the simple radius-temperature-luminosity relation considerations, we can infer that estimates of stellar radii, when Gaia parallaxes known to $<$ 1% will become available for nearby red

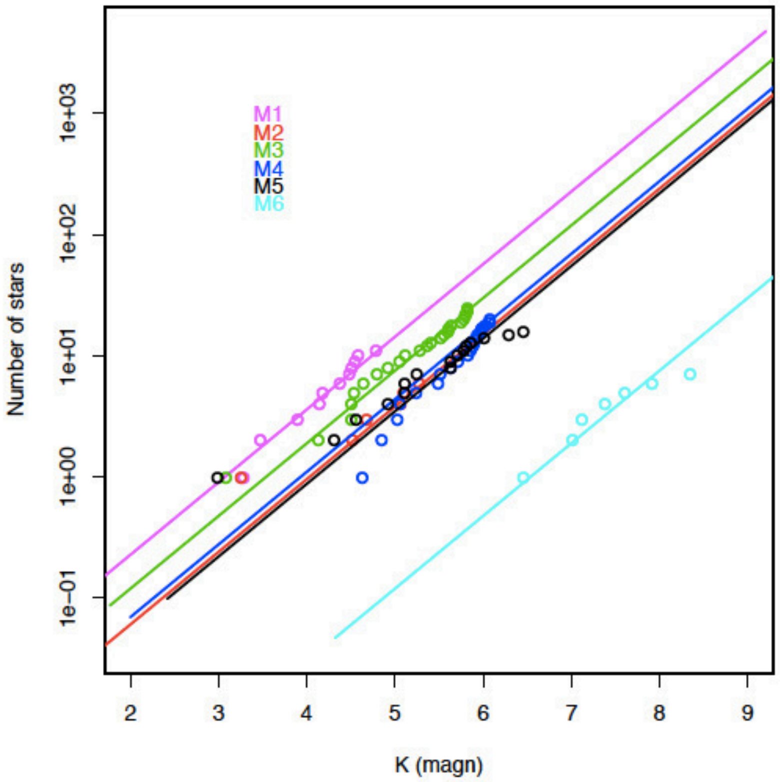

Figure 1.16: Expected number of stars out to 10 pc, for M0-4V and M5-M9V. Dots are stars in K magnitude from the RECONS catalogue and lines represent the expectations, assuming uniform spatial distribution and completeness at 6.6 pc. These plots suggest that the RECONS catalogue is complete only up to 6.6 pc for the earliest spectral types and up to 4.5-6 pc for the M5-6V sample. There are too few objects in the M7-9V range to say anything about completeness/space density of such objects.

stars, will carry much reduced uncertainties, on the order of 1%-3% (Sozzetti *et al.* 2014). Indeed, the precision in the M dwarf effective temperature estimates from spectroscopy or photometric calibrations (currently, 3%-5% at best) will then become the limiting factor in the knowledge of this fundamental quantity.

M dwarfs are of particular importance for the prospects of studying temperate or "habitable zone" (HZ) planets, as the low effective temperature of the star (2900< T_{eff} <3900 K), places the HZ region closer-in to the star than would be the case for a hotter star. Such a HZ planet will hence have a short orbital period and a larger number of transit events will be observable within a given time interval than would be the case for a planet in the HZ of hotter (K, G, F) stars. Figure 1.17 shows periods and transit durations for habitable-zone super-Earths (average surface $T = 287$K) orbiting a range of M stars, which were calculated using the equation derived in Tessenyi *et al.* (2012a):

$$t_t = \frac{PR_*}{\pi a}\sqrt{\left(1+\frac{R_{pl}}{R_*}\right)^2 - b^2} \tag{1.11}$$

where P is the period of the planet, a the semi-major axis, and b the impact factor.

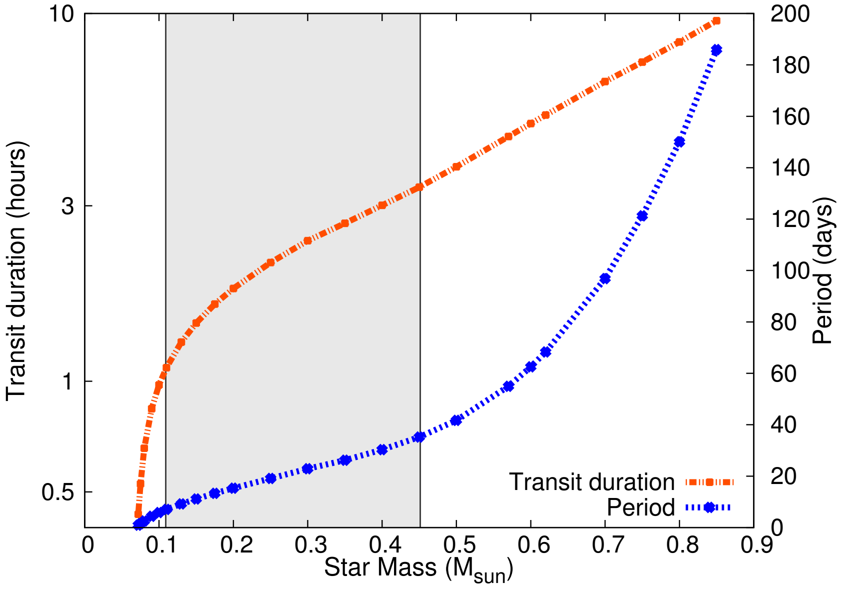

Figure 1.17: Transit durations and orbital periods of habitable-zone (HZ) super-Earths ($T = 287$K) for varying masses of M stars. The optimal range for the HZ is in the mass range delimited by the grey rectangle: between 0.11 and 0.45 $M_\odot$, with orbital periods of 7 to 35 days. From Tessenyi *et al.* (2012a).

1.2.2 Exoplanet detection surveys

The exoplanets found so far have been detected by a combination of ground surveys and two dedicated space missions (Corot (Deleuil *et al.* 2011), and Kepler (Borucki *et al.* 2011)). Building on very successful programmes, these surveys and upcoming instruments are aiming to fill the gaps that are shown on the parameter-space plots (Figures 1.12 and 1.14). In the coming decade, it is expected that the number of planets known will vastly increase, and cover a wider range of planet types than on the currently explored parameter-space.

1.2.2.1 Space missions

GAIA (Casertano *et al.* 2008; Sozzetti 2011) will start taking measurements in 2014, and is expected to find up a thousand planets orbiting nearby stars with astrometric measurements, in addition to mapping the stellar population in our galaxy. More specifically, it will be able to find giant planets orbiting F, G and K stars up to 200 pc from the Sun, and temperate giant planets orbiting M dwarfs at distances up to 30 pc.

TESS, the Transiting Exoplanet Survey Satellite (Ricker *et al.* 2009), is to be launched in 2017, and will find exoplanets using the transit technique like Corot and Kepler have, but will be looking at a larger portion of the sky ($\sim$ 45000 square degrees). It is expected to find over 1600 Neptunes and Jupiters, over 300 Earths and super-Earths, and over 700 sub-neptune planets, as shown in Figure 1.18 along a comparison of planets known in March 2013, and the predicted TESS yield.

CHEOPS (Broeg *et al.* 2013) is also planned to be launched in 2017, and will aim to measure accurately the radius of known transiting exoplanets previously detected by the radial velocity technique, to help study the internal structure of these planets. It will observe up to 250 targets during its lifetime and refine their mass/radius parameters.

1.2.2.2 Ground based surveys

Radial-velocity surveys
ESPRESSO (Pepe *et al.* 2010) will start taking high accuracy radial velocity measurements (10 cm^{-1}) at the VLT from 2016, and is expected to be able to detect rocky planets in the Habitable Zone of late-type stars.

HARPS (-N and -S, North (La Palma) and South (La Silla), respectively) (Cosentino *et al.* 2012; Mayor *et al.* 2003) are dedicated radial-velocity spectrographs in the northern and southern hemispheres. HARPS-S has been operating since 2003 and has found nearly 40 planets, while HARPS-N has been in operation since 2012 and is predicted to discover $\sim$30 planets. HARPS-N is aiming to find super-Earths and mini-Neptunes orbiting early M dwarfs.

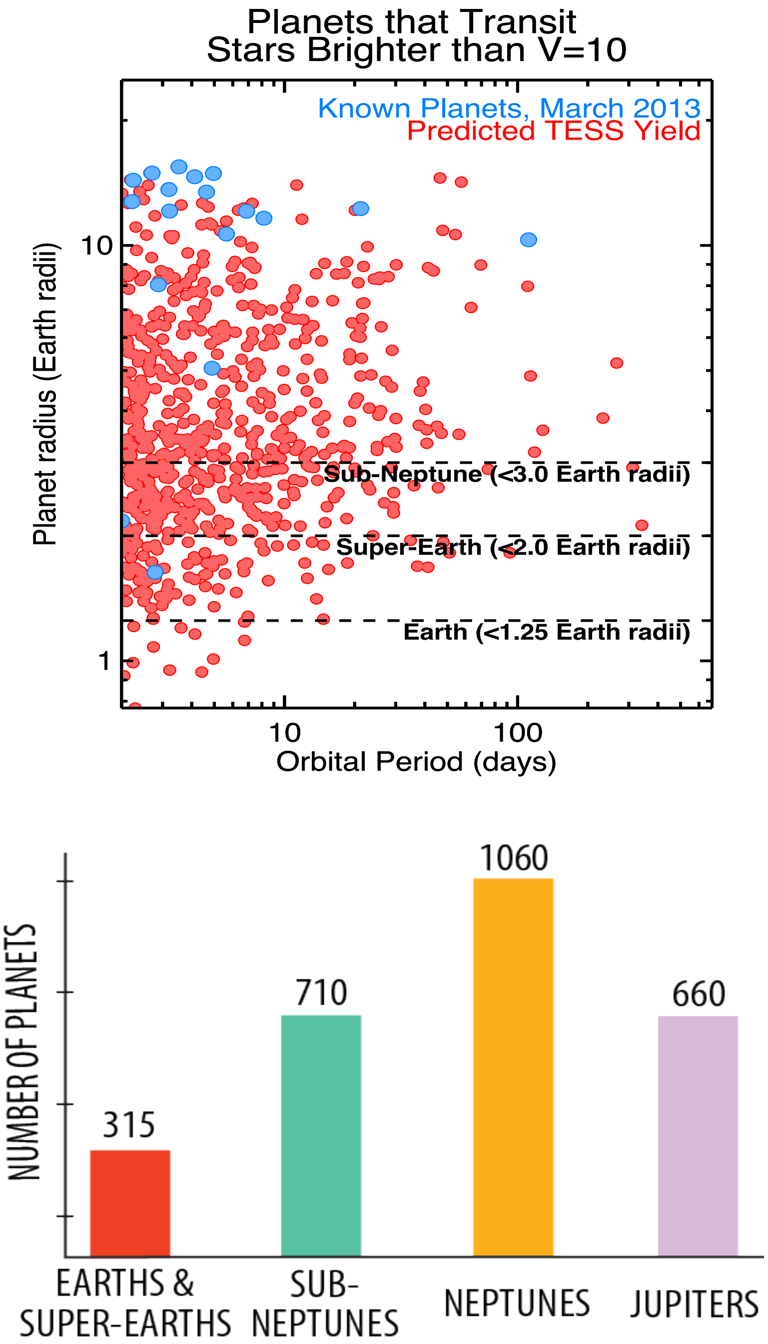

Figure 1.18: Expected distribution of planet radius and orbit period for the TESS yield (*top*) and number of detections expected per planet type (*below*).

Transit surveys

WASP (Pollacco *et al.* 2006) has been operating since 2006, and is optimised for finding planets on orbits <10 days mainly around late F and early G stars, with K magnitudes between 8 and 11. To date it has found just under 100 planets, mostly in the Jupiter mass and radius range.

NGTS (Wheatley *et al.* 2013) Based on the WASP design, the Next Generation Transit Survey (NGTS) built at the ESO Paranal site, will become operational in 2014 and will carry out a five year survey of K and M dwards. The survey is expected to yield a significant sample of Neptunes and super-Earths orbiting bright stars to allow radial-velocity follow up and thus determine the mass of these planets. In addition, it will find Neptunes and super-Earths that are favourable for spectroscopic characterisation. Simulations of the predicted sample of planets have been filtered with the sensitivity limits of the HARPS and ESPRESSO radial-velocity spectrographs to allow mass determination (see Figure 1.19 The simulated results include over 200 Neptunes and ∼40 super-Earths, and a large number of additional Jupiters. A subsample of those results (about 25 for both Neptunes and super-Earths) are expected to be bright enough for spectral characterisation.

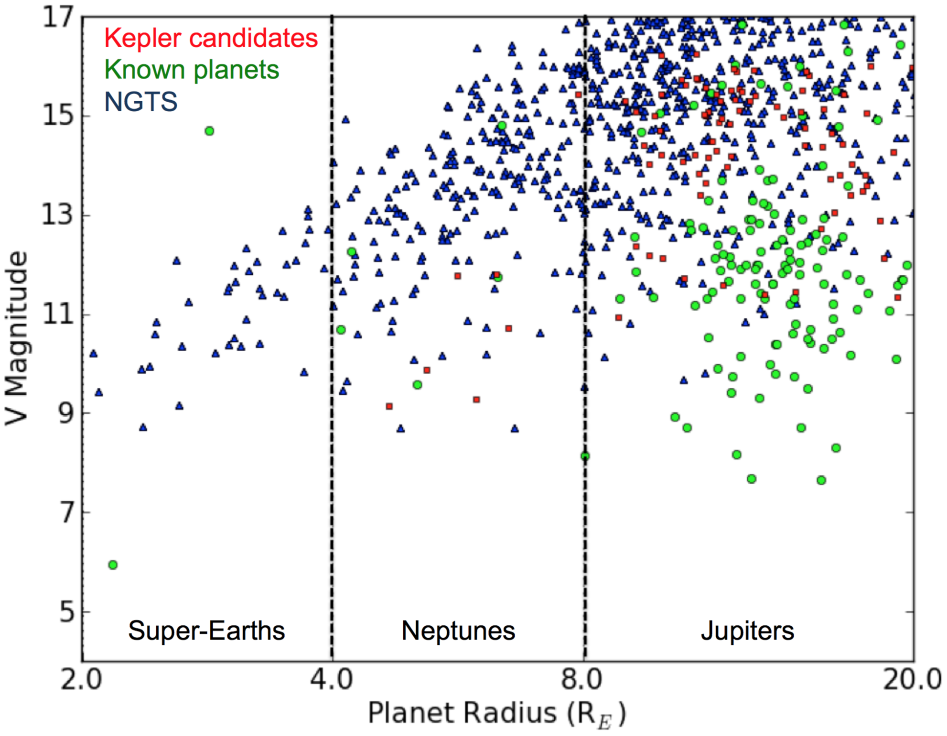

Figure 1.19: Simulation of targets for the NGTS survey after five years of observations. Each planet on this plot will be followed up by radial-velocity measurement to allow accurate mass determination.

MEARTH (Nutzman and Charbonneau 2008) Monitors late type M dwarfs from the Lépine and Gaidos (2011) catalogue, and searches specifically for super-Earths. So far it has found the first super-Earth orbiting an M dwarf, GJ1214b (Charbonneau *et al.* 2009).

APACHE (Sozzetti *et al.* 2013) started operating in the summer of 2012, it targets early and mid M dwards and is expected to be able to detect 1.4-4 $R_{\oplus}$ planets on short period orbits ($P < 10$days). The number of such planets to be detected by the APACHE project is $\sim$6.

HATNet and HATSouth (Bakos *et al.* 2002, 2009) HATNet, a network of automated wide field telescopes, has been operational for 9 years and has already found 50 transiting planets. It is mostly sensitive to Saturn to Jupiter sized planets, orbiting F and G dwarf stars. It is expected to carry on finding about 10 planets per year. HATSouth is the equivalent instrument set up in the southern hemisphere. It has been operational for the past 3 years, and has confirmed 3 discoveries. Many planet candidates are in the pipeline, and the expected yearly yield is about 30 planets per year. HATSouth has bigger optics, so is capable to monitor fainter magnitude stars. HATSouth is expected to be more efficient in detecting Neptunes than its northern counterpart.

1.3 The next challenge: understanding the diversity of these planets

It is clear from the number of surveys already in operation, planned, and proposed, that the effort to find as many planets as possible — and of a diverse nature — is well under way. Some of the new surveys focus on improving the measurement accuracies or obtaining additional parameters of already known planets (e.g. CHEOPS), while others are expected to double the numbers of discoveries (e.g. TESS). With the number of planets found so far and what is expected in the near future, we are entering a new era for planetary science. But to truly understand the formation and evolution of planetary systems we need to observe the atmospheres of these planets. This is illustrated by Figure 0.1, where Earth and Venus would look very much alike based on the parameters that we know currently for exoplanets; yet we know that their atmospheres are very different. Likewise, Jupiter and HD189733b, which have similar mass and radius (although different orbits), appear to have very different atmospheres. Spectroscopic remote sensing is a key tool for understanding distant atmospheres, and this is discussed in the following chapter.

Chapter 2

Probing Planetary Atmospheres through remote sensing spectroscopy

Much of our understanding of the atmospheres in our Solar System has been gained from in-situ measurements and remote sensing, which consists in observing spectroscopically the emitted and reflected light from those atmospheres. This is possible due to the interactions of photons with matter in a gas, which leave a spectral "signature" characteristic of the constituent elements, either through emission or absorption of photons. From the rules of interaction between photons and molecules, it is possible to simulate the atmospheres of planets and generate synthetic spectra. These models have been validated by in-situ experiments on many solar-system planets, starting with many experiments on Earth.

In this chapter we introduce the generic equation of radiative transfer and the absorption phenomena in molecular gases, from which we describe the radiative-transfer programs we used for the work presented in this thesis. This chapter concludes with an example of the two (primary transit and secondary eclipse) radiative-transfer codes applied to the same exoplanet to produce synthetic spectra.

2.1 The Radiative Transfer Equation: Key Concepts

Considering a parcel of gas, a beam of light, of wavelength-dependent intensity I_λ, crossing the medium will be altered by its interaction with matter (Figure 2.1). The intensity I_λ is defined as the amount of radiant energy dE_λ per time interval dt and wavelength interval $d\lambda$, crossing an element of area dA, in the direction of a differential solid angle $d\Omega$, at an angle θ to the normal of dA. This is expressed as:

$$I_\lambda = \frac{dE_\lambda}{\cos\theta \, d\Omega \, d\lambda \, dt \, dA} \tag{2.1}$$

The general form of the radiative transfer equation (Chandrasekhar 1950) describes the amount of change in radiation dI along a small distance ds:

$$dI_\lambda = -I_\lambda \, \sigma_\lambda \, \rho \, ds \; + \; j_\lambda \, \rho \, ds \tag{2.2}$$

where I_λ is the initial wavelength dependent radiation intensity, σ_λ the wavelength dependent mass extinction cross section, j_λ the source function coefficient, and ρ the density of the gas traversed. The first part of the right-hand side term represents the reduction in radiation intensity through the gas, and the second part the strengthening of the signal due to contributing emission sources within the gas. Table 2.1 indicates the units used for these quantities.

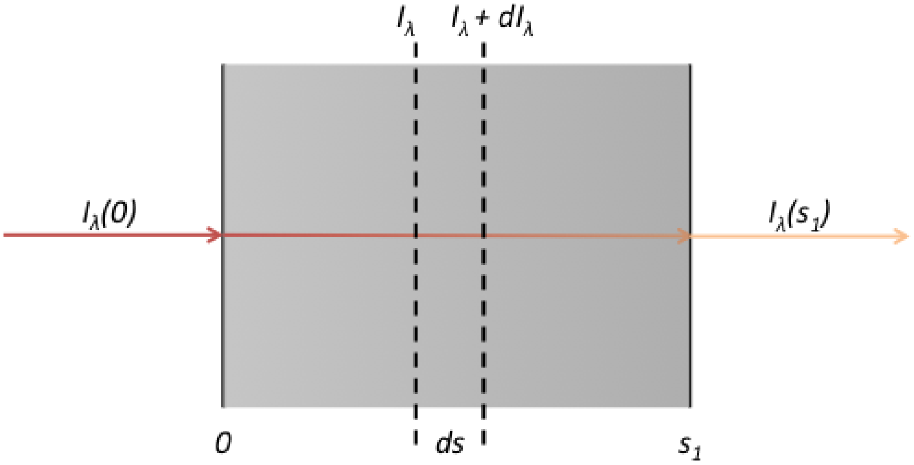

Figure 2.1: Change of radiation intensity through a parcel of gas, along a length s.

The radiative transfer equation can be written as:

$$\frac{dI_\lambda}{\sigma_\lambda\,\rho\,ds} = -I_\lambda + J_\lambda \tag{2.3}$$

Where J_λ is defined as the ratio of emission and absorption in the gas:

$$J_\lambda = \frac{j_\lambda}{\sigma_\lambda} \tag{2.4}$$

so as to have this term expressed in units of radiant intensity. First the simpler case of a solution to an absorbing only gas (equation 2.2) is considered, setting $J_\lambda = 0$, which is then followed by the solution to the case combining absorption and emission.

Symbol	Description	Units
I	Spectral irradiance	$\mathrm{W.m^{-2}.m^{-1}}$
J	Spectral irradiance	$\mathrm{W.m^{-2}.m^{-1}}$
ρ	(Number) Density	$\mathrm{m^{-3}}$
σ	Absorption coefficient	$\mathrm{m^{2}}$
j	Emission coefficient	$\mathrm{W.m^{-1}}$
s	Distance	m

Table 2.1: Terms and units of the radiative transfer equation.

2.1.1 Extinction in a homogeneous gas - Beer-Bouguer-Lambert law

Considering only the extinction properties of a gas, the wavelength dependent radiation change through a medium can be expressed from equation 2.3 as:

$$\frac{dI_\lambda}{\sigma_\lambda \rho ds} = -I_\lambda \tag{2.5}$$

The solution to this equation for the intensity at a distance s is:

$$I_\lambda(s_1) = I_\lambda(s_0)\,\exp\left(-\int_{s_0}^{s_1} \sigma_\lambda\,\rho\,ds\right) \tag{2.6}$$

if integrating over a distance ds, from $s = 0$ (s_0) to $s = 1$ (s_1). The extinction terms are the monochromatic absorption cross section σ_λ and the gas density ρ. If the gas is assumed to be homogeneous, where the absorption cross section σ_λ is not a function of the distance travelled, the path length l can be defined as:

$$l = \int_{s_0}^{s_1} \rho \, ds \tag{2.7}$$

From which the simple expression of the Beer-Bouguet-Lambert law is derived:

$$I_\lambda(s_1) = I_\lambda(s_0) \exp\left(-\sigma_\lambda \, l\right) \tag{2.8}$$

which describes the wavelength dependent loss of intensity through a homogeneous medium, observed over the path length l. If emission of the medium is also considered, this expression gains additional terms.

2.1.2 Extinction and Emission - Schwarzschild's Equation

A gas may also contribute positively to the change of intensity along a path l, from the sources of emission within the medium. In an environment where the molecular radiative relaxation time is longer than the time between molecular collisional de-excitations, a Boltzmann distribution of particles can be assumed. Such an environment is referred to being in local thermal equilibrium (LTE). As an example, in the case of the Earth atmosphere, the conditions for LTE are maintained up to an altitude of 60-70km (Liou 2002). A more complete discussion on the validity of the LTE assumption is presented in appendix E.

Assuming the gas is in LTE and assuming negligible scattering, the radiant intensity term in equation 2.3 can be replaced by Planck's function $B_\lambda(T)$:

$$J_\lambda = B_\lambda(T) \tag{2.9}$$

The radiative transfer equation (2.2) becomes:

$$\frac{dI_\lambda}{\sigma_\lambda \rho ds} = -I_\lambda \, + \, B_\lambda(T) \tag{2.10}$$

which is referred to as Schwartzschild's equation. An optical thickness τ_λ dependent on wavelength can be defined between points s and s_1 along the optical path:

$$\tau_\lambda(s_1, s) = \int_{s}^{s_1} \sigma_\lambda \, \rho \, ds' \tag{2.11}$$

The derivative of the integrated solution for this expression becomes:

$$d\tau_\lambda(s_1, s) = -\sigma_\lambda \, \rho \, ds \tag{2.12}$$

which can be used to express Schwartzschild's equation as:

$$\frac{dI_\lambda(s)}{d\tau_\lambda(s_1, s)} = -I_\lambda(s) + B_\lambda[T(s)] \tag{2.13}$$

The solution to the differential equation 2.10, presented in (Chandrasekhar 1950) is:

$$I_\lambda(s_1) = I_\lambda(0) \exp\left(-\tau_\lambda(s_1, 0)\right) + \int_0^{s1} B_\lambda[T(s)] \exp\left(-\tau_\lambda(s_1, s)\right)\sigma_\lambda \rho ds \tag{2.14}$$

The absorption by the gas is described by the first term on the right-hand side is the equivalent to equation 2.8. The contribution to the intensity from the gas is described by the second term of the right-hand side, which has to be integrated over the path length s numerically.

Both equations 2.8 and 2.14 give a solution as a function of the absorption cross section and the pressure of the gas. The absorption cross section is a function of wavelength and specific to molecular species; it is the key factor to identify the components of a gas.

2.2 Molecular absorption and emission

The change in radiation dI along the path travelled by light depends in part on the absorption coefficient σ_λ through the medium (equation 2.2). This component describes what fraction of photons is absorbed by the gas as a function of wavelength. It depends on the possible transitions between energy states of the molecule (wavelength dependence), and the probability of transitions to occur at the various energy levels (absorption strength). Both components are specific to a molecular species, and provide a unique "signature" of the absorbing gas. These absorption lines can either be measured experimentally or computed using quantum mechanics. Figure 2.2 shows an example of absorption lines near the ν_3 vibration mode for CO_2. The absorption coefficient is expressed either as an extinction cross section (cm^2), mass extinction cross section ($cm^2.g^{-1}$), or extinction coefficient (cm^{-1}). (Or number density extinction cross section (cm^{-3}) and number density mass extinction cross section ($g.cm^{-3}$).)

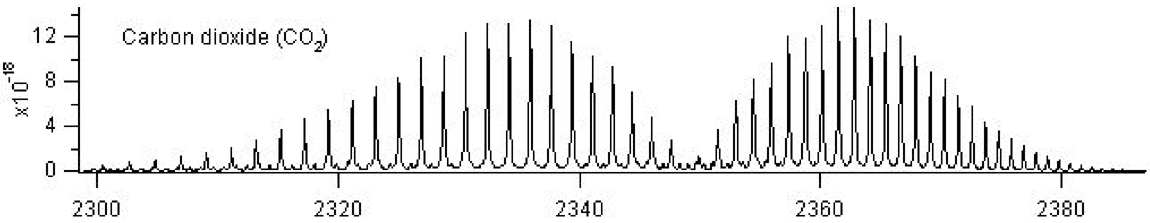

Figure 2.2: CO_2 absorption lines centred on the ν_3 vibration mode ($\tilde{\nu} = 2349$ cm^{-1}). Each line represents a transition in energy state, and the strength of the line (here expressed as cm^{-2}/molecule) represents the probability of a transition to occur. Source: PNNL data from HITRAN website (`http://vpl.astro.washington.edu/spectra/co2.htm`).

A molecule can store energy in various ways: kinetic energy due to movement of the molecule in space, transition of electrons to upper energy levels for each atom, vibrations of the atoms in the molecule, and rotation of the molecule around a central point. With the exception of the kinetic energy component which depends on $k_B T$, k_B the Boltzmann constant and T the temperature, the energy values of state transitions are "quantised" and defined by quantum selection rules, and are unique to each molecular species. The energy of an absorbed or emitted photon has to correspond to one of the possible transition energies to be absorbed and trigger a transition. Conversely, molecules that are in an excited state can jump down to a lower permitted energy level, and release a photon of an equivalent energy difference.

2.2.1 Quantised Energy Transitions

The permitted energy transitions are usually computed by solving the wave function for a molecule, and obtaining the matrix element of the dipole moment, which describes the interactions between the molecule and an electromagnetic field. This matrix element contains all the permitted and forbidden transitions between the energy states of the molecule, which are referred to as *selection rules* (see sections 2.2.1.3 and 2.2.1.4). The description of the quantum theory and methods to obtain the transitions is however beyond the scope of this work. The following description contains approximations, and is presented as a more phenomenological description of the quantised energy transitions in molecules. A more complete description of these processes is available in textbooks by e.g.: Herzberg and Spinks (1950) and Chandrasekhar (1950).

2.2.1.1 Electronic transitions

Historically, with the atom model proposed by Rutherford (1911) based on the experiments of Geiger and Marsden (1909), and using Planck's (1901) theory of energy radiated in specific quanta, Bohr (1913) postulated that atoms have quantised stationary states for electrons, and that energy is only released during a state transition:

$$E_k - E_j = h\nu \tag{2.15}$$

where $h\nu$ is the amount of energy released via a photon for a jump from the higher energy state k to the lower state j, with h the Planck constant and ν the frequency of the photon. Each "quantum jump" between energy levels is linked with an emission or absorption of a photon, which appears as emission or absorption lines in spectra. For example, permitted transition energies for electronic transitions of the hydrogen atom have discrete values:

$$E_n = -\frac{me^4}{8\epsilon_0^2 h^2}\frac{1}{n^2} \tag{2.16}$$

where m is the mass of the electron, e the electron charge, and ϵ_0 the permittivity constant. These electronic transitions involve high energies (a few eV) with corresponding wavenumbers in the order of $\tilde{\nu} \sim 1 \times 10^4$ cm^{-1}, appearing in the ultraviolet, visible and short infrared spectral range.

In addition to electronic transitions, molecules can store energy through changes in their translational, vibrational and rotational degrees of freedom. A molecule composed of N atoms has a total of $3N$ degrees of freedom, of which three are reserved for the orthogonal translational motions. The remaining $3N - 3$ degrees are separated into rotational and vibrational freedoms, with three degrees of rotational freedom available for most polyatomic molecules, and only two degrees of rotation for diatomic and linear molecules (the atoms are aligned along the symmetry axis). As a consequence, there are $3N - 6$ degrees of freedom left for vibrations of non-linear molecules, and $3N - 5$ degrees of freedom for diatomic and linear molecules.

2.2.1.2 Molecular Vibration

Molecular vibration transitions are of higher energy than rotational transitions (see below), and can be examined independently if the effects of rotation on the interatomic separations are neglected. To interact with photons, molecules need to have either a permanent dipole (e.g.: H_2O) or a transient dipole that appears when the charge distributions change due to vibrations of the atoms. In a first approximation, diatomic molecules with symmetric charge distributions such as H_2 or O_2 do not absorb photons and show no roto-vibrational absorption lines in infrared spectra. However in reality, collisions with other molecules can generate collisionally induced dipoles if the molecular abundance is high, which result in absorption lines.

The normal vibrational modes for CO_2, a polyatomic linear molecule found in the atmosphere of most solar system planets, are illustrated in Figure 2.3. The four $(3 \times 3 - 5 = 4)$ normal vibration modes are shown, with the ν_2 mode containing two equivalent vibrational modes, considered degenerate. The first mode (ν_1) is a symmetric stretch, where the charge distribution doesn't change due to the vibrations. For this mode, the molecule has no dipole moment and doesn't absorb photons, and examination of the known line lists for CO_2 shows that there are indeed no absorption lines for the ν_1 mode at $\tilde{\nu} = 1388$ cm^{-1}. Vibrations along its ν_2 and ν_3 modes however change the charge distributions, and create a transient dipole moment with which incoming radiation can interact. The

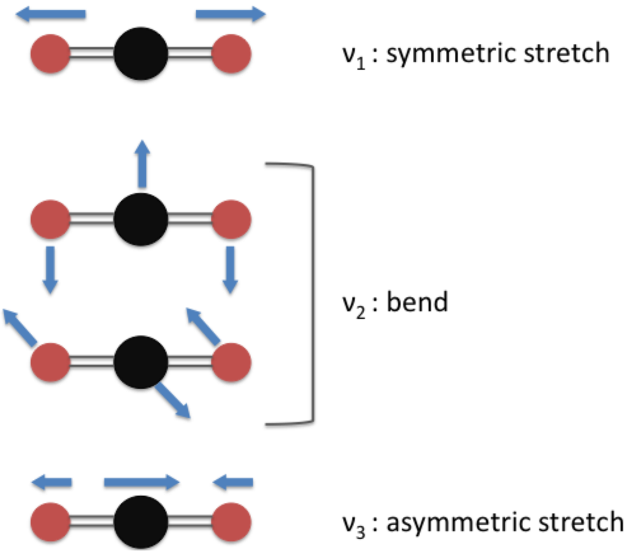

Figure 2.3: Normal vibration modes ν_k $(k = 1, 2, 3)$ for CO_2. While four vibration modes are shown, the two ν_2 modes are degenerate, and exist due the $3N - 5$ vibrational freedom of movement requirement for a linear molecule.

energy transitions for these vibrational modes are visible on spectra at the $\tilde{\nu}_2 = 667$ and $\tilde{\nu}_3 = 2349$ cm^{-1} wavenumbers.

The calculation of the vibrational energies is based on the potential energy surface, e.g. of a harmonic oscillator with additional anharmonic terms, derived from the Hamiltonian. The energy of the lower level vibration states can be approximated as a classical simple harmonic oscillator and is expressed as a sum over the vibrational modes ν_k:

$$E_v = \sum_k h\nu_k(v_k + 1/2) \qquad \text{with} \qquad v_k = 0, 1, 2... \tag{2.17}$$

where ν_k corresponds to the harmonic oscillator frequency for each k mode (e.g. the three modes represented in Figure 2.3 for CO_2), and v_k the vibrational quantum number. The selection rule for vibrational state transitions in this approximation is $\Delta v = \pm 1$, which is called the fundamental transition, but higher energy transitions can occur due to deviations from the classical harmonic oscillator behaviour (overtone bands, with $\Delta v = \pm 2, 3...$) (Herzberg and Spinks 1950). Multiple vibration modes can simultaneously transition between energy states, the associated absorption lines are referred to as combination bands. The harmonic oscillator frequencies ν_k are determined from the corresponding second derivative of the potential energy surface at the equilibrium, which provides the intermolecular force and force constants. The force constants are used to compute the wavenumber corresponding to the harmonic oscillator frequencies, e.g. for a diatomic molecule:

$$\tilde{\nu} = \frac{c}{2\pi}\sqrt{\frac{K}{m_R}} \tag{2.18}$$

where K is the force constant and m_R the reduced mass of the molecule. The typical values for vibrational transitions correspond to $\tilde{\nu} \sim 300 - 3000$ cm^{-1}, depending on the molecule.

In practice, the vibrational transitions are always accompanied by rotational energy transitions, which have lower transition energies and are sensitive to changes to the moment of inertia due to the vibrations of the molecule.

2.2.1.3 Molecular Rotation

For the case of an idealised diatomic rotating molecule, referred to as a "rigid rotator" with no vibrational component, the rotational energy is classically expressed as $E = L^2/2I$, with L the angular momentum and I the moment of inertia. Combining this expression with the quantised energy theory and the selection rules for rotation, the rotational energy is defined as:

$$E_J = BhcJ(J+1) \qquad \text{with} \qquad B = \frac{h}{8\pi^2 Ic} \qquad \text{and} \qquad J = 0, 1, 2... \tag{2.19}$$

where J is a positive integer rotation number, with the selection rule $\Delta J = \pm 1$. B is defined as the rotational constant corresponding to the moment of inertia along one of the rotation axes. The wavenumber corresponding to a rotational energy change is

$$\tilde{\nu} = BJ'(J'+1) - BJ''(J''+1) = 2BJ' \tag{2.20}$$

where J' and J'' are the upper and lower state quantum numbers respectively, and the right-hand side result is obtained by replacing the lower state plus one $(J''+1)$ term by the upper state term J'. These transitions occur at low energies (with wavenumber $\tilde{\nu} \sim 1$ cm^{-1}); pure rotational transition lines appear in the far infrared and microwave parts of the electromagnetic spectrum for molecules with a permanent dipole. CO_2 has no permanent dipole (the dipole arises from the $\nu_{2,3}$ vibration modes) and does not exhibit pure rotational bands in the rigid rotator approximation. From equation 2.20, the wavenumber difference between two states of $\Delta J = 1$ is $\Delta\tilde{\nu} = 2B$ cm^{-1}.

Equation 2.19 is valid for a linear rigid rotator, a more general expression compatible with spherical top and symmetric top molecules (see Table 2.2), is given by (Goody and Yung 1995):

$$E_J = BhcJ(J+1) + hc(A-B)K^2 \tag{2.21}$$

where A is an equivalent rotational constant to B defined in equation 2.19 due to the additional moment of inertia from the third degree of motion, and K a quantised term for the angular moment along the symmetry axis of the molecule. For linear molecules $K = 0$ as there is no rotation along the symmetry axis, and for spherical top molecules $A = B, C$; in both cases equation 2.21 reduces to the shorter form of equation 2.19. It is worth noting that symmetric top molecules contain two sub-categories of symmetry, *oblate* and *prolate*, where the former has its atoms distributed in a plane while the latter has atoms spread also “vertically”. The distinction between these two sub-categories matters for the relative moments of inertia I_A vs. $I_{B,C}$, on which the sign of the last term in equation 2.21 depends. This means that from equation 2.21, prolate ($A > B$) molecules will have higher energy jumps between states than oblate ($A < B$) molecules. Asymmetric top molecules (such as H_2O and O_3) require a more complex expression involving additional terms.

Molecule Type	Examples	Rotational moments of inertia
Spherical top	CH_4, SiH_4	$I_A = I_B = I_C$
Linear	CO, CO_2	$I_A = 0$, $I_B = I_C$
Symmetric top *oblate*	C_2H_4, C_6H_6	$I_A \neq 0$, $I_B = I_C$
Symmetric top *prolate*	NH_3, $ClCH_3$	$I_A \neq 0$, $I_B = I_C$
Asymmetric top	H_2O, O_3	$I_A \neq I_B \neq I_C$

Table 2.2: Symmetries of different molecular types.

2.2.1.4 Roto-vibrations

Most of the observed rotational energy transitions occur simultaneously with vibrational energy transitions, and appear as the “roto-vibrational band” in the mid-infrared part of the spectrum. The higher-energy vibrational transitions change the moment of inertia of the rotating molecule, which has an impact on the rotational energy values. If the molecule has a dipole moment and can interact with radiation, the rotational energy transitions appear as absorption lines on both sides of the vibration wavenumber. Without taking into account interaction terms for an anharmonic oscillator, the energy of a roto-vibrational state for a linear molecule is expressed as:

$$E_{v,j} = BhcJ(J+1) + \sum_k h\nu_k(v_k + 1/2) \tag{2.22}$$

The selection rules are $\Delta v_k = \pm 1$ and $\Delta J = \pm 1$, with $v_k = 0$ the lowest permitted vibrational energy level. Taking the energy difference ΔE between two roto-vibrational states (excited J' and ground J'') gives the transition wavenumber:

$$\tilde{\nu} = \tilde{\nu}_k + B'J'(J'+1) - B''J''(J''+1) \tag{2.23}$$

where $\tilde{\nu_k}$ is the vibrational wavenumber of the k mode. Vibrational energy transitions alone do not change the absorption line wavenumbers, but the energy transitions between rotational states shift the wavenumber right ($\Delta J = J' - J'' = +1$) or left ($\Delta J = J' - J'' =$

-1). When applied to equation 2.23, these shifts provide the wavenumbers of the R and P branches ("Riche" and "Pauvre") respectively:

$$\tilde{\nu}_R = \tilde{\nu}_k + 2B' + (3B' - B'')J'' + (B' - B'')J''^2 \qquad \text{with} \qquad J = 0, 1, 2... \tag{2.24}$$

$$\tilde{\nu}_P = \tilde{\nu}_k - (B' + B'')J'' + (B' - B'')J''^2 \qquad \text{with} \qquad J = 1, 2, 3... \tag{2.25}$$

The absorption lines visible in spectra on both sides of the vibration wavenumbers are formed by these $\Delta J = \pm 1$ transitions.

While the linear molecule case considered so far has no K component, a linear molecule such as CO_2 can have a K component appear due to the ν_2 vibration perpendicular to the symmetry axis of the molecule. For such cases the expression of the rotational energy from equation 2.21 has to be considered, where $K \neq 0$, and where the selection rule allows $\Delta J = 0$ (rigorous) and $\Delta K = \pm 1$ (approximate). This means that the vibrational changes occur at the same $\tilde{\nu}_k$ wavenumber, with the consequent absorption lines referred to as a Q-branch:

$$\tilde{\nu}_Q = \tilde{\nu}_k + (B'' - B')K^2 + (B' - B'')J'' + (B' - B'')J''^2 \qquad \text{with} \qquad \Delta J = 0 \tag{2.26}$$

from which it can be seen that the only change in wavenumber will be due to the difference in moment of inertia between the two states. This effect is visible in the strong Q-branch features appearing in spectra, e.g. for CO_2 at the ν_2 vibration mode (see Figure 2.4).

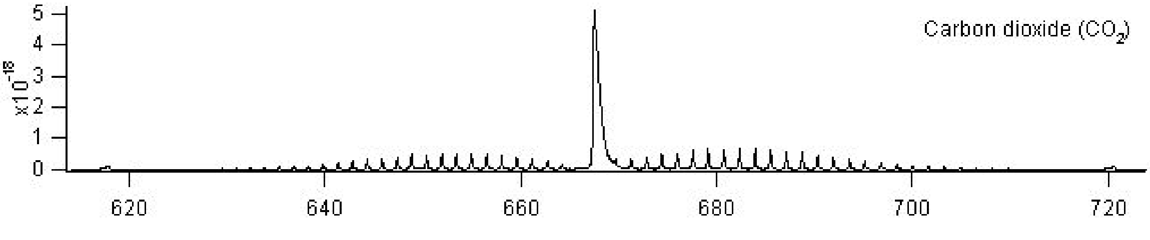

Figure 2.4: CO_2 absorption lines centred on the ν_2 vibration mode ($\tilde{\nu} = 667$ cm^{-1}), showing a strong Q-branch feature of the $\Delta v = \pm 1$, $\Delta J = 0$ transitions stacked together. Source: PNNL data from HITRAN website (`http://vpl.astro.washington.edu/spectra/co2.htm`).

These transitions describe the basic features of simple molecular absorption spectra, but in practice many further interactions occur within the molecule (e.g. parity of transitions). While a full description of the mechanisms is beyond the scope of this work, the ideas described here explain the origin of spectral lines seen in molecular gases such as planetary atmospheres. Each molecular species has characteristic energy transitions, which are mostly located within the visible and infrared part of the spectrum. The strength of the absorption lines reveals information about the environment in which the molecule is.

2.2.2 Line intensity and shape

Among all the energy transitions possible for a molecule, some occur more frequently than others, resulting in differences in transition probabilities. The state of the gas (temperature, energy level distribution of particles), associated with the probabilities of certain transitions to occur, define the strength of the intrinsic transition line. The differences in transition probabilities as a function of the gas environment are the cause of observed line strength variations.

For an energy transition from state E_2 to E_1, the number of transitions depends on the populations of molecules (N_1 and N_2) in either state:

$$N_1 = \frac{g_1 N}{Q_{tot}(T)} \exp\left(-\frac{E_1}{k_B T}\right) \tag{2.27}$$

where g_1 is the statistical weight of the state, N the total number of molecules per unit volume and $Q_{tot}(T)$ the total internal partition sum at temperature T. The same expression is adapted for the number of molecules in another state E_2. The total internal partition sum $Q_{tot}(T)$ is expressed as the sum of all the other states in the gas:

$$Q_{tot}(T) = \sum_{n=0}^{\infty} g_n \exp\left(-E_n/k_B T\right) \tag{2.28}$$

In addition, the probability of a transition to occur is expressed by the Einstein coefficients for spontaneous emission A_{21}, induced emission B_{21} and induced absorption B_{12}. They are linked with the following relations:

$$A_{21} = 8\pi h \nu^3 B_{21} \qquad \text{and} \qquad g_1 B_{12} = g_2 B_{21} \tag{2.29}$$

which are obtained from equating the (induced) absorption terms to the sum of (induced and spontaneous) emission terms under thermodynamic equilibrium conditions. These relations indicate that knowledge of one coefficient is sufficient to derive the others, provided the statistical weights $g_{1,2}$ are known. Among the three coefficients, the spontaneous emission coefficient A is often preferred as the unit is simply the number of spontaneous emissions per unit time (s^{-1}). The Einstein coefficients are derived either from quantum mechanical calculations or extracted from line intensity observations.

The line strength S of each energy transition line thus mainly depends on both the population number of molecules in the two energy states involved, as well as on the probability of induced absorption and emission obtained from the Einstein coefficients. This relationship is expressed by:

$$S = (N_1 B_{12} - N_2 B_{21}) \frac{h\nu_0}{c} \tag{2.30}$$

This value is not an infinitely thin line at the frequency ν_0 however, as the uncertainty principle of not knowing both ΔE and Δt means that for every transition there will be a small broadening $\Delta\nu$ near ν_0. Other mechanisms (listed below) also increase the broadening of the line, so it is convenient to define a frequency dependent spectral absorption coefficient $k(\nu - \nu_0)$:

$$k(\nu - \nu_0) = S f(\nu - \nu_0) \tag{2.31}$$

where $f(\nu - \nu_0)$ is a profile function defining the shape of line strength around ν_0. The spectral absorption coefficient is used in many line-by-line radiative transfer models, and is the preferred format for theoretical calculations for absorption strength.
The profile function is normalised and the integral across the spectral range is:

$$\int_{-\infty}^{\infty} f(\nu - \nu_0) d(\nu - \nu_0) = 1 \tag{2.32}$$

This means that S can be expressed as the integrated absorption coefficient of a single transition line over the spectral range:

$$S = \int_{-\infty}^{+\infty} k(\nu - \nu_0) d(\nu - \nu_0) \tag{2.33}$$

The unit of S is cm^{-2}, and the peak value of the line changes together with the line width due to the normalised profile function.

This line strength S is provided with measured spectral features (e.g. in HITRAN, which measures lines at 296K), where the line is broadened and its peak strength consequently lowered.

The profile function also depends on the temperature and pressure of the gas, with broadening effects affecting the line width and peak value. The two strongest mechanisms observed in planetary atmospheres are the pressure induced collision broadening and Doppler shift broadening:

2.2.2.1 Pressure induced collisions

The collisions of particles undergoing energy transitions affects the phase continuity of the energy transition, and causes a small shift in the absorption energy. In high pressure environments such as lower atmospheres (up to an altitude of ~20km in the Earth atmosphere (Liou 2002)), these collisions occur frequently and cause a broadening of the line widths. The shape of the resulting profile function can be described by a Lorentz profile (see e.g. Liou (2002); Goody and Yung (1995)):

$$f_P(\nu - \nu_0) = \frac{1}{\pi} \frac{\alpha}{(\nu - \nu_0)^2 + \alpha^2} \tag{2.34}$$

where α is the half-width at half-maximum of the line, and is a function of temperature and pressure.

2.2.2.2 Doppler shifting due to thermal velocities

In lower pressure environments (above ~ 50km in the Earth atmosphere (Liou 2002)), the distances travelled by individual molecules are long enough between collisions to add a significant velocity component to their frequency, which seen along the line of sight creates a small Doppler frequency shift:

$$\nu = \nu_0 (1 \pm \frac{v}{c}) \tag{2.35}$$

where v is the velocity of the molecule along the line of sight. The shape of the profile function becomes:

$$f_D(\nu - \nu_0) = \frac{1}{\alpha_D \sqrt{\pi}} \exp\left[-\left(\frac{\nu - \nu_0}{\alpha_D}\right)^2\right] \tag{2.36}$$

with

$$\alpha_D = \nu_0 \left(\frac{2k_B T}{mc^2}\right)^{1/2} \tag{2.37}$$

where m is the mass of the molecule.

The above two broadening processes often occur together, as is the case in the Earth atmosphere at altitudes between 20 and 50 km. The two broadening profiles are thus convolved to form the *Voigt profile*:

$$f_V(\nu - \nu_0) = \frac{1}{\pi^{3/2}} \frac{\alpha}{\alpha_D} \int_{-\infty}^{\infty} \frac{1}{(\nu' - \nu_0)^2 + \alpha^2} \exp\left[\frac{-(\nu - \nu')^2}{\alpha_D^2}\right] d\nu' \tag{2.38}$$

which is used as an approximation in radiative transfer models, although recently more accurate profiles have been developed (Tran *et al.* 2013).

For every line, the final spectral absorption coefficient $k(\nu - \nu_0)$ thus depends on the combination of the line strength S and the intrinsic and external sources of broadening processes. With a unique line for every energy transition, specific to each molecular species, a large number of lines have been identified and compiled into databases.

2.2.3 Line lists

Line lists that catalogue every known energy transition and the corresponding line strength for a large number of molecules are available for use by radiative transfer models. These databases are either populated from laboratory observations, such as the HITRAN[1] catalogue (Rothman *et al.* 2009), the GEISA[2] database (Jacquinet-Husson *et al.* 2011), the CDMS[3] database (Mueller *et al.* 2005), or from quantum mechanical ab-initio calcula-

---

[1] `http://www.cfa.harvard.edu/hitran/`

[2] `http://ether.ipsl.jussieu.fr/etherTypo/?id=950`

[3] `http://www.cdms.de`

tions, such as the ExoMol[4] catalogue (Tennyson and Yurchenko 2012). These catalogues are complementary: the ab-initio calculations need to be calibrated to observed results, but the calculated models expand the number of known lines and temperature ranges of observed molecules. HITRAN (2012) contains $\sim 7\times10^6$ lines for 47 molecules, designed for gases at room temperature (296K); the ExoMol catalogue expands the number of known lines, e.g. for NH_3 alone, the number of calculated transitions is over 1 billion and line strengths valid up to temperatures of 1500K (see Figure 2.5).

While higher-temperature spectra have been measured for a selection of molecules, including water, carbon monoxide and carbon dioxide, it is difficult to observe most molecules at high temperatures (e.g. ammonia dissociates at temperatures over $\sim$ 800K, at pressures between 0.01 and 500 mb[5]). The accuracy of these line lists is critical for the correct determination of the constituents of remotely sensed atmospheres.

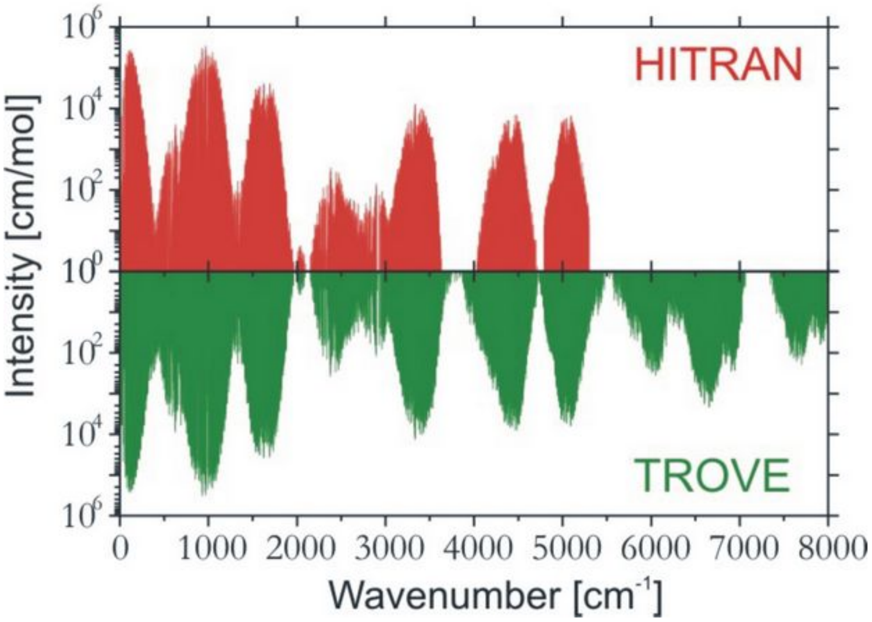

Figure 2.5: Comparison of the measured (HITRAN) and calculated (ExoMol “TROVE”) NH_3 transition lines. The laboratory data are measured at room temperature, while calculated values can be used up to temperatures of T = 1500K. Source: `http://www.spectrove.org/linelist.html`

2.2.4 Scattering

The phenomenon of scattering is an important contributor to the extinction process of radiation through a gas due to the interaction of light with small particles in the medium.

---

[4] `http://www.exomol.com`

[5] O. Venot, private communication

More specifically in an atmosphere, particles responsible for scattering range in size from gas molecules ($\sim 10^{-4}\mu$m) to aerosols ($\sim 1\mu$m), droplets (10μm), ice crystals ($\sim 100\mu$m) and large raindrops/hail particles ($\sim$ 1cm) (Liou 2002). The type of scattering a particle of a certain size will produce can be estimated by the size parameter x:

$$x = \frac{2\pi a}{\lambda} \tag{2.39}$$

where a is the particle radius, and λ the incident radiation wavelength. If x is much lower than 1, Rayleigh scattering is produced, and if x is larger or equal to 1, Lorenz-Mie scattering is produced. In the Rayleigh regime, the scattering cross section is defined as:

$$\sigma_s = \frac{8\pi^3(m_r^2 - 1)^2}{3\lambda^4 N_s^2} f(\delta) \tag{2.40}$$

where m_r is the real part of the refractive index of the molecules, N_s the total number of particles per unit volume, and $f(\delta)$ a correction factor to account for the anisotropic property of molecules. For atmospheric radiative transfer, Rayleigh scattering due to molecules is significant for wavelengths $< 1\mu$m (see equation 2.39); it has to be considered for visible and near-infrared wavelengths for transmission and reflection spectra. For emission spectra in the infrared Rayleigh scattering effects due to molecules can be neglected.

Particles of larger dimensions where the size parameter x is larger than 1 (2.39), are treated in the Lorentz-Mie scattering regime. Equation 2.40 becomes:

$$\sigma_s = \pi a^2 c_1 x^4 (1 + c_2 x^2 + c_3 x^4 + ...) \qquad \text{with} \qquad x = 2\pi a/\lambda \tag{2.41}$$

where a is the radius of the scattering particle, and $c_{1,2,3,...}$ are coefficients depending on the refractive indices of the scattering particles.

The derivation of these equations is given in Liou (2002).

At the regimes where Lorentz-Mie scattering is applicable, for instance clouds and aerosols, particle scatter can significantly reduce transmission of light. Figure 2.6 shows the amount of reflection (albedo) of Venus, Earth and Mars in the 0.4 - 1.6 μm range. Earth is presented with and without cloud cover, and the significant difference in reflection implies a high level of scattering within the atmosphere. On Venus, the high albedo originates from sulfuric acid clouds, which scatter and extinguish radiation in the visible wavelengths. While the impact of scattering in the visible and near-infrared wavelength ranges is clearly

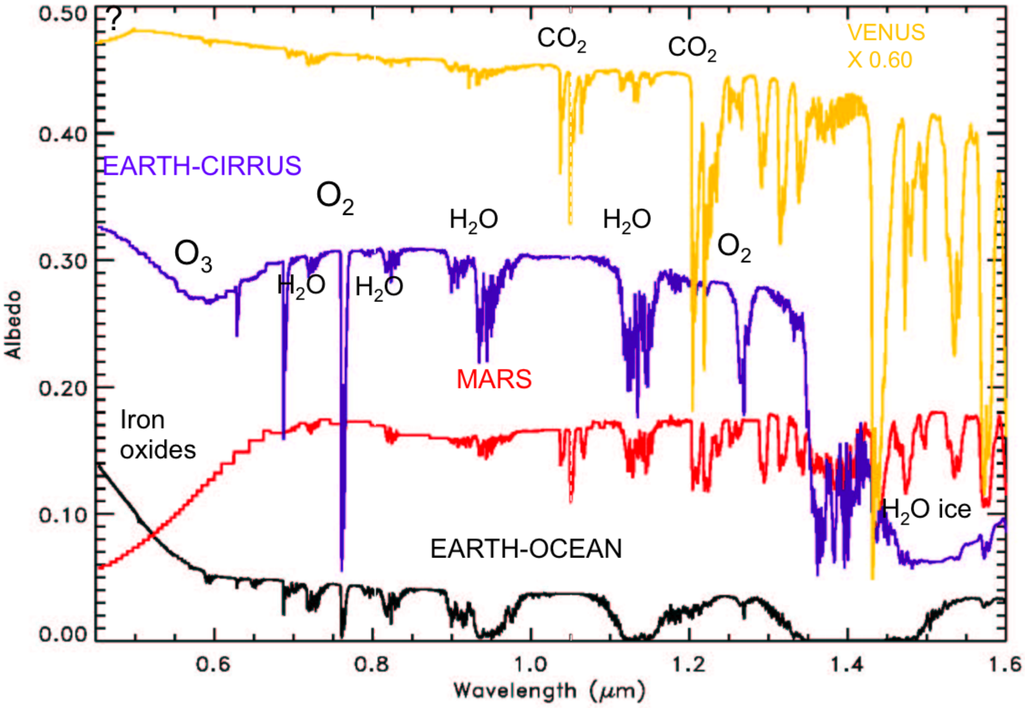

Figure 2.6: Albedo of Venus (yellow), Earth (with cirrus clouds, purple; no cloud cover, black) and Mars (red).

strong, at the longer infrared wavelengths the effects of clouds and scattering are usually of lesser importance. Most of the work presented in this thesis is based on these longer infrared wavelengths, so we will not consider the implementation of scattering effects.

2.3 Non-homogeneity of gas: application to atmospheres

2.3.1 Vertical temperature pressure profiles and mixing ratios

The equation of radiative transfer depends on the density of particles in the atmosphere, and thus on the pressure. The atmospheric pressure decreases with altitude, but depending on the composition of the atmosphere and impinging radiation, the temperature can decrease or increase with altitude. Figure 2.7 shows the temperature-pressure profiles of the solar system planets that are endowed with an atmosphere: the vertical temperature variations span a range of $\sim$ 1000K. As discussed in section 2.2.2, the temperature of the gas plays an important role in the absorption line strengths. Likewise, the abundance of specific molecular species within the gas, quantified by the dimensionless *mixing ratio*, changes the optical depth τ through the atmosphere. The mixing ratio of molecules varies significantly with altitude, as illustrated in Figure 2.8 for the case of Titan, and depends

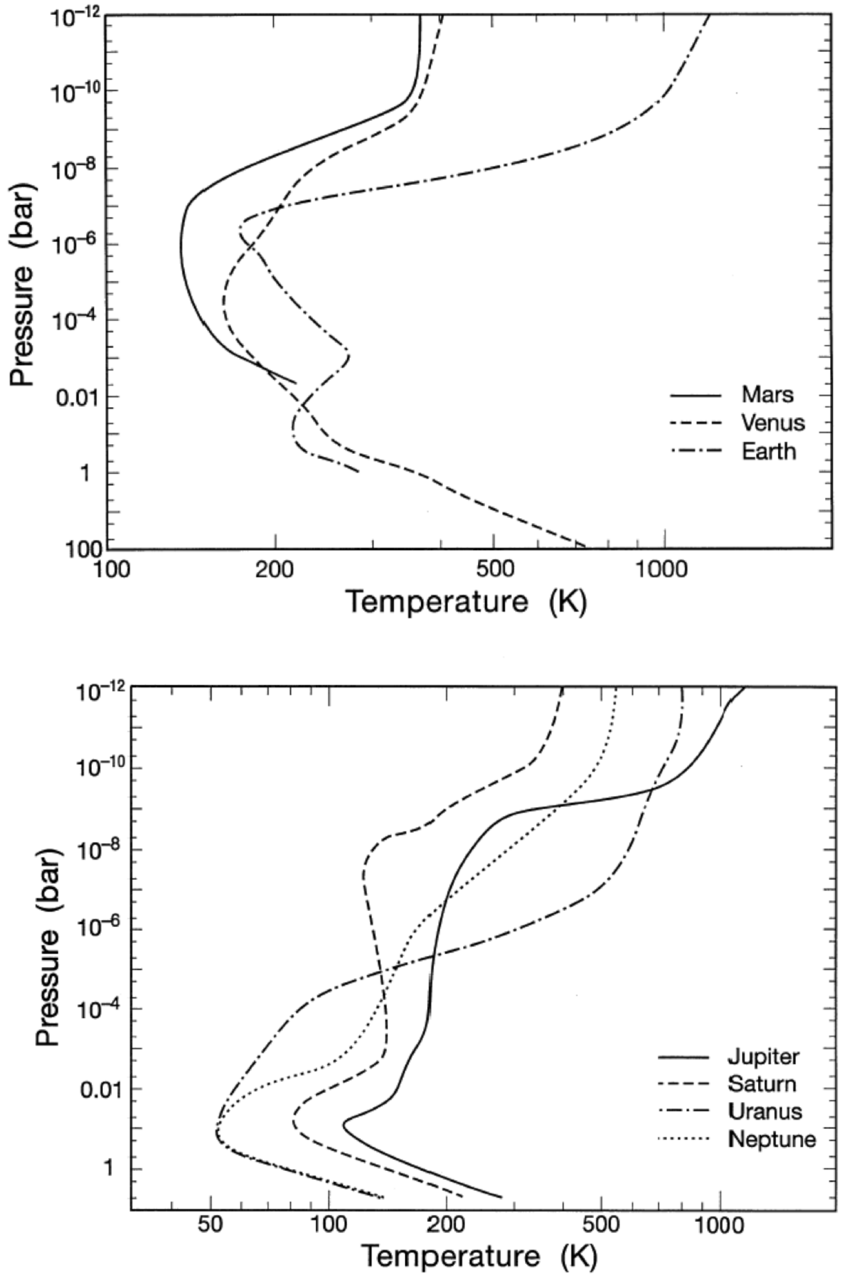

Figure 2.7: Temperature-Pressure profiles of the solar system planets that have an atmosphere. The temperature of these atmospheres spans a range of nearly 3 orders of magnitude.

on the chemistry within the atmosphere, as described below in section 2.4. With the pressure, temperature and abundances of chemical species strongly varying with altitude, it is important to consider the vertical changes of the atmosphere in the radiative transfer models.

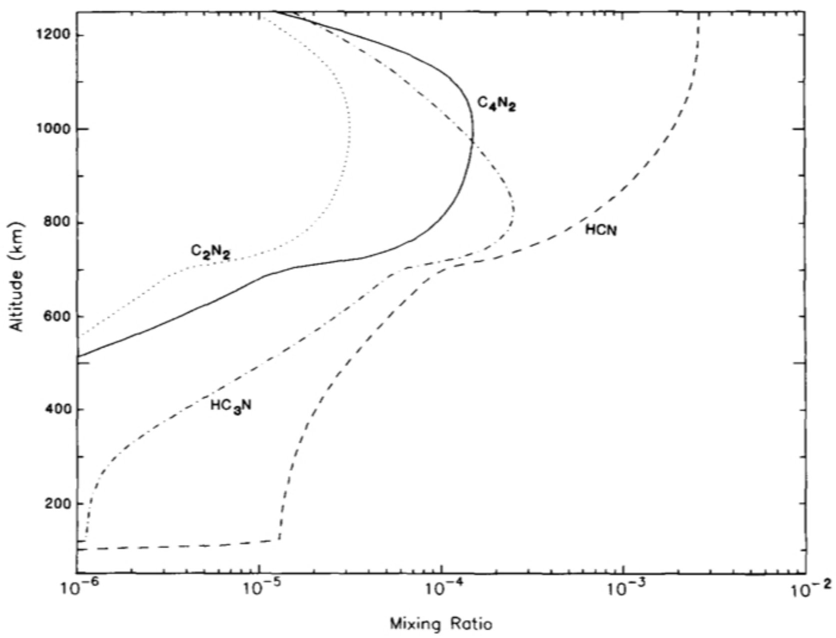

Figure 2.8: Calculated mixing ratio of various elements as a function of altitude in the atmosphere of Titan. From Yung (1987).

2.3.2 Plane-Parallel approximation

Given the main changes of gas state and composition along the vertical axis, it is convenient to divide the atmosphere in plane-parallel layers. We make the additional approximation of local thermal equilibrium in each layer. In each layer the temperature, pressure and mixing ratio of the molecular species are fixed, which simplifies the computations. With these considerations, the radiative transfer equation 2.2 becomes:

$$\cos\theta \frac{dI(z;\theta,\phi)}{\sigma\rho dz} = -I(z;\theta,\phi) + J(z;\theta,\phi) \tag{2.42}$$

where the angle θ is the inclination to the upward normal, ϕ the azimuthal angle along the plane. Defining the normal optical thickness τ (the wavelength dependence is not indicated for clarity of the expressions, but should be considered),

$$\tau = \int_z^\infty \sigma\rho dz' \tag{2.43}$$

Equation 2.42 can be re-written:

$$\mu \frac{dI(\tau;\mu,\phi)}{d\tau} = I(\tau;\mu,\phi) - J(\tau;\mu,\phi) \tag{2.44}$$

where $\mu = \cos\theta$.

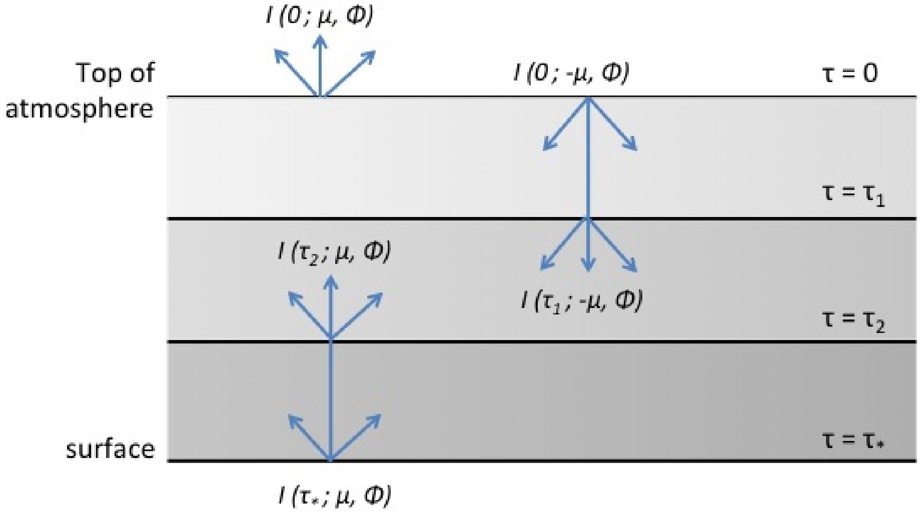

Figure 2.9: Plane-parallel atmosphere: upward (μ) and downward ($-\mu$) radiative intensities at layers $\tau_{1,2}$, τ_* (surface of planet) and $\tau = 0$ (top of atmosphere).

Defining τ at the top of the atmosphere as $\tau = 0$ and τ at the assumed surface of the planet as $\tau = \tau_*$, solving equation 2.44 for the boundaries of a layer gives the intensity upwards at level τ:

$$I(\tau;\mu,\phi) = I(\tau_*;\mu,\phi)\exp\left(-(\tau_*-\tau)/\mu\right) + \int_\tau^{\tau_*} J(\tau';\mu,\phi)\exp\left(-(\tau'-\tau)/\mu\right)\frac{d\tau'}{\mu} \tag{2.45}$$

with $(1 \geq \mu > 0)$, and downwards:

$$I(\tau;-\mu,\phi) = I(0;-\mu,\phi)\exp\left(-\tau/\mu\right) + \int_0^{\tau} J(\tau';-\mu,\phi)\exp\left(-(\tau-\tau')/\mu\right)\frac{d\tau'}{\mu} \tag{2.46}$$

with $(1 \geq \mu > 0)$.

At the top and bottom edges of the atmosphere, the solutions are expressed as:

$$I(0;\mu,\phi) = I(\tau_*;\mu,\phi)\exp\left(-\tau_*/\mu\right) + \int_0^{\tau_*} J(\tau';\mu,\phi)\exp\left(-\tau'/\mu\right)\frac{d\tau'}{\mu} \tag{2.47}$$

for the top layer, and:

$$I(\tau_*;-\mu,\phi) = I(0;-\mu,\phi)\exp\left(-\tau_*/\mu\right) + \int_0^{\tau_*} J(\tau';-\mu,\phi)\exp\left(-(\tau_*-\tau')/\mu\right)\frac{d\tau'}{\mu} \tag{2.48}$$

for the bottom layer. Figure 2.9 shows a representation of the upward and downlard intensities as a function of layer τ.

3-Dimensional models can be derived from these equations, but these are outside the scope of this thesis.

2.3.3 Application to Transmission spectroscopy: Beer-Bouguer-Lambert application

For the case of transmission spectroscopy, we only consider the extinction of radiation as it passes through the atmosphere. Thus we set $J = 0$ for the equations above, as the emission component is neglected.

While the plane-parallel approximation slices the atmosphere vertically, transmission spectroscopy of exoplanets relies on observing the planet transit in front of the host star (see section 1.1.1.4). With this geometry, we observe radiation as it "grazes" the surface of the planet, crossing multiple layers of the atmosphere twice. Figure 2.10 shows the geometry of the path taken by radiation as it travels through the exoplanet atmosphere. In Hollis *et al.* (2013), we have published our line-by-line radiative transfer program "TAU"[6] that simulates the spectral absorption of an atmosphere for planets observed in transmission. Specifically, the algorithm calculates the optical depth of the planetary atmosphere at a particular wavelength, with a hypothesised (model) bulk composition and trace molecular abundances, and given the atmospheric structure and absorbing behaviour of those molecules. Rayleigh scattering in the bulk atmosphere is calculated for all of the specified bulk constituents, and the optical depths due to this and the trace molecular absorption are then used within the geometry of the system (using the plane parallel approximation) to calculate an effective radius of the planet plus atmosphere (i.e. the conventional radius modified by the atmospheric absorption). A transit depth can hence be calculated as the ratio of the squared radii of the planet and the star, and the process repeated for every wavelength in the required spectral range, to build up a spectrum showing absorption as a function of wavelength.

Required input files to the code are a temperature-pressure profile and absorption cross-sections as a function of wavelength for the species hypothesised to be present in the

---

[6] The code is available for download at `http://www.ucl.ac.uk/exoplanets/` and is also reproduced in Appendix D.

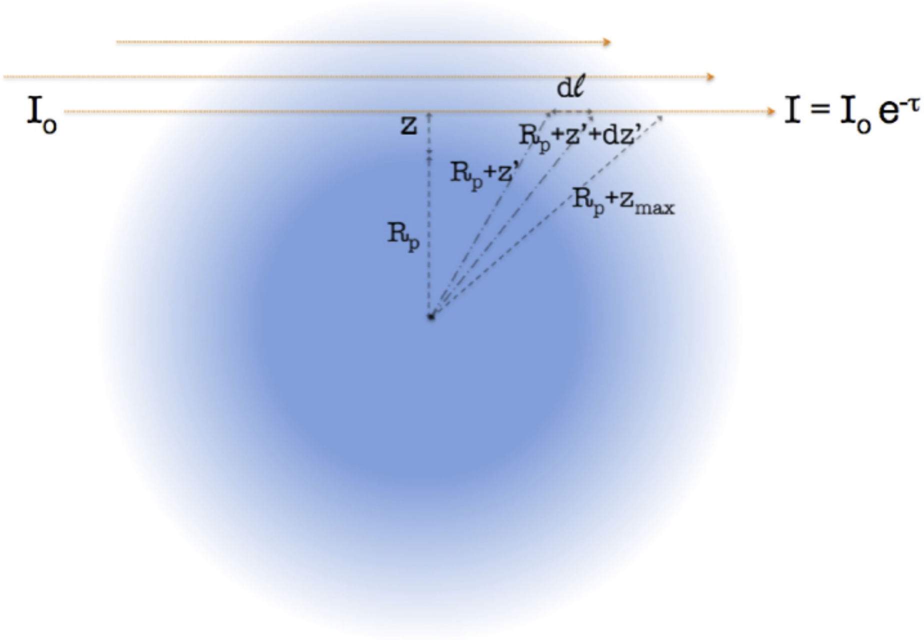

Figure 2.10: Geometry of a primary transit observation, illustrating the paths of the stellar photons filtered through the planetary atmosphere.

atmosphere. Absorption cross-sections are generally available from external sources (see Section 2.2.3), and for the profile and other optional inputs, the sample files provided can be altered as required, or generated anew by other means. The stellar radius as a function of wavelength can either be assumed constant (default) or given as an optional input to the code, as can collision-induced absorption coefficients.

To calculate the absorption due to atmospheric constituents, our program requires a knowledge of the quantity (mixing ratio) of each molecule i in the path, χ_i. The concentration of each molecular species i with number density $\rho_N\,[m^{-3}]$ is defined as $\chi_i\,\rho_N$. Equation 2.43 can be redefined as:

$$\tau_i(\lambda, z) \,=\, 2\int_0^{l(z)} \sigma_i(\lambda)\,\chi_i(z')\,\rho_N(z')\,dl. \tag{2.49}$$

where τ depends on the wavelength λ, the altitude z and the molecule species i. For the overall optical depth involving all the molecules,

$$\tau(\lambda, z) \,=\, \sum_{i=1}^{N} \tau_i(\lambda, z), \tag{2.50}$$

where N is the number of molecular species in the atmosphere. Using the Beer-Bouguer-Lambert law, the equivalent atmospheric depth $A(\lambda)$ is obtained by summing all of the viewing paths:

$$A(\lambda) = 2 \int_0^{z_{max}} (R_p + z)\,(1 - e^{-\tau(\lambda,z)})\,dz, \tag{2.51}$$

The monochromatic "transit depth" $D(\lambda)$ is thus:

$$D(\lambda) = \frac{R_p^2 + A(\lambda)}{R_*^2}. \tag{2.52}$$

Absorption by the molecules present in the atmosphere reduces the overall final transmitted flux at wavelength λ by the factor $(1 - e^{-\tau(\lambda,z)})$, which is the same effect as having a totally opaque body with a slightly larger radius transiting the star. The absorption can therefore be quantified by a simple radius ratio (i.e. a conventional transit depth) at each wavelength, and a spectrum can hence be constructed showing the absorption as a function of wavelength for the input model parameters.

A stellar spectrum is not required in this code. This program has been used for the production of primary transit spectra in this thesis.

2.3.4 Application to Emission spectroscopy: Schwarzschild application

In the case of emission spectroscopy, the plane-parallel approximation equations 2.45 and 2.46 need to be solved numerically. In this scenario the emission term is set to $J = B_\lambda$, where B_λ is the expression of Planck's function. To solve these equations, the method we used for this thesis is the discrete ordinate method (described in chapter 8.2.2 in Goody and Yung (1995)) which takes advantage of an expansion in Legendre polynomials. Equations 2.45 and 2.46 can therefore be transformed into a system of $2n$ first order, non homogeneous differential equations; where $2n$ is the degree of the Legendre polynomial. For the work presented here, we use a line-by-line radiative transfer model (SMART), which is a wrapper for the algorithm provided by DISORT (Stamnes *et al.* 1988).

All the transfer equations considered above are given at a specific angle ($\mu = \cos\theta$). If we are interested in the emission of the entire atmosphere, this information needs to be integrated over the entire disk. This can be done by pixelisation of the sphere and solving the equation for radiative transfer for each pixel with an appropriate angle, and summing the contributions of all the pixels, as discussed in Tinetti *et al.* (2006) and Hearty *et al.* (2009). This is particularly important when scattering processes are considered, due to the importance of the relative angle between the incident radiation and the position of the observer. In practice, for emission spectroscopy, one can approximate the disk averaged contribution using the information on an average angle (typically 60 degrees).

For the incoming radiation to the planet, stellar spectra are obtained from observed and simulated models (Hauschildt *et al.* 1999; Kurucz 1995).

2.4 The Chemistry of Planetary Atmospheres

2.4.1 Initial conditions

The mixing ratios used as inputs in the radiative transfer models are based on the possible chemistry in various atmospheric scenarios. Atmospheric chemistry is governed in part by the initial conditions present in the protoplanetary disk during planetary formation, and in part through the interaction with the stellar radiation and impacts with smaller bodies. Depending on the formation models, gravitational instability or core accretion, the initial conditions can depend on the host star metallicity.

Gravitational instability models predict a rapid formation of a planet during the early phases of protoplanetary disk, which means that the planet atmosphere will have abundances that reflect the formation environment (Baruteau *et al.* 2011; Zhu *et al.* 2012). These atmospheres can sustain post-formation enrichment from external bombardment, although the bulk compositions should reflect the initial environment.

For the core-accretion model, planetesimals are initially formed by the settling of dust grains. This core then accretes surrounding gas, and can either stop at Neptune or super-Earth sized planets, or through runaway accretion reach the size of Jupiter-sized planets. For core accretion models, ice lines of key constituents (distances at which the temperature is low enough for the molecules to freeze) and the migration of accreting planets across them determine the initial compositions of the planet atmospheres. Figure 2.11 shows the ice lines for H_2O, CO_2 and CO in the disk of a solar-type star, and the impact they have on the C/O ratio of gas and solids in the disc. Up to a distance of $\sim$ 2AU, the gas and solid C/O ratio are close to the solar value. Between the H_2O and CO_2 ice lines, frozen water traps oxygen, which decreases the solid C/O ratio, but increases the gas C/O ratio. As carbon based particles freeze, oxygen is freezing at twice the rate, pusihing the gas

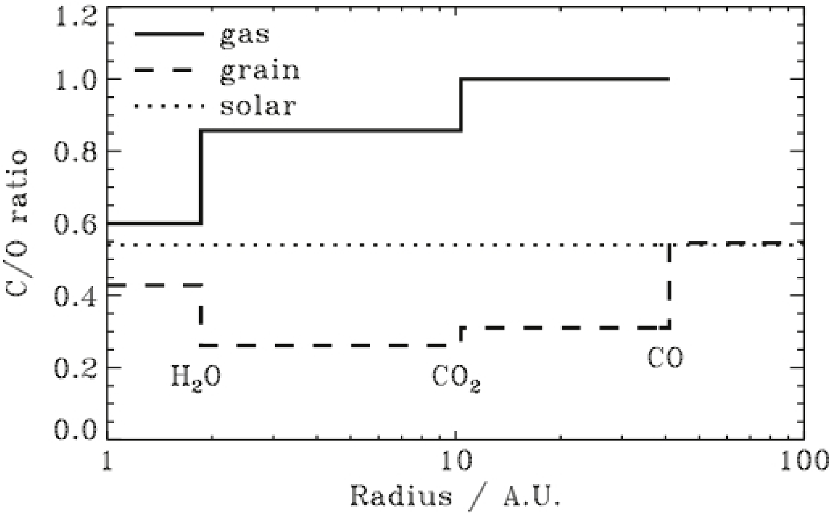

Figure 2.11: Location of the ice lines of H_2O, CO_2 and CO in the solar system and their impact on the C/O ratio of gas and solids. From Öberg *et al.* (2011)

C/O ratio over 1.

In Nelson, Turrini and Barbieri (2013, *in prep.*), formation and migration scenarios explore the possibilities of planetary accretion with migration through ice lines and the impact on the C/O ratio of atmospheres.

2.4.2 Atmospheric evolution and chemistry

As discussed in the previous paragraph, formation processes have a key role in determining the chemistry of planetary atmospheres, but initial conditions are not the only important element. In practice, atmospheres are often out of chemical equilibrium due to a host of physical processes, which include interaction with the external radiation (photochemistry (DeMore and Yung 1998)), atmospheric dynamics (vertical mixing, quenching, eddy diffusion, etc.), and impacts with smaller bodies. However, as explained in Moses (2014), at high planetary temperatures these processes become less effective. At temperatures over ~2000K, non-equilibrium processes should thus play a less critical role. For terrestrial planets the atmospheric composition is often very different from the initial compositions due to escape and outgassing processes which are usually not present for gaseous planets (Forget and Leconte 2014).

To illustrate the differences between equilibrium and non-equilibrium chemistry in an atmosphere, we show in Figure 2.12 the mixing ratios of the main constituents considered in a modeled atmosphere of GJ 3470b (Venot *et al.* 2014). In that paper, we have explored the variations of the CH_4/CO ratio in the atmosphere of GJ 3470b, which is useful for understanding the main reservoirs of carbon and oxygen in gaseous atmospheres. The input parameters that were changed for the models are: metallically, temperature, vertical mixing and stellar UV flux. From a standard model, the four parameters are selectively explored to form 16 models, with the parameters listed in table 2.3. The impact on the mixing ratio of CO and CH_4 is shown in Figure 2.13 with the ratio of the two molecules also plotted. As illustrated by the figures, only certain combinations of parameters produce a CH_4/CO ratio < 1. It thus seems that except for a specific combination of parameters, CH_4 is expected to be the dominant carbon reservoir on GJ 3470b, according to this

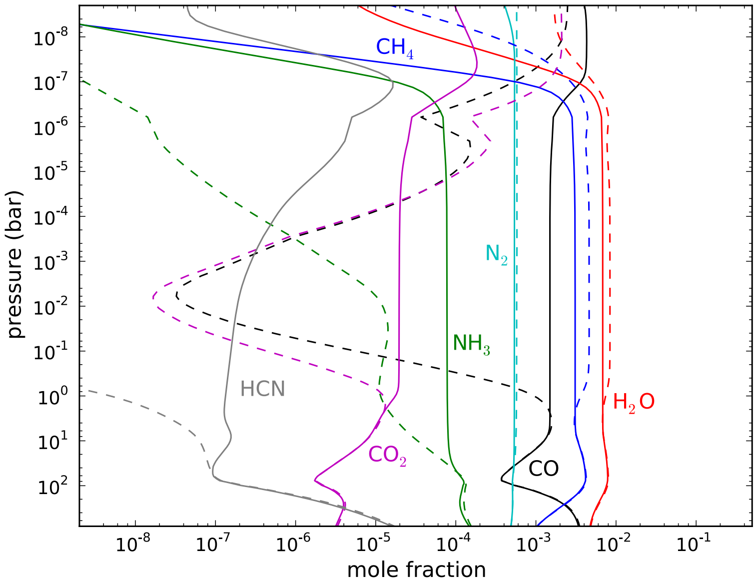

Figure 2.12: Abundances of the main constituents in the modeled atmosphere of GJ 3470b for the case of equilibrium (dashed lines) and non-equilibrium (solid lines). From Venot *et al.* (2014).

Parameter	Range of values	Symbol
Metallicity	Solar ($\zeta = 1$)	ζ_1
	High ($\zeta = 100$)	ζ_{100}
Temperature	Warm atmosphere (+100 K)	T_{+100}
	Cool atmosphere (−100 K)	T_{-100}
Eddy diffusion coefficient	High (K_{zz} ×10)	$K_{zz}^{\times 10}$
	Low (K_{zz} ÷10)	$K_{zz}^{\div 10}$
Stellar UV flux	High irradiation (F_λ ×10)	$F_\lambda^{\times 10}$
	Low irradiation (F_λ ÷10)	$F_\lambda^{\div 10}$

Table 2.3: Parameter space explored by the 16 models in Venot *et al.* (2014).

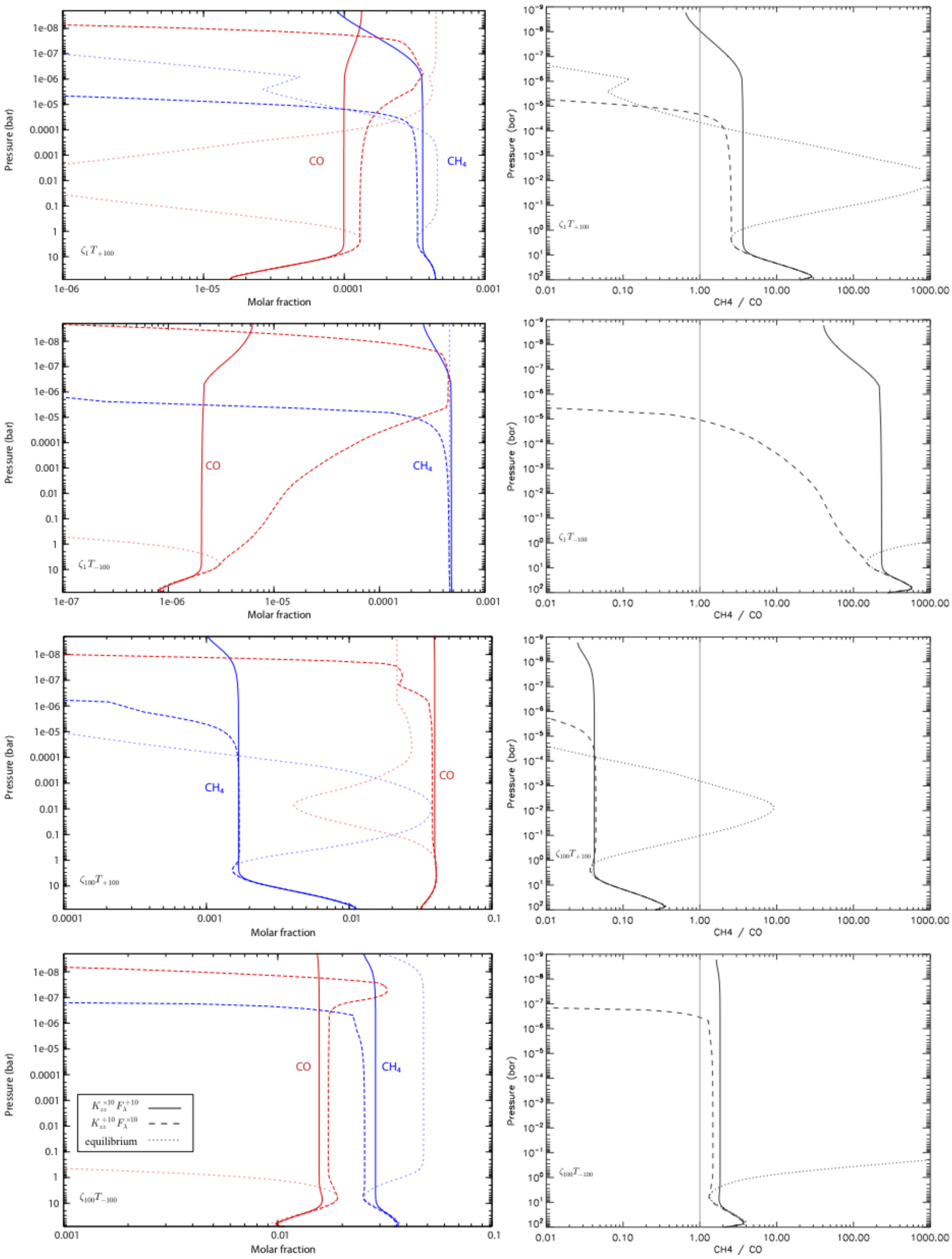

Figure 2.13: CH_4/CO ratio scenarios for GJ 3470b, with four varying parameters: eddy diffusion coefficient, stellar UV flux, metallicity and temperature. See Table 2.3 for the definition of the symbols. From Venot *et al.* (2014)

chemical model.

The chemistry of planetary atmospheres thus depends on the initial formation scenarios but also the dynamic environment of the planet. The changes in these mixing ratios will have an impact on the radiation absorbed through the atmosphere. This in turn will have an impact on the observed spectra, as is shown in the following section with synthetic spectra generated for the 16+1 models in both transmission and emission.

2.5 Simulation of exoplanet atmospheric spectra

As part of the study of chemical variations in the atmosphere of GJ 3470b, we produced emission and transmission spectra to see the impact of model changes. In both simulation modes, the synthetic spectra were generated for a standard case + 16 models that explore the changes in temperature, metallicity, vertical mixing and solar UV flux. The spectra are shown in Figure 2.14, with the transmission plots expressed in planetary radius (in units of $R_\oplus$), and the emission plots as brightness temperature, the inverse of Planck's function $B_\lambda(T)$.

The results appear separated into five groups, for both emission and transmission cases: red ($\zeta_1 T_{+100}$), yellow ($\zeta_{100} T_{+100}$), green ($\zeta_1 T_{-100}$), and purple ($\zeta_{100} T_{-100}$), with the standard case in the middle. Examination of the results show that a $\Delta T = \pm 100$K temperature change combined with a multiplication or division by a factor of 10 for metallicity are the biggest contributors to the shifts. In addition for both types of spectra, the low metallicity (red and green) set of models exhibit broader variations than the others, as the atmospheres have a lower optical depth τ, and the radiation probes more levels of the vertical thermal profile.

In the case of transmission, the models that generate the atmosphere of largest radius are the $\zeta_1 T_{+100}$ cases of low metallicity and high temperature. This is expected as a combination of low mean molecular weight (due to low metallicity) and high temperature increase the value of the scale height H, which describes the expansion of the atmosphere. At the other extreme, the coldest atmosphere with highest metallicity, and thus heaviest atmosphere, $\zeta_{100} T_{-100}$ appears as the lowest radius. The effects of temperature and metallicity are compensating each other for the high temperature high metallicity $\zeta_{100} T_{+100}$ and low metallicity low temperature $\zeta_1 T_{-100}$ cases. We have plotted the experimental data points for this planet measured by Crossfield *et al.* (2013); Demory *et al.* (2013), and Fukui *et al.* (2013). The error bars plotted are best matched by the red ($\zeta_1 T_{+100}$) series of models, although two data points are not captured (2^{nd} and 3^{rd}, left to right). The radius of the planet however is badly determined on gaseous planets, as observations provide the apparent radius which doesn't specify the corresponding pressure level. The 1 bar pressure level has to be estimated, and in the case of GJ 3470b, we used the lower limit of the observed radius 4.28 $R_\oplus$. Changing the 1 bar pressure level radius can shift the spectra vertically. If the radius is changed, the green and yellow sets of models offer a possible

but slightly less convincing fit, but the purple set of models, even if sufficiently shifted, cannot capture the three different set of measurements.
For the emission spectra, the strongest differentiator among the five groups is temperature. The low metallicity / high temperature group of models is clearly the hottest, followed by the high metallicity / high temperature group, which appear slightly colder. Higher metallicity implies higher optical depth τ, so the radiation seen at the top of the atmosphere comes from colder, higher altitude regions. The standard model is placed in between the +100 K and -100 K cases. The colder cases are differentiated again by the metallicity. In the emission cases it is almost impossible to distinguish the effects of UV flux and vertical mixing.

As shown in this chapter, despite many of the models generated having different compositions, it is not always straightforward to discriminate the spectral differences. The problem of spectral retrieval and potential degeneracy of solutions is well known in the field of remote sensing (Conrath *et al.* 1970; Hanel *et al.* 2003). This is the topic of the next chapter, where we specifically try to address the issue of molecular detectability in the atmospheres of exoplanets.

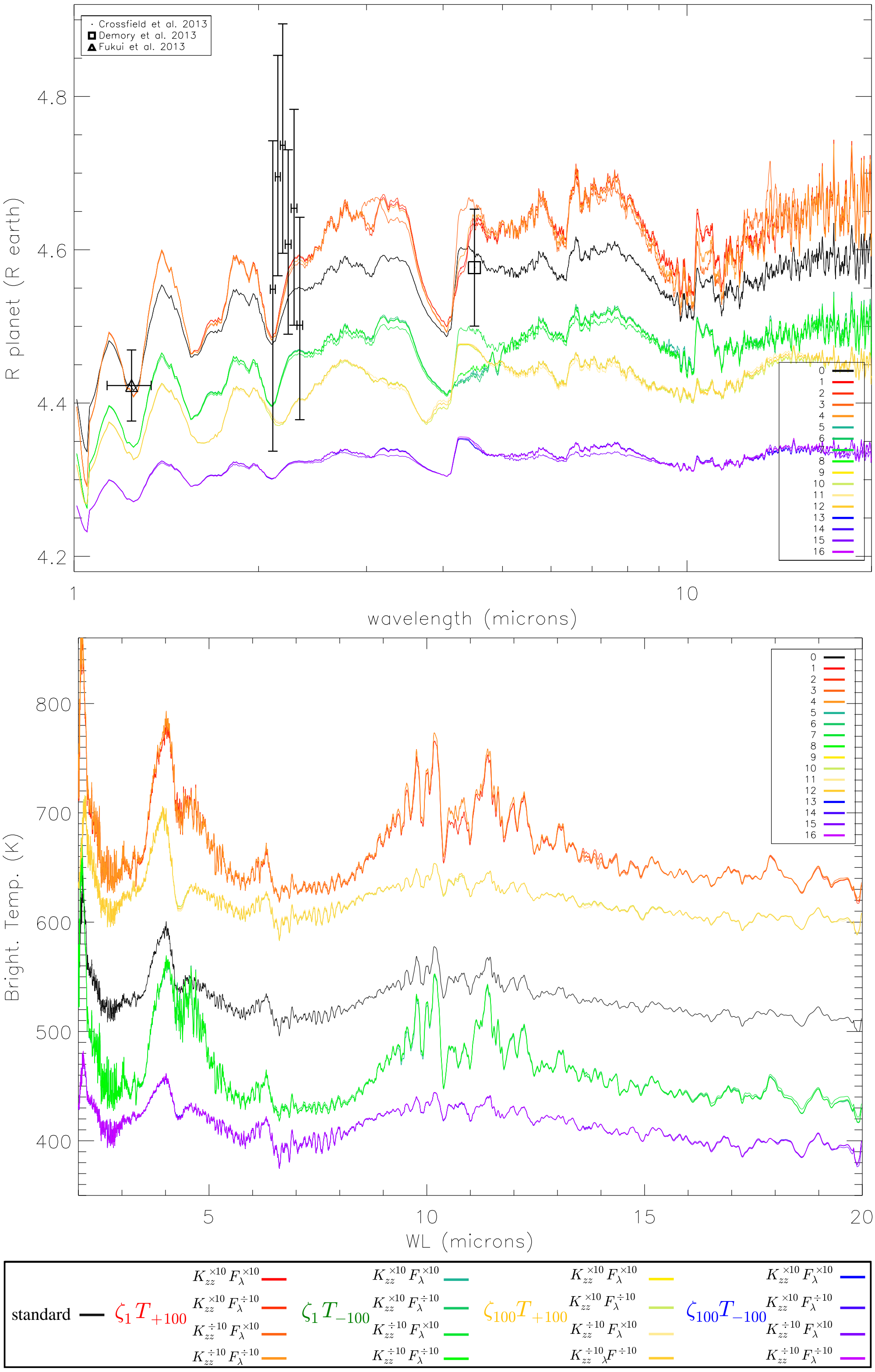

Figure 2.14: Synthetic spectra for GJ 3470b, with a standard model (0) and 16 variations. *Top:* transmission spectra expressed as $R_\oplus$. *Bottom:* emission spectra expressed in brightness temperature. Published in Venot *et al.* (2014)

Chapter 3

Molecular Detectability in Exoplanet Atmospheres

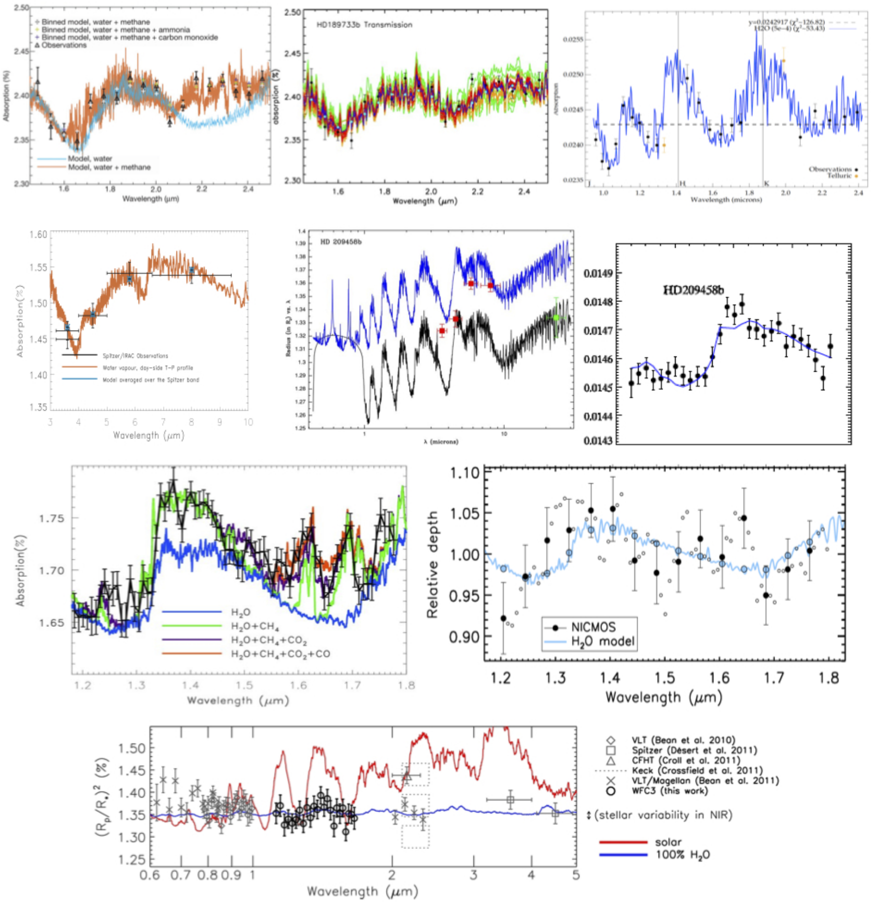

Figure 3.1: A collection of published exoplanet spectral observations. The detectability of molecules is a challenge for all current observations. Figure from Tinetti *et al.* (2013)

Ground and space-based observations (VLT, Keck, IRTF, Spitzer, and the Hubble Space Telescope) of exoplanets have shown the potentials of the transit method: current observations of hot gaseous planets have revealed the presence of alkali metals, water vapour, carbon monoxide and dioxide and methane in these exotic environments (e.g. Charbonneau *et al.* 2002; Harrington *et al.* 2006; Crossfield *et al.* 2010; Knutson *et al.* 2007b; Tinetti *et al.* 2007, 2010b, 2012b; Beaulieu *et al.* 2008, 2010; Swain *et al.* 2008a,b, 2009b,a; Grillmair *et al.* 2008; Stevenson *et al.* 2010; Redfield *et al.* 2008; Snellen *et al.* 2008; Swain *et al.* 2010; Snellen *et al.* 2010; Waldmann *et al.* 2012). However, the instruments used in the past ten years were not optimised for this task, so the available data are mostly photometric or low resolution spectra with low signal to noise (see Figure 3.1). Additionally, multiple observations are often required, during which many effects can alter the signal: from the weather on the planet to other sources of noise including instrument systematics and stellar variability. The interpretation of these — often sparse — data is generally a challenge (Swain *et al.* 2009b,a; Madhusudhan and Seager 2009; Lee *et al.* 2012; Line *et al.* 2012)

With the arrival of new facilities such as Gemini/GPI, VLT/SPHERE, E-ELT and *JWST*, and possibly dedicated space instruments such as *EChO*, many questions need to be tackled in a more systematic way. Among these stands out the question of molecular detectability: *what are the objective criteria that need to be met to claim a molecular detection in an exoplanet?* In this chapter we aim to address this question by focusing on the signatures of a selection of key molecules, with a range of abundances, over a broad wavelength range (1 to 16 μm). To capture the extent of possible chemical compositions of exoplanet atmospheres, we have chosen five planetary cases: hot Jupiter, hot super-Earth, warm Neptune, temperate Jupiter and temperate super-Earth. While our study has been inspired by transit spectroscopy with a hypothetical *EChO*-like space-based instrument, the methodology and results of this chapter are applicable to observations with other instruments and techniques, including direct imaging. The results presented in this chapter are published in Tessenyi *et al.* (2013).

3.1 Fixed SNR detectability - instrument independent results

We select five planets out of a range of sizes (Jupiter, Neptune and super-Earth sizes) and temperatures (hot, warm and temperate), listed in Table 3.1, to describe comprehensively the chemical compositions that can be expected in exoplanet atmospheres. The atmospheric components and their spectroscopic signals depend strongly on the planetary temperature and size, we thus focus on cases delimiting these parameters. Other cases can be constrained by these five planet types. The planetary and stellar parameters assumed for these targets, listed in Table 3.2, are obtained from observations when possible; calculated values are used otherwise. We used HD 189733b (Bouchy *et al.* 2005) as a template for the hot Jupiter case, GJ 436b (Butler *et al.* 2004) for the warm Neptune case, and Cnc 55e (Winn *et al.* 2011) for the hot super-Earth case. We also consider the case of a temperate super-Earth orbiting a late type star. Such a planet could be subjected to intense radiation and be tidally locked; however, an atmosphere on this type of planet is plausible, as has been discussed in the literature (e.g. Joshi *et al.* (1997); Wordsworth *et al.* (2010); Segura *et al.* (2010)).

Temperature/Size	Jupiter-like	Neptune-like	super-Earth
Hot ($\geq$800 K)	**HJ**	HN	**HSE**
Warm (350-800 K)	WJ	**WN**	WSE
Temperate (250-350K)	**TJ**	TN	**TSE**

Table 3.1: Subdivision of planetary atmospheres according to temperature and planet size. The difficulty in the observations increases from left to right and from top to bottom. The categories highlighted in bold are the subject of our study. The observability of other planet types can be extrapolated from these cases. Planets with temperatures below “temperate” have a signal too weak for both transit spectroscopy and direct detection, we consider warmer candidates for this study.

	Hot		Warm	Temperate	
Star	Jupiter	super-Earth	Neptune	Jupiter	super-Earth
Spectral Type	K1V	G8V	M2.5V	K4V	M4.5V
Radius ($R_\odot$)	0.79	0.94	0.46	0.75	0.22
Mass ($M_\odot$)	0.8	0.91	0.45	0.8	0.22
Temperature (K)	4980	5196	3684	4780	3300
Distance (pc)	19.3	12.34	10.2	10	10
Planet					
Radius (R_{jup} / $R_\oplus$)	1.138 / 12.77	0.194 / 2.18	0.365 / 4.10	1.138 / 12.77	0.16 / 1.8
Temperature (K)	1350	2100	750	250	250
Semi-major axis (au)	0.031	0.016	0.029	0.4	0.046
Period (days)	2.2	0.74	2.6	102	7.6
Transit duration (hr)	1.83	1.76	1.03	7.9	1.39
Bulk atm. composition	H_2	H_2O	H_2	H_2	N_2
μ (u)	2.3	18.02	2.3	2.3	28.01
Surfaces ratio	2.20×10^{-2}	4.48×10^{-4}	6.55×10^{-3}	2.43×10^{-2}	5.6×10^{-3}

Table 3.2: Stellar and planetary parameters assumed for this study. The planetary radii are given both in units of Jupiter radii and Earth radii, and the temperatures listed are an average temperature from the adopted temperature-pressure profiles. The mean molecular weight of the atmosphere considered is indicated by μ. The star/planet ratio $(R_{pl}/R_*)^2$ is also listed here to facilitate the comparison among the targets studied.

In this study, we focus on emission spectroscopy in the infrared, obtainable through secondary eclipse observations or direct imaging. For transiting planets, the emission spectra can be obtained by subtracting the stellar signal from the combined light of star+planet. In practice, the measurements and simulations are given as the flux emitted by the planet in units of the stellar flux:

$$F_{II}(\lambda) = \left(\frac{R_p}{R_\star}\right)^2 \frac{F_p(\lambda)}{F_\star(\lambda)} \tag{3.1}$$

where F_p and $F_\star$ are the planetary and stellar spectra. This equation highlights the influence of both the surfaces ratio and the relative temperatures of the planet and star for secondary eclipse measurements.

3.1.1 Methods

3.1.1.1 Planetary and Stellar Spectra

With the range of planetary temperatures and sizes considered, the temperature-pressure (T-P) profile will vary significantly for the five planet cases. The T-P profile describes the change in temperature as a function of pressure in a given atmosphere. Figure 3.2 shows the T-P profiles assumed for the planets. To investigate the effect that the thermal gradient has on the observed signal, two additional more extreme T-P profiles are presented for the Warm Neptune case: a dry adiabatic profile with a steep lapse rate reaching 500 K at ~0.1 bar, and a profile with a lapse rate closer to isothermal, reaching 500K at 10^{-6} bar. Results for these additional profiles are presented in section 3.2.1.1.

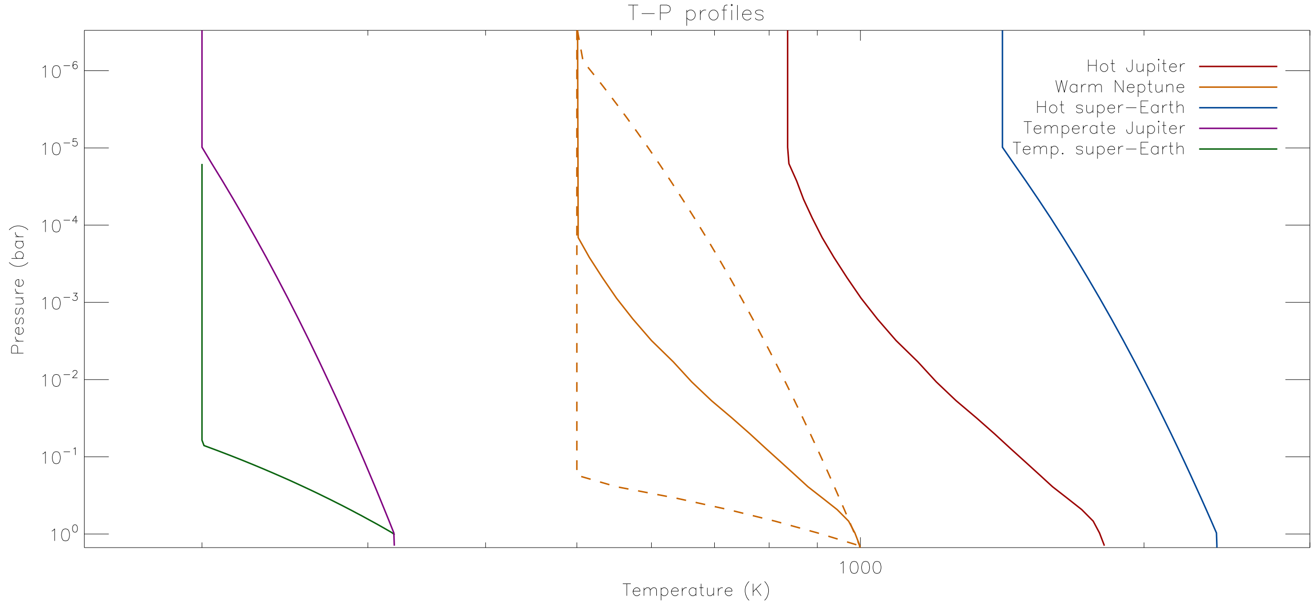

Figure 3.2: Temperature-pressure (T-P) profiles of the five target types presented. *From left to right:* temperate super-Earth and Jupiter, warm Neptune with three possible profiles: a steep dry adiabatic profile (dashed, left), a more isothermal profile (dashed, right) and a simulated one (Beaulieu *et al.* 2011) in between (solid), a hot Jupiter profile (Burrows *et al.* 2008) and a hot super-Earth profile.

In the case of super-Earths, the atmosphere — if present — could be dominated by a variety of molecules, such as hydrogen+helium ($\mu = 2.3u$), water vapour ($\mu = 18.02u$), nitrogen ($28.01u$) or carbon dioxide ($44u$). A change in the main atmospheric component will impact both the atmospheric scale height (H) and the atmospheric lapse rate (γ). For our tests we have assumed a dry adiabatic lapse rate:

$$H = \frac{kT}{\mu g} \qquad\qquad \gamma = -\frac{dT}{dz} = \frac{g}{c_p} \tag{3.2}$$

where k is the Boltzmann constant, g is the gravitational acceleration, T the temperature in degrees Kelvin, μ the mean molecular weight of the atmosphere, z the altitude and c_p the specific heat of the gas. We tested the impact on molecular detectability in an atmosphere composed of hydrogen, water vapour, nitrogen or carbon dioxide. The parameters derived for each of the cases are shown in Table 3.3.

Main constituent	μ (u)	H (km)	γ (K/km)
Hydrogen	2.3	76.6	1.1
Water vapour	18.02	9.8	8.1
Nitrogen	28.01	6.3	14.5
Carbon dioxide	44	4.0	17.8

Table 3.3: Temperate super-Earth atmospheric parameters considered, from a hydrogen dominated atmosphere to a carbon dioxide dominated atmosphere. μ is the molecular weight, H the atmospheric scale height and γ the corresponding dry adiabatic lapse rate.

The infrared emission spectra are calculated using the models described in section 2.3, over a pressure range of 10 to 10^{-6} bars. For every planetary case, an individual spectrum is generated for each molecule (Table 3.4) assuming five mixing ratios, ranging from 10^{-7} to 10^{-3}. The planetary and stellar parameters and spectra are used to calculate the photon flux from the planet and star as a function of wavelength, and are presented as a planet/star contrast spectrum (equation 3.1).

Planet	Molecules considered
Hot Jupiter	CH_4, CO, CO_2, NH_3, H_2O, C_2H_2, C_2H_6, HCN, H_2S and PH_3
Hot super-Earth	H_2O, CO and CO_2
Warm Neptune	CH_4, CO, CO_2, NH_3, H_2O, C_2H_2, C_2H_6, HCN, H_2S and PH_3
Temperate Jupiter	H_2O, CH_4, CO_2, C_2H_2 and C_2H_6
Temperate super-Earth	H_2O, CO_2, NH_3 and O_3

Table 3.4: Molecules considered in the atmospheres of the planets studied. For all planets and molecules, a uniform mixing ratio is assumed across the temperature-pressure range.

We consider the 1 to 16 μm wavelength range to best capture the key molecular features present in a planetary atmosphere with a temperature between 250K and 3000K (Tinetti *et al.* 2013). This spectral interval is also compatible with the currently available or foreseen instruments for transit spectroscopy and direct imaging. The spectral resolution is set to R=300 and R=30 for the 1 to 5 and 5 to 16 μm spectral intervals, respectively, and lowered to R=20 in the 5 to 16 μm spectral interval for the temperate super-Earth. These choices optimise the performances of potential instruments with the number of photons typically available.

The only source of noise assumed in this work is photon noise, and an overall optical efficiency of 0.25 has been considered (e.g. reflectivity of mirrors, throughput of optical system, detector quantum efficiency, etc.). For a given duration of observation and for every resolution bin, the signal to noise ratio (SNR) is calculated for the star and for the planet:

$$SNR_* = N_*/\sqrt{N_*} \tag{3.3}$$

$$SNR_p = F_{II} \times SNR_* = \frac{N_p}{\sqrt{N_*}} \tag{3.4}$$

where N_* is the number of photons received from the star, N_p is the number of photons received from the planet, and F_{II} is the planet/star contrast spectrum (see equation 3.1). One sigma error bars are computed for the planet/star contrast spectrum in every resolution bin:

$$\sigma = \frac{F_{II}}{SNR_p} \tag{3.5}$$

To address the question of molecular detectability, the results in section 3.2 are presented as function of fixed SNR$_p$ (from hereon referred to as SNR) in the spectral intervals where the molecular features are located. In this way, our results are completely independent from the duration of the observations and the instrument design. However, to give an estimate of the observational requirements needed to achieve these SNR values, we show in appendix A the typical SNR values obtainable with a dedicated space-based instrument.

3.1.2 Molecular Detectability

In a planet/star contrast spectrum, the molecular features appear as departures from the continuum. At a fixed T-P profile, the absorption depth or emission feature will depend only on the abundance of the molecular species. We use two approaches to determine the minimum detectable abundance for each molecule: individual bins and likelihood ratio test.

3.1.2.1 Individual bins

This is the most intuitive and conservative approach: we measure in every bin the difference between the planetary signal with or without the absorption of a selected molecule. We claim a detection if a difference of at least 3-sigma (see equation 3.5) is found between the continuum and the molecular signature in a given bin. While the depth of the feature will depend on the abundance of the molecule (at fixed thermal profile), the SNR in that bin will determine the value of sigma. We present in our results the minimum molecular abundance detectable as a function of fixed SNR=5, 10 or 20 and wavelength. Figure 3.3 shows an example of CO_2 and HCN in the atmosphere of a Warm Neptune, with a fixed SNR=10. If the departure from the continuum is less than 3-sigma, we cannot claim a detection. However, given that most spectral features span multiple bins, the likelihood ratio test can use this information in a more optimal manner.

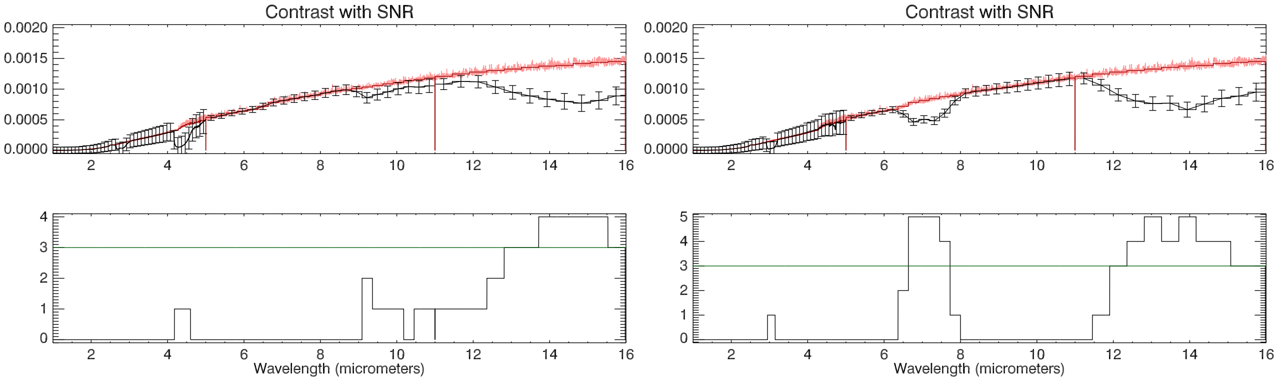

Figure 3.3: Individual bin method to detect the presence of a molecule in the atmosphere of a Warm Neptune. The upper panels show contrast spectra where two different molecules absorb. The error bars are computed with fixed SNR=10. *Left:* CO_2 with mixing ratio=10^{-5}, *Right:* HCN with mixing ratio=10^{-4}. The planet continuum is shown in red. The lower panels show the departure of the molecular signal from the continuum in units of sigma (see eq. 3.5). A 3-sigma departure is required to claim a detection. This threshold is shown here as the green horizontal line.

3.1.2.2 Likelihood Ratio Test

As in the individual bin method, the idea here is to test the hypothesis of a molecular detection in a noisy observation. Also, for every molecule considered, the tests described here are repeated for the five abundance levels, to determine the minimum detectable abundances. The likelihood ratio test (Neyman and Pearson 1928) provides the confidence with which we can reject the “null hypothesis”, i.e. no molecular features are present in our observation. We consider a detection to be valid if we can reject the null hypothesis with a 3-sigma confidence.

In this chapter, we simulate the null hypothesis by a blackbody curve at the planetary temperature. The “alternative hypothesis” is represented by a planetary spectrum containing features carved by a specific molecule at a particular abundance. As we are not using observational data, the planetary and stellar spectra are simulated with the methods described in section 3.1.1.

We perform a likelihood ratio test over the selected wavelength range under two assumptions: first, we consider a signal that has been emitted by a planet with no molecular features present, and second, we consider a signal of a planetary spectrum containing features of a molecule at a selected abundance. These tests are repeated $\sim 10^5$ times to build up an empirical understanding of the noise distribution. To reproduce the observational setting, we combine the planetary signal with a stellar signal. We generate poisson noise for both the star+planet signal and for the star only signal, with means equal to the respective signals. The noisy planetary signal is the difference between these two noisy signals, on which we perform two calculations:

the likelihood of observing the null hypothesis (H_0), i.e. the noisy planet signal as a blackbody curve, and the likelihood of observing the alternative hypothesis (H_1), i.e. the noisy planet signal as a spectrum containing molecular features.

The general form of the likelihood ratio test is given as:

$$D = -2\ln\left(\frac{L_0}{L_1}\right) = -2\ln(L_0) + 2\ln(L_1) \tag{3.6}$$

where L_0 and L_1 are the likelihoods of observing the null hypothesis and the alternative hypothesis, respectively. Both L_0 and L_1 are calculated using the Gaussian distribution, as it is a good approximation to the distribution of the difference of two poisson random variables with large means, over all the spectral bins i:

$$L_0 = \prod_{i=1}^{n} \frac{1}{\sigma_i\sqrt{2\pi}} \exp \frac{-(x_i - \mu_{i,0})^2}{2\sigma_i^2} \tag{3.7}$$

$$L_1 = \prod_{i=1}^{n} \frac{1}{\sigma_i \sqrt{2\pi}} \exp \frac{-(x_i - \mu_{i,1})^2}{2\sigma_i^2} \tag{3.8}$$

where for both equations, x_i is the observed (noisy) data in bin i, μ_i is the expected value of the signal in the bin, and σ_i^2 is the sum of variances of the star+planet and star variances ($\sigma^2 = 2\sigma_{star}^2 + \sigma_{planet}^2 = 2\mu_{star} + \mu_{planet}$), which are both poisson distributions. Both equations 3.7 and 3.8 can be expressed in the logarithm form:

$$\ln(L_{0,1}) = \sum - \frac{(x_i - \mu_{i_{0,1}})^2}{2\sigma_i^2} - \ln \sigma_i - \frac{\ln 2\pi}{2} \tag{3.9}$$

Using equation 3.6, we thus obtain a value D. We repeat these steps $\sim 10^5$ times, generating a new noisy signal at each iteration. We build up a distribution of the likelihood difference values D for the planetary signal generated from a blackbody curve.

Under the second assumption, the planetary signal is replaced with a planetary spectrum containing features of a molecule at a selected abundance. Noise is added as described above, and we compute the likelihood of the null hypothesis (H_0') and the likelihood of the alternative hypothesis (H_1'). Using equation 3.6, we obtain a likelihood ratio value that we call D'. These steps are repeated $\sim 10^5$ times, generating a new noisy signal for each iteration. With these results we build a distribution of the likelihood difference values D' for the planetary signal including molecular features. The two distributions (D and D') are expected to be approximately symmetric as they are obtained by the same test, by switching the null hypothesis and the alternative hypothesis in the signal generation process.

The level of distinction between the two considered signals will depend, as in the individual bin method, on the amount of noise and the strength of the molecular features. If the noise is large on the simulated observations, the two distributions will overlap as the likelihood of the hypotheses H_0 and H_1 are similar. If the signal is strong compared to the noise, there will be little or no overlap between the distributions D and D': the null hypothesis will typically be the most likely in the first test, and the alternative hypothesis will typically be the most likely in the second test. As we investigate in this chapter the smallest abundance at which a detection could be obtained, we only require the rejection of the null hypothesis with a 3-sigma confidence. We do not require a 3-sigma confidence level on the alternative hypothesis; we place a maximum type-2 error (not rejecting the null hypothesis when the alternative hypothesis is true) on our alternative hypothesis of 50%. The D distribution is used to delimit the critical value of the null hypothesis, and the D' distribution is used to limit the type-2 error. With this threshold, half of the observations will give an inconclusive result, and the other half will reject the null hypothesis with 3-sigma certainty.

Figure 3.4 shows an example of a Warm Neptune with CH_4 absorbing at abundance 10^{-5} (lower left panel). The distribution indicated as "blackbody source" corresponds to the distribution of D values (Figure 3.4, right panel). On the same plot, the distribution indicated as "molecule source", corresponds to the distribution of D' values. The two distributions are clearly separated, given that the the noise on the lower left-hand side plot doesn't appear to follow the blackbody signal, and the noise on the upper left-hand side plot doesn't appear to follow the molecular spectrum. If a smaller abundance is considered, e.g. 10^{-7} rather than 10^{-5} (Figure 3.5), the distinction between the two signals from the noisy observation is hard to make. The two distributions here overlap quite significantly. Both Figure 3.4 and 3.5 show a vertical red line marking the 3-sigma deviation from the mean on the "blackbody source" distribution, and a blue vertical line marking the median on the "molecule source" distribution.

We compare the performance of the likelihood ratio test to the individual bin method in Section 3.3.

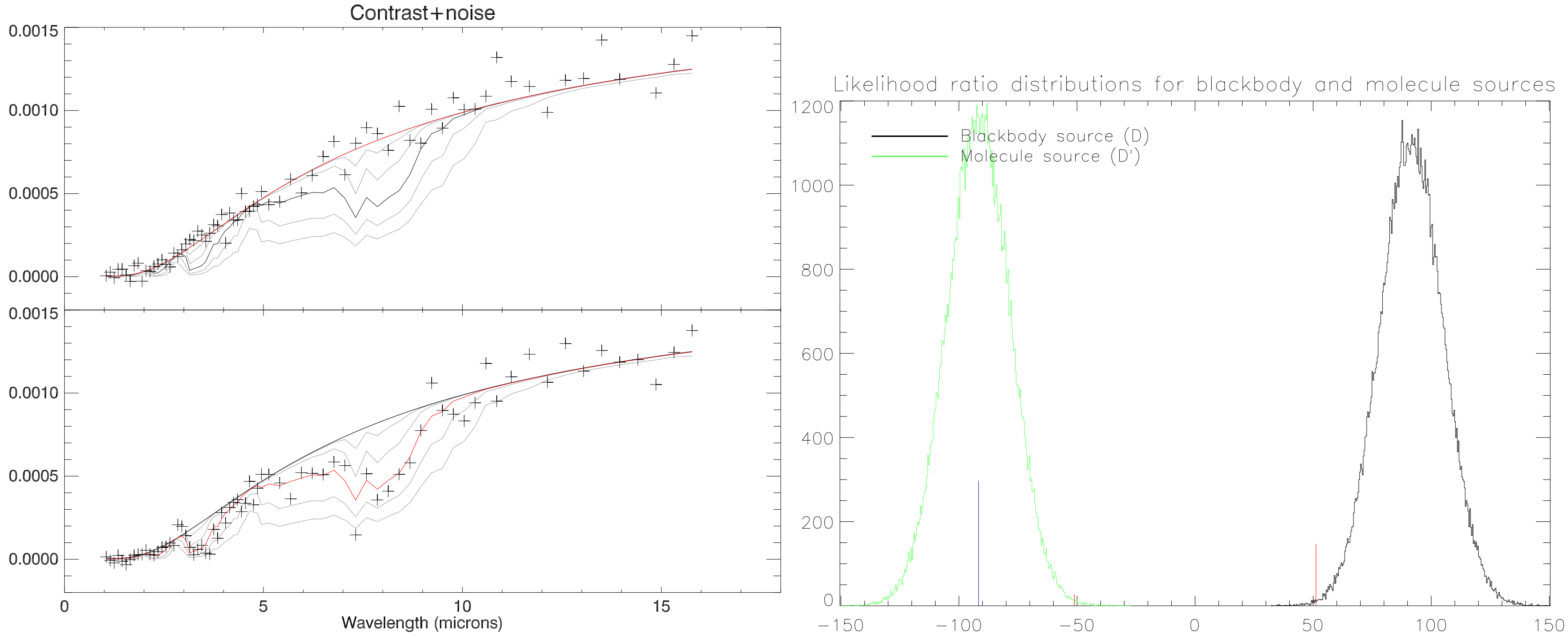

Figure 3.4: Likelihood ratio test results for a Warm Neptune with CH_4 in the atmosphere. *Left:* One transit simulation of the planetary signal. *Top:* Planet/star contrast spectra generated with 5 abundances (in grey). The planetary signal is generated by a blackbody in red. *Bottom:* The planetary signal here is generated by a molecular spectrum with abundance 10^{-5} (red). In both plots, the resolution in the 1 to 5 μm channel has been lowered to R=30 for clarity purposes. *Right:* The two LR distributions including the null hypothesis (D, black) and the alternative hypothesis (D', green). The red line on the null hypothesis distribution marks the 3-sigma limit, and the blue line on the alternative hypothesis distribution marks the median. Here the two distributions are clearly separated, and the null hypothesis of a blackbody planet signal is rejected. Given the result, the detection of this molecule at this abundance is possible for this observation.

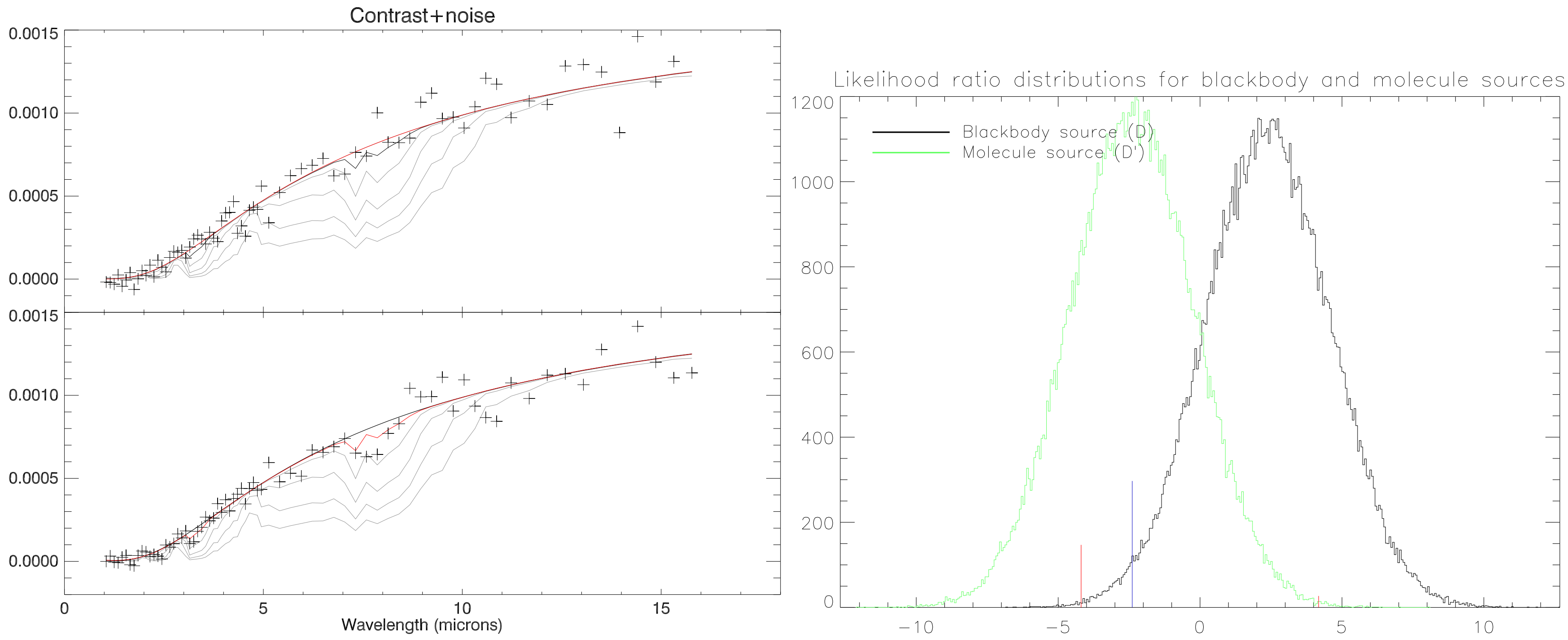

Figure 3.5: Likelihood ratio test results for a Warm Neptune with CH_4 in the atmosphere. *Left:* One transit simulation of the planetary signal. *Top:* Planet/star contrast spectra generated with 5 abundances (in grey). The planetary signal is generated by a blackbody in red. *Bottom:* The planetary signal here is generated by a molecular spectrum with abundance 10^{-7} (red). In both plots, the resolution in the 1 to 5 μm channel has been lowered to R=30 for clarity purposes. *Right:* The two LR distributions including the null hypothesis (D, black) and the alternative hypothesis (D', green). The red line on the null hypothesis distribution marks the 3-sigma limit, and the blue line on the alternative hypothesis distribution marks the median. Here the two distributions overlap, and more than 50% of the alternative hypothesis distribution has crossed the 3-sigma detection limit. Given the result, the null hypothesis is not rejected, and we cannot claim a detection.

3.1.2.3 Detectability Limits in a Wet Atmosphere

In the previous sections we describe the detectability limit tests of a single molecule at a time. However, many molecules are usually present in an atmosphere and they may have overlapping spectral features. In those cases, disentangling the various molecular signals in the spectrum may be a challenging task. The presence of water vapour in particular may severely interfere with an accurate retrieval of other species, as water absorbs from the visible to the far infrared. In comparison, other molecules show sparser spectral features, and we can usually separate their signatures by selecting spectral regions with no significant overlap. The choice of a broad spectral coverage and appropriate spectral resolving power are essential to enable an optimal retrieval process. If these two requirements are not met, the retrieved solutions may not be unique and may present degeneracies. A full analysis on spectral retrieval capabilities and limits is outside the scope of this thesis, we refer to Terrile *et al.* (2008); Swain *et al.* (2009b,a); Madhusudhan and Seager (2009); Lee *et al.* (2012); Line *et al.* (2012) for currently available methods in this domain.

As a test case, we investigate the impact of a water vapour signal on the detectability of key molecules, such as CO, CO_2, CH_4 and NH_3, in the atmosphere of a warm Neptune. We calculate the minimum detectable abundances of these molecules in a wet atmosphere (water vapour abundances ranging from 10^{-3} to 10^{-7}) and compare those to the results presented in section 3.2 for a water free atmosphere. In these tests, the combined (H_2O + molecule) spectra are compared to a water only spectrum, and any deviations from this baseline are tested for 3σ detectability.

The results for these tests are presented in Section 3.4.

3.2 Results - Molecular detectability at fixed SNR

In this section,we present the minimum mixing ratio detectable for a selected molecule, absorbing in a planetary atmosphere, as a function of wavelength and SNR (SNR of planet, SNR$_p$). The SNR here is fixed at 5, 10 and 20. We repeat these calculations for the five planet cases: warm Neptune, hot Jupiter, hot and temperate super-Earth, and temperate Jupiter.

3.2.1 Warm Neptune

We present in Figure 3.6 the contrast spectra corresponding to a warm Neptune case with the following molecules: methane (CH_4), carbon monoxide (CO), carbon dioxide (CO_2), ammonia (NH_3), water (H_2O), hydrogen cyanide (HCN), acetylene (C_2H_2), ethane (C_2H_6), hydrogen sulfide (H_2S) and phosphine (PH_3). For each molecule we present a continuum line corresponding to a blackbody emission from the planet with no molecular absorption, and three planet/star contrast spectra generated with different abundances: 10^{-7}, 10^{-5}, and 10^{-3}. While we study several abundances, for clarity we display only three values on the plots.

In Table 3.5 we list the lowest abundances detectable as a function of SNR.

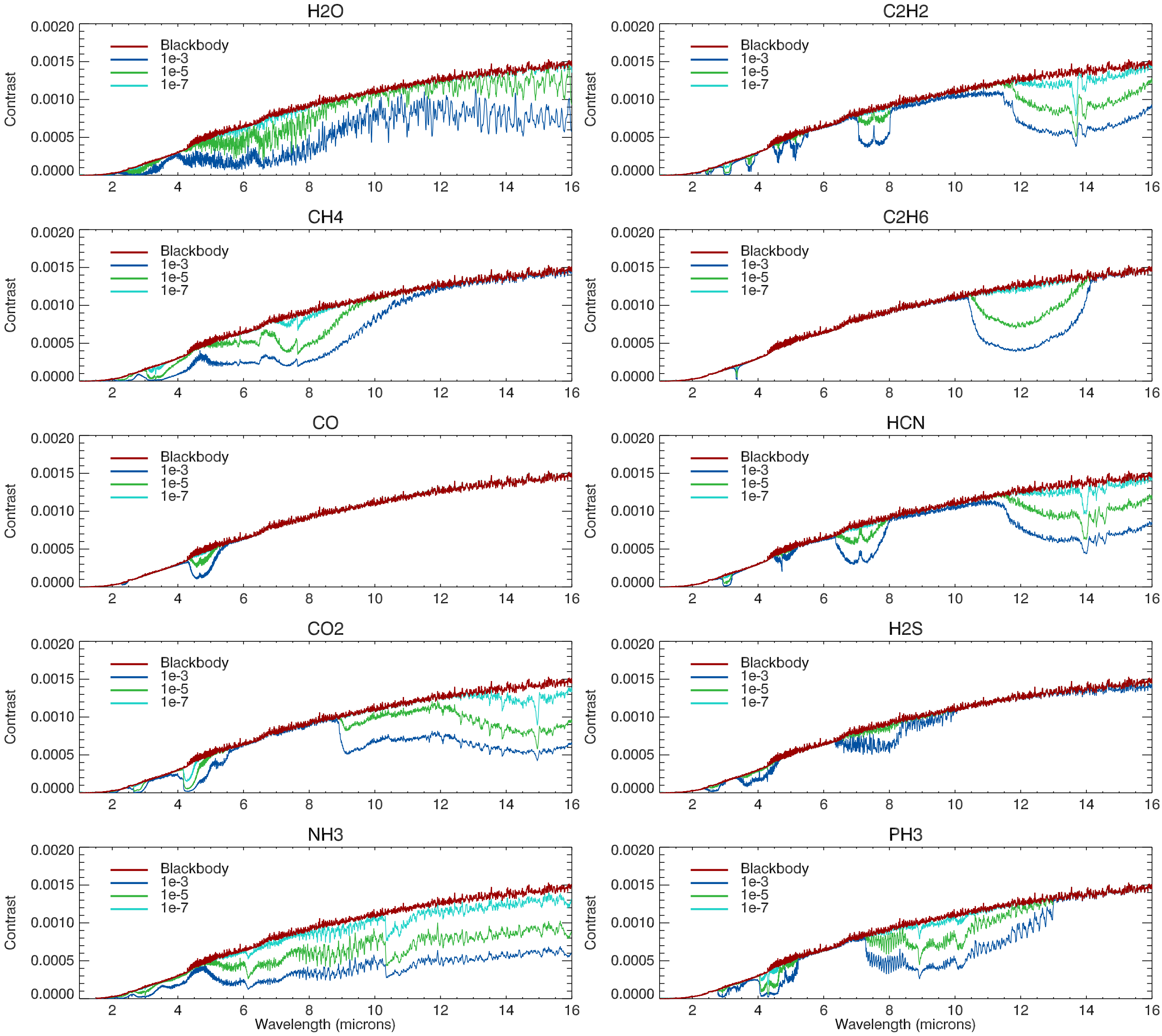

Figure 3.6: Warm Neptune: planet/star contrast spectra simulating the effect of the 10 considered molecules: CH_4, CO, CO_2, NH_3, H_2O, C_2H_2, C_2H_6, HCN, H_2S and PH_3. The red line shows a planetary blackbody emission with no molecules present, divided by a stellar spectrum. The green-blue colored lines depict the molecular features at different abundances. For clarity purposes, only three abundances are plotted out of the five calculated.

	CH_4		CO		CO_2			PH_3	
SNR	3.3 μm	8 μm	2.3 μm	4.6 μm	2.8 μm	4.3 μm	15 μm	4.3 μm	10 μm
20	10^{-7}	10^{-6}	10^{-4}	10^{-6}	10^{-7}	10^{-7}	10^{-7}	10^{-7}	10^{-6}
10	10^{-7}	10^{-6}	10^{-3}	10^{-5}	10^{-6}	10^{-7}	10^{-6}	10^{-7}	10^{-6}
5	10^{-7}	10^{-5}	10^{-3}	10^{-4}	10^{-6}	10^{-7}	10^{-5}	10^{-7}	10^{-5}

	NH_3			HCN			H_2O		
SNR	3 μm	6.1 μm	10.5 μm	3 μm	7 μm	14 μm	2.8 μm	5 - 8 μm	11 - 16 μm
20	10^{-7}	10^{-6}	10^{-7}	10^{-7}	10^{-5}	10^{-7}	10^{-6}	10^{-6}	10^{-5}
10	10^{-6}	10^{-6}	10^{-6}	10^{-6}	10^{-5}	10^{-6}	10^{-6}	10^{-5}	10^{-4}
5	10^{-5}	10^{-5}	10^{-5}	10^{-6}	10^{-4}	10^{-5}	10^{-5}	10^{-5}	10^{-4}

	C_2H_6		H_2S			C_2H_2		
SNR	3.3 μm	12.2 μm	2.6 μm	4.25 μm	8 μm	3 μm	7.5 μm	13.7 μm
20	10^{-6}	10^{-6}	10^{-5}	10^{-4}	10^{-4}	10^{-7}	10^{-5}	10^{-7}
10	10^{-5}	10^{-5}	10^{-5}	10^{-4}	10^{-3}	10^{-7}	10^{-4}	10^{-6}
5	10^{-5}	10^{-5}	10^{-4}	10^{-3}	-	10^{-7}	10^{-3}	10^{-5}

Table 3.5: Warm Neptune: Minimum detectable abundance at fixed SNR=5, 10 and 20.

3.2.1.1 Alternative TP profiles

We repeat these calculations for two alternative TP profiles. In Figure 3.7 and Table 3.6, we show the outcome for CO and CO_2, when a steep dry adiabatic profile and a more isothermal profile are used. Not surprisingly, a steeper thermal gradient is equivalent to an increase in the molecular abundance. A more isothermal profile causes the opposite effect. This shows that simultaneous temperature retrieval is very important for the analysis of secondary transit observations.

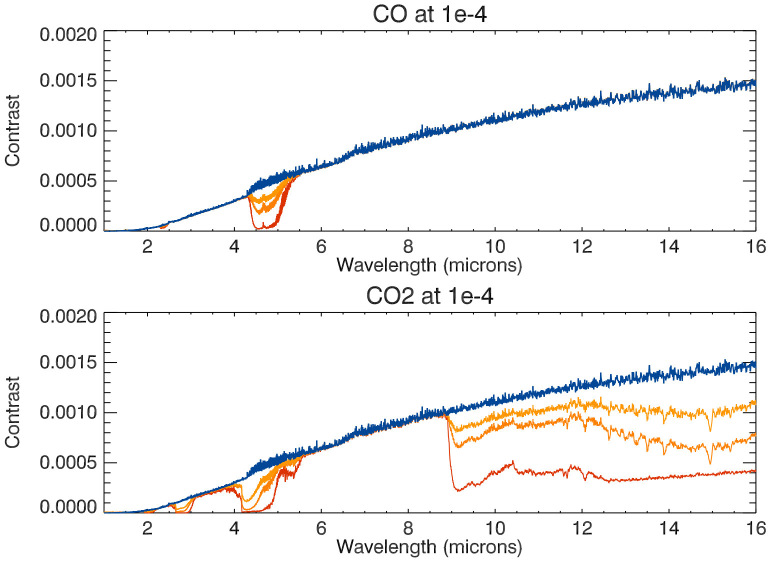

Figure 3.7: Alternative TP profiles (Warm Neptune): planet/star contrast spectra simulating the effect of carbon monoxide (*top*) and carbon dioxide (*bottom*). The blue line shows a planetary blackbody emission with no molecules present, divided by a stellar spectrum. The three spectra show the strength of absorption with the furthest from the continuum corresponding to the dry adiabatic profile (in red), and the nearest to the more isothermal profile (yellow).

	CO		CO_2		
SNR	2.3 μm	4.6 μm	2.8 μm	4.3 μm	15 μm
20	$10^{-(4/\mathbf{4}/5)}$	$10^{-(5/\mathbf{6}/6)}$	$10^{-(7/\mathbf{7}/7)}$	$10^{-(7/\mathbf{7}/7)}$	$10^{-(6/\mathbf{7}/7)}$
10	$10^{-(3/\mathbf{3}/4)}$	$10^{-(4/\mathbf{5}/6)}$	$10^{-(6/\mathbf{6}/7)}$	$10^{-(7/\mathbf{7}/7)}$	$10^{-(5/\mathbf{6}/7)}$
5	$10^{-(-/\mathbf{3}/4)}$	$10^{-(3/\mathbf{4}/6)}$	$10^{-(5/\mathbf{6}/7)}$	$10^{-(6/\mathbf{7}/7)}$	$10^{-(3/\mathbf{5}/7)}$

Table 3.6: Alternative TP profiles: Warm Neptune minimum detectable abundances at fixed SNR=5, 10 and 20, for CO and CO_2, with three TP profiles, at the wavelengths of specific features. The minimum abundance for the three profiles are presented as $10^{-(x,\mathbf{y},z)}$, where x is the result for the more isothermal profile, $\mathbf{y}$ the intermediate profile presented in Table 3.5, and z the result for the dry adiabatic profile.

3.2.2 Hot Jupiter

We apply the procedure explained in section 3.2.1 to the hot Jupiter case. Molecular spectra and minimum detectable abundances as a function of SNR are presented in Figure 3.8 and Table 3.7.

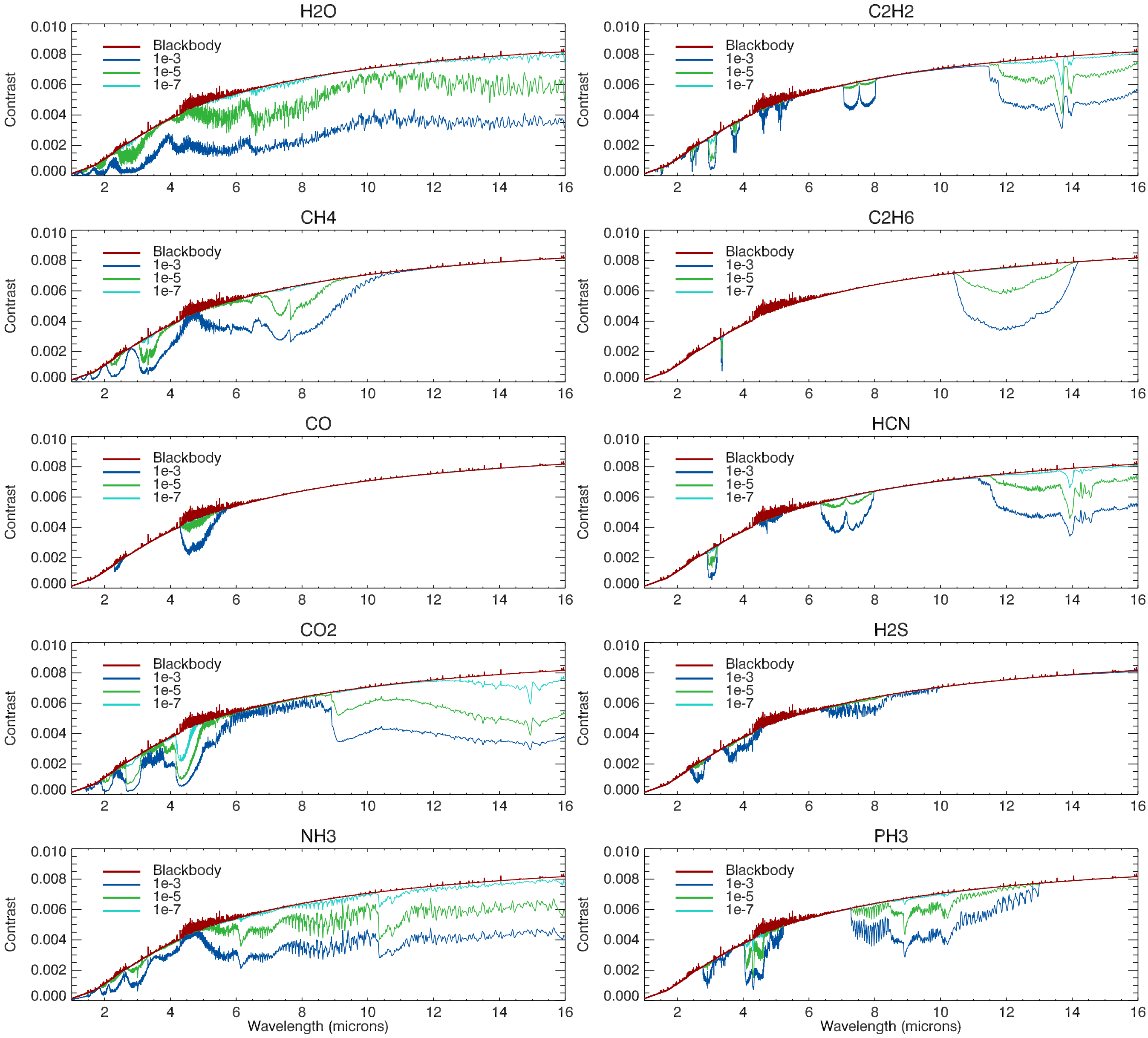

Figure 3.8: Hot Jupiter: planet/star contrast spectra simulating the effect of the 10 considered molecules: CH_4, CO, CO_2, NH_3, H_2O, C_2H_2, C_2H_6, HCN, H_2S and PH_3. The red line shows a planetary blackbody emission with no molecules present, divided by a stellar spectrum. The green-blue colored lines depict the molecule features at varying abundances. For clarity purposes, only three abundances are plotted of the five calculated.

	CH_4		CO		CO_2			PH_3	
SNR	3.3 μm	8 μm	2.3 μm	4.6 μm	2.8 μm	4.3 μm	15 μm	4.3 μm	10 μm
20	10^{-6}	10^{-5}	10^{-3}	10^{-5}	10^{-6}	10^{-7}	10^{-6}	10^{-7}	10^{-5}
10	10^{-6}	10^{-5}	-	10^{-4}	10^{-6}	10^{-7}	10^{-6}	10^{-6}	10^{-4}
5	10^{-6}	10^{-4}	-	10^{-3}	10^{-6}	10^{-7}	10^{-5}	10^{-6}	10^{-3}

	NH_3			HCN			H_2O		
SNR	3 μm	6.1 μm	10.5 μm	3 μm	7 μm	14 μm	2.8 μm	5 - 8 μm	11 - 16 μm
20	10^{-5}	10^{-5}	10^{-6}	10^{-6}	10^{-4}	10^{-5}	10^{-6}	10^{-6}	10^{-5}
10	10^{-5}	10^{-5}	10^{-5}	10^{-5}	10^{-3}	10^{-4}	10^{-5}	10^{-5}	10^{-5}
5	10^{-4}	10^{-4}	10^{-4}	10^{-4}	-	10^{-3}	10^{-5}	10^{-4}	10^{-4}

	C_2H_6		H_2S			C_2H_2		
SNR	3.3 μm	12.2 μm	2.6 μm	4.25 μm	8 μm	3 μm	7.5 μm	13.7 μm
20	10^{-4}	10^{-5}	10^{-4}	10^{-3}	-	10^{-7}	10^{-3}	10^{-4}
10	10^{-4}	10^{-4}	10^{-4}	10^{-3}	-	10^{-6}	10^{-3}	10^{-4}
5	10^{-3}	10^{-3}	10^{-3}	-	-	10^{-6}	-	10^{-4}

Table 3.7: Hot Jupiter: Minimum detectable abundances at fixed SNR=5, 10 and 20.

3.2.3 Hot and Temperate Super-Earth

We present two categories for the super-Earth cases: a hot super-Earth like Cancri 55 e, with a surface temperature of ~2400K and orbiting a G type star, and a temperate super-Earth with a surface temperature of 320K, orbiting a late M type star. Given the different temperatures, we expect different components to be present in those atmospheres. In the hot case, we consider H_2O, CO and CO_2, and in the temperate case, H_2O, CO_2, NH_3 and O_3. In the case of the temperate super-Earth, we have estimated the impact for different main atmospheric components, we show in Figure 3.9 the detectability of CO_2 with three different abundances (10^{-4},10^{-6},10^{-8}).

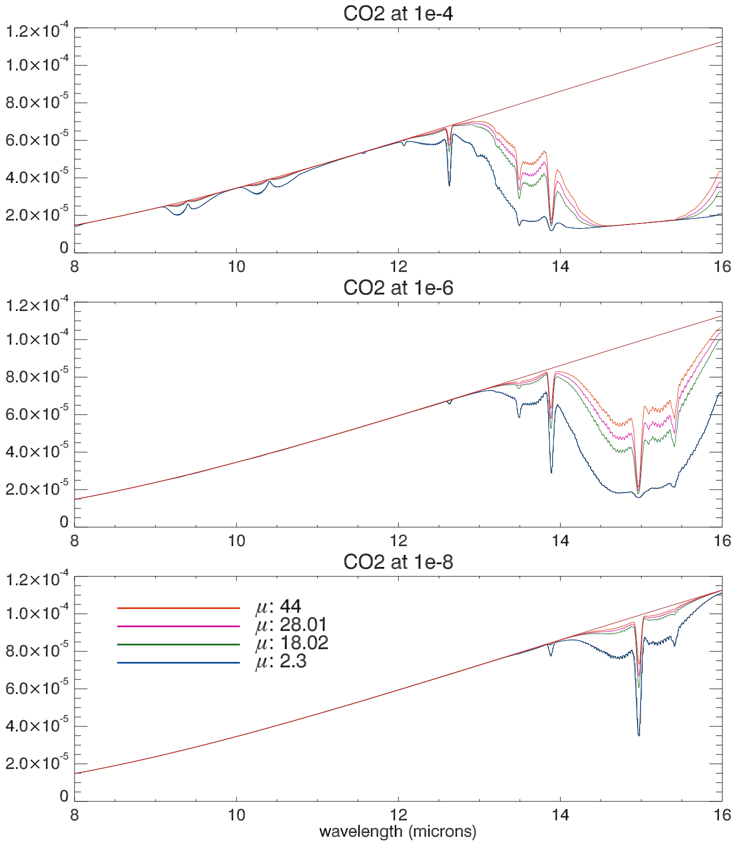

Figure 3.9: Temperate super-Earth: planet/star contrast spectra showing the impact of the mean molecular weight of the atmosphere (μ) on the detectability of CO_2 at abundances 10^{-4},10^{-6},10^{-8}, from top to bottom. The four values for μ are: 2.3 (hydrogen), 18.02 (water vapour), 28.01 (nitrogen) and 44 (carbon dioxide). The small differences between the latter three cases are hardly detectable, while a hydrogen dominated atmosphere will offer improved detectability performances. For our study we select a nitrogen dominated atmosphere.

At the SNR and resolutions considered in this chapter, the small differences between the water vapour, nitrogen and carbon dioxide dominated atmospheres are hardly detectable, with the exception of the hydrogen-rich atmosphere. For these reasons and in analogy with the Earth, we adopt a nitrogen dominated atmosphere with a wet adiabatic lapse rate for the temperate super-Earth. For the hot super-Earth, we consider a water vapour-dominated atmosphere, as can be expected in this mass/radius range (Fressin *et al.* 2013; Valencia *et al.* 2013). Figure 3.10 shows the simulated spectra for the two planet categories, and Table 3.8 reports the minimum abundances detectable. We do not consider SNR=20 for the temperate super-Earth, given the challenge such a measure would present for current and short-term observatories. Our results in the appendix show the SNR values that can be expected for such a planet at various distances.

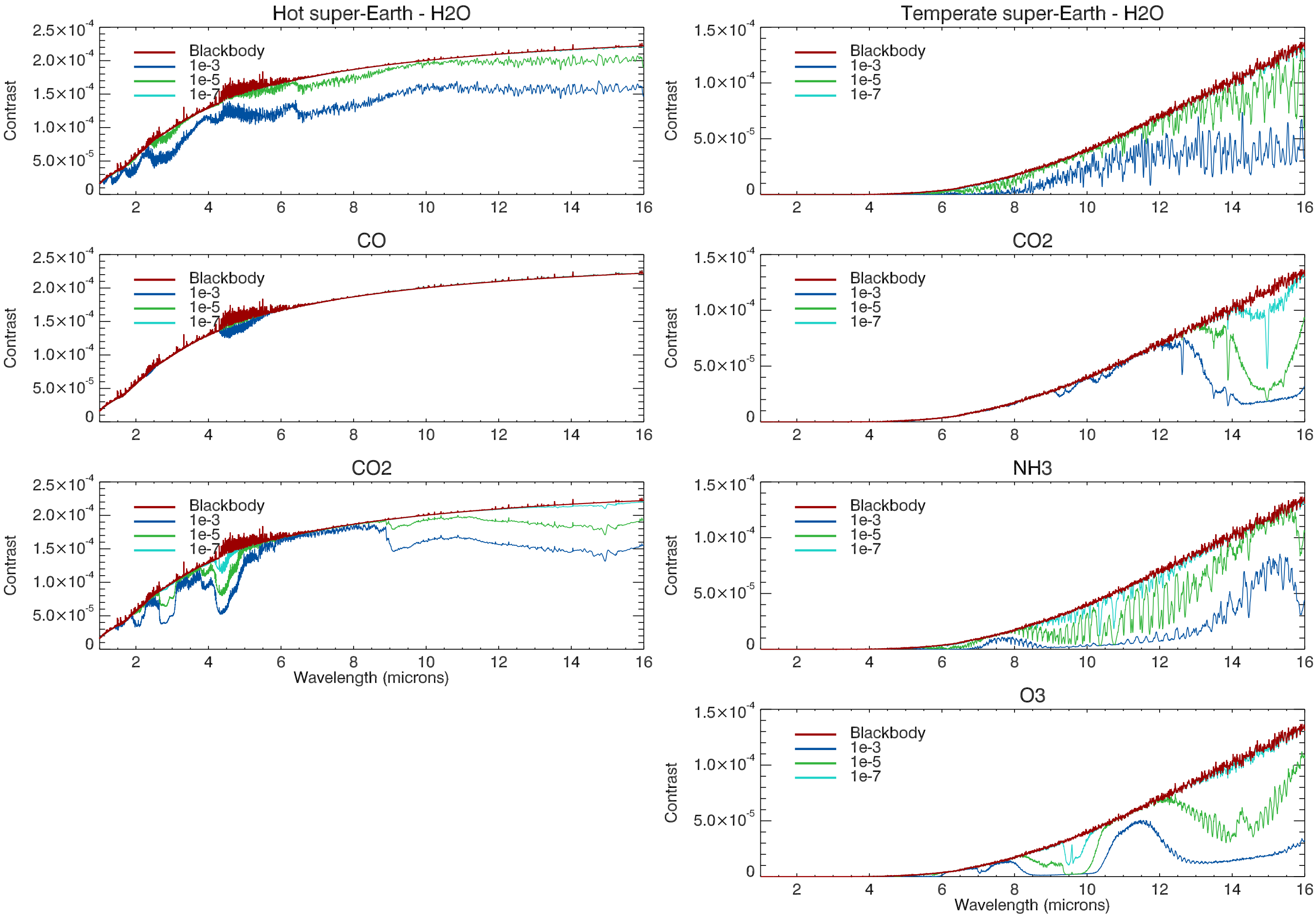

Figure 3.10: Hot (*left*) and temperate (*right*) super-Earth: planet/star contrast spectra simulating the effect of the considered molecules: H_2O, CO and CO_2 for the hot planet, and H_2O, CO_2, NH_3 and O_3 for the temperate case. The red line shows a planetary blackbody emission with no molecules present, divided by a stellar spectrum. The green-blue colored lines depict the molecule features at varying abundances. For clarity purposes, only three abundances are plotted out of the five calculated.

	H_2O			CO_2			CO	
SNR	2.8 μm	5 - 8 μm	11 - 16 μm	2.8 μm	4.3 μm	15 μm	2.3 μm	4.6 μm
20	10^{-4}	10^{-4}	10^{-4}	10^{-5}	10^{-7}	10^{-5}	-	-
10	10^{-4}	10^{-3}	10^{-3}	10^{-5}	10^{-6}	10^{-4}	-	-
5	10^{-3}	-	-	10^{-4}	10^{-5}	-	-	-

	H_2O		CO_2	NH_3		O_3	
SNR	5 - 8 μm	11 - 16 μm	15 μm	6.1 μm	10.5 μm	9.6 μm	14.3 μm
10	10^{-5}	10^{-4}	10^{-6}	10^{-6}	10^{-6}	10^{-7}	10^{-5}
5	10^{-5}	10^{-4}	10^{-6}	10^{-5}	10^{-6}	10^{-7}	10^{-5}

Table 3.8: *Top:* Hot super-Earth, around a G type star: Minimum detectable abundances at fixed SNR=5, 10 and 20. In this specific example, CO is not detectable. The bulk composition of the planet atmosphere in this simulation is H_2O. *Bottom:* Temperate super-Earth, around a late M type star: Minimum detectable abundance at fixed SNR=5 and 10. The bulk composition of the planet atmosphere in this simulation is N_2.

	H_2O		CO_2	CH_4	C_2H_2		C_2H_6
SNR	5 - 8 μm	11 - 16 μm	15 μm	8 μm	7.5 μm	13.7 μm	12.2 μm
20	10^{-6}	10^{-5}	10^{-7}	10^{-7}	10^{-6}	10^{-7}	10^{-6}
10	10^{-6}	10^{-4}	10^{-7}	10^{-7}	10^{-5}	10^{-6}	10^{-6}
5	10^{-5}	10^{-3}	10^{-7}	10^{-6}	10^{-4}	10^{-5}	10^{-5}

Table 3.9: Temperate Jupiter: Minimum detectable abundances at fixed SNR=5, 10 and 20.

3.2.4 Temperate Jupiter

We consider here five molecules: H_2O, CH_4, CO_2, C_2H_2 and C_2H_6. The spectral simulations are presented in Figure 3.11, and Table 3.9 shows the minimum abundances detectable for this planet.

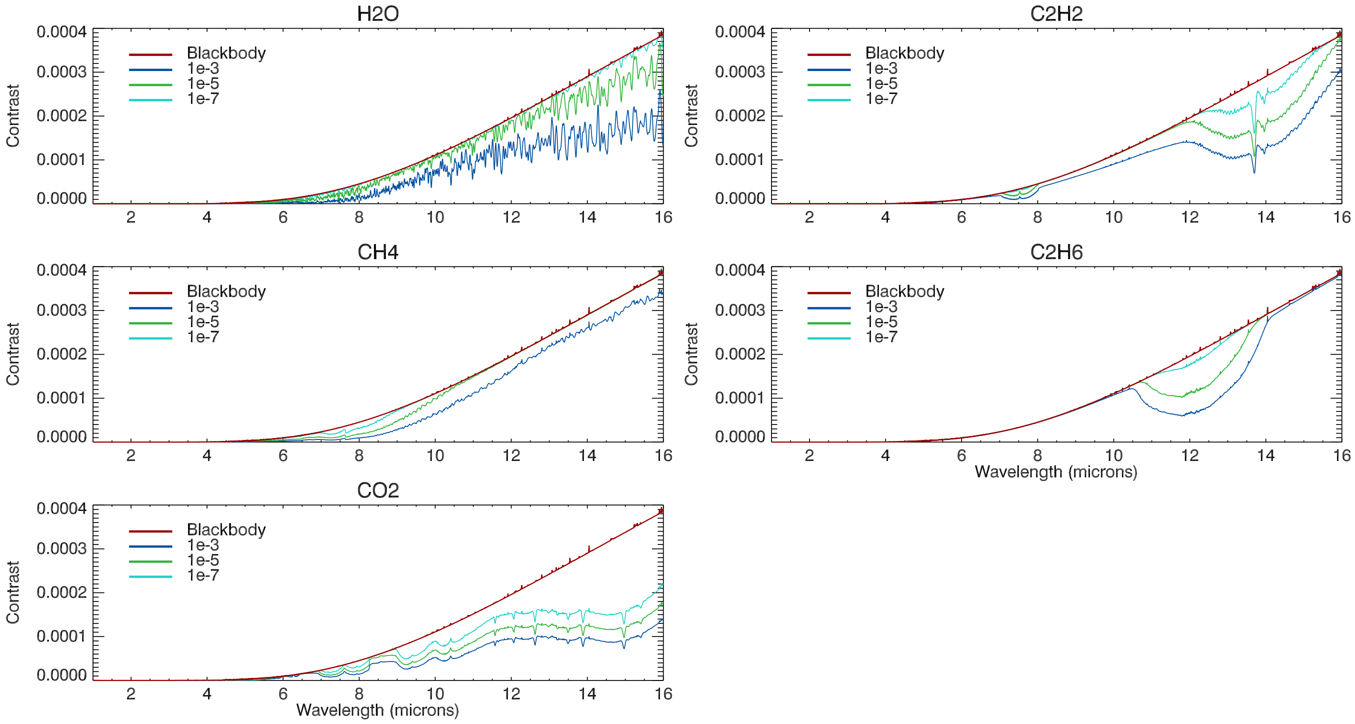

Figure 3.11: Temperate Jupiter: planet/star contrast spectra simulating the effect of the 5 considered molecules: H_2O, CH_4, CO_2, C_2H_2 and C_2H_6. The red line shows a planetary blackbody emission with no molecules present, divided by a stellar spectrum. The green-blue colored lines depict the molecule features at varying abundances. For clarity purposes, only three abundances are plotted out of the five calculated.

3.3 Results II - Comparison with Likelihood Ratio

We compare the results obtained with the likelihood ratio test and the individual bin method by applying the two methods to four examples: a warm Neptune, a hot Jupiter and a hot and temperate super-Earth. These targets are placed at an optimal distance from the observer, where the SNR may reach $\sim$ 5, 10 or 20 (see Appendix A) to facilitate the comparison with the results in section 3.2. The likelihood ratio test, in fact, can not be run with artificially fixed SNRs.

The SNR values per bin are shown in Figure 3.12. Table 3.10 shows the smallest abun-

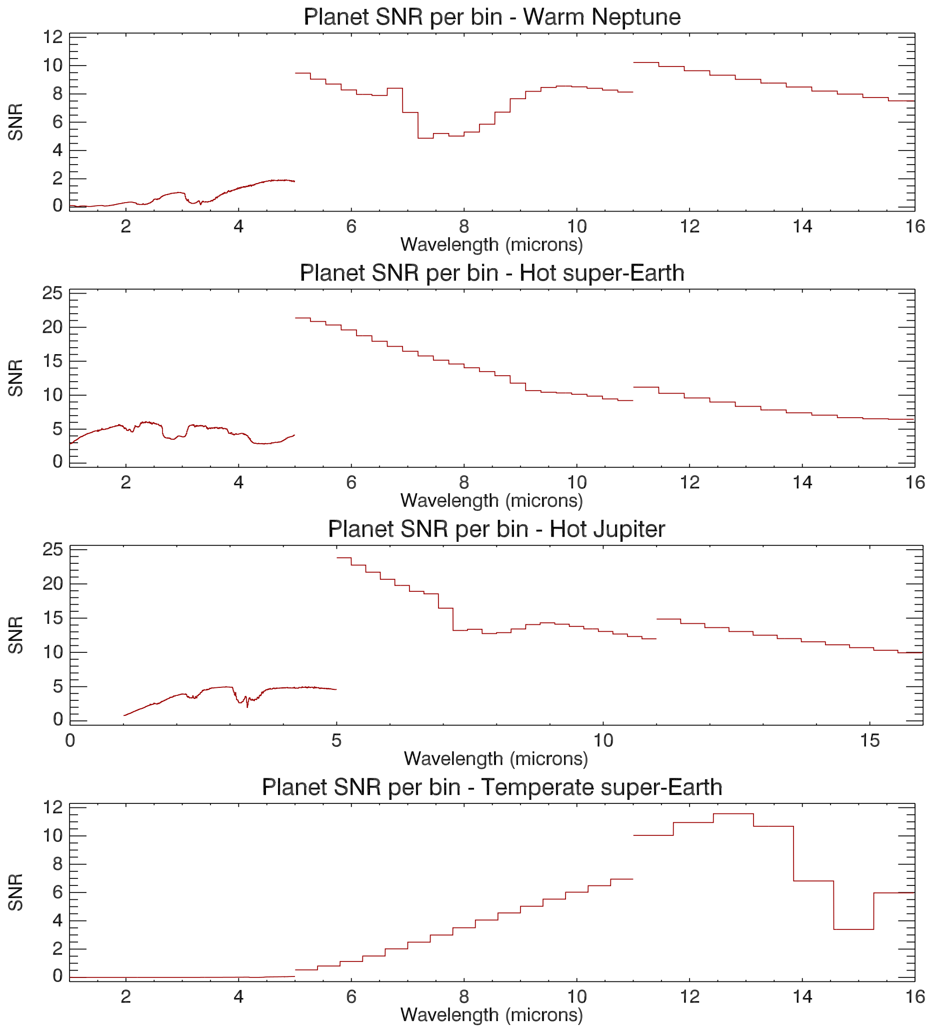

Figure 3.12: SNR value per bin for the four planets considered. *Top diagram:* a warm Neptune planet located at 13.5pc, observed for one transit. In this plot we show the SNR per bin for CH_4 in the atmosphere with an abundance of 10^{-5}. The peak SNR value is of $\sim$ 10 and the spectral feature near 7.5 microns has a SNR value of $\sim$ 5. *Second diagram:* a hot super-Earth located at 12.34pc, observed for five transits, with CO_2 in the atmosphere with an abundance of 10^{-4}. *Third diagram:* a hot Jupiter planet located at 150pc, observed for one transit, with CH_4 in the atmosphere with an abundance of 10^{-5}. The peak SNR value is slightly over 20 and the spectral feature near 7.5 microns has a SNR value of $\sim$ 10. *Bottom diagram:* a temperate super-Earth located at 6pc and observed for 200 transits. This high number of transits and proximity are required to obtain a peak SNR of $\sim$ 10, more distant planets can be observed with a lower peak SNR value. The atmosphere of this case is with CO_2 at an abundance of 10^{-5}.

dances detectable for each method. For the individual bin case, any feature providing a 3-sigma detection will be counted as a detection, while the smallest abundance which allows the rejection of the null hypothesis with 3-sigma confidence will be counted as a detection for the likelihood ratio test. For most cases, the likelihood ratio test improves the sensitivity to the presence of molecular features and the statistical confidence of such detections.

Warm Neptune at 13.5pc, 1 transit

Method	PH_3	CO	CO_2	CH_4	NH_3	HCN	C_2H_2	C_2H_6	H_2S	H_2O
Individual bins	10^{-5}	10^{-3}	10^{-5}	10^{-5}	10^{-5}	10^{-5}	10^{-5}	10^{-5}	10^{-3}	10^{-5}
LRT	10^{-6}	10^{-4}	10^{-7}	10^{-6}	10^{-7}	10^{-6}	10^{-6}	10^{-5}	10^{-3}	10^{-6}

Hot Jupiter at 150pc, 1 transit

Method	PH_3	CO	CO_2	CH_4	NH_3	HCN	C_2H_2	C_2H_6	H_2S	H_2O
Individual bins	10^{-5}	10^{-4}	10^{-6}	10^{-5}	10^{-5}	10^{-5}	10^{-5}	10^{-4}	–	10^{-5}
LRT	10^{-6}	10^{-5}	10^{-7}	10^{-6}	10^{-6}	10^{-6}	10^{-6}	10^{-5}	10^{-4}	10^{-6}

Hot super-Earth at 12.34pc, 5 transits

Method	H_2O	CO_2	CO
Individual bins	10^{-4}	10^{-3}	—
LRT	10^{-5}	10^{-7}	10^{-3}

Temperate super-Earth at 6pc, 200 transits

Method	H_2O	CO_2	NH_3	O_3*
Individual bins	10^{-4}	10^{-6}	10^{-5}	10^{-7}
LRT	10^{-5}	10^{-6}	10^{-6}	10^{-6}

Table 3.10: Comparison of minimum abundance detectable by the individual bin method and the Likelihood Ratio Test (LRT) method, for three planet cases, a warm Neptune, a hot Jupiter and a temperate super-Earth. For the three planet cases the likelihood ratio method typically improves the detectability of the limiting abundances. *: Note that in this example, for the case of ozone on a temperate super-Earth, the LRT performs less well than the individual bin method; the signal consists of a single small feature appearing in one bin only.

3.4 Results III - Detectability Limits in a Wet Atmosphere

As described in section 3.1, we show here the impact of a water vapour signal on the detectability of key molecules (CO, CO_2, CH_4 and NH_3). We consider a warm Neptune planet case with water vapour abundances ranging from 10^{-3} to 10^{-7}. The deviations of the combined (H_2O + molecule) spectra from the water vapour only spectrum are tested for detectability (see Figures 3.13 and 3.14). The minimum detectable abundances are presented in Table 3.11 as a function of SNR, wavelength and water vapour abundance. For all the molecules considered, water vapour abundances of 10^{-5} or less do not significantly interfere with the molecular detectablity. Larger water vapour abundances start to mask the absorption features of other molecules, with a clear impact on detectability limits. These effects can sometimes be mitigated with an increased SNR.

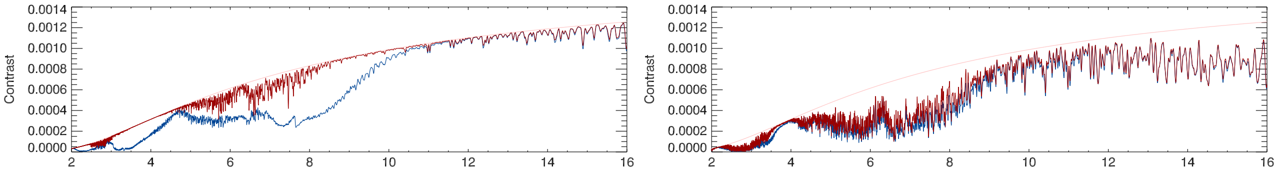

Figure 3.13: Warm Neptune: Planet/star contrast spectra simulating the effect of methane with the addition of water (Left: Water at mixing ratio 10^{-6} and CH_4 at 10^{-4}; Right: Water at mixing ratio 10^{-4} and CH_4 at 10^{-6}).

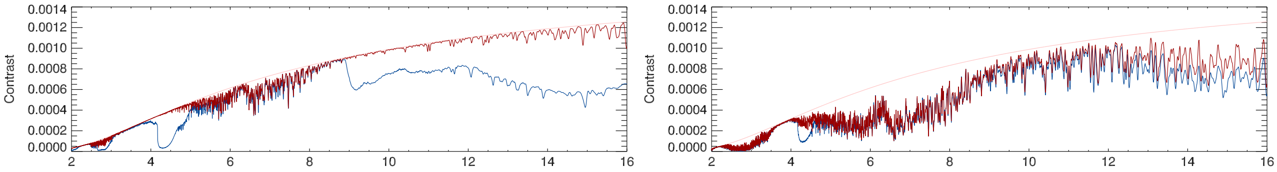

Figure 3.14: Warm Neptune: Planet/star contrast spectra simulating the effect of carbon dioxide with the addition of water (Left: Water at mixing ratio 10^{-6} and CO_2 at 10^{-4}; Right: Water at mixing ratio 10^{-4} and CO_2 at 10^{-6}).

SNR=5

	CH_4		CO		CO_2			NH_3		
H_2O	3.3 μm	8 μm	2.3 μm	4.6 μm	2.8 μm	4.3 μm	15 μm	3 μm	6.1 μm	10.5 μm
0	10^{-7}	10^{-5}	10^{-3}	10^{-4}	10^{-6}	10^{-7}	10^{-5}	10^{-5}	10^{-5}	10^{-5}
10^{-7}	10^{-7}	10^{-5}	10^{-3}	10^{-4}	10^{-6}	10^{-7}	10^{-5}	10^{-5}	10^{-5}	10^{-5}
10^{-6}	10^{-7}	10^{-5}	10^{-3}	10^{-4}	10^{-6}	10^{-7}	10^{-5}	10^{-5}	10^{-5}	10^{-5}
10^{-5}	10^{-7}	10^{-5}	10^{-3}	10^{-4}	10^{-6}	10^{-7}	10^{-5}	10^{-5}	10^{-5}	10^{-5}
10^{-4}	10^{-7}	10^{-4}	10^{-3}	10^{-4}	10^{-6}	10^{-7}	10^{-4}	10^{-5}	10^{-4}	10^{-5}
10^{-3}	10^{-7}	10^{-3}	10^{-3}	10^{-4}	10^{-6}	10^{-7}	–	10^{-4}	10^{-3}	10^{-5}

SNR=10

	CH_4		CO		CO_2			NH_3		
H_2O	3.3 μm	8 μm	2.3 μm	4.6 μm	2.8 μm	4.3 μm	15 μm	3 μm	6.1 μm	10.5 μm
0	10^{-7}	10^{-6}	10^{-3}	10^{-5}	10^{-6}	10^{-7}	10^{-6}	10^{-6}	10^{-6}	10^{-6}
10^{-7}	10^{-7}	10^{-6}	10^{-3}	10^{-5}	10^{-6}	10^{-7}	10^{-6}	10^{-6}	10^{-6}	10^{-6}
10^{-6}	10^{-7}	10^{-6}	10^{-3}	10^{-5}	10^{-6}	10^{-7}	10^{-6}	10^{-6}	10^{-6}	10^{-6}
10^{-5}	10^{-7}	10^{-6}	10^{-3}	10^{-5}	10^{-6}	10^{-7}	10^{-6}	10^{-6}	10^{-5}	10^{-6}
10^{-4}	10^{-7}	10^{-6}	10^{-3}	10^{-5}	10^{-6}	10^{-7}	10^{-5}	10^{-6}	10^{-5}	10^{-6}
10^{-3}	10^{-7}	10^{-5}	10^{-3}	10^{-5}	10^{-6}	10^{-7}	10^{-4}	10^{-4}	10^{-4}	10^{-6}

SNR=20

	CH_4		CO		CO_2			NH_3		
H_2O	3.3 μm	8 μm	2.3 μm	4.6 μm	2.8 μm	4.3 μm	15 μm	3 μm	6.1 μm	10.5 μm
0	10^{-7}	10^{-6}	10^{-4}	10^{-6}	10^{-7}	10^{-7}	10^{-7}	10^{-7}	10^{-6}	10^{-7}
10^{-7}	10^{-7}	10^{-6}	10^{-4}	10^{-6}	10^{-7}	10^{-7}	10^{-7}	10^{-6}	10^{-6}	10^{-7}
10^{-6}	10^{-7}	10^{-6}	10^{-4}	10^{-6}	10^{-7}	10^{-7}	10^{-7}	10^{-6}	10^{-6}	10^{-7}
10^{-5}	10^{-7}	10^{-7}	10^{-4}	10^{-6}	10^{-7}	10^{-7}	10^{-7}	10^{-6}	10^{-6}	10^{-7}
10^{-4}	10^{-7}	10^{-7}	10^{-4}	10^{-6}	10^{-7}	10^{-7}	10^{-7}	10^{-6}	10^{-6}	10^{-7}
10^{-3}	10^{-7}	10^{-7}	10^{-4}	10^{-6}	10^{-7}	10^{-7}	10^{-7}	10^{-5}	10^{-5}	10^{-7}

Table 3.11: Warm Neptune: Minimum detectable abundances at fixed SNR=5, 10 and 20 (top, middle and bottom) with a range of quantities of water in the atmosphere. For each SNR case, the minimum detectable abundance for each molecule without the presence of water is given as comparison (values from Table 4).

3.5 Discussion

In this chapter we have studied the detectability of key molecules absorbing in the atmospheres of representative exoplanet cases. Although we consider only five types of planets, most exoplanets known today have sizes and temperatures that are within the boundaries of these, so results for intermediate cases can be interpolated from our tables. Notice that the results obtained for the super-Earths are the most sensitive to the type of the stellar companion (Tessenyi *et al.* 2012a). For this reason, we have selected one hot target around a G type star, and a temperate one around a late M star. We have adopted thermal profiles from simulations or have extrapolated them from solar system planets. As we focus on emission spectra, the molecular absorption and thermal structure are strongly correlated. To assess this effect, we have repeated our calculations with extreme thermal profiles in the case of the warm Neptune, and have found that our results are reliable within an order of magnitude.

We compared two approaches to assess molecular detectability: the individual bin method (section 3.2) and the likelihood ratio test (section 3.3). We have applied the individual bin method to all the planet cases and key molecules. We fixed the planet SNR artificially to obtain results which are independent of instrument design, observation duration and sources of noise. The individual bin method is robust but very conservative and not optimised for most detections. In particular:
1) the method doesn't take advantage of spectral features that span across multiple bins. Combining the information from multiple bins could increase the level of detection certainty, and allow smaller abundances to be detectable at limiting cases.
2) the confidence level of the detection does not change significantly when distinct features of the same molecule are considered.
By contrast, the likelihood ratio test method is able to combine effectively information from multiple bins and multiple features. The results in section 4 show a consistent improvement on the detection sensitivity over the individual bin method for most of the cases.

We compared our results with the ones calculated by (Barstow *et al.* 2013) with an automatic retrieval method. The test case was a hot Jupiter observed for a single eclipse with an EChO-like mission (see Appendix A). We obtained consistent results for all the molecules with the exception of CO and NH_3, for which we predict easier detectability.

For ammonia, the explanation lies in the different line lists used: HITRAN08 (Rothman *et al.* 2009) for Barstow *et al.* (2013), and Exomol BYTe (Yurchenko *et al.* 2011) at high temperatures in our case. In the case of CO, the spectral features overlap in some spectral regions with CH_4 or CO_2, so it may be harder to detect when not isolated from other species, as it is assumed in this chapter. In section 3.4 we considered the case of a wet atmosphere given that water vapour is almost ubiquitous in warm and hot atmospheres and its signal extends from the visible to the infrared. We found that our conclusions for a dry atmosphere are still valid provided the water abundance does not exceed $\sim 10^{-5}$.

By examining predictions about compositions of hot and warm gaseous planets currently available in the literature (Moses *et al.* 2011; Venot *et al.* 2012; Line *et al.* 2010), the abundances retrievable with SNR$\sim$10 are sufficient to discriminate among the different scenarios proposed. Moreover, at SNR$\sim$10, most of the molecules are detectable in multiple regions of the spectrum, indicating that good constraints on the vertical thermal profile can be obtained.

3.6 Concluding remarks

In this chapter we have addressed the question of molecular detectability in exoplanet atmospheres, for a range of key planet types and key molecules. The five cases considered — hot Jupiter, hot super-Earth, warm Neptune, temperate Jupiter and temperate super-Earth — cover most of the exoplanets characterisable today or in the near future. For other planets, the minimum detectable abundances can be extrapolated from these results.

We used a conservative and straightforward method, with which we delimit the objective criteria that need to be met for claiming 3σ detections. By artificially fixing the signal-to-noise per wavelength bin, we showed the limits in molecular detectability independently of instrument parameters, observation duration and sources of noise. We assumed simulated thermal profiles for the planet atmospheres, but investigated more extreme alternative profiles to quantify their effect on our results. We focused on key atmospheric molecules such as CH_4, CO, CO_2, NH_3, H_2O, C_2H_2, C_2H_6, HCN, H_2S and PH_3. We found that for all planet cases, SNR=5 is typically enough to detect the strongest feature in most molecular spectra, provided the molecular abundance is large enough (e.g. $\sim 10^{-6}/10^{-7}$ for CO_2, $10^{-4}/10^{-5}$ for H_2O). In atmospheres where a molecule has abundances lower than said threshold, SNR$\sim$10 or more may be required. For the temperate super-Earth, we also show that with SNR=5, O_3 can be detected with a constant abundance of 10^{-7} at $9.6\mu m$, and with an abundance of 10^{-5} at $14.3\mu m$ (Note that on Earth, the ozone abundance typically varies as a function of altitude in the 10^{-8} to 10^{-5} range). Other detection methods, such as the likelihood ratio test, combine information from multiple spectral bins and distinctive features. We often find an improved performance in detection sensitivity of $\sim$10 when using this method.

Finally, we tested the robustness of our results by exploring sensitivity to the mean molecular weight of the atmosphere and relative water abundances, and found that our main results remain valid except for the most extreme cases.

To conclude, our analysis shows that detectability of key molecules in the atmospheres of a variety of exoplanet cases is within realistic reach, even with low SNR and spectral resolution values. With new instruments specifically designed for exoplanet spectroscopic observation planned or under construction, the coming decade is set to be a golden age for the understanding of these newly-found worlds.

Chapter 4

Application to EChO

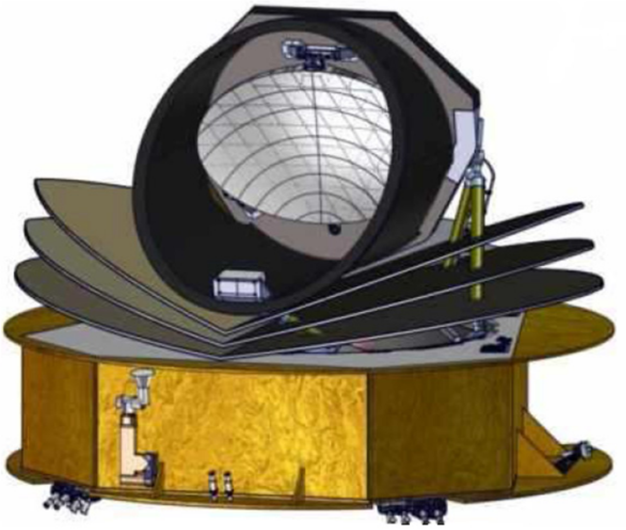

Figure 4.1: The EChO spacecraft design from one of the industry studies.

While the work presented in this chapter is focused on spectral observations with EChO, a proposed dedicated space telescope, a number of new general observatories are being built in the coming decade with designs that will allow spectral observations at a variety of wavelengths. Some aspects of the work presented here will be applicable to these new observatories.

4.1 General Observatories

4.1.1 E-ELT

The European Extremely Large Telescope (E-ELT)[1] is a 39m ground-based facility planned to be built by the early 2020s, with a wavelength range from 0.4 to 5.3 μm. In parallel, other similar projects are being studied, such as the Giant Magellan Telescope (GMT)[2] and the Thirty-Meter Telescope (TMT)[3]. The GMT has a diameter of 24.5m, with a wavelength range between 0.4 and 5 μm. The TMT has a 30m telescope, with a wavelength coverage between 0.3 and 5 μm and 9 to 18 μm. All three projects include multiple very high resolution spectrographs (R=5,000 - 100,000), and will be able to observe atmospheric spectra in limited wavelength ranges. These telescopes should be able to observe small

Telescope	Diameter	Instrument	Spectral Range	Instant coverage	spectral dispersion
E-ELT	39 m	METIS	2.9-5.3 µm	0.1 µm	R=100,000
		HIRES	0.4-2.3 µm	0.4-2.3 µm	R=100,000
		MOS	0.4-1.7 µm	0.4-1.7 µm	R<30,000
GMT	24.5 m	MOS	0.4-1.0 µm	0.4-1.0 µm	R<5000
		NIR-HRS	1.0-5.0 µm	?	R~50-100,000
		VIS-HRS	0.4-1.0 µm	0.4-1.0 µm	?
TMT	30 m	WFOS	0.3-1.0 µm	0.3-1.0 µm	R<7,500
		HROS	0.3-1.0 µm	0.3 -1.0 µm	R~50-90,000
		IRMOS	0.8 - 2.5 µm	0.3 µm	R=2,000-10,000
		MIRES	9-18 µm	8-14 µm	R=100,000
		NIRES	1-5 µm	~2 µm	R=100,000

Table 4.1: Summary of the planned instruments on three extremely large telescope designs.

---

[1] `http://www.eso.org/public/teles-instr/e-elt.html`

[2] `http://www.gmto.org/`

[3] `http://www.tmt.org/`

wavelength portions of exoplanet atmospheres at very high resolution, complementing the lower resolution broadband measurements that EChO is designed to achieve.

4.1.2 JWST

The James Webb Space Telescope (JWST)[4] is the largest space telescope ever conceived, with the spatial resolution of an equivalent telescope diameter of 5.8 m and 25 m^2 "clear" area. It is designed to operate over the visible ($\sim 0.6\mu$m) to mid-infrared waveband (28μm) providing very high sensitivity imaging and spectroscopy of faint astronomical targets. The JWST is currently being assembled, and is planned for launch in late 2018. Both primary and secondary exoplanetary eclipse measurements over the full waveband from 0.6 to 28 μm are possible with the combination of the instruments and modes on JWST (listed in Table 4.2). However, both its extremely high sensitivity and observatory nature mean there are some significant restrictions on the type and number of targets that will be observable. In addition to these instruments/modes there are a number of direct imaging possibilities using JWST.

Instrument	**Mode**	**Resolving power**	**Wavelength range (µm)**	**Comments**
NIRISS	Grism, cross-dispersed, slit-less	700	0.6 - 2.5	Saturates at K<9 at some part of band
NIRCam	Grism, slit-less	2000	2.4 - 5.0	Not proposed for transit spectroscopy in SODRM
NIRSpec	Prism, wide slit (1.6")	100	0.6 - 5.0	Saturates at K<8.5 at some part of the band.
NIRSpec	Grating, wide slit (1.6")	1000 or 2700	(0.7)1.0 - 1.8 1.7 - 3.0 2.9 - 5.0	Uses three grating settings to cover wavelength range (see figures in appendix)
MIRI	Prism, 0.6" slit or slit-less	100	5.0 - 11.0	Saturates at 2.9 Jy at 10 µm (K ~ 6)
MIRI	IFU (0.2" - 0.27"/pixel)	2400 – 3600	5.0 - 7.7 7.7 - 11.9 11.9- 18.3 18.3 - 28.3	Each band uses three sub-bands with separate gratings.

Table 4.2: Summary of the instruments on JWST

---

[4] `http://www.stsci.edu/jwst/doc-archive/white-papers`

4.2 The EChO Instrument

EChO, the Exoplanet Characterisation Observatory[5], is a medium class mission candidate to the second call for medium class missions in the Cosmic Vision 2015 - 2025 programme. The mission was one of four selected in February 2011 for further study in a Phase A assessment study. The full science case of EChO is described in Tinetti *et al.* (2012a).

In this chapter, we analyse the performance and trade-offs of a 1.2/1.4 m space telescope for exoplanet transit spectroscopy from the visible to the mid IR.

We present the signal-to-noise ratio as a function of integration time and stellar magnitude/spectral type for the acquisition of spectra of planetary atmospheres for a variety of scenarios: hot, warm, and temperate planets, orbiting stars ranging in spectral type from hot F to cooler M dwarfs. Our results include key examples of known planets (e.g. HD 189733b, GJ 436b, GJ 1214b, and Cancri 55 e) and simulations of plausible terrestrial and gaseous planets, with a variety of thermodynamical conditions. We conclude that even most challenging targets, such as super-Earths in the habitable-zone of late-type stars, are within reach of a M-class, space-based spectroscopy mission. The results presented in this chapter are published in Tessenyi *et al.* (2012a).

4.2.1 Estimating the integration time

The integration time needed to observe specific targets depends on:

- the parent star: spectral class, type, magnitude in a specified spectral region
- the contrast between the parent star and the companion planet in the observed spectral interval; this can be estimated from known observed or simulated objects
- the observational requirements: spectral region, resolution and signal to noise ratio
- the telescope characteristics: primary mirror diameter, overall transmission, coverage and sensitivity of the detectors
- the focal plane array characteristics during observation: number of pixels used per spectral resolution element, readout time, quantum efficiency, full well capacity, saturation threshold, dark current, readout noise

---

[5] `sci.esa.int/echo/`

We consider then the flux of photons from the planet. This flux (given in photons/seconds/m^2 in the whole spectral interval) is converted into electrons/pixel/seconds/"resolution element" within the defined spectral region using the following expression

$$F_{e^-} = \frac{F_\gamma \cdot A \cdot transmission \cdot QE}{Res \cdot N_{px/Res}} \tag{4.1}$$

where F_{e^-} and F_γ are respectively the electron and photon fluxes, A is the telescope mirror surface area, QE the quantum efficiency, Res the number of spectral elements in the band (resolution) and $N_{px/Res}$ the number of pixels per resolution element. From here on, F will only refer to the electron flux: F_{e^-}. The *transmission* is the overall fraction of energy that reaches the detector (before conversion to electrons). It includes the telescope and instrument (optical) transmission.

Using these values the time required for one detector pixel readout is computed:

$$t_{ro} = \frac{FWC \cdot saturation}{F_\star + F_{pl} + DC} \tag{4.2}$$

where ro stands for read out, FWC for full well capacity, DC for dark current and *saturation* is a fraction of the full well capacity (FWC). Usually, a saturation at 70% of the FWC is taken into account; that is the limit of electrons that can be accumulated in a single exposure.

The number of readouts required is then computed using the following formula:

$$N_{ro} = (SNR)^2 \cdot \frac{F_\star + F_{pl} + DC + (RON^2/t_{ro})}{F_{pl}^2 \cdot t_{ro} \cdot N_{px/Res}} \tag{4.3}$$

where SNR is the signal to noise ratio within the defined spectral band, and RON the detector readout noise. For the secondary eclipse case, F_{pl} is the flux emitted or reflected by the planet, while for the primary transit case, F_{pl} corresponds to the amount of flux (written as a negative) absorbed by the planet's atmosphere:

$$F_{pl} = -\frac{\pi {R_{pl}}^2}{\pi {R_\star}^2}\left(\left(1 + \frac{nH}{R_{pl}}\right)^2 - 1\right) = -\frac{2nHR_{pl}}{{R_\star}^2} \tag{4.4}$$

where n is an atmospheric absorption factor.

With these values, the total integration time is computed by multiplying the duration of a detector pixel readout by the number of readouts required.

The planet/star flux contrast ratio and the star brightness are the obvious main factors affecting integration times. To estimate the contrast, we have considered observed spectra and simulated synthetic spectra of stellar and planetary atmospheres.

4.2.1.1 Instrument detector and validation

Table 4.3 lists instrument setting values we have assumed for our simulator to cover the four bands in which our results are given.

Instrument Values	Visible	2.5 to 5 μm	5 - 11 μm	11 to 16 μm
Detector used (SOFRADIR)	CCD	MWIR	LWIR	VLWIR
Full well capacity (electrons)	$2 \cdot 10^6$	$4 \cdot 10^6$	$2 \cdot 10^7$	$5 \cdot 10^6$
Dark current (electrons/s/pixel)	0.1	10	500	300
Quantum efficiency (electrons/photon)	0.5	0.7	0.7	0.7
Readout noise (electrons/pixel/readout)	10	400	1000	1000
Readout time (seconds)	0.004	0.01	0.03	0.01
Telescope temperature (K)	0	60	60	60
Instrument temperature (K)	0	45	45	45
Telescope transmission	0.85	0.9	0.9	0.9
Instrument transmission	0.7	0.7	0.7	0.7

Table 4.3: Instrument settings used in our simulations, listed for each observing band used. In addition, the two following settings are the same for all four bands considered: a 30 μm pixel size and 2 illuminated pixels per spectral element are assumed. For the N band (7.7 to 12.7 μm) we have used the LWIR setting values. Note that in the case of the VLWIR detector, we have used a dark current value of 300 electrons/s/pixel considering existing technologies and expected future capabilities. Further discussion on these values can be found in section 4.2.4.4. We give in appendix B two other options, compatible with a 1.2 m telescope, and a different selection of detectors and instrument parameters.

For validating our tool, we have incorporated in our instrument simulator the parameters of Hubble NICMOS, and compared our results for hot gaseous planets with observed data from NICMOS. We obtained results in excellent agreement with the observed data.

4.2.2 Additional Model details

In addition to the methods and models described in sections 1.1.1 and 2.3, we consider a few further observational possibilities and modeling methods.

4.2.2.0.1 Infrared observations

For feasibility studies in the infrared, we approximate the planetary and stellar spectra in eq. 1.8 with two Planck curves at temperature T_p and $T_\star$, with T_p being the day-side temperature of the planet. While this approximation is not accurate enough to model specific examples, it is helpful to estimate the general case. The flux ratio is defined as:

$$F_{II}(\lambda) \sim \kappa \frac{B_p(\lambda, T_p)}{B_\star(\lambda, T_\star)} \tag{4.5}$$

where κ is the cross-section ratio defined in equation 1.5. In Fig. 4.2 we show the Planck curves for a few bodies at different temperatures. The planet to star flux contrast will clearly be higher for hot planets. Note that in the IR temperate planets at ~300 K can be observed only at wavelengths longer than 5 μm, as they emit a negligible amount of flux at $\lambda \leq 5\mu$m (Fig. 4.2).

4.2.2.0.2 Optical observations

For observations in the optical, we need to estimate the reflected light from the planet. Eq. (1.8) becomes:

$$F_{II}(\lambda) = \left(\frac{R_p}{R_\star}\right)^2 \frac{F_p(\lambda)}{F_\star(\lambda)} \sim \kappa\, A\, \zeta\, \frac{R_*^2}{a^2}\, \frac{F_\star(\lambda)}{F_\star(\lambda)} = \kappa\, A\, \zeta\, \frac{R_*^2}{a^2} \tag{4.6}$$

where A is the planetary albedo, ζ is the observed fraction of the planet illuminated and a the semi-major axis. The closer the planet to its stellar companion and the higher its albedo, the larger the contrast in the optical will be. For planets colder than $\sim$ 1200K, the reflected light component is predominant in the optical wavelength range ($\lambda < 0.8\mu m$). For hotter planets, both equations 4.5 and 4.6 will bring a contribution (emission and

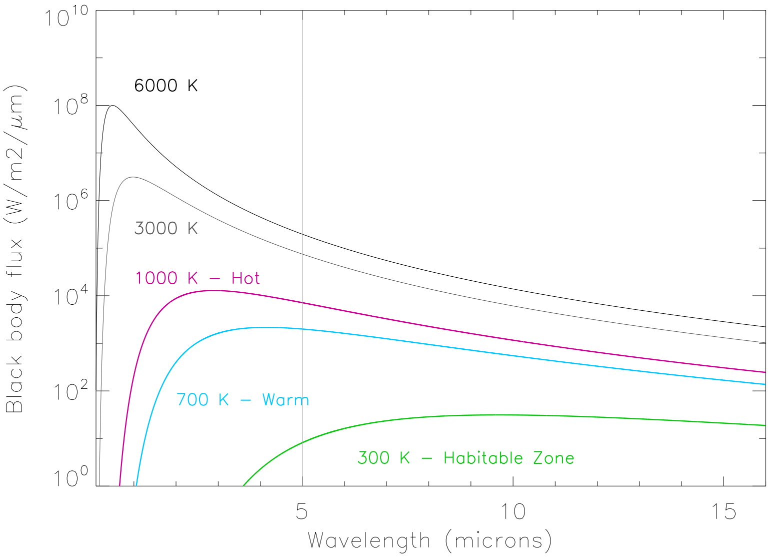

Figure 4.2: Blackbody curves for effective temperatures of 6000, 3000, 1000, 700 and 300 K. The radiation emitted by the 300 K body is negligible at λ shorter than 5 μm.

reflection).

4.2.2.0.3 Planet Phase Variations and Eclipse Mapping

Phase-variations are important in understanding a planet's atmospheric dynamics and the redistribution of absorbed stellar energy from their irradiated day-side to the night-side. These observations can only be conducted from space since the typical time scale of these phase variations largely exceeds that of one observing night. Phase variations are very insightful both at reflected and thermal wavebands. In the infrared case, these kinds of observations are critical to constrain General Circulation Models of exoplanets, of hot gaseous planets in particular. For instance, the infrared $8\mu m$ Spitzer observations of the exoplanet HD189733b have shown the night-side of this hot Jupiter to be only $\sim 300K$ cooler than its day-side (Knutson *et al.* 2007a), suggesting an efficient redistribution of the absorbed stellar energy. In addition, towards the optical wavelength regime, an increasing contribution from reflected light is expected (Snellen *et al.* 2009; Borucki *et al.* 2009).

A great advantage of a dedicated exoplanet mission would be the potential for long campaigns: staring at a known planetary system for a sizable fraction of an orbit (Knutson *et al.* 2007a, 2009a,b) or an entire orbit (Snellen *et al.* 2009; Borucki *et al.* 2009), or —provided the flux calibration is accurate enough— using multi-epoch observations to obtain a more sparsely sampled phase curve (Cowan *et al.* 2007; Crossfield *et al.* 2010).

At thermal wavelengths this may only be interesting for short-period planets, where the diurnal temperature contrast is high. Additionally, non-transiting planets open up interesting possibilities to study seasons (eg, Gaidos and Williams (2004)). Furthermore, the simultaneous multi-band coverage would make it possible to simultaneously probe the longitudinal temperature distribution as a function of pressure, which would be a very helpful constraint for GCMs.

The potential for using phase variations to study non-transiting systems should also be noted (Selsis *et al.* 2011). Non-transiting systems are going to be closer on average than their transiting counterparts. The challenge is stellar and telescope stability over the orbital time of a planet. For planets on circular orbits, thermal phases have limited value because of the inherent degeneracies of inverting phase variations (Cowan and Agol 2008), but for eccentric planets, phase variations will be much richer (Langton and Laughlin 2008; Lewis *et al.* 2010; Iro and Deming 2010; Cowan and Agol 2011). As one considers increasingly long-period planets (warm rather than hot) even more of them will be on eccentric orbits because of the weaker tidal influence of the host star.

For the brightest targets, secondary eclipses can also be used as powerful tools to spatially resolve the emission properties of planets. During ingress and egress, the partial occultation effectively maps the photospheric emission region of the object being eclipsed (Williams *et al.* 2006; Rauscher *et al.* 2007; Agol *et al.* 2010). Key constraints can be placed on 3D atmospheric models through repeated infrared measurements. In this chapter, we will focus on the feasibility of primary transits and secondary eclipses. A more detailed and thorough study of the observability of phase variations and eclipse mapping will be the topic of future publications.

4.2.2.0.4 Comparison between primary and secondary transit techniques

The primary and secondary transit techniques are complementary. Transmission spectra in the infrared, from primary transits, are sensitive to atomic and molecular abundances, but less to temperature gradients. In comparison, emission spectroscopy allows for detection of molecular species alongside constraining the bulk temperature and vertical thermal gradient of the planet. Additionally, during the primary transit we can sound the terminator, whereas during the secondary eclipse we can observe the planetary day-side.

In Table 4.4 we present ratios of signal values from primary transit and secondary eclipse observations for the key examples of planetary classes (see Table 3.1). Given

	Jupiter	Neptune	super-Earth
star:	K	M2.5V	M4V
Hot	0.18	0.98	0.3 / 0.09
Warm	0.42	2.17	0.7 / 0.2
HZ	0.9	10.4	1.2 / 0.3

Table 4.4: Primary / secondary eclipse flux ratio for key examples of the planetary classes listed in Table 3.1. Numbers > 1 indicate that the primary transit is more favourable over the secondary, while numbers < 1 indicate the opposite. The results are obtained by dividing the atmospheric signals calculated from equations 1.6 and 1.8, taken at $\sim 10\mu m$ for all presented cases. For the super-Earth we report two values: a case of an "ocean planet" (1.8 $R_\oplus$, (Grasset *et al.* 2009)) with water vapour being the main component of the planetary atmosphere, and a telluric planet with CO_2 as main atmospheric component (1.6 $R_\oplus$). In the habitable-zone, the ratio for the latter case is less favourable, with 0.3 excluding the possibility of primary transit studies. By contrast, for an "ocean planet", the ratio of 1.2 is similar to the ratio for the habitable-zone Jupiter-like planet.

that long integration times require the co-adding of multiple transit observations, for the primary case, any systematic difference in the stellar flux could hamper results. For example, spot redistributions over the stellar surface could potentially alter the depth of the transit, and could be a reason of concern for late-type stars since, on average, they can be quite active. In the case of M-type star super-Earths, though, we rely mostly on secondary eclipse observations which are quite immune from effects related to stellar activity, as the planetary signal follows directly from the depth of the occultation without the need to model the stellar surface.

4.2.3 Results

We present our results ordered by planetary temperature: hot, warm and temperate (habitable-zone, H-Z). For our key examples we have calculated the flux contrast by using synthetic models (see section 2.3), which either fit existing observations or are extrapolated from our knowledge of the Solar System planets. For feasibility studies we prefer to adopt cruder estimates of atmospheric contributions (i.e. blackbody curves) rather than detailed simulations of each specific case. Plots of flux contrasts are given for each case, accompanied by integration times represented as "number of transits" (based on transit durations and orbital periods, see section 1.2.1), with a maximum number of transits indicated. This number is estimated by dividing the nominal lifetime of a mission (we consider 5 years here) by the orbital period for each target. For each case, integration times are given over a range of stellar magnitudes. The signal-to-noise and resolution (SNR/Res) values vary from table to table, from R=300 to R=10, and SNR=50 to SNR=5. For each target, these values were selected to optimise the scientific return across the magnitude range considered. The selected SNR and Resolution values are in most cases dictated by the “limiting cases”, i.e. the most difficult star+planet combinations to be observed in a specific class of objects. In most tables, the SNR/Res values can be raised for the bright targets, and lowered to curb the integration times for fainter objects. The outcome of our study is summarised in the MIR by showing results averaged over the 7.7 to 12.7 μm spectral window (equivalent to the classical Johnson photometric N-band). In addition, we provide in the appendix results averaged over three spectral bands (5-8.3, 8.3-11, 11-16μm), the reader may compare performances of various bands for the listed targets. For hot planets, observations in the NIR (2.5 to 5μm band) become feasible (see section 4.2.2 with equation 4.6) and planets close to their star can be easily probed in the visible. In such cases, the MIR integration times are followed by NIR and visible results.

4.2.3.1 Hot planets

4.2.3.1.1 Gas giants:

as a template for the hot Jupiter case, the observed hot gas giant HD 189733b is used. A modelled transmission spectrum analogue of primary transit observations and a planet/star contrast ratio, analogue of secondary eclipse measurements, are considered for our simulations (Fig. 4.3). For both cases, integration times are listed in units of number of transits in Table 4.5, where the modelled hot Jupiter is presented orbiting a sample of stars: a Sun-like G2V star, a warmer F3V star and HD 189733, a K1/2V type star (Bouchy *et al.* 2005). HD 189733 has a magnitude in V of 7.67. We extrapolate our results from mag V=5 to V=9, with a resolving power of R=300 and a signal-to-noise ratio SNR=50, chosen for the secondary eclipse, and R=100 and SNR=50 for the primary transit.

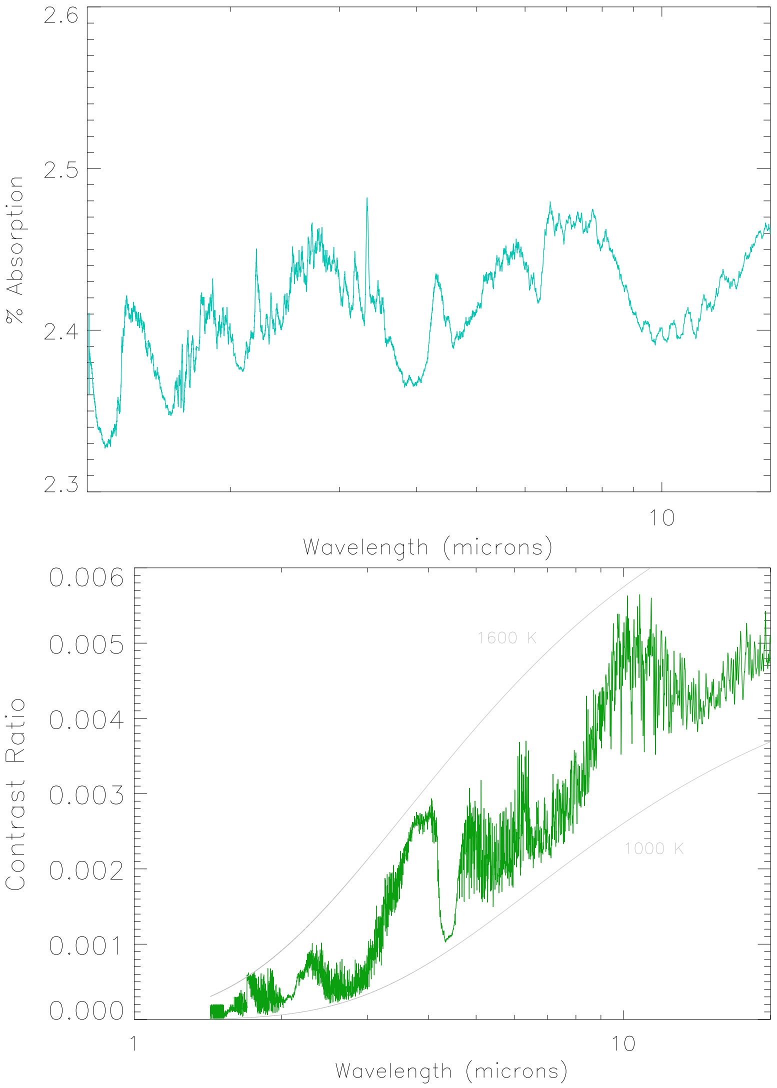

Figure 4.3: Modelled transmission and emission spectra of HD 189733b (Tinetti *et al.* 2010a), a hot-Jupiter around a K1/2V star, mag. V=7.67. *Left:* % absorption of the stellar flux occulted by the planetary atmosphere during the primary transit (transmission spectrum). *Right:* Contrast ratio of the flux from the planet (emission spectrum) over the flux from the star. Blackbody curves at 1000 K and 1600 K are plotted in grey.

Hot-Jupiters –Secondary eclipse, R=300, SNR=50, MIR

Star type	T (K)	R ($R_\odot$)	Contrast ($*10^{-3}$)	Period (days)	$\tau_{transit}$ (hours)	Max. n* (transits)	Integration time (n. transits)				
							V=5	V=6	V=7	V=8	V=9
F3V†	6740	1.56	1	8.4	2.9	218	7	18	51	156	*lower R*
G2V	5800	1	2.9	3.2	2.36	570	0.7	1.8	4.7	14	45
K1V†	4980	0.8	5.6	2.21	1.8	826	0.2	0.4	1	2.9	9
Hot-Jupiters –Primary transit, R=100, SNR=50, MIR											
F3V	6740	1.56	0.28	8.4	2.9	218	32	82	213	*lower R*	
G2V	5800	1	0.68	3.2	2.36	570	4	10	26	70	198
K1V	4980	0.8	1	2.21	1.8	826	1.6	4	10	26	72
Hot-Jupiter in NIR – Secondary eclipse, R=300, SNR=50, NIR											
K1V	4980	0.8	2.6	2.21	1.8	826	0.1	0.2	0.6	1.4	3.5

Table 4.5: Integration times (in units of “number of transits”) needed to obtain the specified SNR and spectral resolution for a given stellar type/brightness (in Mag. V). The upper table lists results for the secondary eclipse scenario in the MIR (equivalent to the classical Johnson photometric N-band) followed by primary transit results in the MIR, and secondary eclipse results in the NIR (between 2.5 and 5 μm). $\tau_{transit}$ is the transit duration given in hours, and “*lower R*” stands for target observable at lower resolution. †: Planet/star systems marked by this sign have additional results listed in the appendix. $*$: The maximum number of transits is computed by dividing a plausible mission lifetime (5 years assumed) by the duration of the planet orbital period.

4.2.3.1.2 Neptunes:

Neptune-like planets are expected to have a similar atmospheric composition to the gas-giants with a smaller radius (R ~0.35 R_j). While we do not directly present results for these targets, by comparison with the hot Jupiter scenario, integration times will be typically similar in the primary transit scenario and higher in the secondary eclipse scenario given the relatively smaller radius of the planet.

4.2.3.1.3 Super-Earths:

we show here two examples: a 2.1 $R_\oplus$ very hot planet in orbit around a G8V star, 55 Cancri e (Winn *et al.* 2011), and a 1.6 $R_\oplus$, 850 K planet in orbit around a range of M stars with temperature varying between $3055 \leq T \leq 3582K$. For the latter case, we approximated the planet/star fluxes with black-body curves to assess feasibility. Primary transit observations for a planet with high gravitational pull might be out of reach (55 Cancri e is reported to be $\sim 8.5M_\oplus$), for this reason we focus on secondary eclipses only. Planet to star flux contrasts are plotted in Figure 4.4 (55 Cancri e left, 850 K super-Earth right), accompanied by integration times in Table 4.6 in the MIR and NIR. For both bands a resolution of R=40 and SNR=10 were selected.

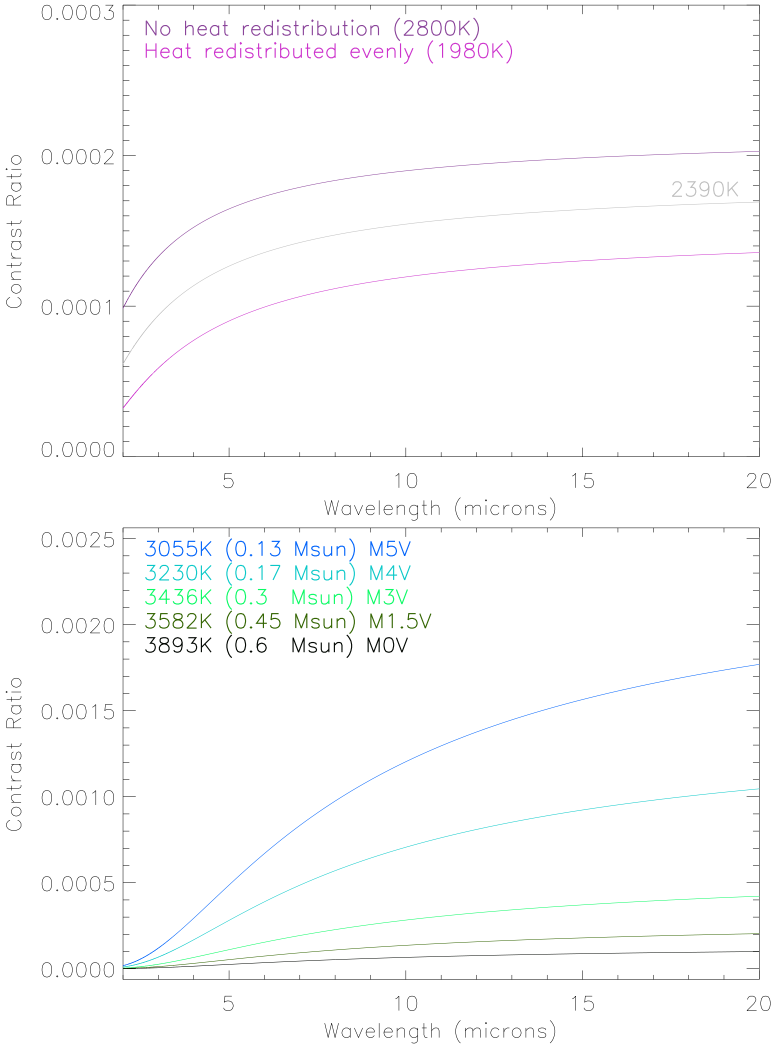

Figure 4.4: *Left:* Secondary eclipse simulated signal for 55 Cancri e, a 2.1 $R_{\oplus}$ hot super-Earth orbiting a G8V star. The atmospheric temperature could vary between 2800 K and 1980 K, depending on the heat redistribution (Winn *et al.* 2011). Both possibilities are presented, alongside an intermediate case of a 2390 K atmosphere used for our results. *Right:* Secondary eclipse signal for a hot super Earth (850K, 1.6 $R_{\oplus}$) orbiting a selection of M stars (from M1.5V to M5V). For the two figures, both the planet and the stellar contributions here are estimated as black-bodies. While this description is too simplistic to capture the properties of a real, specific case, for feasibility tests we do not want to rely on too narrow assumptions.

Hot super-Earths –Secondary eclipse. R=40, SNR=10, MIR

Star	T	R	Contrast	Period	$\tau_{transit}$	Max. n*	Integration time (n. transits)				
type	(K)	($R_\odot$)	($*10^{-4}$)	(days)	(hours)	(transits)	K=5	K=6	K=7	K=8	K=9
M0V	3893	0.57	0.7	2.17	1.6	840	38	97	253	689	*lower R.*
M1.5V†	3582	0.42	1.4	1.22	1.1	1494	13	33	87	236	707
M3V	3436	0.30	2.9	0.79	0.8	2300	4.2	11	28	75	225
M4V	3230	0.20	7.2	0.46	0.5	3955	1	2.7	7	19	58
M5V†	3055	0.16	12.2	0.25	0.4	7450	0.5	1.2	3.1	8	25

Hot super-Earths in NIR –Secondary eclipse, R=40, SNR=10, NIR

M0V	3893	0.57	0.1	2.17	1.6	840	199	499	*lower R.*		
M1.5V	3582	0.42	0.3	1.22	1.1	1494	32	81	203	509	1279
M3V	3436	0.30	0.5	0.79	0.8	2300	15	39	97	243	611
M4V	3230	0.20	1.4	0.46	0.5	3955	3	8	19	18	121
M5V	3055	0.16	2.5	0.25	0.4	7450	1.1	2.8	7	18	45

Hot super-Earth –example of 55 Cancri e in secondary transit, R=40, SNR=10, MIR

Star	T	R	Contrast	Period	$\tau_{transit}$	Max. n*	Integration time (n. transits)				
type	(K)	($R_\odot$)	($*10^{-4}$)	(days)	(hours)	(transits)	V=5	V=6	V=7	V=8	V=9
G8V	5243	0.95	1.6	0.74	1.76	2467	1.4	3.4	9	22	58

Table 4.6: Integration times (in units of "number of transits") needed to obtain the specified SNR and spectral resolution for a given stellar type/brightness (in Mag. K when orbiting M dwarfs, Mag. V when orbiting G star). The upper table lists results for the secondary eclipse scenario in the MIR, followed by secondary eclipse results in the NIR. $\tau_{transit}$ is the transit duration given in hours, and "*lower R*" stands for target observable at lower resolution. $\dagger, *$: *See Table 4.5 caption.*

4.2.3.1.4 Observations in the visible:

we present here two cases: the case of a hot Jupiter and the case of a hot super-Earth. The reasons for our choice are based on Eq. 4.6: reflected light is more prominent for planets close to their star. For the case of the hot super-Earth, we selected a 1.6 $R_\oplus$ planet with a fixed temperature of 850 K and varying albedo values. For the case of the hot Jupiter, we present a fixed orbital distance with varying albedo values (corresponding to temperatures $\sim 1200 - 1500$ K). Notice that the emission from the planet is negligible at these temperatures when compared with reflection in the visible. Results are given in Tables 4.7 and 4.8, with R=40 and SNR=20 for the hot Jupiter, and R=20 and SNR=10 for the hot super-Earth.

Visible band hot Jupiter. With $\zeta = 1$, R=40, SNR=20

Albedo	a	Contrast	Period	$\tau_{transit}$	Max. n*	Integration time (n. of transits)				
Value	(a.u.)	($*10^{-4}$)	(days)	(hours)	(transits)	V=5	V=6	V=7	V=8	V=9
0.1	0.031	0.31	4.7	2.36	570	7	18	44	110	278
0.3		0.92				0.8	1.9	4.9	12	31
0.5		1.54				0.3	0.7	1.8	4.5	11
0.7		2.16				0.1	0.4	0.9	2.3	6

Table 4.7: Integration times (in units of "number of transits") for a hot Jupiter observed in the visible around a G2V star. The orbital distance is fixed and the planetary temperature varies with the albedo. For the studies presented here, we have considered full illumination ($\zeta = 1$), and values of R=40 and SNR=20. When the planet is not fully illuminated ($\zeta < 1$), longer integration times are needed for the same parameters. $*$: *See Table 4.5 caption.*

Visible band hot super-Earth, with $\zeta = 1$, R=20, SNR=10

Albedo	a	Contrast	Period	$\tau_{transit}$	Max. n*	Integration time (n. of transits)				
Value	(a.u.)	($*10^{-4}$)	(days)	(hours)	(transits)	K=5	K=6	K=7	K=8	K=9
0.1	0.006	0.15	0.47	0.8	3916	426	1161	2917	*lower R.*	
0.3	0.006	0.58	0.39	0.7	4728	35	89	223	560	1407
0.5	0.005	1.35	0.30	0.7	6085	7	16	41	103	260
0.7	0.004	3.16	0.20	0.6	8927	1.4	3.5	9	22	55

Table 4.8: Integration times (in units of "number of transits") for a hot super-Earth (850 K) observed in the visible around a M4.5V star. Here the planetary temperature is fixed and the orbital distance varies with the albedo. For the studies presented here, we have considered full illumination ($\zeta = 1$), and values of R=20 and SNR=10. When the planet is not fully illuminated ($\zeta < 1$), longer integration times are needed for the same parameters. "*lower R*" stands for target observable at lower resolution. $*$: *See Table 4.5 caption.*

4.2.3.2 Warm planets

4.2.3.2.1 Gas giants:

In this section we focus on Neptunes and super-Earths, skipping warm gas giants, which fall between the categories of hot Jupiters and warm Neptunes.

4.2.3.2.2 Neptunes:

we considered as example of a warm Neptune GJ 436b, a 4 $R_\oplus$ planet around a M2.5V dwarf star, with a radius of 0.46 $R_\odot$ and magnitude in K of 6.07 (Butler *et al.* 2004; Gillon *et al.* 2007). Spitzer photometric data have been analysed and interpreted (by Beaulieu *et al.* (2011); Stevenson *et al.* (2010); Knutson *et al.* (2011)), observed results captured by simulated spectra are shown in Figure 4.5 (primary transit left, secondary eclipse right). Integration times for a primary transit and secondary eclipse of such a warm Neptune-like planet follow in Table 4.9.

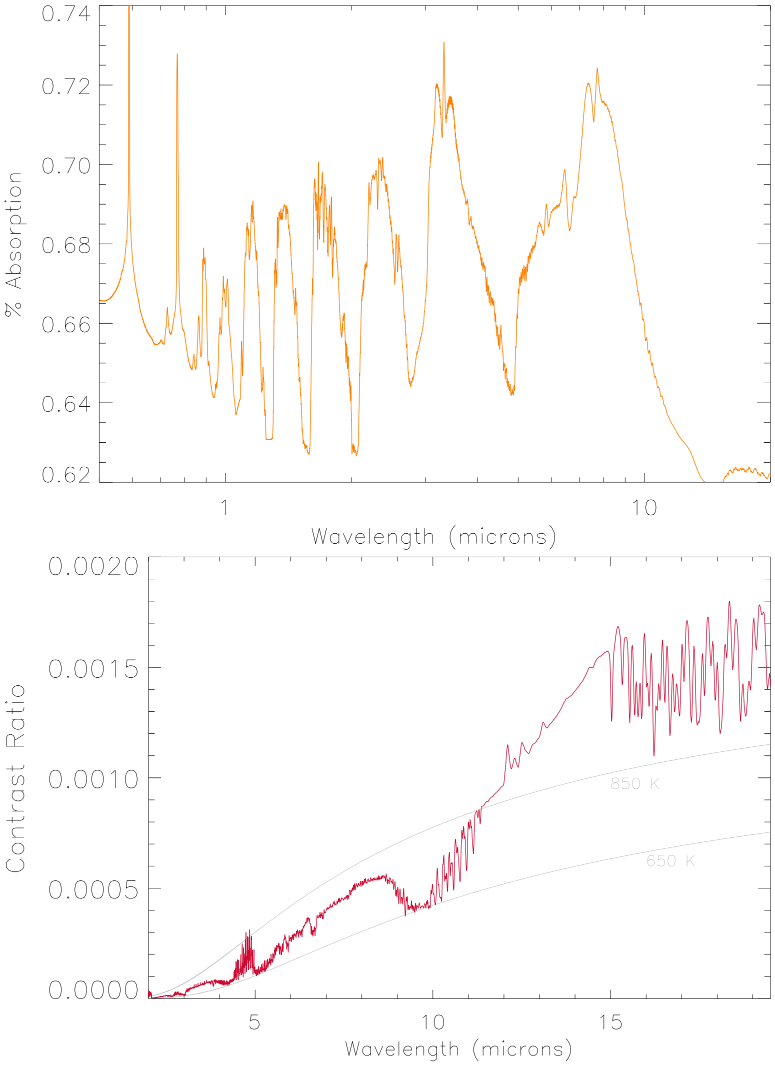

Figure 4.5: Modelled GJ 436b (Beaulieu *et al.* 2011; Stevenson *et al.* 2010), a warm Neptune around a M2.5V star, mag. K=6.07: *Left:* % absorption of the stellar flux occulted by the planetary atmosphere during the primary transit. *Right:* Contrast ratio of the flux from the planet over the flux from the star. Blackbody curves at 650 K and 850 K are plotted in grey.

Warm Neptune –Secondary eclipse, R=50-100, SNR=30-50, MIR

Star type	T (K)	R ($R_\odot$)	Contrast $*10^{-4}$	Period (days)	τ_{trans} (hrs)	Max. n (trans.)	R/SNR	Integration time (n. transits) K=5	K=6	K=7	K=8	K=9
M2.5V†	3684	0.46	4.6	2.64	1.03	691	100/50	80	207	563	*lower Res.*	
							50/30	14	36	95	263	*low* R

Warm Neptune –Primary transit, R=50-100, SNR=30-50, MIR

Star type	T (K)	R ($R_\odot$)	Contrast $*10^{-4}$	Period (days)	τ_{trans} (hrs)	Max. n (trans.)	R/SNR	K=5	K=6	K=7	K=8	K=9
M2.5V	3684	0.46	10	2.64	1.03	691	100/50	17	44	120	358	*low* R
							50/30	3	8	20	56	173

Table 4.9: Integration times (in units of "number of transits") needed to obtain the specified SNR and spectral resolution for a given stellar type/brightness (in Mag. K). The upper table lists results for the secondary eclipse scenario in the MIR, followed by primary transit results in the MIR. Both tables show two selections of SNR and resolution values. $\tau_{transit}$ is the transit duration given in hours, and "*lower R*" stands for target observable at lower resolution. $\dagger, *$: *See Table 4.5 caption.*

4.2.3.2.3 Super-Earths:

GJ 1214b (Charbonneau *et al.* 2009) is a perfect example for the case of a warm super-Earth orbiting a M star. We show in Fig. 4.6 a simulated transmission spectrum of this planet. Since the available observations for this specific planet are not enough to constrain its true composition and atmospheric characteristics (Bean *et al.* 2010), our simulations here just show a possible scenario. We also present in Fig. 4.6 planet/star flux contrasts for a 1.6 $R_\oplus$, 500 K planet in orbit of a range of M stars (from M1.5V to M5V with temperatures ranging from 3055 K to 3582 K). Both the planet and the stellar contributions here are estimated as blackbodies, and only secondary eclipse results are presented. The integration times are listed in Table 4.10 in the MIR, with R=40 and SNR=10.

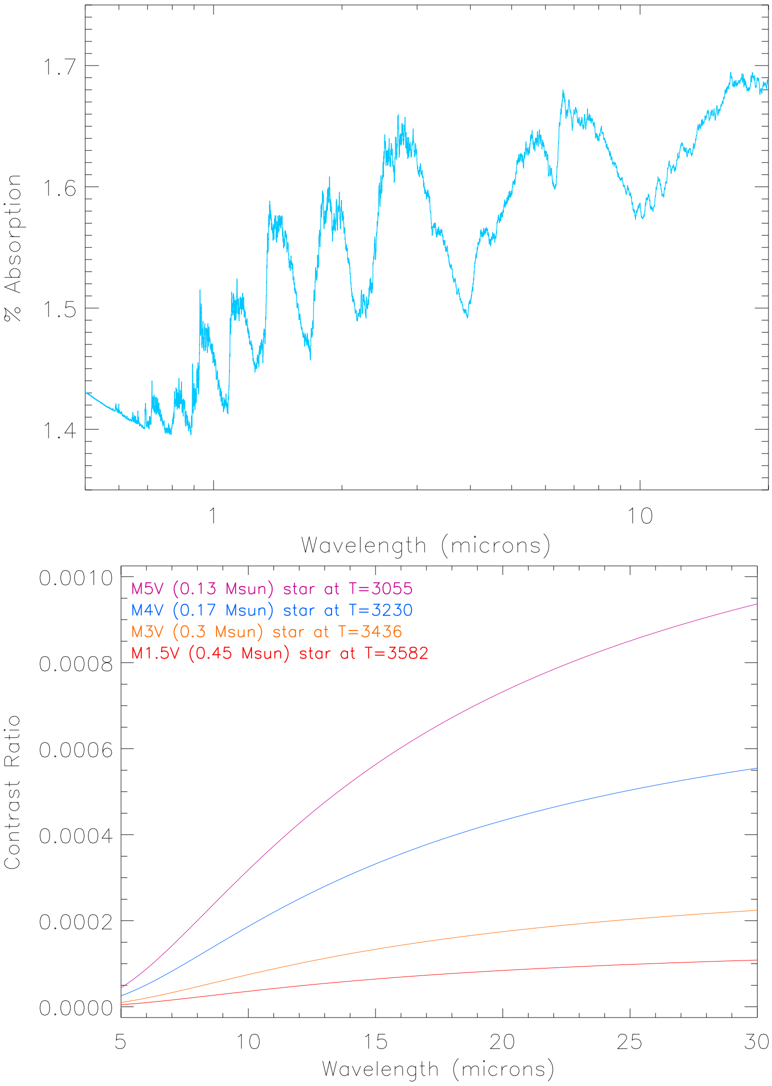

Figure 4.6: *Left:* simulated transmission spectrum for the warm super-Earth GJ 1214b, in units of % absorption of the stellar flux. *Right:* secondary eclipse signal from a warm Super Earth (500 K, 1.6 $R_{\oplus}$) orbiting a range of M stars, from M1.5V to M5V with temperatures ranging from 3055 K to 3582 K.

Warm super-Earths –Secondary eclipse, R=40, SNR=10, MIR

Star type	T (K)	R ($R_\odot$)	Contrast $*10^{-4}$	Period (days)	$\tau_{transit}$ (hours)	Max. n* (transits)	Integration time (n. transits) K=5	K=6	K=7	K=8	K=9
M1.5V	3582	0.42	0.4	6	1.9	304	52	131	335	*low R*	*ph*
M3V	3436	0.30	0.8	3.9	1.3	468	18	44	114	298	*low R*
M4V†	3230	0.20	1.9	2.27	0.9	804	4	10	26	69	192
M5V†	3055	0.16	3.3	1.57	0.7	1163	1.8	4.6	12	31	85
Warm super-Earth –example of GJ1214b in primary transit, R=40, SNR=10, MIR											
M4.5V	2949	0.21	27	1.58	0.88	1155	0.1	0.1	0.3	0.8	2.3

Table 4.10: Integration times (in units of “number of transits”) needed to obtain the specified SNR and spectral resolution for a given stellar type/brightness (in Mag. K). The upper table lists results for the secondary eclipse scenario in the MIR, followed by secondary eclipse results in the NIR. $\tau_{transit}$ is the transit duration given in hours, “*lower R*” stands for target observable at lower resolution, and *ph* stands for photometry. $\dagger, *$*: See Table 4.5 caption.*

4.2.3.3 Habitable Zone Planets

4.2.3.3.1 Gas giants:

we present here the case of a hypothetical "cool" Jupiter, in the Habitable-Zone (HZ) of a K4V star. Figure 4.7 shows our simulated secondary eclipse spectrum, with an atmosphere in which we have included water vapour, methane, hydrocarbons, CO and CO_2 and a thermal profile with temperature decreasing with altitude. In Figure 4.7, the departure from the (315 K) blackbody is noticeable. While our assumptions here are reasonable, this is just one possible scenario, and completeness is beyond the scope of this chapter. Integration times are listed in Table 4.11, for different stellar brightness.

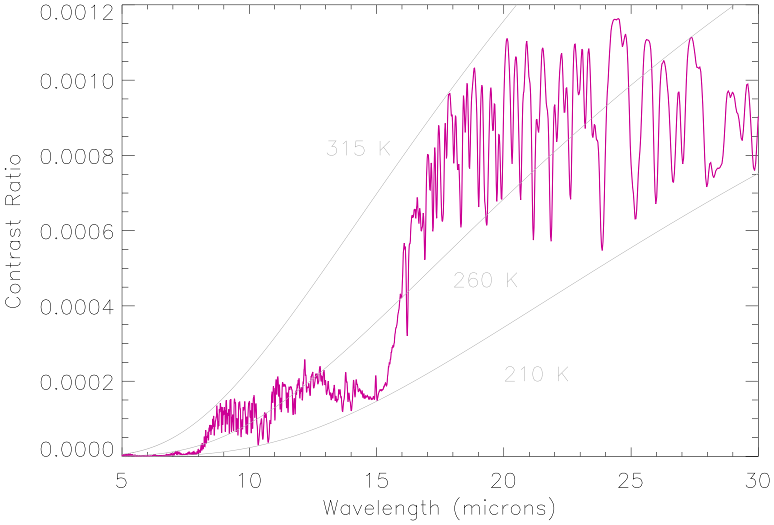

Figure 4.7: Secondary eclipse signal from a conceivable habitable-zone Jupiter around a K4V, 4780 K star –such as HAT-P-11. Blackbody curves at 210 K, 260 K and 315 K are plotted in grey.

Cool Jupiter –Secondary eclipse, R=20-40, SNR=10, MIR

Star type	T (K)	R ($R_\odot$)	Contrast ($*10^{-4}$)	Period (days)	$\tau_{trans.}$ (hrs)	Max. n* (transits)	R/SNR	Integration time (n. of transits) V=5	V=6	V=7	V=8	V=9
K4V†	4780	0.75	1.5	101.6	6.9	18	40/10	0.3	0.6	1.6	4.1	11
							20/10	0.1	0.3	0.8	2	5

Table 4.11: Integration times (in units of “number of transits”) needed to obtain the specified SNR and spectral resolution for a given brightness (in Mag. V). The results are given in the MIR with two selections of SNR and resolution. $\tau_{trans.}$ is the transit duration given in hours. Notice that the orbital period for a planet in the HZ of a K4V star is more than 100 days, so the observation can be repeated less than 20 times in 5 years. $\dagger, *$: *See Table 4.5 caption.*

4.2.3.3.2 Neptunes:

we skip the case of a habitable-zone Neptune, as the secondary eclipse falls between the categories of a HZ Jupiter and a HZ super-Earth. In the case of primary transits, on the contrary, we expect a much more favourable result, as indicated in Table 4.4.

4.2.3.3.3 Super-Earths:

here we present a 1.8 $R_\oplus$ telluric planet, with three plausible atmospheres: Earth-like, Venus-like and hydrogen-rich (i.e. small Neptune). Figure 4.8 shows the planet to star flux contrast obtained for a 1.8 $R_\oplus$ super-Earth orbiting a M4.5V star with T=3150 K, with the three mentioned atmospheres in two spectral resolutions: R=200 and R=20. Blackbody curves at 200, 250, 300, 350 K are included. The change in contrast for the different atmospheric cases is noticeable: for instance, the presence of water vapour in the Earth-like and small Neptune cases marks a sharper departure from the blackbody curve. H_2O, CO_2 and ozone absorption are still detectable even at very low resolution, but less abundant hydrocarbon species become more difficult to capture. Table 4.12 lists integration times in the MIR for the case of a 300 K atmosphere and a range of stars spanning in type and brightness. While a resolution of R=10 and SNR=5 were selected to cover the broadest range of stellar types in the table, the cooler stars in the table will allow for higher SNR/Resolution values.

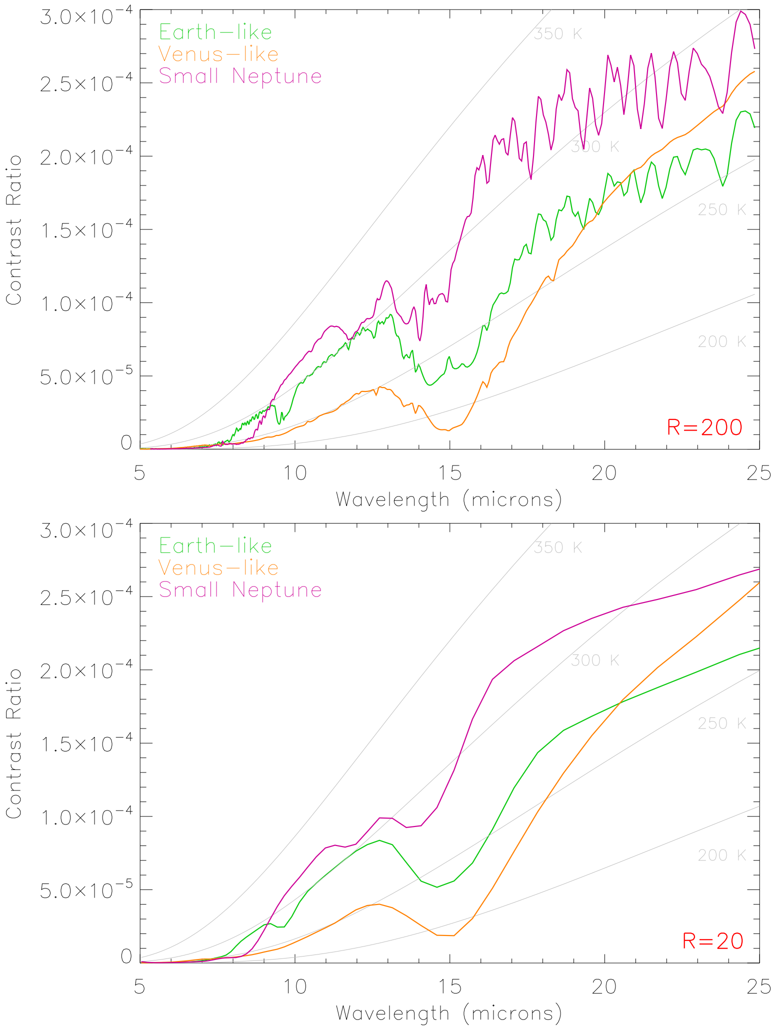

Figure 4.8: *Left:* Earth-like, Venus-like and small Nepture secondary eclipse spectra at R=200, with marked blackbody contrast curves as temperature indicators (from left to right: 350, 300, 250 and 200 K). The three atmospheres belong to a 1.8 $R_\oplus$ super Earth around an M4.5V star (at T=3150 K). *Right:* Same case at a resolution of R=20.

Habitable Zone super-Earth –Secondary eclipse, R=10, SNR=5, MIR

Star type	T (K)	R ($R_{\odot}$)	Contrast ($*10^{-5}$)	Period (days)	$\tau_{transit}$ (hours)	Max. n* (transits)	Integration time (in N. transits)				
							K=5	K=6	K=7	K=8	K=9
M2.5V	3475	0.34	1.1	23.7	2.6	77	54		*photometry*		
M3V	3436	0.30	1.4	20.6	2.3	88	37		*photometry*		
	3380	0.26	1.9	17.3	2.1	105	22	55	*photometry*		
M4V†	3230	0.20	3.5	12	1.6	152	9	22	54	140	*ph.*
	3150	0.17	4.6	10	1.4	182	6	14	36	94	*ph.*
M5V†	3055	0.16	6	8.3	1.3	220	3.6	9	23	60	158
	2920	0.14	8.5	6.4	1.1	286	2.2	5	14	36	94

Table 4.12: Integration times (in units of "number of transits") needed to obtain the specified SNR and spectral resolution for a given stellar type/brightness (in Mag. K) in the MIR. $\tau_{transit}$ is the transit duration given in hours, *ph* stands for photometry, where a few wavelenghts can be probed for the most challenging targets. †, ∗: *See Table 4.5 caption.*

4.2.4 Discussion

4.2.4.1 Stellar Variability

Our simulations do not include the effects of stellar variability on transit observations. Kepler is reaching photometric stability of 200 ppm/min on an V=11 mag star and 40 ppm/min on a V=7 mag star. For timescales between 3-16 days, based on the analysis of 100,000 stars (first release of 43 days of Kepler data), Basri *et al.* (2010, 2011) show that 57 % of G stars are active and tend to be more active than the Sun (up to twice the activity level is typical). This fraction increases to 87% of K and M dwarfs (figure 4 of Basri *et al.* (2010)). The peak of the histogram of amplitude distribution is centered at 2 mmag. Scatter plots from Basri et al. show that for K and M stars indeed the dominant source of scatter is variability, not Poisson noise. The bulk of the periodicities is found at periods larger than 10 days, with amplitudes ranging from 1-10 mmag. Ciardi *et al.* (2011) found that 80% of M dwarfs have dispersion less than 500 ppm over a period of 12 hours, while G dwarfs are the most stable group down to 40 ppm.

It is important to note here that the photometric variability is significantly lower in the near infrared than in the Kepler band (Agol *et al.* 2010; Knutson *et al.* 2011), because of the lower contrast between spots and the stellar photosphere at larger wavelengths (Ballerini *et al.* 2012). For instance, Agol *et al.* (2010) measured that the infrared flux variations in the case of the active K star HD 189733 are about 20% of the optical variations. This is in agreement with the theoretical estimates by Ballerini *et al.* (2012).

Most importantly, all the timescales related to stellar activity patterns are very different from the timescales associated to single transit observations (a few hours), and thus can be easily removed. CoRoT-7 b provides a good example. The activity modulations are of the order of 2% and yet CoRoT managed to find a transit with a depth of 0.03%. This was made possible by the continuous monitoring provided by CoRoT and the different timescale compared with the transit signal that allowed for the removal of the activity effects and the discovery of variations smaller than the overall modulation by a factor of 70. The same situation has been encountered by the Kepler team, which have disentangled stellar activity modulations and transit events, often with the former being far greater than the latter (Basri *et al.* 2013).

In conclusion, the overall (random) photometric jitter of the star should not be a crucial factor with the right strategy to adequately correct for modulations caused by spot variations. Time series can be used as an “activity monitor” by the visible part of the spectrum. As mentioned in 4.2.2.0.4, systematic differences in the stellar flux could hamper multiple transit combinations. However, where primary transit observations are subject to these effects, secondary eclipse observations are preferred as they are immune to them.

4.2.4.2 Planetary Variability

Upper limits about eclipse variability have been reported by Agol *et al.* (2010) and Knutson *et al.* (2011). We do not know the nature of this variability, but the chance of observing multiple spectra rather than photometric bands might be helpful to explore the potential sources of atmospheric variability (thermal changes? chemical changes? clouds/hazes?) for the most favorable targets. In the case of faint targets, for which co-adding eclipse observations is necessary, only spatially/temporally-averaged information will be available. From the experience with the planets in our own Solar System, this information, although more limited, is expected to be still very significant.

4.2.4.3 Stellar Population

The integration times required to study habitable-zone super-Earths (given in table 4.12) show that characterisation of these targets is possible provided they orbit late type dwarfs. While bright targets are preferred, as they provide a higher photon signal, our results cover a range of magnitudes from K=5 to K=9. In parallel, the M type population found in the RECONS catalogue (RECONS 2011), which lists 100 stars up to 6.6pc in the Sun’s local neighbourhood, is mostly formed of bright targets with a significant fraction having magnitudes between K=4 and K=6 (see Fig. 1.16). Extrapolation from the catalogue up to magnitude K=9 yields however a much larger stellar population that can be studied for super-Earths. Thus, combining the feasibility of studying targets up to K=9, while keeping a preference for brighter sources, and the greater amount of fainter stars up to mag. K=9, creates a common area ideal for super-Earth observations centered around the K=7-8 magnitude region. A mission that aims to characterise habitable-zone super-Earths should have detectors optimised for this magnitude range.

4.2.4.4 Instrument Transmission

Throughout this chapter we have considered an instrumental transmission value of 0.7. In practical applications, many factors can reduce this transmission value. While most of the cases presented allow for slightly longer observations, the most challenging category of habitable-zone super-Earths will require high instrumental transmission values to remain feasible. Instrument designs with high levels of transmission, such as fourier transform spectrographs, can be considered a possibility for the characterisation of these most challenging targets.

4.2.4.5 Systematic Effects

We presented here idealised cases where systematic errors (such as detector time constants, pointing jitter, re-acquisition errors, temperature fluctuations, etc.) were not accounted for. Instrumental settings for our results from the visible to the infrared were based on available technology and can be considered realistic. With these considerations, the results presented in this chapter highlight that in the coming years habitable-zone super-Earths are realistically within reach. In future work, we will update our models as information on the systematic effects of specific instruments becomes available.

4.2.5 Concluding remarks

We have presented in this chapter a detailed study of the performances and trade-offs of a M-class transit spectroscopy mission dedicated to the observation of exoplanetary atmospheres. We have demonstrated that, in principle, with a 1.2/1.4 m space telescope performing simultaneous spectroscopy from the visible to the mid-IR, we are able to secure the characterisation of a plethora of exoplanets, ranging from the hot, gaseous down to the temperate ones approaching the size of the Earth. According to our simulations, the spectra of hot-Jupiters orbiting F, G and K-type stars with V mag. brighter than 10 can be obtained by integrating from a fraction of transit up to few tens of transits to reach a spectral resolution of 300 and SNR = 50. Habitable-zone super-Earths are undoubtedly the most challenging category of targets due to their small size, low temperature and their relatively large separation from the star. We show however, that these targets can be observed at low resolution in the Mid-IR, provided their hosting star is a bright M dwarf. While most of the Sun's neighbourhood is composed of these late-type stars, efforts still need to be directed at increasing the number of low mass stars known and constraining their properties. The 2MASS catalogue sample, completed with current and planned dedicated ground-based surveys, as well as space missions such as WISE and GAIA should offer a viable solution to this critical issue in the next five years.

In future work, we will update our current instrument models by including a more realistic treatment of the systematics.

Chapter 5

Conclusions

I have been very fortunate to start my Ph.D. in the field of exoplanets at this time. The fast-paced developments of the field have taken us from a handful of landmark discoveries 20 years ago, to dedicated space missions finding thousands of planets orbiting distant stars today. Even better, space agencies across the world are building and considering designs of space missions that will probe the atmospheres of exoplanets. Meanwhile, major ground-based telescope designs all include exoplanet atmosphere characterisation as part of their specifications. With such high levels of interest and global involvement, the coming decade looks set to be a golden age for the understanding of these newly-found worlds.

My aim in the last three years was to analyse comprehensively the possibilities and limits of spectroscopic remote sensing of exoplanets in the context of these developments. In this thesis I have reported the results from the studies that were completed in parallel with the evolution of the dedicated spacecraft design EChO. The EChO instrument design has clearly changed since the first version was proposed, and consequently some of the calculations in this paper will need to be repeated — and they currently are, Varley *et al.* (2014). However, most of the results have been presented either independently of instrument parameters (e.g. fixed SNR results in 3.1) or in a way that they can scale with other configurations or designs. Throughout these three years, I have used radiative transfer models to simulate exoplanet atmospheres for a range of key planet types, combined

with integration time estimations based on a variety of instrument designs and performances, and have computed SNR requirements as a function of abundances for molecular detectability.
I thus hope that this *theoretical framework for understanding the diversity of exoplanet atmospheres* will be of use for future instrument design considerations.

As a final note, whether EChO is selected or not for the M3 ESA mission slot in February 2014, having worked alongside the members of the EChO team and the international consortium in the past 3 years has truly been a privilege. I have been very lucky to be closely involved with the developments of a mission that if selected I am certain will deliver revolutionary results.

Appendix A

The results in section 3.2 are obtained using a fixed SNR=5, 10 and 20. We show here what observational requirements are needed to obtain these SNR values with a dedicated space instrument similar to EChO (Tinetti *et al.* 2012a).
For the five planet cases, we show a planet with and a planet without molecular absorptions, orbiting stars located at 3 distances from the observer. Photon noise and an overall optical efficiency of 0.25 (to account for possible loss of signal through the instrument) are considered. The resolution is set to R=300 and 30 for the 1-5 and 5-16 μm ranges, respectively. Because of a weaker and colder signal, we only consider the 5-16 μm spectral interval for the temperate super-Earth, and lower the resolution to 20. The orbital parameters used for these calculations are listed in Table 3.2.

A.0.6 Warm Neptune

Figures A.1 and A.2 show the SNR per bin and the planet/star contrast spectra of a warm Neptune, without molecular absorption and with the presence of C_2H_2 at abundance 10^{-4}. The planet is placed at three distances (5, 10 and 20pc) from the observer. The maximum SNR value with no absorptions is ~30 for the 5pc target, while the 20pc target has a maximum SNR value of ~7. With the presence of an absorbing feature at ~7.5μm, the SNR drops to ~5 for the 20pc target. A stronger absorbing feature will lower the SNR below 5. With a distant Warm Neptune, the SNR may be too low for a single transit observation, and the co-adding up of multiple transits will be required. In addition, the shorter wavelength range (1 to 5 μm) will require co-adding of transits, as a single transit is not sufficient to obtain SNR of 5 or more, even for the closest target.

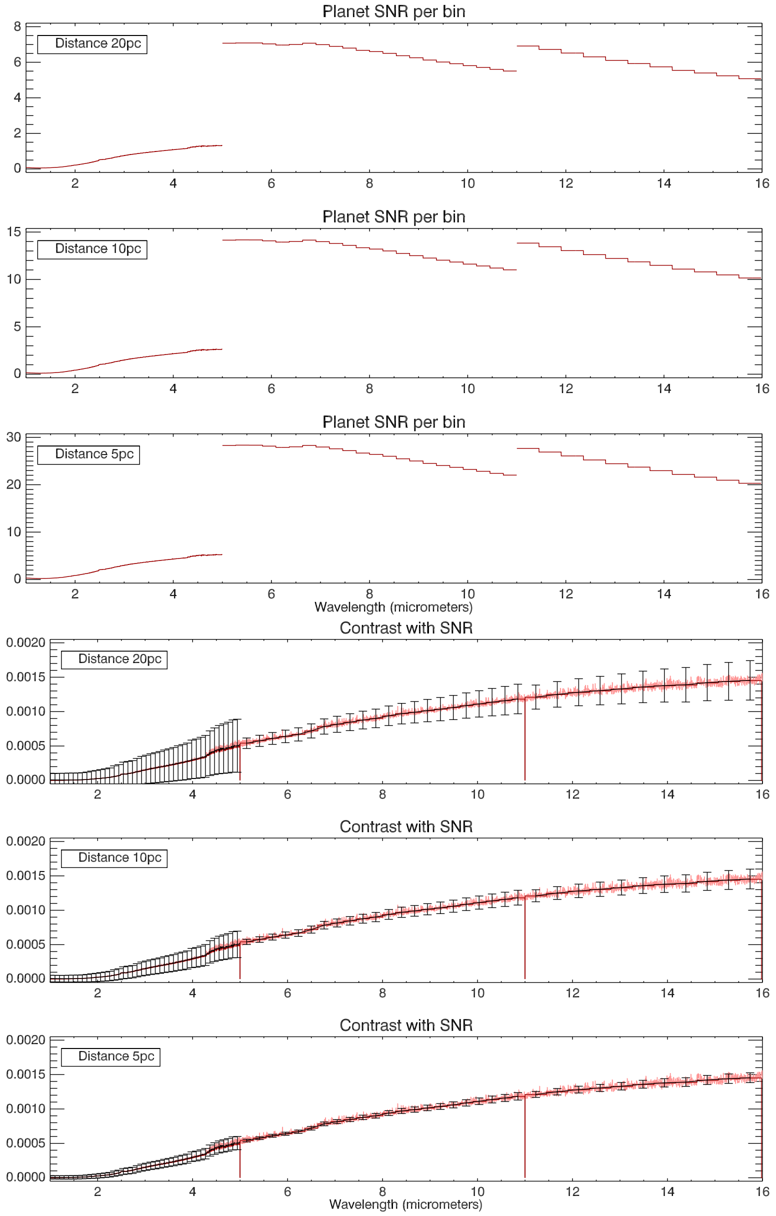

Figure A.1: A single transit of a warm Neptune with no molecules absorbing. *Top three diagrams:* SNR per resolution bin for a target located at 20, 10 and 5pc from the observer. *Bottom three diagrams:* Planet/star contrast spectra with 1-sigma error bars.

A.0.7 Hot Jupiter

In comparison with the warm Neptune, the signal of a hot Jupiter is stronger due to the combination of a larger and hotter planet+star, leading to higher SNR values per bin. Given the high SNR values from this planet, and to place the results from section 3.2 into

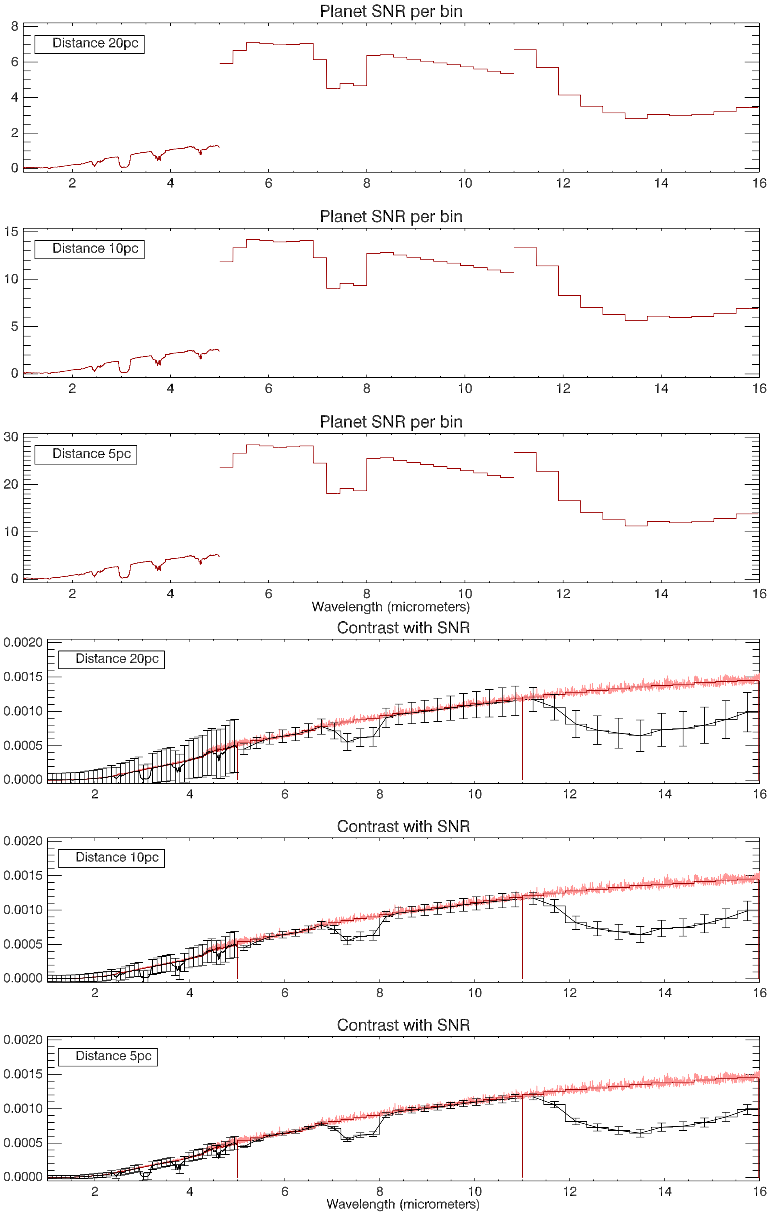

Figure A.2: A single transit of a warm Neptune with C_2H_2 in the atmosphere (mixing ratio=10^{-4}). *Top:* SNR per resolution bin for a target located at 20, 10 and 5pc from the observer. *Bottom:* Planet/star contrast spectra with 1-sigma error bars.

context, the distances for this planet are changed to 100, 50 and 20 pc (HD189733b, our template of hot Jupiter, is located at 19.3pc). Figure A.3 shows the SNR per resolution bin and corresponding planet/star contrast spectra for a blackbody case, and Figure A.4 shows the change in SNR due to the presence of C_2H_2 in the atmosphere with a mixing ratio of 10^{-4}.

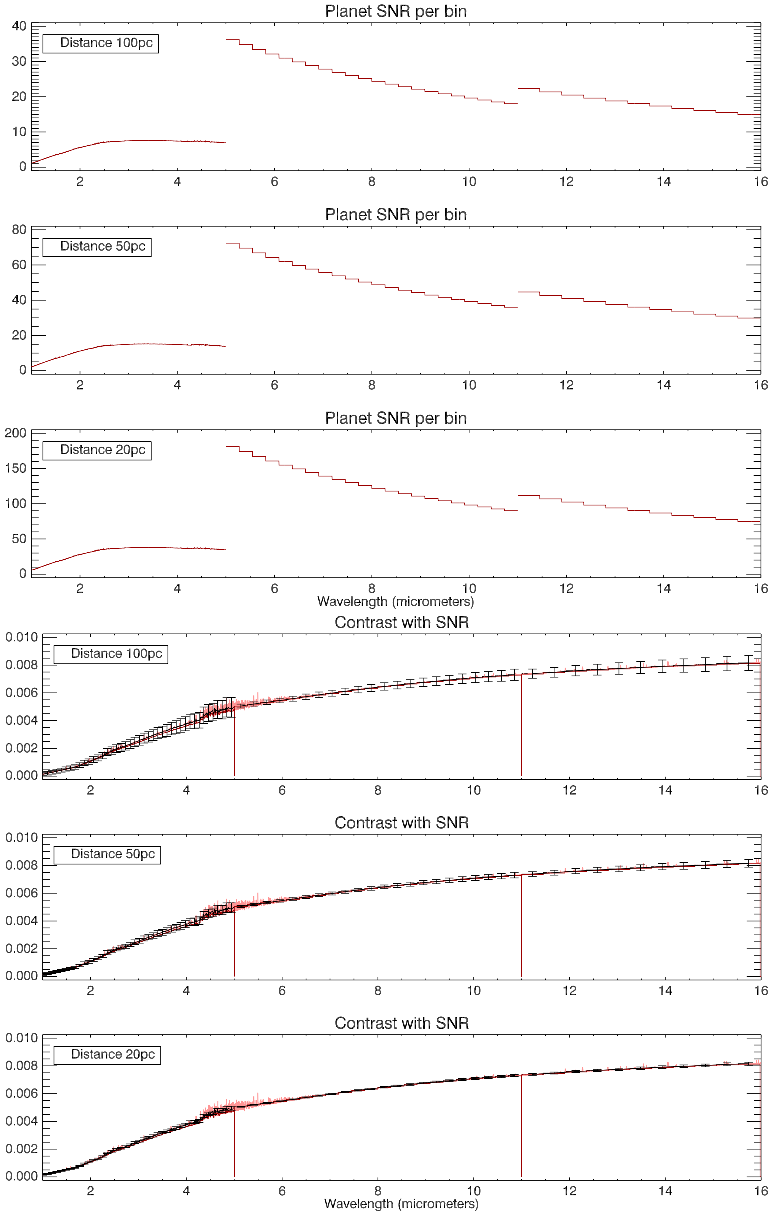

Figure A.3: A single transit of a hot Jupiter with no molecules absorbing. *Top:* SNR per resolution bin for a target located at 100, 50 and 20pc from the observer. *Bottom:* Planet/star contrast spectra with 1-sigma error bars.

A.0.8 Hot super-Earth

The planet/star surface ratio is less favorable here than the warm Neptune and hot Jupiter cases, however the temperature on this planet is assumed to be 2390 K, presenting a strong emission signal. The distances thus considered are 5, 10 and 20 pc (*55 Cnc* is located at 12.34 pc). The SNR per bin for a blackbody case is shown in Figure A.5 alongside the planet/star contrast spectra. The same planet is also shown with the presence of CO_2 in the atmosphere with abundance 10^{-4}, in Figure A.6. At a distance of 20pc, co-adding of

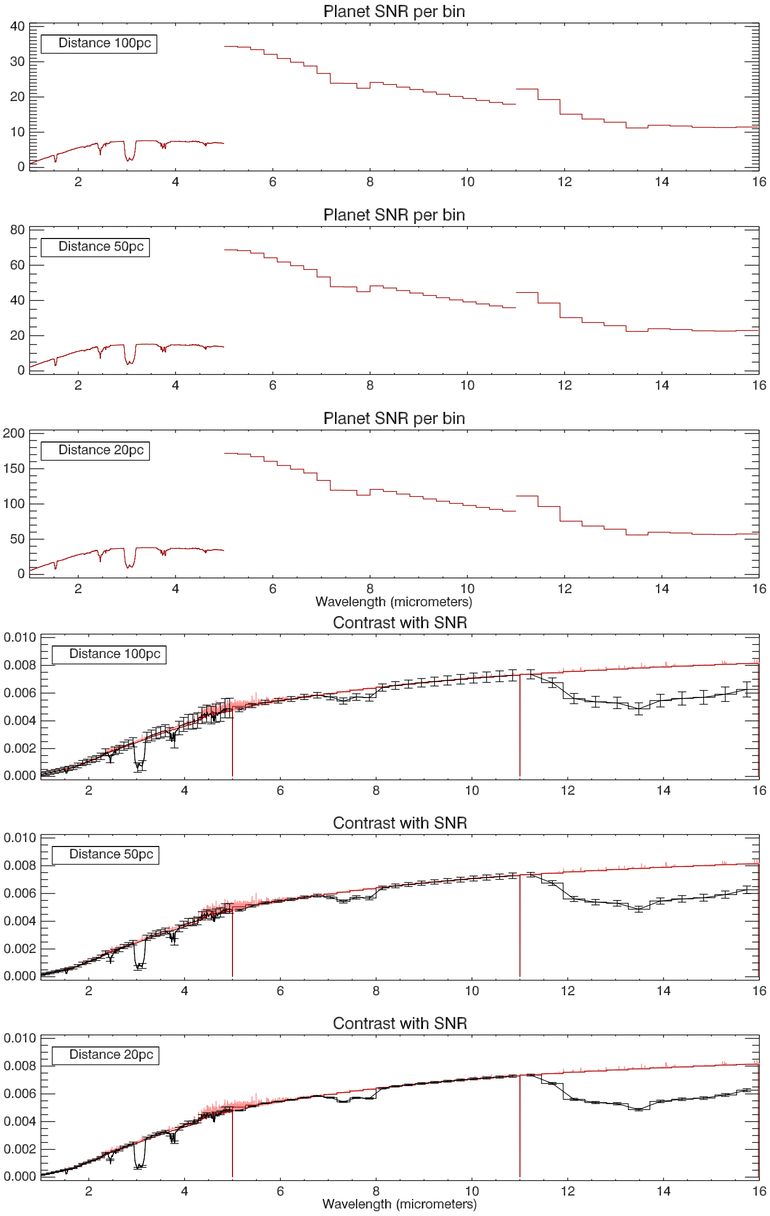

Figure A.4: A single transit of a hot Jupiter with C_2H_2 in the atmosphere (mixing ratio=10^{-4}). *Top:* SNR per resolution bin for a target located at 100, 50 and 20pc from the observer. *Bottom:* Planet/star contrast spectra with 1-sigma error bars.

transits will be necessary to obtain higher SNR values in the longer wavelength range: in Figure A.6, the signature of CO_2 at 10 μm gives a SNR per bin that is below 3. The 1 to 5 μm range will need to have multiple transits added to obtain higher SNR values, even for a close-by target.

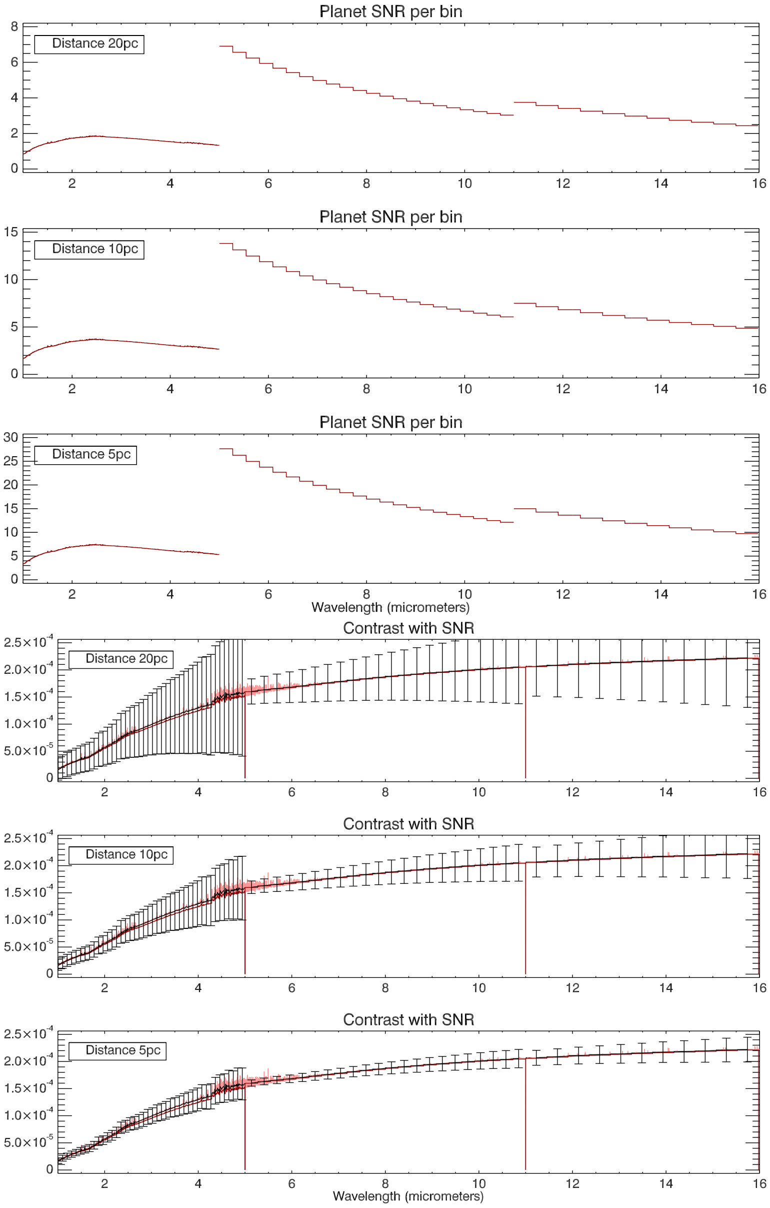

Figure A.5: A single transit of a hot super-Earth with no molecules absorbing. *Top:* SNR per resolution bin for a target at 20, 10 and 5pc. *Bottom:* Planet/star contrast spectra with 1-sigma error bars.

A.0.9 Temperate Jupiter

Of the five planet cases, the Temperate Jupiter has the strongest planet/star surface ratio. In addition, a single transit of this planet lasts 7.9 hours. This allows us to consider distances of 5, 10 and 20pc, for both a blackbody continuum planet (Figure A.7) and a planet with C_2H_2 at abundance 10^{-5} in the atmosphere (Figure A.8). The temperature of the planet at 320K will emit mostly around 10μm, and no signal will be visible at wavelengths below 5 μm. The more distant planets will require co-adding of transit

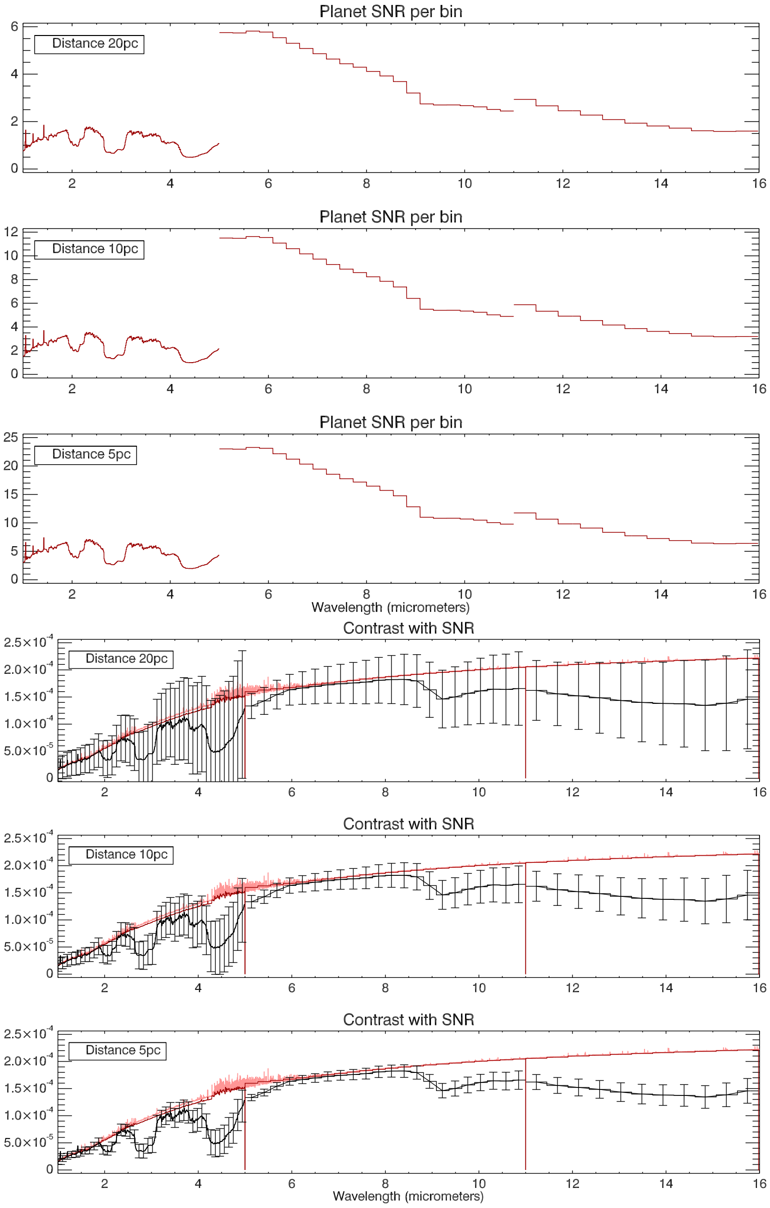

Figure A.6: A single transit of a hot super-Earth planet with only CO_2 in the atmosphere (abundance 10^{-4}). *Top:* SNR per resolution bin for a target at 20, 10 and 5pc. *Bottom:* Planet/star contrast spectra with 1-sigma error bars.

observations to reach SNR values of 5 to 10 in the 5 to 11 μm wavelength range.

A.0.10 Temperate super-Earth

We consider this planet to be a 1.8 Earth radii telluric planet orbiting a M4.5V star, with a surface ratio similar to the Warm Neptune case. However the smaller and dimmer star combined with a colder planet provide a weaker emission signal. In this case, a single transit can not be used, as the SNR values will be of the order of 10^0, illustrated in Figure

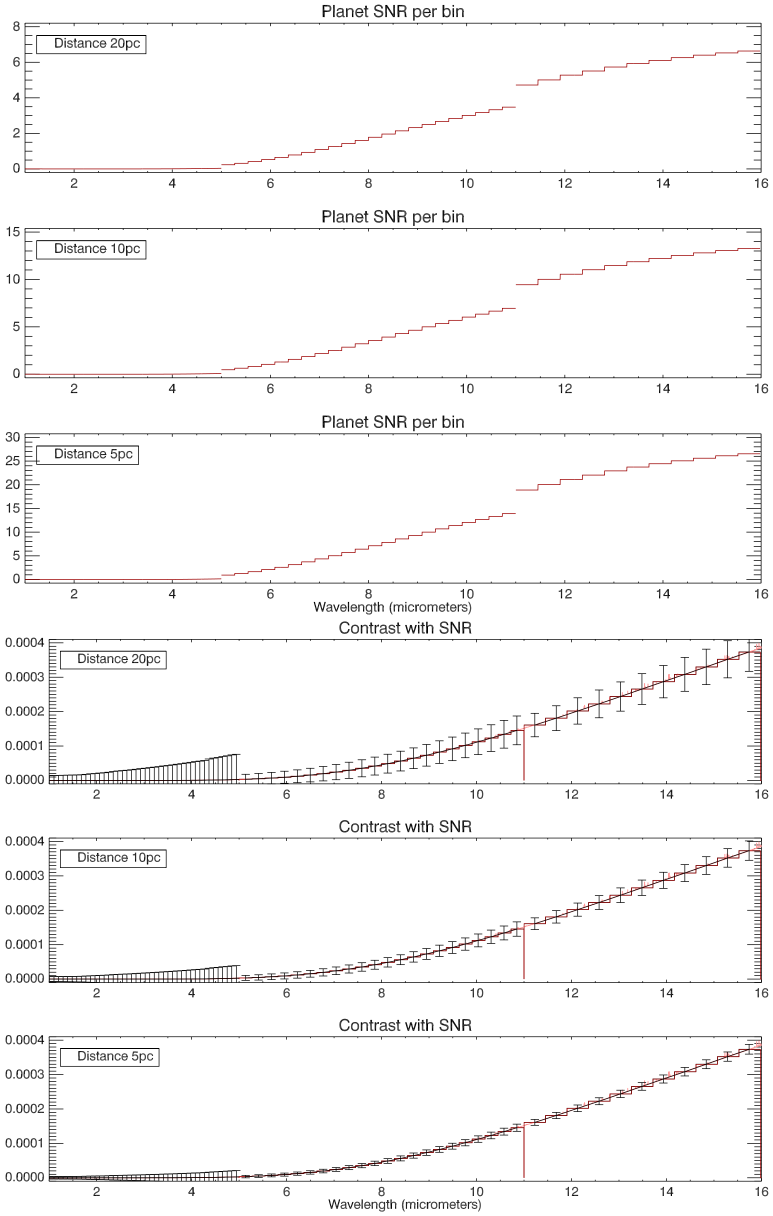

Figure A.7: A single transit of a Temperate Jupiter with no molecules absorbing. *Top:* SNR per resolution bin for a target at 20, 10 and 5pc. *Bottom:* Planet/star contrast spectra with 1-sigma error bars.

A.9, with a nearby (5pc) target. We present here the results of co-added transits (200) to obtain SNR values that are similar to the other target cases, for a target located at 5, 10 and 15 pc (Figure A.10). We show the SNR per resolution bin and the planet+star contrast spectra for a blackbody continuum planet and a planet with a CO_2 at abundance 1×10^{-4} atmosphere (Figure A.11). As in the Temperate Jupiter case, this planet has a temperature of 320K, with peak emission near 10 μm, and no emission signal will be visible below 5 μm. The resolution in the 5 - 16 μm range is lowered to 20, to maximise

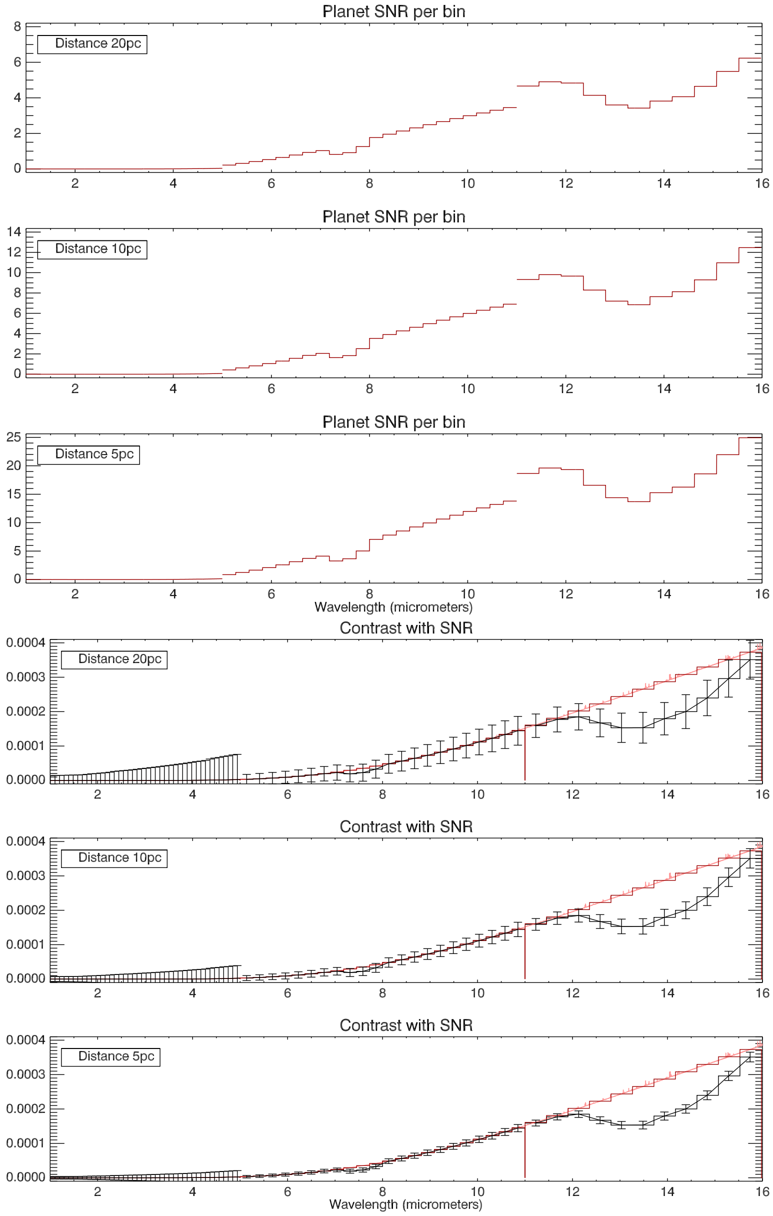

Figure A.8: A single transit of a Temperate Jupiter planet with only C_2H_2 in the atmosphere (abundance 1×10^{-5}). *Top:* SNR per resolution bin for a target at 20, 10 and 5pc. *Bottom:* Planet/star contrast spectra with 1-sigma error bars.

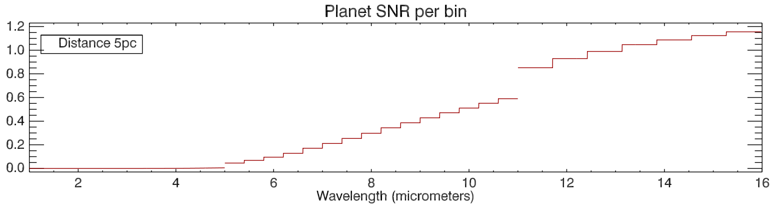

Figure A.9: A single transit of a temperate super-Earth planet with no atmosphere at 5pc. The SNR per bin is very low, and multiple transits will be needed for this type of target.

the number of photons.

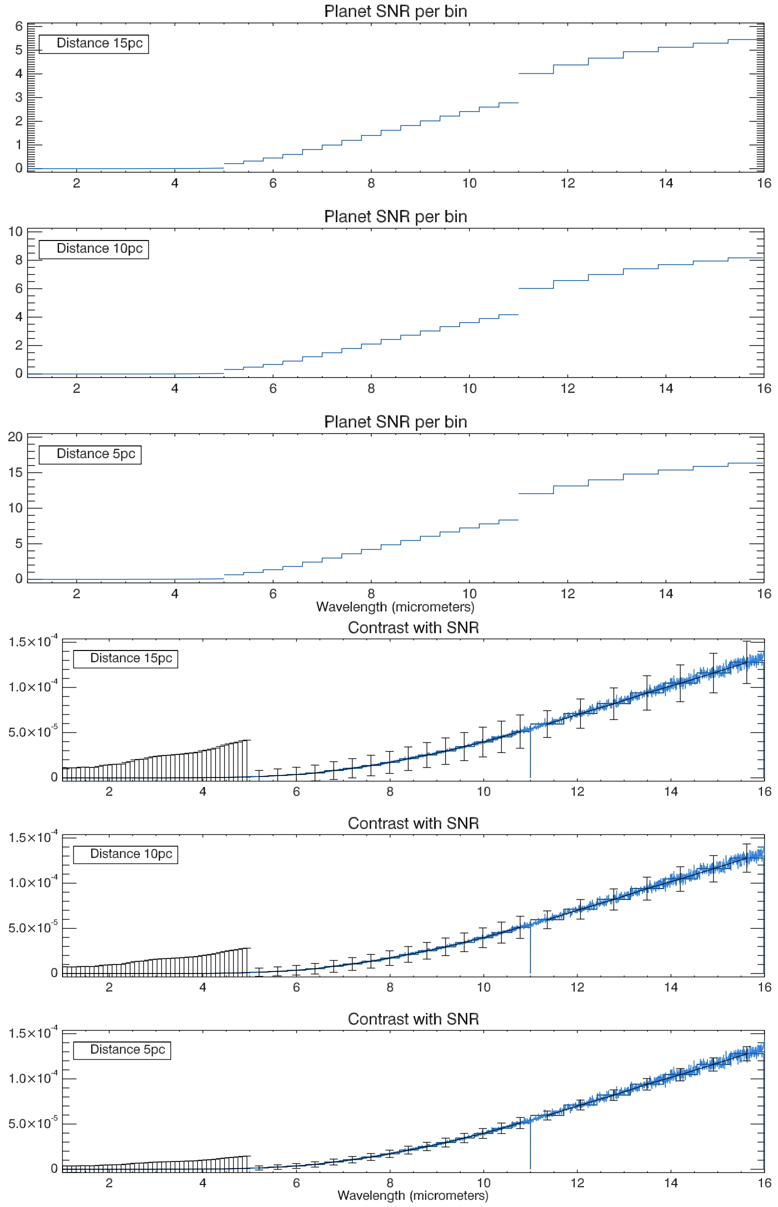

Figure A.10: 200 transits of a temperate super-Earth with no molecules absorbing. *Top:* SNR per resolution bin for a target at 15, 10 and 5pc. *Bottom:* Planet/star contrast spectra with 1-sigma error bars.

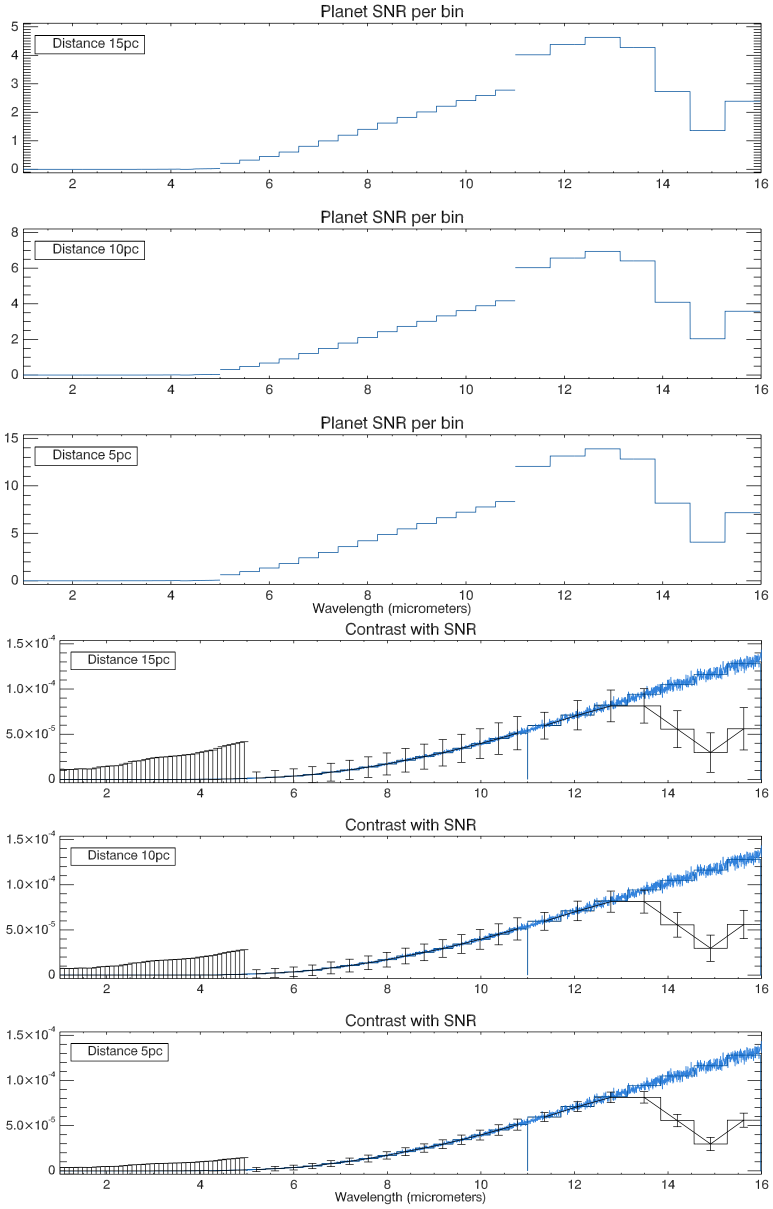

Figure A.11: 200 transits of a temperate super-Earth planet with only CO_2 in the atmosphere (abundance 1×10^{-4}). *Top:* SNR per resolution bin for a target at 15, 10 and 5pc. *Bottom:* Planet/star contrast spectra with 1-sigma error bars.

Appendix B

In addition to the numbers presented throughout chapter 4 for a 1.4m telescope, we provide here two supplementary sets of results for a 1.2m telescope. We detail in Table B.1 the parameters adopted for the two cases. The results are displayed in the following way: Number of transits: Case 1 *(Case 2)*.

Parameters for a 1.2m telescope	Case 1		Case 2
Detector used	SOFRADIR		RAYTHEON
	LWIR	VLWIR	JWST Si:As
Spectral range considered (μm)	5 - 11	11 - 16	5 - 16
Full well capacity (electrons)	$2 \cdot 10^7$	$5 \cdot 10^6$	$2 \cdot 10^5$
Dark current (electrons/s/pixel)	500	300	0.2
Quantum efficiency (electrons/photon)	0.7	0.7	0.7
Readout noise (electrons/pixel/readout)	1000	1000	15
Readout time (seconds)	0.03	0.01	3
Telescope temperature (K)	< 60	< 60	< 60
Instrument temperature (K)	45	45	45
Telescope transmission	0.9	0.9	0.85
Instrument transmission	0.7	0.7	0.4

Table B.1: List of parameters used in the two sets of appendix results. In the first case, two detectors are needed to cover the 5 to 16 micron range, while for the second set of results, which represents an alternate design of the instruments, one detector is used for the full range. The results are split into four columns representing wavelength bands used. The first column lists values in the photometric N band, which is also the band used for results presented throughout the paper, followed by three channels: 5 to 8.3 μm, 8.3 to 11 μm and 11 to 16 μm. A 30 μm pixel size and 2 illuminated pixels per spectral element are assumed (For the N band (7.7 to 12.7 μm) we have used the LWIR setting values). In the case of the VLWIR detector, we have used a dark current value of 300 electrons/s/pixel considering existing technologies and expected future capabilities. Further discussion on these values can be found in section 4.2.4.4.

B.0.11 1.2m telescope, Hot Planets

Bands:	N (7.7 to 12.7)	5 to 8.3	8.3 to 11	11 to 16
1) Contrasts:	1.01E-03	5.13E-04	8.34E-04	7.21E-04
V=5	9.56 *(15.71)*	12.62 *(21.22)*	13.60 *(22.38)*	41.05 *(58.11)*
V=6	25.29 *(39.49)*	32.30 *(53.31)*	35.94 *(56.21)*	111.60 *(157.43)*
V=7	71.63 *(99.33)*	84.94 *(133.92)*	101.47 *(141.22)*	LR *(LR)*
V=8	LR *(LR)*	LR *(LR)*	LR *(LR)*	LR *(LR)*
V=9	LR *(LR)*	LR *(LR)*	LR *(LR)*	LR *(LR)*
2) Contrasts:	5.56E-03	2.89E-03	4.61E-03	3.93E-03
V=5	0.21 *(0.36)*	0.27 *(0.50)*	0.30 *(0.50)*	0.90 *(1.28)*
V=6	0.54 *(0.89)*	0.67 *(1.13)*	0.77 *(1.26)*	2.35 *(3.33)*
V=7	1.44 *(2.24)*	1.73 *(2.84)*	2.04 *(3.18)*	6.42 *(9.05)*
V=8	4.12 *(5.64)*	4.55 *(7.14)*	5.80 *(7.98)*	19.33 *(27.07)*
V=9	13.42 *(14.23)*	12.76 *(17.95)*	18.81 *(20.06)*	68.83 *(95.35)*
3) Contrasts:	1.38E-04	8.61E-05	1.32E-04	1.69E-04
K=5	17.86 *(30.06)*	15.30 *(36.55)*	19.15 *(32.23)*	25.47 *(36.29)*
K=6	45.71 *(75.54)*	38.68 *(65.21)*	48.97 *(80.96)*	66.87 *(95.81)*
K=7	120.18 *(189.99)*	98.68 *(163.79)*	128.52 *(203.40)*	186.32 *(270.04)*
K=8	335.66 *(478.83)*	257.50 *(411.44)*	357.59 *(511.12)*	583.75 *(863.62)*
K=9	1056.31 *(1212.80)*	707.50 *(1033.57)*	1117.56 *(1285.18)*	LR *(LR)*
4) Contrasts:	1.22E-03	7.78E-04	1.17E-03	1.48E-03
K=5	0.63 *(1.06)*	0.51 *(1.23)*	0.67 *(1.13)*	0.90 *(1.29)*
K=6	1.61 *(2.66)*	1.28 *(2.16)*	1.72 *(2.84)*	2.73 *(3.40)*
K=7	4.23 *(6.69)*	3.27 *(5.44)*	4.51 *(7.13)*	6.60 *(9.56)*
K=8	11.82 *(16.87)*	8.54 *(13.65)*	12.54 *(17.92)*	20.63 *(30.52)*
K=9	37.19 *(42.72)*	23.42 *(34.30)*	39.18 *(45.07)*	77.42 *(117.64)*

Table B.2: 1: Integration times in number of transits for a hot Jupiter orbiting a F3.0V star. The four columns compare integration times in different bands for the same target. The contrast value and number of resolution elements are given for each band. The five rows list results for the specified star with varying magnitude (here in mag. V). The star temperature used is 6740 K, and the transit duration assumed is 2.90 hours. A spectral Resolution of 300 and a SNR value of 50 are used. A dash '-' signifies that the number of transits required is over the maximum number of transits that can be covered over a mission lifetime. 'LR' stands for Lower Resolution, and is indicated when observations need to be done at a lower spectral resolution to fit within the time constrains of a mission, and 'phot' stands for photometry at selected wavelengths, where lower resolution is not feasible.
2: Planet: Hot Jupiter, Star: K1V, temp: 4900K, R=300, SNR=50.
3: Planet: Hot SE, Star: M1.5V, temp: 3582K, R=40, SNR=10.
4: Planet: Hot SE, Star: M5V, temp: 3055K R=40, SNR=10.

B.0.12 1.2m telescope, Warm Planets

Bands:	N (7.7 to 12.7)	5 to 8.3	8.3 to 11	11 to 16
1) Contrasts:	4.61E-04	3.10E-04	4.10E-04	1.28E-03
K=5	19.39 *(32.52)*	14.12 *(27.06)*	23.82 *(39.97)*	5.31 *(7.57)*
K=6	49.84 *(81.74)*	35.75 *(60.11)*	61.18 *(100.40)*	14.03 *(20.07)*
K=7	132.40 *(205.61)*	91.55 *(151.00)*	162.21 *(252.24)*	39.56 *(57.18)*
K=8	378.10 *(518.31)*	241.00 *(379.32)*	461.30 *(633.88)*	126.66 *(186.27)*
K=9	LR *(LR)*	675.07 *(LR)*	LR *(LR)*	490.38 *(LR)*
2) Contrasts:	1.93E-04	7.12E-05	1.75E-04	2.94E-04
K=5	5.55 *(9.40)*	13.49 *(65.35)*	6.62 *(11.22)*	5.06 *(7.22)*
K=6	14.08 *(23.63)*	34.00 *(65.35)*	16.79 *(28.18)*	13.13 *(18.86)*
K=7	36.22 *(59.41)*	86.06 *(144.73)*	43.14 *(70.78)*	35.62 *(51.91)*
K=8	96.34 *(149.68)*	220.38 *(363.54)*	114.42 *(177.86)*	106.09 *(159.04)*
K=9	275.81 *(378.73)*	580.07 *(LR)*	325.63 *(447.17)*	371.25 *(580.26)*
3) Contrasts:	3.29E-04	1.22E-04	2.98E-04	4.98E-04
K=5	2.46 *(4.17)*	5.86 *(28.50)*	2.93 *(4.96)*	2.25 *(3.21)*
K=6	6.24 *(10.47)*	14.76 *(28.51)*	7.43 *(12.47)*	5.84 *(8.39)*
K=7	16.05 *(26.33)*	37.36 *(62.82)*	19.09 *(31.32)*	15.84 *(23.08)*
K=8	42.69 *(66.33)*	95.65 *(157.81)*	50.62 *(78.69)*	47.15 *(70.67)*
K=9	122.22 *(167.84)*	251.71 *(396.40)*	144.07 *(197.85)*	164.88 *(257.66)*

Table B.3: See Table B.2 for additional explanation.
1: Planet: Warm Neptune, Star: M2.5V, temp: 3480K, R=50, SNR=30.
2: Planet: Warm SE, Star: M4V, temp: 3230K, R=20, SNR=10.
3: Planet: Warm SE, Star: M5V, temp: 3055K, R=20, SNR=10.

B.0.13 1.2m telescope, HZ Planets

Bands:	N (7.7 to 12.7)	5 to 8.3	8.3 to 11	11 to 16
1) Contrasts:	1.53E-04	2.12E-06	1.27E-04	1.58E-04
V=5	0.35 *(1.86)*	phot *(-)*	0.49 *(2.70)*	0.69 *(1.75)*
V=6	0.87 *(1.86)*	- *(-)*	1.24 *(2.70)*	1.74 *(2.47)*
V=7	2.21 *(3.72)*	- *(-)*	3.12 *(5.26)*	4.44 *(6.32)*
V=8	5.65 *(9.36)*	- *(-)*	7.98 *(13.22)*	11.63 *(16.66)*
V=9	14.83 *(LR)*	- *(-)*	LR *(LR)*	LR *(LR)*
2) Contrasts:	3.54E-05	4.97E-06	2.89E-05	8.15E-05
K=5	11.60 *(36.69)*	phot *(-)*	16.91 *(59.39)*	4.60 *(7.84)*
K=6	29.28 *(52.81)*	phot *(-)*	42.68 *(76.96)*	11.87 *(18.20)*
K=7	74.47 *(132.80)*	- *(-)*	108.43 *(phot)*	31.75 *(49.50)*
K=8	phot *(-)*	- *(-)*	phot *(-)*	92.00 *(phot)*
3) Contrasts:	8.46E-05	1.21E-05	6.92E-05	1.93E-04
K=5	2.95 *(10.42)*	47.51 *(-)*	4.29 *(15.55)*	1.18 *(2.08)*
K=6	7.46 *(13.87)*	119.51 *(-)*	10.83 *(20.15)*	3.04 *(4.81)*
K=7	18.96 *(34.87)*	phot *(-)*	27.53 *(50.61)*	8.13 *(13.07)*
K=8	49.10 *(87.83)*	phot *(-)*	71.12 *(127.18)*	23.53 *(39.10)*
K=9	132.62 *(222.11)*	- *(-)*	191.12 *(phot)*	78.75 *(137.79)*

Table B.4: See Table B.2 for additional explanation.
1: Planet: HZ Jup, Star: K4V, temp: 4780K, R=40, SNR=10.
2: Planet: HZ SE, Star: M4V, temp: 3230K, R=10, SNR=5.
3: Planet: HZ SE, Star: M5.5V, temp: 2920K, R=10, SNR=5.

Appendix C

Updated Results for the EChO Payload Design

The Exoplanet Characterisation Observatory (EChO) is a proposed 1.2m space-based telescope currently under study at the European Space Agency, as a M class mission part of the Cosmic Vision programme (Tinetti *et al.* 2012a). EChO will provide simultaneous, multi-wavelength spectroscopic observations on a stable platform for a wide selection of exoplanets, from the visible to the mid-infrared. In Tessenyi *et al.* (2012a) we have studied the feasibility and general performance of an EChO like mission for a broad selection of targets. In that paper, we considered a number of instrument tradeoffs, which included two telescope sizes and several possible choices for the detector technology. In this study, published in Tessenyi *et al.* (2012b), we focus on the performances of our most recent payload design, studied during the assessment phase by our instrument consortium (Swinyard *et al.* 2012; Reess *et al.* 2012). The updated instrument design consists of a 1.2m telescope and detector settings which are listed in Table C.1. Further studies will include results from EChOSIM Waldmann *et al.* (2013a), an end-to-end instrument simulator currently under development by our instrument consortium.

Instrument Values	Visible	2.5 to 5 μm	5 - 11 μm	11 to 16 μm
Detector used	MCT	MCT	Si:As	Si:As
Full well capacity (electrons)	$2 \cdot 10^6$	$4 \cdot 10^6$	$2 \cdot 10^5$	$2 \cdot 10^5$
Dark current (electrons/s/pixel)	0.1	10	0.2	0.2
Quantum efficiency (electrons/photon)	0.5	0.7	0.7	0.7
Readout noise (electrons/pixel/readout)	10	400	15	15
Readout time (seconds)	0.004	0.01	3	3
Telescope temperature (K)	-	60	60	60
Instrument temperature (K)	-	45	45	45
Detector temperature (K)	170	< 45	7	7
Telescope transmission	0.86	0.86	0.86	0.86
Instrument transmission	0.7	0.32	0.35	0.35

Table C.1: Instrument settings used in our simulations, listed for each observing band used. In addition, the two following settings are the same for all four bands considered: a 30 μm pixel size and 4 illuminated pixels per spectral element are assumed.

C.1 Planets considered

In Tessenyi *et al.* (2012a) a wide variety of target cases are considered, here the focus is on four key cases: a Hot Jupiter and Warm Neptune as examples of gaseous planets (HD 189733b and GJ 436b, respectively), and a Hot super-Earth and temperate super-Earth (Cnc 55 e and a possible 1.8 $R_\oplus$, 5 $M_\oplus$ super-Earth in the habitable-zone of a M dwarf). The parameters assumed for these targets are listed in Table C.2.

Star	Hot Jupiter	Warm Neptune	Hot super-Earth	Temperate super-Earth
Spectral Type	K1V	M2.5V	G8V	M4.5V
Radius ($R_\odot$)	0.8	0.464	0.95	0.22
Mass ($M_\odot$)	0.8	0.452	0.91	0.22
Temperature (K)	4980	3684	5196	3300
Planet				
Radius (R_{jup} — $R_\oplus$)	1.138 — 12.77	0.365 — 4.10	0.194 — 2.18	0.16 — 1.8
Temperature (K)	1350	750	2390	250
Semi-major axis (au)	0.031	0.029	0.016	0.046
Period (days)	2.219	2.644	0.737	7.64
Transit duration (hr)	1.83	1.03	1.76	1.39

Table C.2: Star and planet parameters assumed for the selected targets of this study. The planet radii are given both in units of Jupiter radius and Earth radius, and the temperatures listed are an average temperature from the temperature-pressure profile.

Where possible, the spectra of the planets presented are modelled atmospheres, and blackbody curves are used when no observational data is available. Figure C.1 shows the planet/star flux ratio (contrast) of the Hot Jupiter and the Warm Neptune, which were obtained using radiative transfer codes as described in Tessenyi *et al.* (2012a). These simulations either fit existing observations (e.g., Knutson *et al.* (2007a); Tinetti *et al.* (2007); Charbonneau *et al.* (2008); Grillmair *et al.* (2008); Swain *et al.* (2008b); Stevenson *et al.* (2010); Beaulieu *et al.* (2011)) or are an extrapolation from our knowledge of Solar System planets.Figure C.2 shows the contrast values used for the Hot and Temperate super-Earths. For the Hot super-Earth case, the planet temperature is expected to be

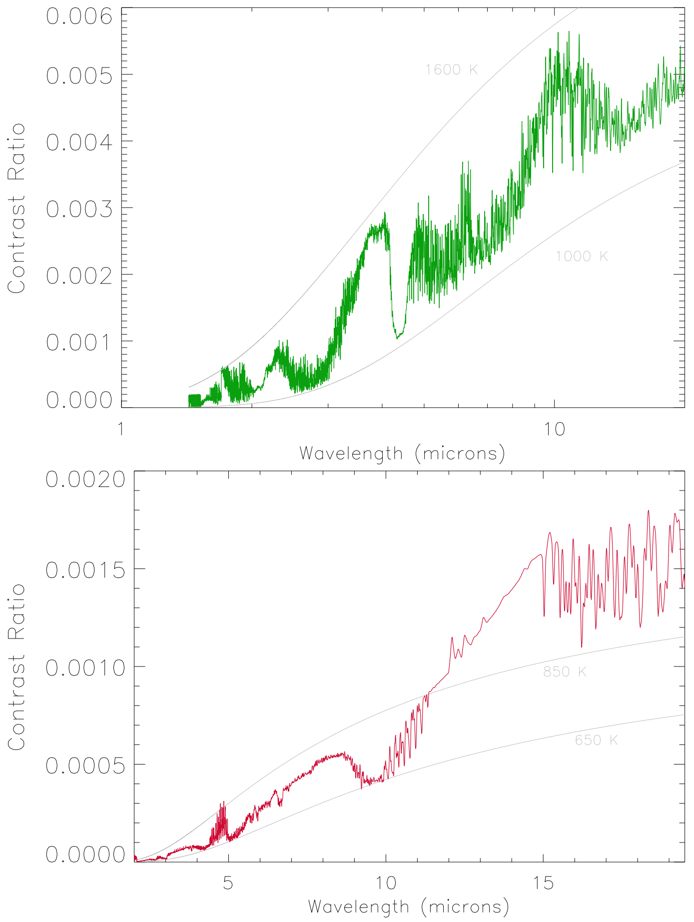

Figure C.1: *Top:* Modeled emission spectrum of HD 189733b (Tessenyi *et al.* 2012a), a hot-Jupiter around a K1/2V star, mag. V=7.67, presented as planet/star flux ratio. Blackbody curves at 1000 K and 1600 K are plotted in grey for indication. *Bottom:* Modeled planet/star flux ratio of GJ 436b (Tessenyi *et al.* 2012a), a warm Neptune orbiting a M2.5V star, with 650 K and 850 K blackbody curves plotted for indication.

between 1980 and 2800 K, depending on the heat redistribution on the planet (Winn *et al.* 2011). For the integration time calculations, a mean temperature of 2390 K is used. For the

Temperate super-Earth three possible atmospheres are presented: an Earth-like, Venus-like and a Small Neptune-like spectrum, reflecting the effect of atmosphere compositions on the emitted signal. An average temperature of 300 K, fitting within the temperature range of the atmosphere types, is used as planet/star flux ratio. These Temperate super-Earths will be the most challenging targets to observe, with flux ratios in the $10^{-5} - 10^{-4}$ range, and will require low resolution observations. The spectra presented for this target in Figure C.2 are set at R=20.

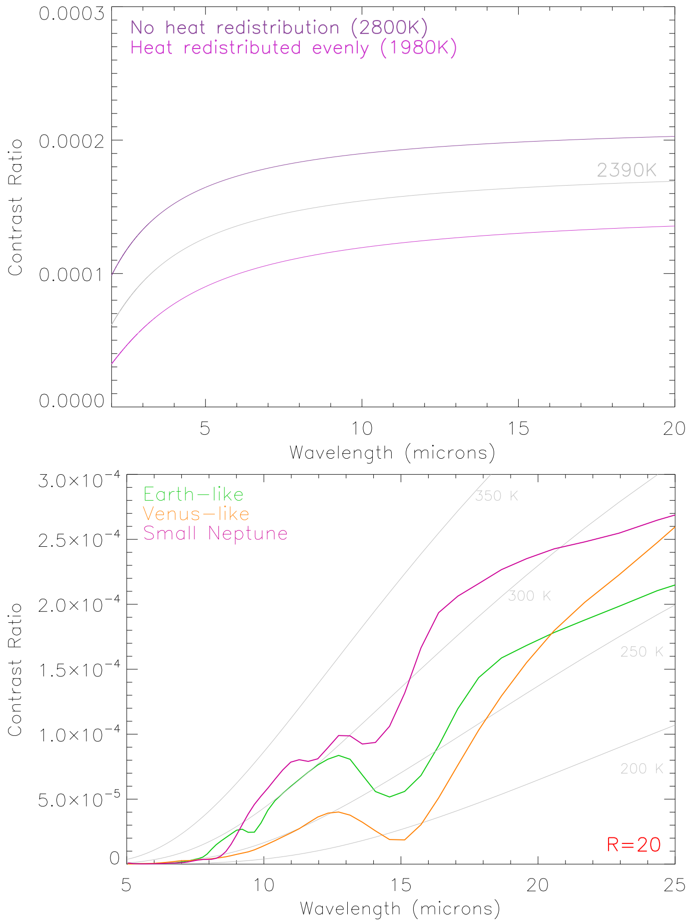

Figure C.2: *Top:* Blackbody planet/star flux ratio for Cnc 55 e, a 2.1 $R_{\oplus}$ Hot super-Earth, orbiting a G8V star. The planet temperature is estimated to be between the 2800 K and 1980 K limits, depending on the heat redistribution in the atmosphere (Winn *et al.* 2011). A mean temperature of 2390 is used for this study. *Bottom:* Low resolution (R=20) Earth-like, Venus-like and Small Neptune-like planet/star flux ratio for a possible 1.8 $R_{\oplus}$ Temperate super-Earth, orbiting a 3150 K M4.5V star. The three spectra show possible atmospheric types that could exist in this temperature regime. An average temperature of T=300 K is used for our calculations.

C.2 Updated results

Hot Jupiter – Secondary eclipse, SNR=5

Channel range	λ (μm)	Res. Power	Contrast ($*10^{-3}$)	Integration time (n. transits)				
				V=5	V=6	V=7	V=8	V=9
1-5	3	300	0.40	0.1	0.2	0.5	1.4	3.5
5-11	7.5	30	2.77	< 0.1				
11-16	13.5	30	3.93	< 0.1				

Secondary eclipse, SNR=50

Integration time (n. transits)				
V=5	V=6	V=7	V=8	V=9
9	22	55	138	348
0.3	0.3	0.5	1.2	3
0.2	0.4	1	2.5	7

Warm Neptune – Secondary eclipse, SNR=5

Channel range	λ (μm)	Res. Power	Contrast ($*10^{-3}$)	Integration time (n. transits)				
				K=5	K=6	K=7	K=8	K=9
1-5	3	300	0.02	351	*Lower Resolution*			
5-11	7.5	30	0.45	0.3	0.7	1.9	5	12
11-16	13.5	30	1.28	0.2	0.4	1.1	3.2	11

Secondary eclipse, SNR=25

Integration time (n. transits)				
K=5	K=6	K=7	K=8	K=9
Lower Resolution				
8	19	47	117	293
3.8	10	27	80	277

Table C.3: **Top:** Hot Jupiter integration times (in units of "number of transits") needed to obtain the specified SNR (5 and 50) per channel for a given brightness (in Mag. V), with a 0.8 $R_\odot$, K1V star at 4980 K. For the SNR=5 requirement this planet case is easy to observe. The SNR=50 requirement requires adding up of observations, mostly due to the higher resolution required in the first channel. Within the proposed 5 year mission lifetime, this planet will complete 826 orbits. **Below:** Integration times (in units of "number of transits") for a Warm Neptune, orbiting a M2.5V star at 3150 K. Results are given per channel for two SNR cases (5 and 25) and a given brightness (in Mag. K). For this target, in the 1-5 μm channel, binning of the signal to a lower resolution will be required to obtain enough photons, as the contrast is low in this band. In 5 years this planet will complete 691 orbits.

Hot super-Earth – Secondary eclipse, SNR=5

Channel range	λ (μm)	Res. Power	Contrast ($*10^{-4}$)	Integration time (n. transits)				
				V=5	V=6	V=7	V=8	V=9
1-5	3	300	0.94	2	4.9	13	31	78
5-11	7.5	30	1.45	1	1	2.2	6	14
11-16	13.5	30	1.62	1.1	2.8	7	19	51

Secondary eclipse, SNR=25

Integration time (n. transits)				
V=5	V=6	V=7	V=8	V=9
49	122	307	771	1944
26	26	54	135	339
28	69	176	460	1268

Temperate super-Earth – Secondary eclipse, SNR=5

Channel range	λ (μm)	Res. Power	Contrast ($*10^{-4}$)	Integration time (n. transits)				
				K=5	K=6	K=7	K=8	K=9
5-11	7.5	10	0.13	159	214	*Photometry*		
11-16	13.5	10	1.06	6	14	39	115	*Ph.*

Table C.4: **Top:** Hot super-Earth integration times (in units of "number of transits") needed to obtain the specified SNR (5 and 25) per channel for a given brightness (in Mag. V), with a 0.95 $R_{\odot}$, G8V star at 5196 K. As the Hot Jupiter, with the SNR=5 requirement this planet case is easy to observe. The SNR=25 requirement requires adding up of observations, mostly due to the higher resolution required in the first channel. Within the proposed 5 year mission lifetime, this planet will complete 2467 orbits. **Below:** Integration times (in units of "number of transits") for a Temperate super-Earth, orbiting a M4.5V star at 3300 K. Results are given per channel with an SNR=5, resolution of 10 and a given brightness (in Mag. K). For this target the 1-5 μm channel is not used as a 300 K blackbody object will emit no radiation below $\sim 5\mu m$. Given the lower contrast values for this target, only the SNR=5 case is considered, and for the more distant stars, photometry may be required to observe a target. In 5 years this planet will complete 239 orbits.

The results are given as integration times in number of transits required (integration time divided by the transit duration) in Tables C.3 and C.4. The computed contrast value is sampled at three different wavelengths: 3, 7.5 and 13.5 μm, for a wavelength bin corresponding to a single resolution element of the channel (resolving power 300, 30 and 30 for the three channels, respectively). The integration time is computed in the bins for a range of stellar magnitudes, either in V mag of K mag, with the given contrast and a desired signal-to-noise ratio(SNR) value. A minimum SNR=5 setting is used for all targets, and where the signal permits, higher SNR integration times are presented. Table C.3 shows the results for the Hot Jupiter and the Warm Neptune cases, and Table C.4 presents the results for the Hot and Temperate super-Earths.

C.3 Conclusions

We have presented updated results of our previous work estimating the performance of EChO, building on the evolution of the instrument design. We have shown that with a 1.2m space-based telescope and an updated payload design, key cases of transiting exoplanets can be observed spectroscopically from the visible to the mid-infrared, with a choice of SNR/resolution observation modes. These updated results confirm the strengths of EChO: a wide range of planet types can be observed within 5 years, with the flexibility of observing bright targets either at high accuracy or repeatedly at lower SNR and resolution. The repeated observation of bright targets will allow the study of atmospheric circulations, or the “slicing” of planet observations to map the planet surface during ingress and egress, maximising the science return of the mission. Challenging targets such as Temperate super-Earths can be observed with lower SNR/resolution, provided they orbit close-by and late type M dwarfs. Overall, EChO will provide full emission (and transmission) spectra from the visible to the mid-infrared for a wide variety of targets, contributing to the advancement of this new, exciting field.

Appendix D

Source code of TAU

This appendix reproduces the code TAU that was published in Hollis *et al.* (2013), and which is available for download at `http://www.ucl.ac.uk/exoplanets/`. My personal contribution was writing the first version of the code, which contained the setup of the geometrical path, and worked as a simple case of absorption by one molecule without scattering contributions. The code was then significantly improved by Morgan D. J. Hollis, who added support for: multiple-molecules, Rayleigh scattering, collision-induced absorption coefficients, cloud coefficients, and finally openMP functions for parallelisation.

D.0.1 Tau.cpp

```
/*******************************************************************************
** TAU.CPP - Marcell Tessenyi 2011 - v0.1
**                   - Morgan Hollis 2012 - v1.8c
**
**
** This code is a 1D radiative transfer code for transmission spectroscopy of
**      extrasolar planets. It uses a line-by-line integration scheme to model
**      transmission of the radiation from a parent star through the atmosphere of an
**      orbiting planet, in order to compare to observations of the radius ratio as a
**      function of wavelength in primary transit, and hence to infer the abundances of
**      trace absorbers present in the planetary atmosphere.
**
** The code reads in an atmospheric profile and absorption cross-sections (filenames
**      input by user on prompt) for the required absorbers and calculates the optical
**      path length exp(-tau) in the transit geometry, outputting the transit depth
**      (radius ratio) as a function of wavelength.
**
** Run './tau' to display usage instructions and run modes.
**
**
```

```
** INPUTS:  - atmospheric temperature-pressure profile file, e.g. ”profile.atm”
**                              10-line header, then 39 atmosphere levels,
**                              column 1: Pressure, in Pascal
**                              column 2: Temperature, in Kelvin
**                              column 3: Altitude, in kilometres
**
**                      - absorption cross-section files, e.g. ”molecule1.abs”
**                              one per molecule/absorber, containing,
**                              column 1: wavelength (in microns)
**                              column 2: absorption cross-section (in cm^2)
**
**                      - [OPTIONAL] stellar radius as a function of wavelength, e.g. ”rad_star.rad”
**                              with,
**                              column 1: wavelength (in microns)
**                              column 2: stellar radius (in m)
**
**                              N.B. if this option is used (and sw_rad set), the user must ensure that
**                                      the designated file wavelength values span the entire specified
**                                      wavelength range for the model, in order for the interpolation to
**                                      function correctly.
**
**                      - [OPTIONAL] H2-H2 Collision-Induced Absorption coefficient file,
**                              e.g. ”h2_h2_1000K.cia”, with,
**                              column1: wavelength (in microns)
**                              column2: absorption coefficient (in cm^-1 amagat^-2)
**
**                      - [OPTIONAL] opacities from cloud models if available, e.g. ”cloud1.cld”
**                              formatted as,
**                              column 1: wavelength (in microns)
**                              column 2: mass opacities (in cm^2 g^-1)
**
**
** OUTPUT:      - ”tau_output.dat” - file containing wavelengths (column 1, in microns) and
**                                                              absorption/radius ratio (column 2, dimensionless).
**
**
** For more details, see M. D. J. Hollis et al., ”TAU: A 1D radiative transfer code
**      for transmission spectroscopy of extrasolar planet atmospheres”. Comp. Phys. Comm.
**      (2013).
**
** Email mdjh@star.ucl.ac.uk with any questions or bugs, and I'll try to help!
**
************************************************************************************/
#include ”functions.h”

int main(int argc, char *argv[])
{
/*************************** Define run variables ******************************/
const double prog_start=omp_get_wtime();


   /* Run parameters */
   const float rad_fac=-0.0;            // increase planet radius by (rad_fac)%
                                                                //      i.e. rad_fac > 0
                                                                        for input Rp lowers
                                                                        radius @ 1bar

   const float s_rad_fac=+0.0;          // increase stellar radius by (s_rad_fac)%
```

```
double lambda_min=0.00;               // define wavelength range for model (in microns)
double lambda_max=20.00;

float lambda_res=0.01;                        // resolution of new wavelength grid (o/p
     spectrum) in microns
//    if(lambda_max>lambda_min) lambda_res = (lambda_max-lambda_min) / 2000.0;

const float mixdef = 1.0e-5;                  // default mixing ratio value


/* System parameters - e.g. for HD189733b..... */
const float Rp =  1.138 *(1. - (rad_fac/100.)) *RJUP; // planet radius @ 1bar level: *Jupiter
      radius (m)
const float Rstar =  0.788 *(1. - (s_rad_fac/100.)) *RSOL; // stellar radius: *Sun radius (m)
const float semimajor = 0.03142 *AU; // semi-major axis: *1 AU (m)

const float grav=23.45;                       // gravitational acceleration at planetary
     surface (m s^-2)
const float temp=1500;                        // atmospheric temperature (K)


/* Atmosphere parameters */
Atmos atmos;

const Mol H2("H2",2.0,2.0e-9,1.0001384);              // define possible bulk atmosphere
     constituents
const Mol He("He",4.0,1.0e-9,1.0000350);

atmos.ADD_MOL(H2,0.85);               // add molecules to atmosphere, with corresponding mass
     mixing ratios (fractional abundances), such that sum = 1
atmos.ADD_MOL(He,0.15);

if( atmos.CHECK_ATMOS() ) atmos.GET_MMW();    // check composition adds up to 100% and get
     mean relative molecular weight of atmosphere
else {
     cout<< "WARNING:␣Bulk␣atmosphere␣composition␣doesn't␣add␣up!" <<endl;
     exit(1);
}
              // ...to calculate atmospheric scale height (km)
const float H = (RGAS * temp) / (atmos.mu * grav);


/* Filenames and switches for external file inputs (0=off, 1=on) */
const int sw_rad=0;           // Vary stellar radius with wavelength
const int sw_cia=0;           // Include H2-H2 CIA
const int sw_cld=0;           // Read in extra optical depths due to clouds, set switch to
     equal number of files to be read in


const char* rad_file={"./run/rad_star.rad"};          // file from which to read stellar
     radius R*(lambda)

const char* cia_file={"./run/h2_h2_1500K.cia"};       // file from which to read CIA
     coefficients

const char* cld_file[]={"./run/cloud1.cld"};          // files from which to read optical
     depths for extra opacities (e.g. clouds)


string arg_outFile = "./out/tau_output.dat";          // file to contain final spectrum
```

```
/***************************** Sorting options *******************************/
  string arg_atmFile;
  vector<string> arg_btFile;

  char *atmFile, *outFile;
  vector<char*> btFile;
      // multiple abs file inputs possible --> vector CONTAINING some number of pointers to
          chars
      //vector<char> *btFile;          whereas this would be one pointer TO a vector containing
           chars


  int option=0;

  if (argc > 1) option = atoi (argv[1]); // arg-to-int: convert character from 1st argument to
      integer
  else {
   cout << "\nPlease␣use␣option␣'0',␣'1'␣or␣'9'.\n" << endl;
   instructions(argv[0]); // if no arguments provided at program execution, display usage
       instructions
  }

  optionSort(option,argc,argv,arg_btFile,arg_atmFile);


  /* Assign and check some run parameters */
  int n_gas=arg_btFile.size();
      if( !n_gas ) cout<<"No␣molecules␣entered!␣"<<endl;

  const int n_cld=sw_cld;

  cout << endl << "Files␣used:\n␣Atm:␣" <<"\t"<< arg_atmFile <<"\n"<< "␣Abs:␣";
  for(int i=0;i<arg_btFile.size();i++) cout<<"\t"<< arg_btFile[i] <<endl;

  if(sw_rad) cout<< "␣R*:␣"<<"\t"<< rad_file <<endl;
  if(sw_cia) cout<< "␣CIA:␣"<<"\t"<< cia_file <<endl;
  if(sw_cld){
             cout<< "␣Cld:␣";
             for(int i=0;i<n_cld;i++) cout<<"\t"<< cld_file[i] <<endl;
  }

  cout<< "␣n_gas␣=␣"<<n_gas <<endl;
  cout<<endl<< "␣O/P:␣" <<"\t"<< arg_outFile << endl;

  float thres = 50.0 * (atmos.mol_list[0].radius * 1.0e6);          // NB converting
      particle radius to microns
  if(lambda_min<thres){
      cout<< "\nWARNING:␣Rayleigh␣scatter␣not␣calculated␣for␣wavelengths␣below␣"<<thres<<"␣
          microns!" <<endl;
  }

  cout<<endl;


  /* Convert string type to char array (to pass to functions) */
  atmFile=new char[arg_atmFile.size()+1];
  atmFile[arg_atmFile.size()]=0;
  memcpy(atmFile,arg_atmFile.c_str(),arg_atmFile.size());

  for(int i=0;i<arg_btFile.size();i++){
             btFile.push_back(new char[arg_btFile[i].size()+1]);
             btFile[i][arg_btFile[i].size()]=0;
```

```
                memcpy(btFile[i],arg_btFile[i].c_str(),arg_btFile[i].size());
    }

    outFile=new char[arg_outFile.size()+1];
    outFile[arg_outFile.size()]=0;
    memcpy(outFile,arg_outFile.c_str(),arg_outFile.size());





/***************************** Get data from .abs file(s) *******************************/

    /* Create array of data vectors for wavelengths and abs coeffs for 'n_gas' gases */
    vector<vector<double> > sigma_array;

    sigma_array.resize(n_gas+1);          // resize to height=n_gas+2

    /* Interpolate cross-sections to same wavelength grid */
    if(lambda_min<TINY) lambda_min=TINY;          // avoid potential zero division errors in
        scattering functions
    if(lambda_max>VBIG) lambda_max=VBIG;
    interpolateAbs(btFile,sigma_array,lambda_min,lambda_max,lambda_res,n_gas);


    vector<double> &gridwl=sigma_array[0];        // i.e. top row for wavelengths, and each middle
         row is a different gas
    int linecount = gridwl.size();
    cout<<"\nNew␣linecount:␣"<<linecount<<endl;
        // even though this is now number of columns in sigma_array



    /* Interpolate CIA coefficients etc. to the model wavelength grid */
    vector<double> rad_star, cia_coeffs;          // vectors for stellar radius, CIA coefficients
        as a function of wavelength

    vector< vector<double> > cld_coeffs;          // vector for cloud optical depths, one row for
        each cloud file
    cld_coeffs.resize(n_cld);




    for(int i=0;i<linecount;i++) rad_star.push_back(Rstar);              // stellar radius
        constant with wavelength if not read in from file
        if(sw_rad) interpolateCS(rad_file,gridwl,rad_star);


    for(int i=0;i<linecount;i++) cia_coeffs.push_back(0.0);              // CIA has no effect if
        no file input
        if(sw_cia) interpolateCS(cia_file,gridwl,cia_coeffs);


    for(int n=0;n<n_cld;n++){
        // clouds have no effect if no file input
                for(int i=0;i<linecount;i++) cld_coeffs[n].push_back(0.0);
    }
    double low_p_bound[n_cld], up_p_bound[n_cld];

        if(sw_cld){
                for(int n=0;n<n_cld;n++){
                        low_p_bound[n]=1.0e-3;          // pressure (in bar) of lower pressure/
                            upper altitude cloud bound
```

```
                        up_p_bound[n]=0.1e0;            // pressure (in bar) of upper pressure/
                             lower altitude cloud bound
                                 // set cloud vertical extent

                        interpolateCS(cld_file[n],gridwl,cld_coeffs[n]);
                }
        }




/**************************** Get data from .atm file *******************************/

   int nlayers = getNumberLines(atmFile);                // number of usable lines from atm file
   cout << endl << "Number␣of␣layers␣from␣file:␣" << nlayers << endl;


   /* For each level, get..... */
   float p[nlayers];                       // pressure (in Pascal)
   float Tp[nlayers];                      // temperature (in Kelvin)
   float z[nlayers];                       // altitude (in kilometres)

   vector<vector<float> > X;               // mixing ratios

   float rho[nlayers], rho_prime[nlayers];
   float tau[nlayers], exptau[nlayers];


   readAtmFile(atmFile,nlayers,p,Tp,z,X);        // read the file and send reference of arrays (p
        ,Tp,z,X) which will have contents replaced
   //cout << "Values obtained from file " << atmFile << ":" <<endl << endl;


   /* Set default mixing ratios for gases */
   if(option==9){                          // 'testing' mode
        for(int n=0;n<n_gas;n++){
                for(int m=0;m<nlayers;m++) X[n][m] = mixdef;
        }
   } else {
        if(n_gas != X.size()){
                cout<< "\nEXITING:␣number␣of␣.abs␣file␣don't␣match␣mixing␣ratio␣columns␣in␣.atm␣
                     file!" <<endl;
                exit(1);
        }
   }


   /* Calculate number density for each layer and display atm file readout */
   float rho_tot=0.0;

   for (int layer = 0; layer < nlayers; layer++){

                rho[layer] = (p[layer])/(KBOLTZ*Tp[layer]);              // convert p/T to number
                      density, in m^-3

                rho_tot += rho[layer];                                                  // to
                     get total number density along a vertical path (dz)
   }

   cout<< "Number␣density␣at␣surface:␣" << rho[0] << "␣m^-3" <<endl;
   cout<< "Total␣number␣density␣(dz):␣" << rho_tot << "␣m^-3" <<endl;
```

```
/**************************** Calculate path length integral *******************************/

        cout<<endl<<"=========================================="<<endl;
        cout<<"Performing␣calculation....."<<endl;

        cout << endl << "nlayers:␣" << nlayers;
        cout << endl << "Rp:␣" << (Rp/1000.0) << "␣km\t\tz[nlayers]␣(Atm)␣:␣" << (z[nlayers
             -1]/1000.0) << "␣km" << endl;
        cout << "Rp+Atm:␣" << ((Rp+z[nlayers-1])/1000.0) << "␣km" << endl;
        cout << "Scale␣height:␣H␣=␣" << H << "␣km" << endl;
        cout << "MMW:␣mu␣=␣" << atmos.mu << "␣g/mol" << endl << endl;


        float dl, Rsig, Rtau, Csig, Ctau, cld_tau;
                // initialise optical quantities
        double p_bar=0.0, bounds[3]={0.0}, cld_log_rho=0.0, absorption[linecount];
                // initialise cloud parameters and absorption variables


        for (int wl=0;wl < linecount; wl++)             // loop through wavelengths
        {
                /* Calculate scattering cross-sections (wavelength dependence) */
                Rsig = 0.0;                     // Rayleigh cross-section
                Csig = 0.0;                     // CIA cross-section

                if(gridwl[wl]>thres){
                        for(int i=0;i<(atmos.mol_list).size();i++) {
                                Rsig += ( atmos.fraction[i] * scatterRayleigh(gridwl[wl],atmos.
                                     mol_list[i]) );                    // Rayleigh cross-section
                        }
                }

                Csig += scatterCIA(cia_coeffs[wl],atmos.fraction[0]);


                /* Calculate optical path length */
                for (int j=0; j<nlayers; j++)   // loop through atmosphere layers, z[0] to z[
                     nlayers]
                {
                /* Calculate layer lengths, and get optical path */
                        dl = 0.0;                                               // element of path
                             length
                        Rtau = 0.0;                                             // sum of Rayleigh
                             optical depth
                        Ctau = 0.0;                                             // sum of CIA optical
                             depth
                        cld_tau = 0.0;                                          // sum of cloud optical
                             depth
                        tau[j] = 0.0;                                           // total optical depth


                        for (int k=1; k < (nlayers-j); k++) // loop through each layer to sum up
                              path length
                        {
                                dl = 2.0 * (sqrt(pow((Rp + z[k+j]),2) - pow((Rp + z[j]),2)) -
                                     sqrt(pow((Rp + z[k-1+j]),2) - pow((Rp + z[j]),2)));
                                        // Calculate half-path length, and double (from system
                                             geometry) to get full path distance
```

```
                /* Sum up taus for all gases for this path, recall sigma_array
                     [0][*] = wavelengths */
                for(int l=0;l<n_gas;l++) tau[j] += (sigma_array[l+1][wl] * X[l][
                     k+j] * rho[k+j] * dl);


                /* Calculate bulk atmos Rayleigh contribution (wavelength,
                     density, layer length dependence) for this element of path
                     */
                Rtau += Rsig * rho[k+j] * dl;


                /* Calculate CIA contribution (wavelength, density, layer length
                      dependence) for this element of path */
                Ctau += Csig * rho[k+j] * rho[k+j] * dl;

                /* Calculate cloud contribution (wavelength, layer length
                     dependence) for this element of path */
                p_bar = p[k+j] * 1.0e-5;
                                                // convert pressure from Pa to bar

                for(int n=0;n<n_cld;n++){
                        if( (p_bar<up_p_bound[n]) && (p_bar>low_p_bound[n]) ){
                            // then cloud exists in this layer [k+j]

                                bounds[0]=log(low_p_bound[n]);
                                bounds[1]=log(up_p_bound[n]);
                                bounds[2]=log(p_bar);

                                cld_log_rho = interpolateValue(bounds,-6,-1);
                                        // = log(cloud density), assuming linear
                                              decrease with decreasing log
                                             pressure
                                        // following Ackerman & Marley (2001),
                                             Fig. 6

                                cld_tau += ( cld_coeffs[n][wl] * (dl*1.0e2) * (
                                     exp(cld_log_rho)*1.0e-6) );      // convert
                                     path lenth from m to cm, and density from g
                                     m^-3 to g cm^-3

                                //cout<<"Pressure = "<<p[k+j]*1.0e-5<<" bars =
                                     "<<p[k+j]<<" Pa at level "<<k<<endl;
                                //cout<<"Path "<<j<<", section "<<k+j<<": kappa
                                     ="<<cld_coeffs[0][wl]<<" cm^2 g^-1, dl="<<dl
                                     <<" m, rho="<<exp(cld_log_rho)<<"g m^-3"<<
                                     endl;
                                //cout<< "\twl: "<<gridwl[wl]<<"\tCloud tau: "
                                     << cld_tau <<endl<<endl;
                        }
                }

        }


        /* Include extra opacities (scattering etc.) */
        tau[j] += Rtau;
        tau[j] += Ctau;
        tau[j] += cld_tau;

        exptau[j] = exp(-tau[j]);
}
```

```
                /* Calculate area of circles of atmos (mediated by e^-tau), and sum */
                double integral=0.0;
                double dz[nlayers];
                for(int j=0; j<(nlayers-1); j++) dz[j] = z[j+1] - z[j];
                for(int j=(nlayers-1); j<nlayers; j++) dz[j] = dz[j-1];
                for(int j=0; j<nlayers; j++) integral += ((Rp+z[j])*(1-exptau[j])*dz[j]);
                integral*=2.0;

                absorption[wl] = ((Rp*Rp) + integral) / (rad_star[wl]*rad_star[wl]);

        }


        /* Output to file */
        ofstream myfile (outFile);
        if (myfile.is_open()){
                for(int wl=0;wl < linecount; wl++){
                        myfile << gridwl[wl] << "\t␣" << absorption[wl] << endl;
                        //cout << gridwl[wl] << "\t " << absorption[wl] << endl;
                }
                myfile.close();

        } else {
                cout << "Unable␣to␣open␣file" << endl;
                exit(1);
        }
        cout << "Complete.\nData␣in␣" << outFile << ",␣in␣2␣columns:\n\n\tWL␣(microns)␣\
            tAbsorption\n\n";


const double prog_end=omp_get_wtime();
cout<<"Total␣runtime:␣"<< prog_end-prog_start <<endl;

return(0);

}
```

D.0.2 Functions.h

```
/**************************** The headers ***************************/
#include <iostream>
#include <iomanip>
#include <fstream>
#include <string.h>
#include <string>
#include <sstream>
#include <cstdlib>
#include <ctime>
#include <cmath>
#include <limits>
#include <algorithm>
#include <vector>
#include <omp.h>
using namespace std;



/**************************** The definitions *************************/
#define EVER ;;
#define TINY std::numeric_limits< double >::min()
#define VBIG std::numeric_limits< double >::max()
#define PI 3.14159265   // pi
#define d2s 86400               // day-to-second conversion constant
#define d2r PI/180.             // degree-to-radian conversion constant
#define r2d 180./PI             // radian-to-degree conversion constant

const double    RSOL=6.955e8;                   // radius of the Sun (m)
const double    MSOL=1.9891e30;                 // mass of the Sun (kg)
const double    RJUP=6.9911e7;                  // radius of Jupiter (m)
const double    MJUP=1.8986e27;                 // mass of Jupiter (kg)
const double    REARTH=6.371e3;                 // radius of Earth (m)
const double    MEARTH=5.9736e24;               // mass of Earth (kg)
const double    AU=1.49e11;                             // 1 AU (m)
const double    KBOLTZ=1.380648813e-23; // Boltzmann's constant (J/K)
const double    AMU=1.660538921e-27;    // Atomic mass unit (kg)
const double    AVOGADRO=6.0221415e23;  // Avogadro's number
const double    RGAS=AVOGADRO*KBOLTZ;   // Universal gas constant (J/K/mol)
const double    LO=2.68676e+25;                 // Loschmidt's number (m^-3)
const double    AMA=2.68676e+25;                // Amagat (molecules m^-3)



/**************************** The classes ***************************/

class Mol {
  public:
        Mol(string mol, double wt, double rad, double rdx) {
                name=mol;               // molecule name
                weight=wt;              // relative molecular weight (amu)
                radius=rad;             // molecular radius (m)
                rindx=rdx;              // refractive index
        }       // class constructor

        string name;
        double weight, radius, rindx;
};


class Atmos {
```

```
  public:
        Atmos() {mu=0.0;def_mu=2.3;}     // class constructor

        vector<Mol> mol_list;
        vector<double> fraction;
        double def_mu;  // default atmos 85% H2, 15% H2 --> mu~2.3
        double mu;

        void ADD_MOL(Mol, double);
        void GET_MMW();
        int CHECK_ATMOS();
};

void Atmos::ADD_MOL(Mol mol, double frac){
        // input mass mixing ratio as 'frac', such that e.g. if atmosphere 80% H2, frac_H2=0.8

        mol_list.push_back(mol);
        fraction.push_back(frac);
}

void Atmos::GET_MMW(){
        int nmols=mol_list.size();

        for(int i=0;i<nmols;i++) mu += (fraction[i] * mol_list[i].weight);
}

int Atmos::CHECK_ATMOS(){
        int nmols=mol_list.size();
        double tot_frac=0.0;

        for(int i=0;i<nmols;i++) tot_frac += fraction[i];

        return((tot_frac != 1.0) ? 0 : 1);
}



/*************************** The functions ***************************/

/* Usage instructions */
#ifndef instructions_H
#define instructions_H
void instructions(char argv[256])
{
        cout << "Usage:␣" << argv << "␣0␣[[atmfile]]␣[absfile]" << endl;
        cout << "\tor␣" << argv << "␣1␣[atmfile]" << endl;

        cout << "\n\t0,1:␣Only␣options␣for␣now.␣\n\t"
        << "atmfile:␣optional␣(if␣no␣absfile␣specified).␣If␣not␣provided,␣default␣atm␣file␣used\
            n\t"
        << "absfile:␣optional.␣If␣not␣provided,␣default␣abs␣file␣used\n\t" << endl;
        exit(1);
}
#endif



/* Option sorting */
#ifndef optionSort_H
#define optionSort_H
void optionSort(int option, int argc, char* argv[], vector<string> &arg_btFile, string &
    arg_atmFile)
{
```

```
// What to do with entered options
        int trigger2=0,trigger3=0;

        if (argc <= 1)          // if no arguments provided at program execution, display usage
             instructions
        {
                instructions(argv[0]);
        }
        else if (argc <= 3)             // prevent console giving rubbish values into arguments.
              Checks count of arguments
        {
                trigger2=1;
        }
        else if (argc <=4)
        {
                trigger2=1;
                trigger3=1;             // if we have 4 argv: (filename, 0, myatm, myabs) myatm
                     and myabs MUST be present!
        }


        if (option == 0)  // what to do with arguments 0= single file read; 1= user input abs
             files
        {
                if (!argv[2])           // if no argument #2 given, switch to default
                {
                        arg_atmFile = "./run/profile.atm";
                        cout << "\nNo␣atm␣file␣provided␣in␣arguments,␣using␣code␣default...\n";


                }
                else {
                        arg_atmFile = argv[2];
                        cout << "You␣have␣provided␣atm␣file:␣" << arg_atmFile << endl;
                }

                if (!argv[3] || (trigger3 == 0))        // if no argument #3 given, console
                     sends garbage as value 3 sometimes, use trigger to prevent this
                {
                        arg_btFile.push_back("./run/h2o_1500K.abs");
                        cout << "No␣abs␣file␣provided␣in␣arguments,␣using␣code␣default...\n";
                }
                else {
                        arg_btFile.push_back(argv[3]);
                        cout << "You␣have␣provided␣abs␣file:␣" << arg_btFile[0] << endl;
                }

        }
        else if (option == 1)  // what to do with arguments 0=file read 1= user input abs files
        {
                if (!argv[2])           // if no argument #2 given, switch to default
                {
                        arg_atmFile = "./run/profile.atm";
                        cout << "\nNo␣atm␣file␣provided␣in␣arguments,␣using␣code␣default...\n";


                }
                else {
                        arg_atmFile = argv[2];
                        cout << "You␣have␣provided␣atm␣file:␣" << arg_atmFile << endl;
                }
```

```
                string input="";
                cout<< "\nEnter␣names␣of␣gas␣absorption␣coefficient␣files"<<endl;
                cout<< "\t(enter␣'x'␣when␣done):␣" <<endl;

                for(EVER){
                   getline(cin, input);
                   if(input=="x") break;
                   else arg_btFile.push_back(input);
                }

        }
        else if (option == 9)           // testing mode
        {
                arg_atmFile = "./run/profile.atm";

                arg_btFile.push_back("./run/h2o_1500K.abs");
        }
        else{   // END OF FILE READ
                cout << "\nPlease␣use␣option␣'0',␣'1'␣or␣'9'.\n" << endl;
                instructions(argv[0]);
        }
}
#endif



/* Get number of lines in a file, assuming header of 11 lines present at TOF */
#ifndef getNumberLines_H
#define getNumberLines_H
int getNumberLines(const char* filename)
{
        string line, line1;
        ifstream myfile (filename);     // open once to count number of lines (up to ***** line OR file end)
        int linecount=1, totalline;
        if (myfile.is_open())
        {
                while ( myfile.good() )
                {
                        getline (myfile,line);
                        if (line == "******") break;
                        linecount++;
                }
                totalline = linecount;
                linecount=1;
        }
        else
        {
                cout << "\nUnable␣to␣open␣file␣" << filename << endl << "Exiting␣program...\n" << endl;
                exit(1);
        }

        myfile.close();                                 // close file

        //cout << "Total lines: " << totalline << endl;

        return totalline-11;

}
#endif
```

```
/* Function to read in file of absorption cross-sections */
#ifndef readAbsFile_H
#define readAbsFile_H
int readAbsFile(char *file, vector<double> &wl, vector<double> &sig)
{
        /* Read data in (abs c/s file, with wavelength in micron, sigma in cm^2) */
        ifstream the_file (file);
        vector<double> in_data;
        double  d=0.0;

        if(!the_file.is_open()){
          cout<< "Error␣opening␣data␣file␣'" << file << "'" <<endl;
          return(1);
        }
        else while(the_file >> d) in_data.push_back(d); // read from file and put in in_data

        the_file.close();        // close file after read-in


        /* Re-organise data, and convert sigma units to m^2 */
        int n_cols=2;

        if(in_data[0]<in_data[2]){        //reverse order (into wavelength decreasing)
                for(int i=in_data.size()-1;i>0;i-=n_cols){
                   wl.push_back(in_data[i-1]);
                   sig.push_back(in_data[i]*1.0e-4);
                }
        } else{
                for(int i=0;i<in_data.size();i+=n_cols){
                   wl.push_back(in_data[i]);
                   sig.push_back(in_data[i+1]*1.0e-4);
                }
        }

   int btlines = getNumberLines(file);
   btlines+=11; // due to totallines-11 in readNumberLines
   cout << "\nabs␣lines␣read:␣" << btlines << endl;

return(0);
}
#endif




/* Function to interpolate single values */
#ifndef interpolateValue_H
#define interpolateValue_H
double interpolateValue(double *bounds, double sig1, double sig2)
{
  /* Extract bounds... */
  const double y_low = *(bounds);
  const double y_high = *(bounds+1);
  const double new_y = *(bounds+2);
  //cout<< "Interpolating between "<< *(bounds) << " and " << *(bounds+1) << "....." <<endl;

  /* ...and define a useful value */
  const double factor = (new_y - y_low) / (y_high - y_low);


  /* Calculate new values */
  double new_val = sig1 + ((sig2-sig1) * factor);
```

```
        //interpolation formula

return(new_val);
}
#endif




/* Function to interpolate absorption cross-section files to same wavelength grid */
#ifndef interpolateAbs_H
#define interpolateAbs_H
int interpolateAbs(vector<char*> &files, vector<vector<double> > &sigma, double wl_min, double wl_max, float res, int &n_gas)
{
        /* Define some data vectors */
        vector<double> data_xx, data_yy;        // for input data
        vector<vector<double> > xx, yy;         // for valid input data


        /* Read in .abs files */
        for(int i=0;i<files.size();i++){
           if(!readAbsFile(files[i],data_xx,data_yy)){          // then .abs file read succesful
                        xx.push_back(data_xx);                  // add input data to 'valid data' array s.t. each row is a different gas
                        yy.push_back(data_yy);

                        data_xx.clear();
                        data_yy.clear();
           }
        }


        /* Calculate over defined range, or largest range covered by absorption cross-sections */
        if(wl_max<wl_min){
                if(xx.size()>1){

                        wl_max=max(xx[0][1],xx[1][1]);
                        wl_min=min(xx[0][xx[0].size()-2],xx[1][xx[1].size()-2]);
                                // get largest and smallest overall wavelength values (initial values from first file)

                        for(int i=2;i<n_gas;i++){
                                wl_max=max(wl_max,xx[i][1]);
                                wl_min=min(wl_min,xx[i][xx[i].size()-2]);
                                        // NB need an extra value each end for upper/lower interpolation bounds for max/min values
                        }
                        // updating initial values if range is different for subsequent files

                } else{
                        wl_max=xx[0][0];
                        wl_min=xx[0][xx[0].size()-1];
                }

        } else if(wl_max == wl_min){
                        cout<<"Zero␣range!␣Exiting....."<<endl;
                        exit(1);
        }
        cout<<"\tfrom␣"<<wl_min<<"␣to␣"<<wl_max<<"␣microns"<<endl;


        if(n_gas != xx.size()) cout<<"New␣n_gas␣=␣"<<xx.size()<<endl;
```

```
if(!(n_gas=xx.size())) cout<<"No␣molecules␣entered!␣"<<endl;

const double startTime = omp_get_wtime();


/* Layout wavelength grid at even intervals */
int i=0;
for(i=0;(wl_max-(i*res)) > wl_min;i++) sigma[0].push_back(wl_max - (i*res));
        // top row of sigma 2d array is for wavelengths,
        // and now i=number of lines=wl.size()=sigma[0][*].size()


/* Interpolate from files */
for(int n=0;n<n_gas;n++){                       // loop through gases

        /* Initialise gas abs coeff slots for gas n */
        for(int i=0;i<sigma[0].size();i++) sigma[n+1].push_back(0.0);


        /* Create a parallel region */
        //#pragma omp parallel num_threads(1)                // specify num_threads
            ...
        #pragma omp parallel                                                    // ...or
             use default num_threads
        {
                const int thread_id=omp_get_thread_num();      // get thread id on
                     first pass
                if(n==0){
                        // #pragma omp single
                        //      cout<<endl<<"My name is Legion, for we are "<<
                             omp_get_num_threads() <<endl<<endl;
                }

                double bounds[3]={0.0};


                /* Start parallel loop */
                #pragma omp for schedule(static) nowait
                for(int j=0;j<sigma[0].size();j++){
                /* for every (new) wavelength, find equivalent location in wl grid of
                     original file by going down original file and checking if new value
                     is between orig_wl[k] and orig_wl[k+1] */

                        /* Get interpolation bounds */
                        for(int k=0;k<xx[n].size()-1;k++){             // NB need an
                             extra value each end for upper/lower interpolation bounds
                             for max/min values

                                if(sigma[0][j]==xx[n][k]) sigma[n+1][j] = yy[n][k];
                                        // no interpolation needed - e.g. endpoints of
                                             smallest input file

                                if((sigma[0][j]<xx[n][k]) && (sigma[0][j]>xx[n][k+1])){
                                        /* NB TAKE CARE WITH EQUALITY SIGNS - wl vector
                                             is in DECREASING order, so need
                                                val < orig_wl[k] and
                                                val > orig_wl[k+1] */

                                        bounds[0]=xx[n][k+1];
                                                // TAKE CARE WITH VECTOR ORDER AGAIN
                                        bounds[1]=xx[n][k];
                                        bounds[2]=sigma[0][j];
```

```
                                /* And actually assign value */
                                                sigma[n+1][j] = interpolateValue(bounds,yy[n][k
                                                     +1],yy[n][k]);
                                                        // TAKE CARE WITH VECTOR ORDER AGAIN
                                                break;
                                        }
                                }       // end of interpolation for wavelength lambda_j

                        }       // end of (parallel) loop over wavelengths

                }       // end of parallel region

        }       // end of loop over gases



/* Debug - check interpolation *//*
const double endTime = omp_get_wtime();
const double totalTime = endTime - startTime;

cout<<"Interpolation time: "<< totalTime <<" seconds"<<endl;
/**/

/* Debug - check output *//*
for(int n=0;n<n_gas;n++){

cout<<"Gas "<<n<<"\n================================================"<<endl;
for(int j=0;j<sigma[0].size();j++){
cout<<setprecision(10)<<j<<"\t\t"<<sigma[0][j]<<"\t\t"<<sigma[n+1][j]<<endl;
}
cout<<endl;

}/**/

return(0);
}
#endif





/* Function to interpolate single files to same wavelength grid */
#ifndef interpolateCS_H
#define interpolateCS_H
int interpolateCS(const char *in_file, vector<double> &wl, vector<double> &cs)
{
/*
        VARIABLES:      wl[] = base wavelength grid
                                cs[] = interpolated values at wl[]
                                xx[] = original file wavelength grid
                                yy[] = original file data values
*/


        /* Read data in */
        ifstream the_file (in_file);
        vector<double> in_data;
        int     n_cols=2;
        double  d=0.0;
        vector<double>  xx,yy;          // storage vectors for input cs data

        if(!the_file.is_open()){
```

```
  cout<<endl<< "Error␣opening␣file␣'" << in_file << "'" <<endl;
  return(1);
}
else while(the_file >> d) in_data.push_back(d); //read from file and put in in_data

the_file.close();       //close file after read-in

/* Put input cs data into data vectors */
for(int i=0;i<in_data.size()-1;i+=n_cols){
        xx.push_back(in_data[i]);               // wavelength
        yy.push_back(in_data[i+1]);             // data value
}


/* Interpolate data to base wavelength grid, wl[] */

        /* Create a parallel region */
        #pragma omp parallel
        {
                const int thread_id = omp_get_thread_num();             // get thread id

                double bounds[3]={0.0};


                /* Start parallel loop */
                #pragma omp for schedule(static) nowait
                for(int j=0;j<cs.size();j++){
                /* for every (new) wavelength, find equivalent location in wl grid of
                     original file by going down original file and checking if new value
                     is between orig_wl[k] and orig_wl[k+1] */

                        /* Get interpolation bounds */
                        for(int k=0;k<xx.size()-1;k++)  // NB need an extra value each
                             end for upper/lower interpolation bounds for max/min values
                        {
                                if(wl[j]==xx[k]) cs[j] = yy[k];
                                        //no interpolation needed (values match)

                                else if((wl[j]<xx[k]) && (wl[j]>xx[k+1])){
                                        /* NB TAKE CARE WITH EQUALITY SIGNS - wl vector
                                            is in DECREASING order, so need
                                                val < orig_wl[k] and
                                                val > orig_wl[k+1] */

                                        bounds[0]=xx[k+1];
                                                //TAKE CARE WITH VECTOR ORDER AGAIN
                                        bounds[1]=xx[k];
                                        bounds[2]=wl[j];

                        /* And actually assign value */
                                        cs[j] = interpolateValue(bounds,yy[k+1],yy[k]);
                                        break;
                                }
                        }       // end of interpolation for wavelength lambda_j

                }       // end of (parallel) loop over wavelengths

        }       // end of parallel region


if( (wl.front()>xx.front()) || (wl.back()<xx.back()) ){        //TAKE CARE WITH VECTOR
    ORDER AGAIN
```

```
                cout<< "WARNING:␣range␣doesn't␣match␣model␣wavelength␣grid␣for␣file␣" << in_file
                     <<endl;
        }


/* Debug - check output *//*
for(int j=0;j<cs.size();j++){
        cout<<setprecision(6)<<j<<"\t\t"<<wl[j]<<"\t\t"<<cs[j]<<endl;
}
cout<<endl;
/**/


return(0);
}
#endif






/* Get number of gases in .atm file */
#ifndef getNumberGases_H
#define getNumberGases_H
int getNumberGases(char* filename)
{
        string line, line1;
        ifstream myfile (filename);      // open once to count number of layers (up to ***** line
             OR file end)
        int linecount=1, totalline;
        if (myfile.is_open())
        {
                while ( myfile.good() )
                {
                        getline (myfile,line);
                        if (line == "******") break;
                        linecount++;
                }
                totalline = linecount;
                linecount=1;
        }
        else
        {
                cout << "\nUnable␣to␣open␣file␣" << filename << endl << "Exiting␣program...\n"
                    << endl;
                exit(1);
        }

        myfile.close();                                 // close file

        //cout << "Total lines: " << totalline << endl;

        return totalline-11;

}
#endif




/* Function to read in .atm file */
#ifndef readAtmFile_H
#define readAtmFile_H
```

```
void readAtmFile(char* filename, int numlines, float* arrayP, float* arrayT, float* arrayZ,
    vector<vector<float> > &arrayX)
{

        string line,line1;
        int linecount = 1, totalline=numlines+11, colcount=0, chicount;

        float input1, input2, input3;

        ifstream myfile2 (filename);            // re-open for data read.
        if (myfile2.is_open())
        {


                while ( myfile2.good() )
                {
                        if ((linecount > 10) && (linecount < totalline))
                        {
                                /* Count number of columns in first line of data */
                                if(colcount==0){
                                        string buf;
                                        stringstream ss(line1);
                                        vector<string> tokens;

                                        while(ss >> buf) tokens.push_back(buf);

                                        colcount=tokens.size();
                                        chicount=colcount -3;

                                        if(colcount>3) arrayX.resize(chicount);         //
                                            resize to height=n_chi_cols
                                        else{
                                                cout<< "\nWARNING:␣.atm␣file␣must␣have␣columns␣
                                                    of␣'p,␣T,␣z,␣X1␣[,␣X2,␣...]'!" <<endl;
                                                exit(1);
                                        }
                                }


                                myfile2 >> input1;
                                myfile2 >> input2;
                                myfile2 >> input3;

                                arrayP[totalline-(linecount+1)] = input1;
                                arrayT[totalline-(linecount+1)] = input2;
                                arrayZ[totalline-(linecount+1)] = input3*1000;  // convert from
                                    km to m


                                /* Get mixing ratios in remaining columns */
                                float input4[chicount];
                                for(int i=0;i<chicount;i++){
                                        myfile2 >> input4[i];
                                        arrayX[i].push_back(input4[i]);
                                }

                        }
                        else {
                                //cout << "Ignored line: " << line1 << endl;
                        }
                        getline (myfile2,line1);

                                linecount++;
```

```
                }
                myfile2.close();
        }


}
#endif






/* Function to calculate H2 Rayleigh scattering cross-section */
#ifndef scatterRayleigh_H
#define scatterRayleigh_H
double scatterRayleigh(double lambda, Mol species)
{
/* Formula from Liou 2002, 'An Introduction to Atmospheric Radiation', pp.92-93. Also uses '
    minimum volume' approximation pg.97,
                N_dens = 1 / V_particle .

        Optical depth given by tau = sigma * L * c ; sigma = abs cross-section (m^2), L = path
            length (m), c = concentration (m^-3)

        NB This is for bulk atmos scattering ONLY (assumptions: particles much smaller than
            wavelength, gas sufficiently dense),
        cloud Rayleigh + Mie included in scatterMie function.

        IN: Wavelength (in um), path length (in m)

        OUT: Rayleigh scattering opacity cross-section per particle (in m^2)
*/


   double sigma_R=0.0;                  // Rayleigh absorption coefficient (from Liou, An
        Introduction to Atmospheric Radiation)

   double wl=lambda *1.0e-6;            // convert wavelengths to m

   double rad=species.radius;           // molecular radius (m)

   double r_ind=species.rindx;          // molecular refractive index
   double r_sq=r_ind*r_ind;
   double r_red = (r_sq-1) / (r_sq+2);

   double delta = 0.035;                                        // molecular anisotropy factor
   double f_delta = (6.0+(3.0*delta)) / (6.0-(7.0*delta));      // King correction factor
        if(species.name == "He") f_delta = 1.0;         // no asymmetry for helium molecules

   /* Find cross-section */
   sigma_R = (128.0/3.0) * (pow(PI,5) * pow(rad,6) / pow(wl,4)) *r_red*r_red *f_delta;
        // gives sigma_R in m^2


return(sigma_R);
}
#endif






/* Function to convert H2-H2 CIA coefficients from A. Borysow data into cross-sections */
```

```
#ifndef scatterCIA_H
#define scatterCIA_H
double scatterCIA(double coeff, double amount)
{
/* Optical depth given by tau = alpha * L * c_1 * c_2 ; alpha = abs coeff (cm^5 mol^-2), L =
     path length (cm), c_i = concentration of collider i (mol cm^-3)

        IN: CIA coeffs in (cm^-1 amagat^-2), grid wavelength (in um), path length (in m) and
             total number density dz (in m^-3)

        OUT: H2-H2 collision-induced absorption coefficient (in m^5 mol^-2)
*/


        /* Calculate unit conversion factor from (cm^-1 amagat^-2) to (cm^5 mol^-2), i.e. into
             HITRAN cia format... */
        double conv_factor = 1.0 / pow((AMA*1.0e-6),2);
                // conversion factor from absorption coefficient alpha (cm^-1 amagat^-2) to (cm
                     ^5 mol^-2)
                //        = 1/(AMA^2), with AMA in mol cm^-3

        //double conv_factor = 1.0;


        /* ...and calculate cross-section */
        double alpha = coeff * conv_factor;                     // converting from (cm^-1 amagat
             ^-2) to (cm^5 mol^-2)...

        alpha *= (amount*amount) * 1.0e-10;                     // e.g. composition 85% H2, and
             convert from cm^5 to m^5

return(alpha);
}
#endif
```

Appendix E

Assumption of Local Thermal Equilibrium

In an environment where the molecular radiative relaxation rate is lower than the rate of molecular collisional de-excitations, a Boltzmann distribution of particles can be assumed. Under these conditions, local thermal equilibrium (LTE) is usually assumed, which simplifies radiative transfer calculations.

I investigate here the atmospheric conditions where this assumption holds, for the specific case of the H_2O molecule (in the atmosphere of a hot Jupiter, Earth and Titan), by I calculating the critical density below which radiative relaxation rates are higher than collisional de-excitation rates (i.e. where LTE is no longer valid).

The collisional de-excitation term C_{10} (expressed in s^{-1}) from the upper energy level 1 to the lower level 0, can be expressed as the product of the rate coefficient k_0 (typically expressed as $\mathrm{cm}^3\ \mathrm{s}^{-1}$) and the atmospheric density N (expressed as cm^{-3}):

$$C_{10} = k_0 N \tag{E.1}$$

The rate coefficient k_0 depends on the mean velocity of collisions but also on the probability for a collision to induce a transition out of a vibrationally excited state; this probability needs to be measured or calculated. Equating the Einstein A_{10} coefficient (also expressed in s^{-1}) for spontaneous emissions (from the upper energy level 1 to the lower level 0) to the collisional de-excitation term C_{10}, gives the critical density ($N = N_C$):

$$A_{10} = C_{10} = k_0 N_C \quad \text{(E.2)}$$

$$N_C = A_{10}/k_0 \quad \text{(E.3)}$$

Let us consider the critical density at which the spontaneous emission rate is equal to the collisional de-excitation rate for the H_2O molecule (colliding with H_2). Fig. E.1 shows the rate coefficient k_0 as a function of temperature for the ν_2 vibration transition (010 → 000, at 6.27μm), from Faure *et al.* (2005). For the same vibrational transition, the Einstein A_{10} coefficient rate is 24.460 s^{-1} (Barber *et al.* 2006). The critical density N_C (eq. E.3) for this vibrational transition of H_2O in the context of collisions with H_2 molecules is obtained as a function of temperature. Table E.1 shows the calculated critical densities for a selection of temperature values measured on Fig. E.1.

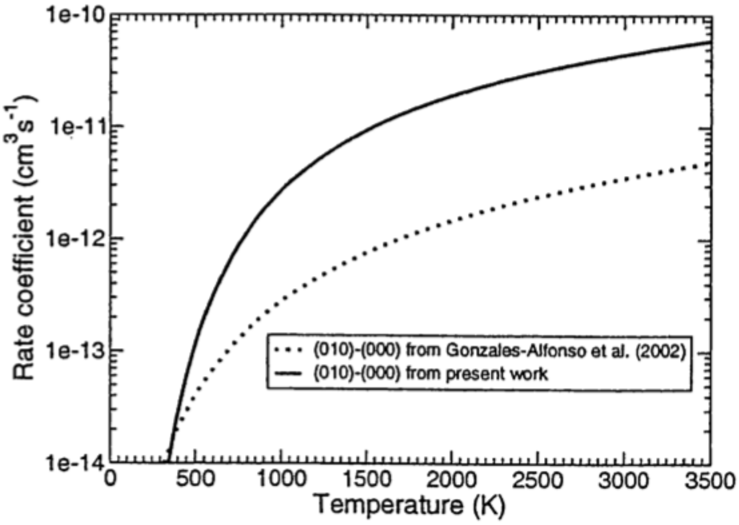

Figure E.1: Rate coefficient k_0 as a function of temperature for the vibrational transition (010) → (000). Figure from Faure *et al.* (2005)

Temperature (K)	250	500	750	1000
Critical Density (cm^{-3})	2.45×10^{15}	2.45×10^{14}	2.45×10^{13}	8.15×10^{12}
Temperature (K)	1250	1500	1750	2000
Critical Density (cm^{-3})	4.89×10^{12}	3.06×10^{12}	2.45×10^{12}	1.22×10^{12}

Table E.1: Critical densities as function of temperature for $H_2O - H_2$ collisional de-excitation rates.

To understand where the location of LTE breakdown in an atmosphere is, the density N of planetary atmospheres can be calculated as a function of pressure and temperature, and compared to these critical densities. Tables E.2, E.3 and E.4 show the results of calculations of atmospheric density as a function of the altitude. The last row in each table shows the ratio of atmospheric density over critical density (N/N_C): where the value is larger than unity, LTE can be assumed. For all three cases considered, the LTE breakdown happens in the upper atmospheres, at very low pressures (typically, below 0.1 mbar). For our radiative transfer calculations, the bulk of absorption and emission phenomena considered occur at much higher pressures, where the LTE assumption is valid. We include atmospheric layers above the LTE limit for the calculation of the optical path.

It is important to note that the $H_2O - H_2$ collisions considered in this discussion are ideal for hydrogen-dominated atmospheres, such as hot Jupiters. For the case of Earth and Titan, the atmospheres are nitrogen-dominated, where the heavier nitrogen molecules lower the critical density, and hence increase the altitude at which the LTE assumption breaks down[1]. The values presented here with $H_2O - H_2$ should thus be regarded as conservative for Earth and Titan. These results agree however with LTE limits presented in the literature, both for Earth (LTE breakdown between 60-70km, (Liou 2002) and Titan (LTE breakdown near 10^{-4} bar, Yelle and Griffith (2003)).
Other measurements of non-LTE signatures on solar system planets, such as the fluorescence of CH4 on Jupiter and Saturn, show LTE breakdown at lower pressures still (order of 10^{-6} bar, Drossart *et al.* (1998)).

---

[1] Tennyson J., private communication

Altitude (km)	0	20	40	60	80	100	120
Pressure (Pa)	1.0×10^5	5.0×10^3	3.0×10^2	2.0×10^1	1.0×10^0	1.0×10^{-2}	5.0×10^{-3}
Temperature (K)	285	221	265	236	185	220	310
Density (cm^{-3})	$2.54{\times}10^{19}$	$1.64{\times}10^{18}$	$8.20{\times}10^{16}$	$6.14{\times}10^{15}$	$3.92{\times}10^{14}$	$3.29{\times}10^{12}$	$1.17{\times}10^{12}$
N/N_C	$1.04{\times}10^4$	$6.69{\times}10^2$	$3.35{\times}10^1$	$2.51{\times}10^0$	$1.60{\times}10^{-1}$	$1.34{\times}10^{-3}$	$4.77{\times}10^{-4}$

Table E.2: Limit of LTE on Earth for $H_2O - H_2$ collisions: the density over critical density N/N_C ratio falls below unity between 60/80km, indicating breakdown of LTE.

Altitude (km)	0	1310	2480	3800	4870	5700	6600	8750
Pressure (Pa)	1.4×10^5	1.7×10^4	1.9×10^3	8.8×10^1	4.6×10^0	4.0×10^{-1}	2.7×10^{-2}	6.1×10^{-5}
Temperature (K)	1815	1551	1263	1000	870	837	837	837
Density (cm^{-3})	$5.59{\times}10^{18}$	$7.94{\times}10^{17}$	$1.09{\times}10^{17}$	$6.37{\times}10^{15}$	$3.83{\times}10^{14}$	$3.46{\times}10^{13}$	$2.34{\times}10^{12}$	$5.28{\times}10^9$
N/N_C	$2.28{\times}10^5$	$3.25{\times}10^4$	$4.45{\times}10^3$	$2.61{\times}10^2$	$1.57{\times}10^1$	$1.42{\times}10^0$	$9.55{\times}10^{-2}$	$2.16{\times}10^{-4}$

Table E.3: Limit of LTE in a hot Jupiter atmosphere for $H_2O - H_2$ collisions: the density over critical density N/N_C ratio falls below unity near an altitude of 6000km, indicating breakdown of LTE.

Altitude (km)	0	100	200	400	700	1000	1200
Pressure (Pa)	1.0×10^5	1.0×10^3	1.0×10^2	1.0×10^0	5.0×10^{-3}	5.0×10^{-5}	1.0×10^{-6}
Temperature (K)	50	140	170	170	150	175	175
Density (cm^{-3})	$1.45{\times}10^{20}$	$5.17{\times}10^{17}$	$4.26{\times}10^{16}$	$4.26{\times}10^{14}$	$2.41{\times}10^{12}$	$2.07{\times}10^{10}$	$4.14{\times}10^8$
N/N_C	$5.92{\times}10^4$	$2.12{\times}10^2$	$1.74{\times}10^1$	$1.74{\times}10^{-1}$	$9.87{\times}10^{-4}$	$8.46{\times}10^{-6}$	$1.69{\times}10^{-7}$

Table E.4: Limit of LTE on Titan for $H_2O - H_2$ collisions: the density over critical density N/N_C ratio falls below unity near an altitude of 200-400km, indicating breakdown of LTE (consistent with Yelle and Griffith (2003), who found the breakdown at ~ 0.1 mbar).

Bibliography

Agol, E., Cowan, N. B., Knutson, H. A., Deming, D., Steffen, J. H., *et al.* *ApJ*, 721:1861–1877 (2010). `arXiv:astro-ph/10074378`.

Bakos, G., Afonso, C., Henning, T., Jordán, A., Holman, M., *et al.* In *Transiting Planets, Proceedings of the International Astronomical Union, IAU Symposium*, volume 253, pages 354–357 (2009).

Bakos, G. Á., Lázár, J., Papp, I., Sári, P., and Green, E. M. *PASP*, 114:974–987 (2002). `arXiv:astro-ph/0206001`.

Ballerini, P., Micela, G., Lanza, A. F., and Pagano, I. *A&A*, 539:A140 (2012). `arXiv:astro-ph/12013514`.

Barber, R. J., Tennyson, J., Harris, G. J., and Tolchenov, R. N. *MNRAS*, 368:1087–1094 (2006). `arXiv:astro-ph/0601236`.

Barstow, J. K., Aigrain, S., Irwin, P. G. J., Bowles, N., Fletcher, L. N., and Lee, J.-M. *MNRAS*, 430:1188–1207 (2013).

Baruteau, C., Meru, F., and Paardekooper, S.-J. *MNRAS*, 416:1971–1982 (2011). `arXiv:astro-ph/11060487`.

Basri, G., Walkowicz, L. M., Batalha, N., Gilliland, R. L., Jenkins, J., *et al.* *ApJL*, 713:L155–L159 (2010). `arXiv:astro-ph/10010414`.

Basri, G., Walkowicz, L. M., Batalha, N., Gilliland, R. L., Jenkins, J., *et al.* *AJ*, 141:20 (2011). `arXiv:astro-ph/10081092`.

Basri, G., Walkowicz, L. M., and Reiners, A. *ApJ*, 769:37 (2013).

Batalha, N. M., Rowe, J. F., Bryson, S. T., Barclay, T., Burke, C. J., *et al.* *ApJSS*, 204:24 (2013). `arXiv:astro-ph/12025852`.

Bean, J. L., Miller-Ricci Kempton, E., and Homeier, D. *Nature*, 468:669–672 (2010). `arXiv:astro-ph/10120331`.

Beaulieu, J.-P., Bennett, D. P., Fouqué, P., Williams, A., Dominik, M., *et al.* *Nature*, 439:437–440 (2006). `arXiv:astro-ph/0601563`.

Beaulieu, J. P., Carey, S., Ribas, I., and Tinetti, G. *ApJ*, 677:1343–1347 (2008). `arXiv:astro-ph/07112142`.

Beaulieu, J. P., Kipping, D. M., Batista, V., Tinetti, G., Ribas, I., *et al.* *MNRAS*, 409:963–974 (2010). `arXiv:astro-ph/09090185`.

Beaulieu, J.-P., Tinetti, G., Kipping, D. M., Ribas, I., Barber, R. J., *et al.* *ApJ*, 731:16 (2011). `arXiv:astro-ph/10070324`.

Berta, Z. K., Irwin, J., Charbonneau, D., Burke, C. J., and Falco, E. E. *AJ*, 144:145 (2012). `arXiv:astro-ph/12064715`.

Beuzit, J.-L., Feldt, M., Dohlen, K., Mouillet, D., Puget, P., *et al.* In *Society of Photo-Optical Instrumentation Engineers (SPIE) Conference Series*, volume 7014 (2008).

Bohr, N. *Philosophical Magazine Series 6*, 26(151):1–25 (1913).

Bonnefoy, M., Boccaletti, A., Lagrange, A.-M., Allard, F., Mordasini, C., *et al.* *A&A*, 555:A107 (2013). `arXiv:astro-ph/13021160`.

Borucki, W. J., Koch, D., Jenkins, J., Sasselov, D., Gilliland, R., *et al.* *Science*, 325:709 (2009).

Borucki, W. J., Koch, D. G., Basri, G., Batalha, N., Brown, T. M., *et al.* *ApJ*, 736:19 (2011). `arXiv:astro-ph/11020541`.

Bouchy, F., Udry, S., Mayor, M., Moutou, C., Pont, F., *et al.* *A&A*, 444:L15–L19 (2005). `arXiv:astro-ph/0510119`.

Bracewell, R. N. *Nature*, 274:780 (1978).

Broeg, C., Fortier, A., Ehrenreich, D., Alibert, Y., Baumjohann, W., *et al.* In *European Physical Journal Web of Conferences*, volume 47, page 3005 (2013). `arXiv:astro-ph/13052270`.

Burrows, A., Budaj, J., and Hubeny, I. *ApJ*, 678:1436–1457 (2008). `arXiv:astro-ph/07094080`.

Butler, R. P., Vogt, S. S., Marcy, G. W., Fischer, D. A., Wright, J. T., *et al.* *ApJ*, 617:580–588 (2004). `arXiv:astro-ph/0408587`.

Casertano, S., Lattanzi, M. G., Sozzetti, A., Spagna, A., Jancart, S., *et al.* *A&A*, 482:699–729 (2008).

Casertano, S. and Sozzetti, A. In *Working on the Fringe: Optical and IR Interferometry from Ground and Space*, *Astronomical Society of the Pacific Conference Series*, volume 194, page 171 (1999).

Cassan, A., Kubas, D., Beaulieu, J.-P., Dominik, M., Horne, K., *et al.* *Nature*, 481:167–169 (2012). `arXiv:astro-ph/12020903`.

Chandrasekhar, S. *Radiative transfer.* International series of monographs on physics. Clarendon Press (1950).

Charbonneau, D., Berta, Z. K., Irwin, J., Burke, C. J., Nutzman, P., *et al.* *Nature*, 462:891–894 (2009). `arXiv:astro-ph/09123229`.

Charbonneau, D., Brown, T. M., Noyes, R. W., and Gilliland, R. L. *ApJ*, 568:377–384 (2002). `arXiv:astro-ph/0111544`.

Charbonneau, D., Knutson, H. A., Barman, T., Allen, L. E., Mayor, M., *et al.* *ApJ*, 686:1341–1348 (2008). `arXiv:astro-ph/08020845`.

Ciardi, D. R., von Braun, K., Bryden, G., van Eyken, J., Howell, S. B., *et al.* *AJ*, 141 (2011). `arXiv:astro-ph/10091840`.

Conrath, B. J., Hanel, R. A., Kunde, V. G., and Prabhakara, C. *Journal of Geographical Research*, 75:5831 (1970).

Cosentino, R., Lovis, C., Pepe, F., Collier Cameron, A., Latham, D. W., *et al.* In *Society of Photo-Optical Instrumentation Engineers (SPIE) Conference Series*, volume 8446 (2012).

Cowan, N. B. and Agol, E. *ApJL*, 678:L129–L132 (2008). `arXiv:astro-ph/08033622`.

Cowan, N. B. and Agol, E. *ApJ*, 726:82 (2011). `arXiv:astro-ph/10110428`.

Cowan, N. B., Agol, E., and Charbonneau, D. *MNRAS*, 379:641–646 (2007). `arXiv:astro-ph/07051189`.

Crossfield, I. J. M., Barman, T., Hansen, B. M. S., and Howard, A. W. *A&A*, 559:A33 (2013). `arXiv:astro-ph/13086580`.

Crossfield, I. J. M., Hansen, B. M. S., Harrington, J., Cho, J. Y.-K., Deming, D., *et al.* *ApJ*, 723:1436–1446 (2010). `arXiv:astro-ph/10080393`.

Crouzet, N., McCullough, P. R., Burke, C., and Long, D. *ApJ*, 761:7 (2012). `arXiv:astro-ph/12105275`.

Currie, T., Burrows, A., Madhusudhan, N., Fukagawa, M., Girard, J. H., *et al.* *ApJ*, 776:15 (2013). `arXiv:astro-ph/13060610`.

de Kok, R. J., Brogi, M., Snellen, I. A. G., Birkby, J., Albrecht, S., and de Mooij, E. J. W. *A&A*, 554:A82 (2013). `arXiv:astro-ph/13044014`.

Deleuil, M., Moutou, C., and Bordé, P. In *European Physical Journal Web of Conferences*, volume 11, page 1001 (2011). `arXiv:astro-ph/11051887`.

Deming, D., Wilkins, A., McCullough, P., Burrows, A., Fortney, J. J., *et al.* *ApJ*, 774:95 (2013). `arXiv:astro-ph/13021141`.

DeMore, W. and Yung, Y. *Photochemistry of Planetary Atmospheres.* Oxford University Press, USA (1998). ISBN 9780195344509.

Demory, B.-O., Torres, G., Neves, V., Rogers, L., Gillon, M., *et al.* *ApJ*, 768:154 (2013). `arXiv:astro-ph/13016555`.

Drossart, P., Fouchet, T., Crovisier, J., Lellouch, E., Encrenaz, T., *et al.* In *AAS/Division for Planetary Sciences Meeting Abstracts #30*, *Bulletin of the American Astronomical Society*, volume 30, page 1066 (1998).

Einstein, A. *Science*, 84:506–507 (1936).

Faure, A., Wiesenfeld, L., Wernli, M., and Valiron, P. In *ESA Special Publication*, volume 577, pages 361–362 (2005).

Forget, F. and Leconte, J. *Phil. Trans. R. Soc. A*, 372 (2014). `arXiv:astro-ph/13113101`.

Fressin, F., Torres, G., Charbonneau, D., Bryson, S. T., Christiansen, J., *et al.* *ApJ*, 766:81 (2013). `arXiv:astro-ph/13010842`.

Frith, J., Pinfield, D. J., Jones, H. R. A., Barnes, J. R., Pavlenko, Y., *et al.* *MNRAS*, 435:2161–2170 (2013). `arXiv:astro-ph/13080501`.

Fukui, A., Narita, N., Kurosaki, K., Ikoma, M., Yanagisawa, K., *et al.* *ApJ*, 770:95 (2013). `arXiv:astro-ph/13027257`.

Gaidos, E. and Williams, D. M. *New Astronomy*, 10:67–77 (2004).

Gaudi, B. S. *Microlensing by Exoplanets*, pages 79–110. University of Arizona Press, Tucson, AZ (2011). ISBN 978-0-8165-2945-2.

Geiger, H. and Marsden, E. *Proceedings of the Royal Society of London. Series A*, 82(557):495–500 (1909).

Gillon, M., Pont, F., Demory, B.-O., Mallmann, F., Mayor, M., *et al.* *A&A*, 472:L13–L16 (2007). `arXiv:astro-ph/07052219`.

Goody, R. and Yung, Y. *Atmospheric Radiation: Theoretical Basis.* Oxford University Press, Oxford, UK (1995). ISBN 9780195356106.

Gould, A. and Yee, J. C. *ApJ*, 764:107 (2013). `arXiv:astro-ph/12121732`.

Grasset, O., Schneider, J., and Sotin, C. *ApJ*, 693:722–733 (2009). `arXiv:astro-ph/09021640`.

Grillmair, C. J., Burrows, A., Charbonneau, D., Armus, L., Stauffer, J., *et al.* *Nature*, 456:767–769 (2008). `arXiv:astro-ph/09014774`.

Hanel, R. A., Conrath, B. J., Jennings, D. E., and Samuelson, R. E. *Exploration of the Solar System by Infrared Remote Sensing: Second Edition.* Cambridge University Press (2003). ISBN 9780521818971.

Harrington, J., Hansen, B. M., Luszcz, S. H., Seager, S., Deming, D., *et al.* *Science*, 314:623–626 (2006). `arXiv:astro-ph/0610491`.

Hartung, M., Macintosh, B., Poyneer, L., Savransky, D., Gavel, D., *et al.* In *Proceedings of the Third AO4ELT Conference* (2013). `arXiv:astro-ph/13114423`.

Hauschildt, P. H., Allard, F., and Baron, E. *ApJ*, 512:377–385 (1999). `arXiv:astro-ph/9807286`.

Hearty, T., Song, I., Kim, S., and Tinetti, G. *ApJ*, 693:1763–1774 (2009). `arXiv:astro-ph/08102957`.

Herzberg, G. and Spinks, J. *Molecular Spectra and Molecular Structure: Diatomic molecules*. Prentice-Hall physics series. Van Nostrand (1950).

Hollis, M. D. J., Tessenyi, M., and Tinetti, G. *Astrophysics Source Code Library*, page 5014 (2013). Record ascl:1305.014, `arXiv:astro-ph/13052787`.

Iro, N. and Deming, L. D. *ApJ*, 712:218–225 (2010).

Jacquinet-Husson, N., Crepeau, L., Armante, R., Boutammine, C., Chdin, A., *et al.* *Journal of Quantitative Spectroscopy and Radiative Transfer*, 112(15):2395 – 2445 (2011). ISSN 0022-4073.

Janson, M., Brandt, T. D., Kuzuhara, M., Spiegel, D. S., Thalmann, C., *et al.* *ApJL*, 778:L4 (2013). `arXiv:astro-ph/13104183`.

Joshi, M. M., Haberle, R. M., and Reynolds, R. T. *Icarus*, 129:450–465 (1997).

Jovanovic, N., Guyon, O., Martinache, F., Clergeon, C., Singh, G., *et al.* In *Proceedings of the Third AO4ELT Conference* (2013). `arXiv:astro-ph/13100476`.

Knutson, H. A., Charbonneau, D., Allen, L. E., Fortney, J. J., Agol, E., *et al.* *Nature*, 447:183–186 (2007a). `arXiv:astro-ph/07050993`.

Knutson, H. A., Charbonneau, D., Cowan, N. B., Fortney, J. J., Showman, A. P., *et al.* *ApJ*, 690:822–836 (2009a). `arXiv:astro-ph/08021705`.

Knutson, H. A., Charbonneau, D., Cowan, N. B., Fortney, J. J., Showman, A. P., *et al.* *ApJ*, 703:769–784 (2009b). `arXiv:astro-ph/09081977`.

Knutson, H. A., Charbonneau, D., Noyes, R. W., Brown, T. M., and Gilliland, R. L. *ApJ*, 655:564–575 (2007b). `arXiv:astro-ph/0603542`.

Knutson, H. A., Madhusudhan, N., Cowan, N. B., Christiansen, J. L., Agol, E., *et al.* *ApJ*, 735:27 (2011). `arXiv:astro-ph/11042901`.

Konopacky, Q. M., Barman, T. S., Macintosh, B. A., and Marois, C. *Science*, 339:1398–1401 (2013). `arXiv:astro-ph/13033280`.

Kurucz, H. L. In *Laboratory and Astronomical High Resolution Spectra*, *Astronomical Society of the Pacific Conference Series*, volume 81, pages 17–31 (1995).

Langton, J. and Laughlin, G. *ApJ*, 674:1106–1116 (2008). `arXiv:astro-ph/07112106`.

Lee, J.-M., Fletcher, L. N., and Irwin, P. G. J. *MNRAS*, 420:170–182 (2012). `arXiv:astro-ph/11102934`.

Lépine, S. and Gaidos, E. *AJ*, 142:138 (2011). `arXiv:astro-ph/11082719`.

Lewis, N. K., Showman, A. P., Fortney, J. J., Marley, M. S., Freedman, R. S., and Lodders, K. *ApJ*, 720:344–356 (2010). `arXiv:astro-ph/10072942`.

Lindegren, L. In *IAU Symposium*, volume 261, pages 296–305 (2010).

Line, M. R., Liang, M. C., and Yung, Y. L. *ApJ*, 717:496–502 (2010). `arXiv:astro-ph/10044029`.

Line, M. R., Zhang, X., Vasisht, G., Natraj, V., Chen, P., and Yung, Y. L. *ApJ*, 749:93 (2012). `arXiv:astro-ph/11112612`.

Liou, K. *An Introduction to Atmospheric Radiation*. International geophysics series. Academic Press (2002). ISBN 9780124514515.

Madhusudhan, N. and Seager, S. *ApJ*, 707:24–39 (2009). `arXiv:astro-ph/09101347`.

Marois, C., Zuckerman, B., Konopacky, Q. M., Macintosh, B., and Barman, T. *Nature*, 468:1080–1083 (2010). `arXiv:astro-ph/10114918`.

Mayor, M., Pepe, F., Queloz, D., Bouchy, F., Rupprecht, G., *et al.* *The Messenger*, 114:20–24 (2003).

Mayor, M. and Queloz, D. *Nature*, 378:355–359 (1995).

Moses, J. I. *Phil. Trans. Roy. Soc. A*, 372 (2014). `arXiv:astro-ph/13075450`.

Moses, J. I., Visscher, C., Fortney, J. J., Showman, A. P., Lewis, N. K., *et al.* *ApJ*, 737:15 (2011). `arXiv:astro-ph/11020063`.

Mueller, H. S., Schlder, F., Stutzki, J., and Winnewisser, G. *Journal of Molecular Structure*, 742(13):215 – 227 (2005). ISSN 0022-2860.

Neyman, J. and Pearson, E. S. *Biometrika*, 20A(1/2):pp. 175–240 (1928). ISSN 00063444.

Nutzman, P. and Charbonneau, D. *PASP*, 120:317–327 (2008). `arXiv:astro-ph/07092879`.

Öberg, K. I., Murray-Clay, R., and Bergin, E. A. *ApJL*, 743:L16 (2011). `arXiv:astro-ph/11105567`.

Pepe, F. A., Cristiani, S., Rebolo Lopez, R., Santos, N. C., Amorim, A., *et al.* In *Society of Photo-Optical Instrumentation Engineers (SPIE) Conference Series*, volume 7735 (2010).

Perryman, M. A. C. and ESA. In *ESA Special Publication*, volume 1200 (1997).

Planck, M. *Annalen der Physik*, 309(3):553–563 (1901). ISSN 1521-3889.

Pollacco, D. L., Skillen, I., Collier Cameron, A., Christian, D. J., Hellier, C., *et al. PASP*, 118:1407–1418 (2006). `arXiv:astro-ph/0608454`.

Rauscher, E., Menou, K., Seager, S., Deming, D., Cho, J. Y.-K., and Hansen, B. M. S. *ApJ*, 664:1199–1209 (2007). `arXiv:astro-ph/0612412`.

RECONS. *The Research Consortium on Nearby Stars.* `http://www.recons.org` (2011).

Redfield, S., Endl, M., Cochran, W. D., and Koesterke, L. *ApJL*, 673:L87–L90 (2008). `arXiv:astro-ph/07120761`.

Reess, J. M., Tinetti, G., Baier, N., Beaulieu, J. F., Bernardi, P., *et al.* In *Society of Photo-Optical Instrumentation Engineers (SPIE) Conference Series*, volume 8442 (2012).

Ricker, G. R., Latham, D. W., Vanderspek, R. K., Ennico, K. A., Bakos, G., *et al.* In *American Astronomical Society Meeting Abstracts*, volume 214, page 306.05 (2009).

Roeser, S., Demleitner, M., and Schilbach, E. *AJ*, 139:2440–2447 (2010). `arXiv:astro-ph/10035852`.

Rothman, L. S., Gordon, I. E., Barbe, A., Benner, D. C., Bernath, P. F., *et al.* *Journal of Quantitative Spectroscopy & Radiative Transfer*, 110:533–572 (2009).

Rutherford, E. *Philos. Mag*, 21:669 (1911).

Schneider, J. *The extrasolar planets encyclopaedia.* `http://exoplanet.eu/catalog.php` (2014).

Segura, A., Walkowicz, L. M., Meadows, V., Kasting, J., and Hawley, S. *Astrobiology*, 10:751–771 (2010). `arXiv:astro-ph/10060022`.

Selsis, F., Wordsworth, R. D., and Forget, F. *A&A*, 532:A1 (2011). `arXiv:astro-ph/11044763`.

Snellen, I. A. G., Albrecht, S., de Mooij, E. J. W., and Le Poole, R. S. *A&A*, 487:357–362 (2008). `arXiv:astro-ph/08050789`.

Snellen, I. A. G., de Kok, R. J., de Mooij, E. J. W., and Albrecht, S. *Nature*, 465:1049–1051 (2010). `arXiv:astro-ph/10064364`.

Snellen, I. A. G., de Mooij, E. J. W., and Albrecht, S. *Nature*, 459:543–545 (2009). `arXiv:astro-ph/09041208`.

Sozzetti, A. In *EAS Publications Series*, volume 42, pages 55–77 (2010a). `arXiv:astro-ph/09022063`.

Sozzetti, A. *Highlights of Astronomy*, 15:716–717 (2010b). `arXiv:astro-ph/09094465`.

Sozzetti, A. In *EAS Publications Series*, volume 45, pages 273–278 (2011). `arXiv:astro-ph/10123346`.

Sozzetti, A., Bernagozzi, A., Bertolini, E., Calcidese, P., Carbognani, A., *et al.* In *European Physical Journal Web of Conferences*, volume 47, page 3006 (2013). `arXiv:astro-ph/13031275`.

Sozzetti, A., Giacobbe, P., Lattanzi, M. G., Micela, G., Morbidelli, R., and Tinetti, G. *MNRAS*, 437:497–509 (2014). `arXiv:astro-ph/13101405`.

Stamnes, K., Tsay, S.-C., Jayaweera, K., Wiscombe, W., *et al.* *Applied optics*, 27(12):2502–2509 (1988).

Stevenson, K. B., Harrington, J., Nymeyer, S., Madhusudhan, N., Seager, S., *et al.* *Nature*, 464:1161–1164 (2010). `arXiv:astro-ph/10104591`.

Swain, M., Deroo, P., Tinetti, G., Hollis, M., Tessenyi, M., *et al.* *Icarus*, 225:432–445 (2013). `arXiv:astro-ph/12054736`.

Swain, M. R., Bouwman, J., Akeson, R. L., Lawler, S., and Beichman, C. A. *ApJ*, 674:482–497 (2008a). `arXiv:astro-ph/0702593`.

Swain, M. R., Deroo, P., Griffith, C. A., Tinetti, G., Thatte, A., *et al.* *Nature*, 463:637–639 (2010). `arXiv:astro-ph/10022453`.

Swain, M. R., Tinetti, G., Vasisht, G., Deroo, P., Griffith, C., *et al.* *ApJ*, 704:1616–1621 (2009a). `arXiv:astro-ph/09084010`.

Swain, M. R., Vasisht, G., and Tinetti, G. *Nature*, 452:329–331 (2008b).

Swain, M. R., Vasisht, G., Tinetti, G., Bouwman, J., Chen, P., *et al.* *ApJL*, 690:L114–L117 (2009b).

Swinyard, B., Tinetti, G., Eccleston, P., Adriani, A., Beaulieu, J.-P., *et al.* In *Society of Photo-Optical Instrumentation Engineers (SPIE) Conference Series*, volume 8442 (2012).

Tennyson, J. and Yurchenko, S. N. *MNRAS*, 425:21–33 (2012). `arXiv:astro-ph/12040124`.

Terrile, R., Lee, S., Tinetti, G., Fink, W., von Allmen, P., and Huntsberger, T. L. In *Aerospace Conference, 2008 IEEE*, pages 1–9 (2008). ISSN 1095-323X.

Tessenyi, M., Beaulieu, J.-P., Ollivier, M., Tinetti, G., Coudé du Foresto, V., and Reess, J.-M. In *SF2A-2012: Proceedings of the Annual meeting of the French Society of Astronomy and Astrophysics*, pages 255–259 (2012b).

Tessenyi, M., Ollivier, M., Tinetti, G., Beaulieu, J. P., Coudé du Foresto, V., *et al.* *ApJ*, 746:45 (2012a). `arXiv:astro-ph/11111455`.

Tessenyi, M., Tinetti, G., Savini, G., and Pascale, E. *Icarus*, 226:1654–1672 (2013). `arXiv:astro-ph/13084986`.

Tinetti, C. A., G. et al., Swain, M. R., Deroo, P., Beaulieu, J. P., Vasisht, G., *et al. Faraday Discussions*, 147:369 (2010a).

Tinetti, G., Beaulieu, J. P., Henning, T., Meyer, M., Micela, G., *et al. Experimental Astronomy*, 34:311–353 (2012a). `arXiv:astro-ph/11122728`.

Tinetti, G., Deroo, P., Swain, M. R., Griffith, C. A., Vasisht, G., *et al. ApJL*, 712:L139–L142 (2010b). `arXiv:astro-ph/10022434`.

Tinetti, G., Encrenaz, T., and Coustenis, A. *Astronomy and Astrophysics Review*, 21:63 (2013).

Tinetti, G., Meadows, V. S., Crisp, D., Fong, W., Fishbein, E., *et al. Astrobiology*, 6:34–47 (2006).

Tinetti, G., Tennyson, J., Griffith, C. A., and Waldmann, I. *Royal Society of London Philosophical Transactions Series A*, 370:2749–2764 (2012b).

Tinetti, G., Vidal-Madjar, A., Liang, M.-C., Beaulieu, J.-P., Yung, Y., *et al. Nature*, 448:169–171 (2007).

Tran, H., Ngo, N., and Hartmann, J.-M. *Journal of Quantitative Spectroscopy and Radiative Transfer*, 129(0):199 – 203 (2013). ISSN 0022-4073.

Valencia, D., Guillot, T., Parmentier, V., and Freedman, R. S. *ApJ*, 775:10 (2013). `arXiv:astro-ph/13052629`.

Varley, R., Waldmann, I., Pascale, E., Tessenyi, M., Hollis, M., *et al. Experimental Astronomy, Submitted* (2014). `arXiv:astro-ph/14030357`.

Venot, O., Agúndez, M., Selsis, F., Tessenyi, M., and Iro, N. *A&A*, 562:A51 (2014). `arXiv:astro-ph/13125163`.

Venot, O., Hébrard, E., Agúndez, M., Dobrijevic, M., Selsis, F., *et al. A&A*, 546:A43 (2012). `arXiv:astro-ph/12080560`.

Waldmann, I. P., Pascale, E., Tessenyi, M., Spencer, L., Amaral-Rogers, A., *et al. European Planetary Science Congress 2013*, 8:EPSC2013-507 (2013a). `arXiv:astro-ph/13026425`.

WALDMANN, I. P., TINETTI, G., DEROO, P., HOLLIS, M. D. J., YURCHENKO, S. N., and TENNYSON, J. *ApJ*, 766:7 (2013b). `arXiv:astro-ph/13014041`.

WALDMANN, I. P., TINETTI, G., DROSSART, P., SWAIN, M. R., DEROO, P., and GRIFFITH, C. A. *ApJ*, 744:35 (2012). `arXiv:astro-ph/11040570`.

WHEATLEY, P. J., POLLACCO, D. L., QUELOZ, D., RAUER, H., WATSON, C. A., *et al.* In *European Physical Journal Web of Conferences*, volume 47, page 13002 (2013). `arXiv:astro-ph/13026592`.

WILLIAMS, P. K. G., CHARBONNEAU, D., COOPER, C. S., SHOWMAN, A. P., and FORTNEY, J. J. *ApJ*, 649:1020–1027 (2006). `arXiv:astro-ph/0601092`.

WINN, J. N., MATTHEWS, J. M., DAWSON, R. I., FABRYCKY, D., HOLMAN, M. J., *et al.* *ApJL*, 737:L18 (2011). `arXiv:astro-ph/11045230`.

WOLSZCZAN, A. and FRAIL, D. A. *Nature*, 355:145–147 (1992).

WORDSWORTH, R. D., FORGET, F., SELSIS, F., MADELEINE, J.-B., MILLOUR, E., and EYMET, V. *A&A*, 522:A22 (2010). `arXiv:astro-ph/10055098`.

YELLE, R. V. and GRIFFITH, C. A. *Icarus*, 166:107–115 (2003).

YUNG, Y. L. *Icarus*, 72(2):468 – 472 (1987). ISSN 0019-1035.

YURCHENKO, S. N., BARBER, R. J., and TENNYSON, J. *MNRAS* (2011). 413:1828-1834, `arXiv:astro-ph/10111569`.

ZHU, Z., HARTMANN, L., NELSON, R. P., and GAMMIE, C. F. *ApJ*, 746:110 (2012). `arXiv:astro-ph/11116943`.

Acknowledgements

I would like to thank my supervisor Professor Giovanna Tinetti for all her invaluable help throughout the past three years. It is with her guidance that I decided to start a Ph.D., and she has always provided the right vision and direction ever since. More importantly, I think I have learned a lot more than what is written in this document by having been exposed to the front lines of submitting a space mission proposal. Giovanna has always encouraged me to take an active role in the many aspects of this process, and towards the end of this Ph.D. I was strongly involved in the project management. It was a genuine pleasure to work with all the international collaborators on EChO, and I have learned many very valuable lessons throughout this experience.

I want to thank my second supervisor, Professor Alan Aylward, who introduced me to the field of exoplanet research while supervising my MSc. thesis here at UCL, and who has given me very useful advice during my first steps in academic research. In addition, I want to thank all the staff members at UCL who have helped me out at various times and patiently explained things I should probably have been able to understand by myself. In particular, Dr Giorgio Savini, Professor Bruce Swinyard, Professor Jonathan Tennyson and Dr Sergey "Seryoga" Yurchenko.
I also thank my examiners, Professor Ian Howarth and Dr Pierre Drossart, for their thorough review of this thesis and very constructive comments, which have helped improve the quality of the final document.

The best part of the past three years, however, was sharing offices with the Group-A people. The social environment of this department surpasses any I have seen elsewhere — this was one of the reasons why I applied to UCL. By far the most fun I've had was in

G18, and while things calmed down a bit with the years (to the relief of the department), we carried on having a great time together. I've made many friends over these years, and I will keep fond memories of my time as a Ph.D. student here.

Finally, I would like to thank my family, without whose support and care I would have not been able to come close to completing a Ph.D., and my close friends who made sure I stayed (more or less) on schedule with the duration of the Ph.D. ("Have you got a real job yet?").

Last but not least, Mathilde, merci pour tout.